MAGNETISATION DYNAMICS IN MULTILAYER SPINTRONIC MATERIALS

A THESIS SUBMITTED TO THE UNIVERSITY OF MANCHESTER
FOR THE DEGREE OF DOCTOR OF PHILOSOPHY
IN THE FACULTY OF SCIENCE AND ENGINEERING

2021

Harry J. Waring

School of Engineering
Department of Computer Science

Contents

Word Count: 43595

List of Symbols and Abbreviations

The following lists describes the meaning of the symbols and abbreviations used throughout this document.

Symbols-Greek

α	Gilbert damping constant or, in some instances, used to denote angle
α_{eddy}	Eddy current contribution to Gilbert damping
α_s	Spin current contribution to Gilbert damping
Γ	Torque
γ	Gyromagnetic Ratio
Δf	Linewidth (Full Width at Half Max) of frequency swept Ferromagnetic Resonance
Δf_0	Inhomogenous broadening
ΔM	Difference of layer magnetisations
Δt	Time-step
$\Delta\Psi$	Angle between magnetisations in FM/NM/FM multilayers
δ_s	Amplitude of surface roughness
δ_{sd}	Skin depth
δ_w	Domain wall width
ε_r	Permittivity of free space
ε_r	Relative permittivity
ε_w	Energy per domain wall area
θ	Angle of incidence and reflection in specular reflection of X-rays from a surface or, in some instances, used to denote angle of magnetisation vector from specified direction.

Λ	Period of RKKY interlayer exchange coupling
λ	X-ray wavelength
λ_F	Fermi wavelength
λ_{LL}	Landau-Lifshitz damping constant
λ_S	Spontaneous magnetostriction
μ	Isolated magnetic moment
μ_B	Bohr Magneton
μ_0	Permeability of free space
μ_{Perm}	Permeability
μ_r	Relative permeability
ξ'	Mixing between real and imaginary components of magnetic susceptibility
ρ	Resistivity
σ	Conductivity
σ_d	Magnitude of dipolar (Néel) coupling
σ_{film}	Film roughness
σ_{stress}	Uniaxial stress
τ	Relaxation time
ϕ	Flux
ϕ_{Diff}	Phase difference of two resonating magnetic layers
χ	Magnetic susceptibility
$\bar{\bar{\chi}}$	Magnetic susceptibility in tensor form
χ'	Real component of magnetic susceptibility
χ''	Imaginary component of magnetic susceptibility

ω Angular frequency

ω_{antires} Antiresonance angular frequency

ω_H Represents field contributions to dynamic behaviour.

ω_M Represents magnetisation contribution to dynamic behaviour.

ω_{eff} Represents effective magnetisation contribution to dynamic behaviour.

ω_{res} Resonance angular frequency

Symbols-Latin

A Cross-sectional area

A_{ex} Exchange Constant

b Linear background present in S_{12} data

C Curie Constant

c Speed of light

D Exchange Stiffness

d_{L} Half the lattice parameter of a material

E Energy

E_{ani} Magnetic anisotropy energy

E_{ex} Exchange energy

E_{mag} Magnetostatic energy

E_{MCA} Magnetocrystalline anisotropy energy

E_{shape} Shape anisotropy energy

E_{strain} Strain anisotropy energy

E_{surf} Surface anisotropy energy

E_{tot} Total magnetic energy

E_{Zee} Zeeman energy

$\mathcal{E}$ Energy density

$\mathcal{E}_{\mathrm{mag}}$ Magnetostatic energy density

$\mathcal{E}_{\mathrm{surf}}$ Energy density of surface anisotropy

$\mathcal{E}_{\mathrm{tot,sw}}$ Total energy density

$\mathcal{E}_{\mathrm{uni}}$ Uniaxial anisotropy energy density

$\mathcal{E}_{\mathrm{Zee}}$ Energy density of Zeeman energy

e Magnitude of charge of electron

f_{ex} In-plane exchange spin wave frequency

f_{max} Nyquist frequency

f_{res} Resonant frequency

f_{s} Sampling frequency

f Frequency

f_L Larmor frequency

f_{PSSW} Perpendicular stationary spin wave frequency

f_{res} Resonant frequency

g Spectroscopic g-factor

g' Magnetomechanical g-factor

$g_{\mathrm{eff}}^{\uparrow\downarrow}$ Effective interfacial spin mixing conductance

H Externally applied magnetic field (in context of experimental results presented)

H_{c} Coercive field (coercivity)

H_{demag} Demagnetising field

H_{eff} Effective field

H_{k} Anisotropy field

$\mathcal{H}_{\mathrm{ex}}$ Exchange Hamiltonian

H_{ext} Externally applied magnetic field (in context of magnetism theory background)

h The Planck Constant

h_{rf} Small perturbating magnetic field

$\hbar$ The reduced Planck Constant

$\mathcal{J}$ Exchange Integral

J_{IEC} Interlayer exchange coupling strength

J_1 Bilinear coupling constant

J_2 Biquadratic coupling constant

K Spin wave wavevector

k_B Boltzman Constant

$K_{1,2,\ldots,n}$ n^{th} order anisotropy energy density constant

K_f Wavevector of reflected X-ray in X-ray Reflectivity

K_f Wavevector of incident X-ray in X-ray Reflectivity

K_{strain} Strain contribution to anisotropy

K_{surf} Surface contribution to anisotropy

$K_{u,n}$ n^{th} order uniaxial anisotropy energy density constant

K_{Tot} Total anisotropy

K_{vol} Bulk contribution to anisotropy

$k_{\|}$ In-plane wavevector

L Orbital angular momentum of multi-electron system

l Periodicity of roughness

L	Angular momentum of orbital moment in multi-electron system
ℓ	Angular momentum of orbital moment of electron
J	Total angular momentum of multi-electron system
j	Total angular momentum of single electron
j_s	Spin current
M	Magnetisation
M_{Eff}	Effective magnetisation
M_{R}	Remnant magnetisation
m	Reduced magnetisation
m_e	Mass of electron
m_ℓ	Orbital magnetic quantum number
m_s	Spin magnetic quantum number
N	Number of turns of coil or number of time-steps
$\mathcal{N}$	Demagnetising tensor
n	Integer value, see context of equation.
P	Peak amplitude of fit to S_{12} data
p	Mode number of perpendicular stationary spin wave
q	Change of wavevector in X-ray Reflectivity
S_{mn}	Transmission coefficient for a wave sourced at port n and received at port m
S_x	Power spectral density
r_a	Atomic radius
r_{3d}	Radius of $3d$ electrons
S	Total spin quantum number of multi-electron system

s Angular momentum of spin moment of an electron

T Temperature

T_C Curie temperature

t Time

t_{FM} Thickness of ferromagnetic layer layer

t_{NM} Thickness of spacer layer

y_0 Baseline of fit to S_{12} data

V Volume

V_{EMF} Electromotive force

Z Impedance

Z_C Characteristic impedance

Z_c Number of atoms per unit cell

Abbreviations

AF Antiferromagnetic

AFM Atomic force microscopy

AM Acoustic mode

BB Bloch-Bloembergen

CGS Centimeter-gram-second

CPU Central processing unit

CPW Coplanar waveguide

DC Direct current

EA Easy axis

EM Electromagnetic

FDM Finite difference methods

FEM Finite element methods

FFT Fast Fourier transform

FM Ferromagnetic

FMR Ferromagnetic resonance or Fundamental resonance mode

FOM Figure of merit

GMR Giant magnetoresistance

GPU Graphical processing unit

HA Hard axis

IoT Internet of things

IP In-plane

LL Landau-Lifshitz

LLG Landau-Lifshitz-Gilbert

ML Monolayer

MRAM Magnetoresistive random access memory

NM Nonmagnetic

OM Optic mode

OOP Out-of-plane

PDE Partial differential equation

PSD Power spectral density

PSSW Perpendicular stationary spin wave

PVD Physical vapour deposition

RKKY Ruderman–Kittel–Kasuya–Yosida

RF Radio frequency

rms Root mean square

SAF Synthetic antiferromagnet

SFM Synthetic ferromagnet

SI International system of units

SNR Signal to noise ratio

SOLT Short-open-load-through

STT Spin transfer torque

SW Stoner-Wohlfarth

TEM Transverse electromagnetic

VNA Vector network analyser

VNA-FMR Vector network analyser-ferromagnetic resonance

VSM Vibrating sample magnetometry

XRR X-ray Reflectivity

Abstract

The search for new advanced materials to enable technology to operate at ever faster speeds still is one of the key challenges as the information society develops. This has led to an interest in exploiting the high frequency dynamics observable in ultra-thin multilayer magnetic films. The functionality of these multilayers is dependent on the many aspects of the structure such as interface quality, interlayer couplings and magnetism energies. Thus, the study of the magnetisation dynamics of these systems through techniques such as ferromagnetic resonance spectroscopy is essential for the adoption of such materials into technology and is the focus of the work reported in this thesis.

An investigation concerning the dynamics of the Synthetic Antiferromagnets (SAFs) CoFeB/Ru/CoFeB is detailed with the highest resonant frequency at zero applied field observed in a SAF to date reported. This work also demonstrates the importance of interface quality to achieving high frequency 10s GHz dynamics at zero field. The results have been successfully modelled using an analytical approach allowing static and dynamic magnetic parameters to be extracted.

Studies concerning the high frequency dynamics of synthetic ferromagnets are also reported. Through experiments and numerical simulations, it is shown that the dynamic response of the two ferromagnetic layers has an orthogonal dependence on the difference in layer magnetization and interlayer coupling allowing both parameters to be determined accurately. Subsequently, the phase relations of the resonant modes can be determined, hitherto a challenging experimental measurement.

Magnetisation dynamics depend on the exchange interaction which is parameterised by the exchange constant. Perpendicular Stationary Spin Waves (PSSWs) are increasingly used to determine this parameter where the value of the exchange constant is extracted from first order PSSWs and analysed assuming a rigid surface pinning model. The work presented in this thesis demonstrates through a systematic study of multiple PSSW modes in NiFe films, where both thickness and cap layer material are varied, that this simple analysis does not adequately describe the experimental data. Specifically, a single value of the exchange constant cannot be used to fit all the data measured, as is expected from a consideration of the physics of the material. However, adopting a dynamic pinning model where the magnetic properties close to the surface are different to those of the bulk of the film does allow a complete description of the data. This approach is verified through a comprehensive set of micromagnetic simulations which are able to reproduce the key features of the experimental data. This work demonstrates that the current practice of using first order mode PSSWs to determine the exchange constant through a rigid surface pinning model must be treated with caution.

Declaration

No portion of the work referred to in this thesis has been submitted in support of an application for another degree or qualification of this or any other university or other institute of learning.

Copyright

Acknowledgements

I wish to thank my supervisors Professor Tom Thomson and Dr Ivan Vera-Marun for providing the opportunity to carry out this exciting research project. Their unfailing support, guidance and expertise has been an invaluable part in completing this journey. A special thanks also goes to Dr Ernie Hill, who provided insightful discussions that were key to overcoming very difficult aspects of the thin film growth required for this research. This section would not be complete without a special thanks to my research group NEST for providing such a friendly, supportive and encouraging lab environment.

I would like to extend my gratitude to all those who made my time in Manchester so enjoyable. In particular I would like to thank Charlotte Bull who brought a welcoming and friendly atmosphere to the lab and supplied endless cups of tea, Yu Li who was an exceptional desk-mate and extraordinary collaborator and Danielius Banys who provided cheerful and supportive company. The time spent in my PhD would also not have been the same without Lucas Mogg whose great friendship and encouragement were boundless throughout.

Lastly, I would like to thank my family for their support at all stages of my academic pursuits especially my mother Geraldine and my late father Ian who passed away throughout my PhD studies. Without their love, understanding and endless encouragement much of my academic success would not have been possible and for that I am forever grateful.

Chapter 1

Introduction

The study and exploitation of magnetic materials is an endeavor which has encompassed millennia [1]. However, it was only in the mid-1940s that the physics of magnets and magnetism was further enriched with the first investigations regarding their dynamic properties reported [2, 3]. The earliest insights into this aspect of magnetism followed investigations by V.K. Arkad'ev in 1911, who discovered the resonant absorption of microwaves by ferromagnetic (FM) materials, and by Dorfamn in 1923, who advanced a qualitative quantum interpretation of such effects [2]. For the introductory reader, it should be noted that in this context microwaves are a manifestation of electromagnetic radiation characterised by wavelengths between approximately 1 mm to 1 m corresponding to frequencies between 300 GHz and 300 MHz respectively [4]. This culminated with Griffiths demonstrating the phenomena of ferromagnetic resonance (FMR) in 1946 [5]. The theoretical underpinnings of the resonant behaviour of magnetic materials were provided by the work of Kittel [6]. In subsequent decades dynamical magnetism has blossomed into an intensively studied research field [7]. Indeed, the wide time scale of magnetic processes [8], ranging from $1\text{x}10^{-3}$ s to $1\text{x}10^{-15}$ s, and the abundant range of physical processes that can be supported therein have been of key importance to the advancement of both fundamental scientific understanding and technological applications.

Today, magnetic materials are essential components of high frequency technology such as data storage [9–11], sensors [11–15], signal processors as well as a host of microwave applications [1, 16–21]. Many of the advances have been made possible by the development of deposition techniques such as sputtering, which has enabled the fabrication of high quality magnetic thin films. This was a key enabling step for a range of technological areas such as microelectronics fabrication [22], decorative and functional coatings [23, 24] and the field of spintronics (spin electronics) which comprises the study of the control and manipulation of spin degrees of freedom in solid-state systems [10–12, 25]. The maximum speed of operation and frequency range possible from the use of a magnetic thin film is determined by its ferromagnetic resonance frequency [17, 19], the frequency at which the precessional motion of the magnetisation

of a FM material occurs [1, 3, 6]. Hitherto the capabilities to tailor the properties of thin films, such as microstructure and composition, has realised the enhancements in ferromagnetic resonance frequencies required to keep pace with technological progress. Most notably this has enabled the increase of the high frequency response of single layer magnetic films at zero applied magnetic field from the low-MHz region into the X-band region ($\approx 10\,\text{GHz}$) [26]. This compares well with the current frequencies employed by radio frequency and microwave devices which operate in the low-GHz range. This includes technologies such as the Internet of Things (IoT) (0.3-5.5 GHz) and public mobile networks (2G-4G operating in the frequency band 0.7-3 GHz) [27]. However further enhancement of the zero field ferromagnetic resonance frequency of current materials is increasingly difficult, thus motivating new approaches.

The search for new advanced materials to enable technology to operate at ever faster speeds still is one of the key challenges as the information society develops. In particular, there is a demand for communications at 5G and beyond which would require magnetic thin films to support frequencies into the 10s GHz range [16, 19, 28, 29]. A significant problem with current materials is that they require large magnetic fields to reach these higher operational frequencies. The application of such high fields will not satisfy the requirements of future devices such as the need for high density, energy efficiency and low cost. Thus, further innovations in the development of high frequency spintronic materials are required [19, 27].

These concerns have very recently led to a considerable interest in exploiting the high frequency dynamics observable in ultrathin ($\lessapprox 10\,\text{nm}$) magnetic films [19, 30], with the opportunities presented by these spintronic materials in microelectronics recently highlighted [27]. Antiferromagnets in particular offer great increases in functionality due to their characteristic dynamic response lying in the 100s GHz range [31, 32], as outlined in the Magnetism Roadmap 2017 [33]. However, there are issues with the adoption of antiferromagnets into current technology including the fact that whilst they are ubiquitous only a small number are metallic [32, 34, 35]. There are also challenges associated in the fabrication of layers thinner than 10 nm [36] and difficulties in impedance matching these materials to current radio frequency technologies with only a limited number of antiferromagnets possessing resonances in this frequency range [37].

An alternative to the use of typically metallic alloys consisting of natural FM or antiferromagnetic (AF) materials are magnetic multilayers [19, 30]. This is where atomically engineered layers are combined to create a novel types of heterostructures

consisting of alternating layers of magnetic and nonmagnetic (NM) thin films. Such materials offer a route to create advanced high frequency material systems with properties that can be tailored through the individual layers and their magnetic interactions [1, 38]. Multilayer stacks have generated much research activity due to their unique magnetic and electronic properties compared to their single layer counterparts [39]. Thus, such layer engineering provides a versatile method to meet the future needs of devices.

The phenomena of RKKY interlayer exchange coupling in such artificially layered structures underpins many spintronic technologies and has been a rich, widely studied area [38, 40, 41]. This phenomena is where the FM layers of a multilayer stack are indirectly coupled through a magnetic interaction known as *exchange*. It was first observed independently by Fert [42] and Grünberg [43] in the mid-1980s, when AF coupling between Fe/Cr layers was realised. It has had a significant disruptive effect on magnetics research, launching the field of spintronics [10] and revolutionising the data storage industry [12]. Indeed, modern spintronic devices rely on multilayer structures where the coupling between magnetic layers has to be controlled to achieve the desired magnetic properties [44].

A commonly studied magnetic multilayer structure is comprised of a FM/NM/FM trilayer where the thickness of the NM layer is no greater than a few nanometers. The interlayer exchange coupling established in such a structure can either promote a parallel or antiparallel alignment of the layer magnetisations, known as a Synthetic Antiferromagnet (SAF) or Synthetic Ferromagnet (SFM) respectively [45]. Hitherto, such SAF or SFM multilayers have been widely utilised for their static properties, acting only as passive components within spintronic devices to provide a source of exchange bias or dipole field control [46]. These applications demonstrate that such trilayers can be incorporated into manufacturable devices and the recent commercial availability of Spin-Transfer-Torque Magnetic Random-Access Memory (STT-MRAM) chips shows that integration of magnetic systems and CMOS processes can be performed at scale [47]. However, the dynamics of such systems have not been exploited or necessarily widely researched, despite the promise they hold in terms of enhancing device capability. Notably, these structures can support a variety of beyond-Kittel resonance modes which can be tailored by control of their layer properties [40, 48]. SAFs in particular have the potential of supporting zero field resonances towards 100 GHz [49], significantly greater than that attainable in single layer ferromagnetic films, with the key limitation to the maximum frequencies being the strength of the interlayer coupling

present. The magnetic profiles of such multilayers can differ significantly from their single layer constituents and is dependent upon properties such as layer magnetisation, interlayer coupling and magnetic anisotropies. This is especially true in the case of where the FM layers are ultra-thin as their properties are more dependent on interfacial effects. As such, to fully realise the potential of these artificially layered materials the development of experimental, lab-based techniques to provide a greater insight into the physical parameters governing the high frequency response of such multilayer films is required.

The work reported in this thesis seeks to provide additional insights into the wide potential of atomically engineered magnetic multilayers with tailored properties for high frequency spintronic devices. Details of lab-based methodologies developed throughout the project to characterise important physical properties of such structures are described. These techniques relied upon the study of the dynamic response of magnetic multilayers through FMR spectroscopy, a widely used and powerful method to analyse the fundamental properties of magnetic thin films. For example, the study of the variation of resonant frequency and linewidth with applied field can permit the determination of the saturation magnetisation, anisotropies, interlayer couplings and damping [3, 50]. In the work reported here the ferromagnetic resonant frequency was explored through both experiment and simulation, the comparison of which allowed a great insight into the magnetisation dynamics of the studied thin films and the extraction of parameters which are typically difficult to measure. Due to the applications outlook of this work, the ferromagnetic materials investigated are NiFe and CoFeB, materials which are widely used in spintronic devices due to their range of desirable properties and compatibility with current microfabrication processes.

1.1 Research Aims and Objectives

The central aims of this PhD project, which occurred in parallel, are

1. To increase the understanding of the dynamic response of ultrathin magnetic multilayer films.

2. The development of new techniques to characterise the important parameters governing the resonant dynamics exhibited by magnetic multilayers, the lack of which has been a severe limitation in terms of both device applications and in micromagnetic modelling.

To this end, the work reported in the thesis is comprised of the results of a number of research strands with the following objectives

1. The fabrication of high quality magnetic multilayer thin films. In particular, due to the large focus of the work presented in this thesis upon exchange coupled FM/NM/FM trilayers, a key enabling step was the development of a sputtering process to achieve this magnetic system.

2. The study of the ferromagnetic resonance frequency of the samples both experimentally and through micromagnetic simulation to elucidate on resonant dynamics and magnetic properties.

All in all, the outlined aims and objectives have been satisfied through three research branches i) The study of SAFs to explore high frequency optic mode dynamics. ii) The study of SFMs to determine the difference in magnetisation of the FM layers and the interlayer couplings present in these structures. Furthermore, the ramifications of these parameters on the resonant phases of the FM layers were explored. iii) The determination of the exchange constant from Perpendicular Stationary Spin Waves (PSSWs) in thin NiFe thin films with different capping layers. In the next section, the structure of the thesis is described and the performed studies are introduced in greater detail.

1.2 Thesis Outline

The seven following chapters comprise relevant magnetism background theory, the experimental methods used within the project and reports of the studies performed. The initial chapters are included to provide the reader with the background material necessary to understand the results presented. Specifically, Chapter 2 and Chapter 3 detail the theoretical underpinnings for fundamental magnetism and magnetism dynamics respectively. Chapter 4 introduces the range of experimental techniques used in the project to fabricate, characterise and simulate the thin films studied. In Chapters 5, 6 and 7 the results of the investigations carried out throughout this PhD are reported. Chapter 8 summarises the detailed investigations and includes suggestions of opportunities for further work in these areas. A brief summary of each chapter follows.

Chapter 2- Fundamentals of Magnetism

This part of the thesis includes a discussion regarding the history of the study of magnetism, its origins along with the types of magnetic materials and their characteristic energies. Furthermore, a range of static magnetic phenomena such as magnetisation reversal and domain walls are also introduced. The chapter then advances to consider the case of magnetic multilayers and the different effects this layering can introduce.

Chapter 3- Magnetisation Dynamics

This chapter introduces the dynamic properties of magnetic materials with a particular focus on the physics of magnetisation precession. It first establishes the equations of motion for magnetic precession and culminates in a detailed description of the high frequency responses of magnetic materials. Higher-order spin wave phenomena and the damping which eventually returns a magnetic system to equilibrium are also elaborated upon. Following this, the phenomena of interlayer coupling is discussed from a dynamical perspective with the rich resonant behaviour supported by magnetic multilayers detailed.

Chapter 4- Experimental Methods and Techniques

The experimental methods and techniques used to carry out the project are presented. Firstly, the technique of magnetron sputtering is discussed as this was utilised for the fabrication of the thin film samples. The experimental techniques used to characterise the samples are then detailed. The structure of the samples was explored using X-ray reflectivity. The magnetic properties were investigated using vector Vibrating Sample Magnetometry for the static properties with the dynamical behaviour explored using Vector Network Analyser - Ferromagnetic Resonance (VNA-FMR) spectroscopy. This chapter then concludes by introducing the micromagnetics simulation software and methods employed throughout this project to allow the numerical modelling of the dynamical behaviour observed experimentally.

Chapter 5- Synthetic Antiferromagnetic Dynamics

This chapter contains a report regarding the properties of the SAFs that were fabricated and characterised in this project. The reader should note that this study has recently been published in Physical Review Applied [51]. The wide range of zero field resonant

frequencies obtained from the studied SAF samples are presented with the highest zero field resonance observed in a SAF to date demonstrated. In contrast to previous SAF reports which focused only on the first RKKY AF coupling peak, it is shown that a higher zero field frequency is obtained for the second RKKY AF coupling peak. This is ascribed to the smoother interfaces associated with a thicker NM layer. This finding demonstrates the importance of interface quality to achieving high frequency optic mode dynamics entering the many 10s GHz range. Furthermore, the measured resonance data has been fit to an analytical model which allow important magnetic parameters to be extracted.

Chapter 6- Synthetic Ferromagnetic Dynamics

In this chapter investigations performed regarding the dynamic response of SFMs are detailed. The explored samples exhibit an RKKY coupling consistent with that expected with coupling on the first RKKY FM peak. This investigation has recently been published in Physical Review B [52]. Through experiment and numerical simulation, it is shown that the dynamic response of the two FM layers has an orthogonal dependence on the difference in layer magnetization and interlayer coupling. Thus, both parameters can be determined accurately. In addition we are able to obtain the phases of the resonant modes, a hitherto challenging measurement, and thus show that the conventional acoustic (in-phase) and optical (out-of-phase) description does not fully capture the intricacies of SFM dynamics.

Chapter 7- Perpendicular Stationary Spin Waves

A study with the objective to provide a more comprehensive understanding of the exchange constant is reported in this chapter. Multiple PSSW modes were observed and analyzed for a series of $Ni_{80}Fe_{20}$ samples of varying thickness and capping layer. It is found that the frequencies displayed by the PSSW modes is different to that expected based on assuming a rigid surface pinning model. However, adopting a dynamic pinning model where the magnetic properties close to the surface are different to those of the bulk of the film does allow a complete description of the data. This approach is verified through a comprehensive set of micromagnetic simulations which are able to reproduce the key features of the experimental data. This work demonstrates that the current practice of using first order mode PSSWs to determine the exchange constant through a rigid surface pinning model must be treated with caution. A publication

reporting the study detailed in this chapter is in preparation.

Chapter 8-Conclusions and Future Work

This chapter summarises the investigations reported in this thesis. Moreover, avenues for further studies are discussed.

Appendices

Two appendices are included in this thesis. In Appendix A, a list of awards, presentation and publications arising from the work detailed in this thesis is detailed. In Appendix B, the Mumax^3 simulation code used in the micromagnetics simulation aspect of the reported work is available for the reader's reference.

1.3 Author Contributions

It is important to note that aspects of the work reported in the thesis has involved the contribution of other people, without which the project would not have been successful. The author would like to take this opportunity to thank all those involved for their time, effort and for sharing their expertise. To be specific, the contributions were as listed. The author, Harry J. Waring, carried out all sample fabrication along with structural and magnetic, both static and dynamic, characterisation. Furthermore, all analytical modelling reported was carried out by the author. The VNA-FMR spectrometer used widely in this project was designed and constructed by Dr N.A.B. Johansson. The reported micromagnetics modelling, utilising the Mumax^3 simulation software, was performed with Mr Yu Li who wrote and ran the simulation scripts used in this project (as presented in Appendix B). The simulation aspect of the investigation was directed by discussions between both the author, Harry J. Waring, and Mr Yu Li with both then contributing to the analysis of the simulations results and comparisons to experimental measurements.

1.4 A note on units

The work reported in this thesis predominantly uses the Centimeter-Gram-Second (CGS) system of units as opposed to the International System of Units (SI), following the widely adopted approach in the field of magnetism and magnetic materials

research. A notable departure from this approach is seen in the chapters introducing the underlying theory of magnetism pertinent to the derivation of the high frequency response of magnetic materials where SI version of equations are presented alongside their equivalent CGS versions.

The reader should note that the electromagnetic unit of current, voltage and magnetic dipole moment (emu) are equivalent to SI values of 10 A, 10 nV and 10^{-3} Am^2 respectively. Furthermore derived units include the erg (=10^{-7} J), such that the energy density of 10 $ergcm^{-3}$ is equal to 1 Jm^{-3}. In a significant deviation from the SI Units, the permeability of free space (μ_0) has value 1 GOe^{-1} and is generally omitted form CGS equations. The most commonly used conversions between CGS units and their SI counterparts are shown in table 1.1.

CGS	**SI**
1G	0.1 mT
1 Oe	79.58 Am^{-1}
1 emu	1 mAm^2
1 $emucm^{-1}$	1 kAm^{-1}

Table 1.1: Useful conversions from the centimeter-gram-second (CGS) unit system to the more prominent SI system

Further information regarding CGS units and their conversions to SI can be found in excellent textbooks provided by Coey [1] and Cullity [35].

Chapter 2

Fundamentals of Magnetism

The study of magnets is a pursuit which has spanned millennia. In that time, the physics underlying the behaviour of these materials has been unravelled and magnets have become an integral part of modern technology. In this chapter, the fundamental properties of magnetic materials, for example origins, types and behaviour, are introduced.

2.1 History

Since antiquity, magnetic materials have commanded the attention of curious philosophical minds with the development in the understanding of the inner workings of magnets contemporaneous with the evolution of science and technology. The earliest records of the study of magnetism pertain to the unique magic of naturally occurring lodestones, rocks mainly composed of Magnetite (the iron oxide Fe_3O_4) magnetised by the huge electric currents present in lightning strikes, that were widely prevalent in ancient civilisations [1, 35]. The first examples of the properties of magnetic materials being harnessed for device application is the 'South pointer', with its key functional component a lodestone carved in to the shape of a spoon [1, 53]. Guided by the Earth's magnetic field lines, the spoon would re-orientate to align towards the magnetic south pole. Subsequent developments of the first permanent magnets, due to findings that iron could be more readily magnetised whilst heated, led to the invention of navigational compasses in 1088 [54]. In terms societal impact the integration of the earliest magnetic technology into human civilisation ushered the Age of Discovery, with this navigational magnetic technology used in famous voyages such as Christopher Columbus' journey to the Americas in 1492 and the discovery of Africa by Chinese explorers in 1433 [1].

The first decoupling of scientific fact and mystical, superstitious belief regarding the underlying nature magnetic materials was performed by William Gilbert (1540-1602) [35]. This famous intervention occurred in the 1600 monograph *De Magnete*, a

paper which is debatedly the first modern scientific text [55]. Insightfully, he inferred the existence of the Earth's magnetic field from the study of the dipolar field present at the surface of a lodestone. Further advances were made throughout the Age of Enlightenment, with a notable example being that magnets were disabused of the notion that they possessed a soul. The invention of a horseshoe magnet in 1743, an enduring archetype symbolising magnetism, which was capable of maintaining its own demagnetising field due to its shape was also a significant step forward to the adoption of magnetic technologies [1].

Perhaps the greatest stride in the understanding of the origin of magnetism occurred through the work of Hans Christian Oersted in 1820 where it was demonstrated that an electric current is capable of generating a magnetic field [54]. Subsequent studies by renowned scientists such as Amprére and Faraday solidified the correspondence between the phenomena of magnetism, electricity and light. The unification of magnetic and electric forces came about in the work of James Clerk Maxwell (1831-1879) and resulted in the founding of the field of electromagnetism, epitomised in the four famous Maxwell's equations [56]. Thus, a mathematical structure to understand the *wave-like* nature of these interactions, that they consist of oscillating electric and magnetic fields propagating at the speed of light, was formed. However, despite all the triumphs of these theories of electromagnetism, the explanation of the ways in which a solid could exhibit magnetic phenomena remained absent. The underlying quantum mechanical nature of magnets responsible for this spontaneous magnetisation was only conceived in the early 20^{th} century [1, 7].

In recent decades the application of magnetic materials to the technologies which underpin society has been colossal; encompassing telecommunications, computing and electrical machines such as motors and generators. These technologies were made possible through the advances in the fields of magnetic recording, high frequency dynamics and permanent magnetism [1, 19, 35, 57].

2.2 Magnetic Dipole Moment

At its most fundamental level magnetism is a consequence of the *quantisation of the angular momentum of elementary particles*, a concept which arises from quantum mechanics [1, 7, 35]. The relation between magnetism and angular momentum, referred to as the Einstein-de Haas effect, was first shown in an experiment by John Stewart

in 1917 [58]. Due to the large mass of nucleons, magnetic moments in solids are associated with the electron [1]. The magnetic contribution of the electron derives from its angular momentum which itself has two sources: its *orbital motion around the nucleus* ($\boldsymbol{\ell}$) and its *spin* ($\boldsymbol{s}$). The total angular momentum is the vector sum $\boldsymbol{j} = \boldsymbol{\ell} + \mathbf{s}$ [7]. The reader should note we use lower case letters ℓ, s and j to represent the quantum numbers of a single electron, with upper case L, S and J correspondingly utilised to denote these values in a multi-electron system. The bold symbols denote the angular momentum vectors, which are quantised in terms of $\hbar$ [1]. Further discussion regarding these angular momentum components of an electron from a dynamical perspective is available in section 3.1.

2.2.1 Orbital Moment

The orbital moment originates from the orbital motion of the electron around the nucleus, an effect can be described through the Bohr atom model (where the electron traverses a classical circular orbit around an atomic nucleus due to a Coulomb potential) as presented in Figure 2.1. The electron therefore possesses a magnetic moment $\boldsymbol{\mu}$ and a quantised, antiparallel angular momentum $\boldsymbol{\ell}$.

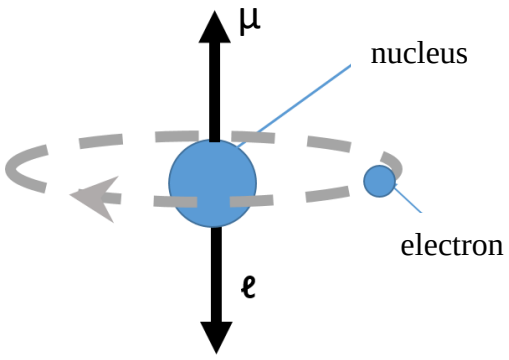

Figure 2.1: A diagram of the Bohr model of an atom, reproduced from [1]. The magnetic moment of the electron μ and its angular momentum $\boldsymbol{\ell}$ arising due to its orbital motion are antiparallel.

This motion of the electron can be modelled as equivalent to a current loop, where the current direction is opposite to the direction of travel of the electron due to its

negative charge. The magnetic moment associated to this current loop is

$$\boldsymbol{\mu} = -\frac{e}{2m_e}\boldsymbol{\ell} \tag{2.1}$$

where e and m_e are magnitude of the charge and the mass of the electron respectively. The minus sign indicates that $\boldsymbol{\mu}$ and $\boldsymbol{\ell}$ are antiparallel due to the negative electron charge. The relationship between the magnetic moment and angular momentum is

$$\boldsymbol{\mu} = -\gamma\boldsymbol{\ell} \tag{2.2}$$

where γ is the proportionality factor known as the gyromagnetic ratio. In this case, where we are concerned with orbital angular momentum, the gyromagnetic ratio is the orbital gyromagnetic ratio defined as

$$\gamma_{\text{orb}} = \frac{e}{2m_e} \tag{2.3}$$

From substituting the electronic mass and charge into equation 2.3, it is seen that $\frac{\gamma_{\text{orb}}}{2\pi} = 14\,\text{GHz/T}$. Though these relations have been derived classically, the reader should note that they are also valid quantum mechanically [1, 7].

At this point in the discussion, it is pertinent to introduce the *Bohr magneton*, a natural unit for electronic magnetism, defined as

$$\mu_B = \frac{e\hbar}{2m_e} \tag{2.4}$$

where $\mu_B = 9.274 \times 10^{-24}\,\text{Am}^2$. From this, it is possible to express a component of $\boldsymbol{\mu}$ in a particular direction chosen here as z as

$$\mu_z = -\frac{e\hbar}{2m_e}m_\ell = -m_\ell\mu_B \text{ where } m_\ell = 0, \pm1, \pm2... \tag{2.5}$$

where m_ℓ is an orbital magnetic quantum number, $\hbar$ is the reduced Planck constant (which is the Planck constant h divided by 2π). The relation shown in equation 2.2 can also be written in terms of a g-factor, defined as the ratio of the magnitude of the magnetic moment (in units μ_B) and the magnitudes of angular momentum (in units of $\hbar$). In the case of orbital motion considered here this has the form $\frac{|\boldsymbol{\mu}|}{\mu_B} = g\frac{|\boldsymbol{\ell}|}{\mu_B}$ and it follows that g is 1 [1].

2.2.2 Spin Moment

In 1922, the Stern-Gerlach experiment demonstrated that an electron possesses an intrinsic property which creates its own magnetic dipole moment, independent of any orbital motion [59]. This property is labelled spin ($\boldsymbol{s}$) and is assigned the spin magnetic quantum number $m_s = \pm\frac{1}{2}$ depending on its orientation to the applied magnetic field [7, 60]. It should be noted that this spin can only be described through quantum mechanical interpretations, with a classical concept of a spin, a spinning ball for instance, incompatible with the fundamental point-like nature of the electron [1, 7]. It has been shown that the magnetic moment associated with spin is approximately one μ_B and that the g-factor is close to 2, specifically 2.0023 when higher order corrections from quantum electrodynamics are taken in to account [2, 61]. The component of spin along any axis is $\pm\frac{1}{2}\hbar$ as

$$\mu_z = -\frac{e}{m_e} m_s \hbar \text{ where } m_s = \pm\frac{1}{2} \tag{2.6}$$

with the spin gyromagnetic ratio given by

$$\gamma_{\text{spin}} = \frac{e}{m_e} \tag{2.7}$$

where $\frac{\gamma_{\text{spin}}}{2\pi}$ has a value 28 GHz/T [7]. As a result, the spin angular momentum is twice as efficient as orbital angular momentum at generating a magnetic moment [1]. For further discussion regarding the spin angular momentum in a magnetic material, including the convention underlying the correct labelling of the spins present, the reader is refereed to section 2.3.2.

2.2.3 Spin-Orbit Interaction

The coupling of these two angular momenta, as is usually the case if we consider an atomic electron, occurs through the spin-orbit interaction. The resultant total electronic angular momentum is denoted $\boldsymbol{j}$ [1]. In a multi-electron system with the presence of both spin and orbital angular momenta,

$$\boldsymbol{\mu} = \gamma_{\text{orb}} (\mathbf{L} + 2\mathbf{S}). \tag{2.8}$$

In this case, μ and $\mathbf{J}$ are no longer strictly parallel. However, it has been demonstrated that only the component of μ parallel to $\mathbf{J}$ possesses a measurable value. Therefore,

$$\boldsymbol{\mu} = -\gamma \mathbf{J} \tag{2.9}$$

where

$$\gamma = g\frac{e}{2m_e} \tag{2.10}$$

where g is referred to as the Landé g-factor. As aforementioned, it has the value 1 for pure orbital and 2 for pure spin angular momenta [7]. For mixtures of these momenta, it alters value based on the projection of μ along $\mathbf{J}$. In the case where S^2, L^2 and J^2 are very large [7]

$$g = \frac{3}{2} + \left(\frac{S^2 - L^2}{2J^2}\right). \tag{2.11}$$

2.3 Magnetic Materials

Materials display magnetic properties when constituent atoms or ions possess a permanent magnetic moment. We can further classify these materials by stratifying based on whether these moments exhibit a long range order (below a certain critical temperature) and, in the cases where ordering is present, the particular arrangements that the magnetic moments exhibit [7]. The magnetic properties of materials can be succinctly classified through reference to the dimensionless scalar form of the magnetic susceptibility defined as [35]

$$\chi = \frac{M}{H}. \tag{2.12}$$

and related to the magnetic response of a sample through

$$M = M_0 + \chi H \tag{2.13}$$

where M is net macroscopic moment per unit volume (or magnetisation), H is the applied field which is assumed to be small, and M_0 is the spontaneous magnetisation when no external magnetic field is applied [1, 7]. The magnetic effects discussed in this work operate in the linear regime where the external fields are small enough that equation 2.13 is valid. The susceptibility is related to the magnetic permeability (μ_{perm}) through [1] [35]

$$\mu_{\text{perm}} = 1 + 4\pi\chi \text{ (CGS)} \quad ; \quad \mu_{\text{perm}} = \mu_0(1+\chi) \text{ (SI)} \tag{2.14}$$

In the following, the different classes of magnetic materials are detailed and their unique characteristics discussed.

2.3.1 Weak Magnetism

Diamagnetism ($\chi<0$)

Diamagnetic materials do not possess atoms or ions with a permanent magnetic moment. Such materials instead display a characteristic negating effect to an induced magnetisation generated by the application of an external field. This response can be considered a microscopic example of the well known Lenz's law where upon the application of the external field, electronic orbital motions alter in such a way to create an opposing field. Thus, they are classified as possessing a negative scalar susceptibility. It is notable that virtually all materials exhibit a diamagnetic response to externally applied fields, with the response of permanent magnetic moments simply eclipsing these effects in some materials. This is due to diamagnetism is typically being a weak effect, with a susceptibility of order 10^{-6} in most materials [7, 57].

Paramagnetism ($\chi>0$)

Paramagnetic materials possess permanent magnetic moments due to the presence of unpaired electrons, that is where only one electron occupies an orbital of an atom rather than as part of an electron pair leading to an uncompensated magnetic dipole moment. In such materials, these electrons lack a spontaneous long range order, however [1]. Instead, in the absence of an external field, these moments are randomly oriented and the net moment is zero. As it is typical for moments to align parallel to the applied field, isotropic paramagnets possess a positive scalar susceptibility. Due to the impact thermal fluctuations can exert on magnetic ordering, paramagnetic susceptibility is inversely proportional to the temperature [7, 57].

2.3.2 Ordered Magnetism ($\chi \gg 0$)

This describes the case where the elementary permanent moments within a material spontaneously align in an ordered manner, at least below certain temperatures. The

emergence of a spontaneous ordering can only be understood through quantum mechanical interpretations, where the presence of a quantum mechanical exchange interaction is strong enough to overcome dipolar interactions. Dipolar interactions are electrostatic interactions between magnetic dipole moments. Indeed, it was demonstrated by Bohr [62] and van Leeuwen [63] that from classical understanding it is impossible for a macroscopic medium to possess a magnetic moment leading to significant misunderstandings of this effect until a detailed description of quantum mechanics was formulated [7]. Ordered magnetic materials can have a multitude of spin configurations resulting in vastly differing exhibited magnetic properties [1]. It is convention to define electron spins as *spin up* for the majority spins and *spin down* in the case of minority spins, which correspond to the electron spin components of $+\frac{1}{2}\hbar$ and $-\frac{1}{2}\hbar$, as introduced in section 2.2.2, respectively [1]. The types of ordering pertinent to this project is detailed below and presented in Figure 2.2.

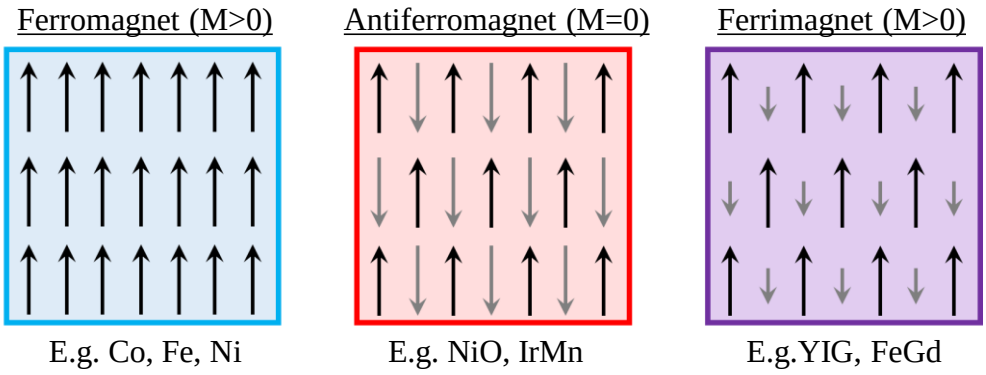

Figure 2.2: Different classes of ordered magnetic materials along with their characteristic magnetisation. The arrows represent the spins of the electrons, with their length representing the contribution to the magnetisation of the material.

Ferromagnetism

Ferromagnetic (FM) materials occur when the elementary permanent moments spontaneously align in parallel [57]. This class of magnet was the first to be discovered and studied due to the effect its stray field exerts on its immediate environment. The effects of thermal fluctuations can have a dramatic impact on this magnetic ordering. At temperatures in excess of a certain critical temperature, known as the Curie Temperature (T_C), this ordering collapses and the material exhibits paramagnetic responses to external fields. The dependence of the magnetic susceptibility on temperature (T) is

described by the Curie-Weiss law

$$\chi = \frac{C}{T - T_C} \tag{2.15}$$

where C is the Curie constant [1, 7, 64].

Antiferromagnetism and Ferrimagnetism

Antiferromagnetic (AF) and *ferrimagnetic* materials occur when there is an antiparallel ordering of the neighboring magnetic moments. Indeed, in these cases the spin lattice is configured as two opposing ferromagnetic sublattices. The instances where the two sublattices have an equal net magnetisations are referred to as antiferromagnets whereas the cases where these sublattices have unequal net magnetisation are known as ferrimagnets. In the latter case, more than two sublattices can be present with the key criterion being that the structure contains layers with unequal magnetisation which results in a net moment being observed. Historically, these classes of materials remained undiscovered until the 1930s due to a lack of a stray field or, in the case of ferrimagnets, being considered as a normal ferromagnet [1]. This type of ordering overcomes thermal effects at temperatures up to the Néel temperature [64].

2.4 Magnetism Energies

Magnetism arises due to a complex interplay of many different energies and interactions. At its most fundamental level this phenomena results from the manifestation of a long-range ordering of the electronic magnetic moments. Thus, any mechanism which impacts this ordering can influence the behaviour of a magnetic system. A physical description of a magnetic system usually involves the adoption of an effective field of magnetisation ($\mathbf{H}_{\text{eff}}$) which accounts for all the contributions to the energy of the magnet. This effective field can be written as

$$\mathbf{H}_{\text{eff}} = -\frac{d\mathcal{E}}{d\mathbf{M}} \ (\text{CGS}) \qquad ; \qquad \mathbf{H}_{\text{eff}} = -\frac{1}{\mu_0}\frac{d\mathcal{E}}{d\mathbf{M}} \ (\text{SI}) \tag{2.16}$$

where the contributing energies are calculated as a volume integral of the local energy densities ($\mathcal{E}$) over the total considered volume (V) following the formalism

$$\mathcal{E} = \frac{dE}{dV} \tag{2.17}$$

where E is the energy. The total magnetic energy E_{tot} is a summation of the following contributions

$$E_{\text{tot}} = E_{\text{ex}} + E_{\text{mag}} + E_{\text{zee}} + E_{\text{ani}} \tag{2.18}$$

where E_{ex} is the exchange energy, E_{mag} is the energy of the magnetostatic interaction including demagnetising effects, E_{zee} is the Zeeman energy (that is the energy of a magnetised sample due to an external magnetic field), and E_{ani} is the energy associated with the magnetic anisotropy. In the static case, as opposed to the dynamic case discussed in the next chapter, the equilibrium state can be found by minimising the total energy E_{tot} of a system. In the following, the most commonly contributing energy terms to the effective field are elucidated [1, 65].

2.4.1 Exchange Interaction

As aforementioned, it was proved by Bohr [62] and van Leeuwen [63] that through the tenants of classical physics it is impossible for a macroscopic medium to exhibit a magnetic moment [7]. It is only through quantum mechanics and the concept of quantisation of the magnetic moment that it possible to overcome this boundary of physics. This approach relies upon the quantum mechanical *exchange interaction*, a short range force that influences the arrangement of magnetic moments within a material. The length scale of this force is such that it acts upon neighboring or next-to-nearest neighbor atoms [1, 7, 57]. This aligning exchange interaction is present in all magnetic materials. Notably, as discussed in later sections, this interaction is also at interfaces between two magnetic materials (known as direct) and in some cases between magnetic layers separated by nonmagnetic (NM) spacer layers (indirect).

The exchange interaction contributes strongly to the energy of a magnetic system and arises due to the interplay between Coulomb repulsion and the Pauli exclusion principle [1, 7]. A quantum mechanical effect, it forbids electrons that possess the same spin from occupying equivalent energy states and therefore modifies the Coulomb interaction between neighboring electrons. For energy minimisation, two electrons of parallel spins will align further apart as opposed to two electrons of different spins being less spatially separated. Thus, the strength of this nearest neighbor interaction is capable of producing a long range ordering within magnetic materials. The exchange energy for two neighboring atoms with spins $\mathbf{s_i}$ and $\mathbf{s_j}$ is

$$E_{\text{ex}} = -2J_{\text{ex}}\mathbf{s_i} \cdot \mathbf{s_j} \tag{2.19}$$

where J_{ex} is referred to as the exchange integral [35]. In instances where J_{ex} is positive the exchange energy promotes parallel alignment of the electronic moments whilst a negative J_{ex} promotes an antiparallel alignment. From equation 2.19, it is clear that there is an energy penalty in cases where neighboring spins are not aligned. To rationalise the different magnetic behaviour of materials the Bethe-Slater curve, presented in Figure 2.3, was devised. It provides a heurisic description of the evolution of the magnetism and magnetic ordering of the $3d$ transition metal elements [57, 66]. Specifically, the value of the exchange integral of a magnetic material is predicted based upon the ratio r_a/r_{3d} where r_a is the radius of the atom and r_{3d} the radius of its $3d$ electrons [35, 67].

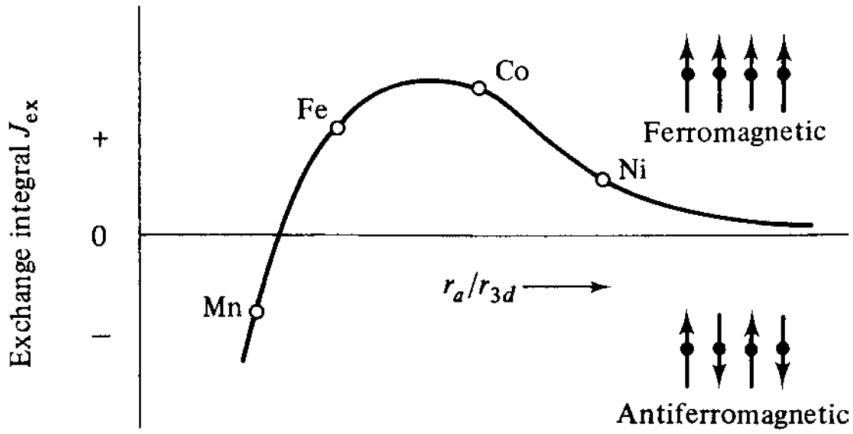

Figure 2.3: The Bethe-Slater Curve presenting how J_{ex} varies with the ratio of the radius of the atom r_a to the radius of its $3d$ electrons r_{3d} [35].

For a macroscopic medium the exchange energy density is given by

$$\mathcal{E}_{ex} = A_{ex}(\nabla \mathbf{m})^2 \tag{2.20}$$

where $\mathbf{m}$ is the reduced magnetisation equivalent to $\frac{\mathbf{M}}{M_S}$ and A_{ex} is the exchange constant, considered to be the macroscopic equivalent to the exchange integral J_{ex}. A_{ex} is used to characterise the strength of the exchange interaction within a material and can be approximated as

$$A_{ex} \approx \frac{J_{ex} S^2 Z_c}{a_0} \tag{2.21}$$

where Z_c is number of atoms per unit cell and a_0 is the lattice parameter [1, 35, 65].

A common technique to measure this exchange constant is through the study of spin phenomena such as thermal magnons, usually by exploring the variation of M_S at

low temperature. This exploits the association of the energy of long-wavelength spin waves, a magnetic phenomena elaborated on in section 3.3, with a gradual twist of the magnetisation and the variation of A_{ex} with temperature. This relation is

$$A_{\text{ex}}(T) = \frac{M_S(T)D}{2g\mu_B} \tag{2.22}$$

where D is the exchange stiffness constant [1]. It is brought to the reader's attention that the exchange stiffness constant D should not be confused with the exchange constant A_{ex}, with the two parameters connected by the relation [68]

$$D = 2\frac{A_{\text{ex}}}{M_S}. \tag{2.23}$$

Moreover, D is correspondingly linked to J_{ex} through [1]

$$D = 2J_{\text{ex}}Sa^2. \tag{2.24}$$

There are numerous limitations to the described technique. In particular, it is only valid in the low temperature regions due to the vanishingly small thermal energies required to excite long-wavelength spin waves [1, 69]. Furthermore, these measurements are also susceptible to other energies which influence the internal magnetic field of the sample, such as the crystalline anisotropies and the saturation magnetisation. This results in difficulties in achieving sufficient accuracy due to the incorporation of the uncertainties associated with these additional magnetic parameters [68]. Typical values of A_{ex} for widely used ferromagnets such as permalloy or cobalt are 1×10^{-6}erg/cm and 3.1×10^{-6}erg/cm respectively [1].

There is also a characteristic length scale associated with the exchange interaction, referred to as the exchange length (l_{ex}). This represents the shortest distance over which the magnetisation can be twisted to minimise the dipolar interaction. It is defined by the competition of exchange with the magnetostatic energy, described in section 2.4.2. As such [70]

$$l_{\text{ex}} = \sqrt{\frac{A_{\text{ex}}}{2\pi M_S^2}}. \tag{2.25}$$

The exchange length plays a key role in the physics of domain walls and dynamic phenomena, as discussed in later sections. Magnetic films with thickness comparable or less than l_{ex} are referred to as ultrathin due to the moments being locked together throughout the film thickness by the exchange interaction [71].

2.4.2 Magnetostatic Energy

Magnetostatic energy refers to the energy of the magnetic moments in a field due to all the moments present. Whereas the individual interaction between two dipoles is weak, with the exchange interaction always stronger at short distances, the magnetostatic interaction is a long range interaction and acts non-locally on every magnetic moment. This enables it to determine the magnetic microstructure [1, 65]. This energy is minimised when there are no stray fields and flux loops are closed, which gives rise to the formation of a demagnetising field ($\mathbf{H}_{\text{demag}}$) defined as

$$\mathbf{H}_{\text{demag}} = -\mathcal{N}\mathbf{M} \tag{2.26}$$

where $\mathcal{N}$ is the demagnetising tensor which is a 3×3 matrix governed by the shape of the sample [35]. The calculation of the demagnetising factor is complicated in general, though it has been reported in this case of a a uniformly magnetised ellisoid, with a coordinate system aligned along its principle axis, it has the form [1, 35]

$$\mathcal{N} = \begin{pmatrix} N_x & 0 & 0 \\ 0 & N_y & 0 \\ 0 & 0 & N_z \end{pmatrix} \tag{2.27}$$

where

$$N_x + N_y + N_z = 4\pi \ \ (1 \text{ in SI Units}). \tag{2.28}$$

As all the samples studied in the investigations reported in this thesis are thin films with in-plane (IP) magnetisation, a discussion of this particular case follows. The shape anisotropy present in thin film promotes an IP magnetisation with the demagnetising field described as

$$\mathbf{H}_{\text{demag}} = -\begin{pmatrix} 0 & 0 & 0 \\ 0 & 0 & 0 \\ 0 & 0 & 4\pi \end{pmatrix} \mathbf{M} = -4\pi M_S \tag{2.29}$$

Furthermore, the energy density of the magnetostatic interaction is given by [1, 35]

$$\mathcal{E}_{\text{mag}} = -\frac{1}{2}\mathbf{M}\cdot\mathbf{H}_{\text{demag}} \ \text{(CGS)} \qquad ; \qquad \mathcal{E}_{\text{mag}} = -\frac{\mu_0}{2}\mathbf{M}.\cdot\mathbf{H}_{\text{demag}} \ \text{(SI)} \tag{2.30}$$

2.4.3 Zeeman Energy

The *Zeeman energy* arises from the application of an external magnetic field $\mathbf{H}_{\text{ext}}$ to a magnetic system. This energy density is given by [1, 57]

$$\mathcal{E}_{\text{Zee}} = -\mathbf{M}\cdot\mathbf{H}_{\text{ext}}\ (\text{CGS}) \qquad ; \qquad \mathcal{E}_{\text{Zee}} = -\mu_0\mathbf{M}\cdot\mathbf{H}_{\text{ext}}\ (\text{SI}) \tag{2.31}$$

Thus, it follows that this energy is minimised in instances where the magnetisation is aligned to the external field.

2.4.4 Magnetic Anisotropy Energy

The phenomena of *magnetic anisotropy* refers to the preferential magnetisation directions that exist within a magnetic system [7]. It leads to formation of a favoured direction of magnetisation known as an Easy Axis (EA). Correspondingly, this is accompanied by the presence of a Hard Axis (HA) which is perpendicular to the EA direction. In energy terms, the anisotropy is quantified as the difference in energy of the system in cases where the magnetisation is directed along the EA or the HA. The ramifications of the presence of anisotropy in a magnetic system are significant. Indeed, the control of this property is integral to many technologies as it determines magnetic quantities such as domain sizes and coercive fields [1, 35]. The strength of the magnetic anisotropy present in a material is quantified by a measurement of the external field required to saturate the system in its HA direction, which is referred to as the anisotropy field (H_k) [57].

The three main sources of this anisotropy are i) sample shape (accounted for by the demagnetising field term discussed in section 2.4.2) ii) crystalline structure and iii) induced anisotropy related to the atomic or microscale texture. Of these contributions, only the crystalline structure, formally known as the magnetocrystalline anisotropy, is *intrinsic*. This phenomena manifests as the preferential alignment of the magnetisation along crystallographic directions and thus reflects the symmetries of the crystalline lattice. It has roots in the spin-orbit coupling, crystal-field interaction along with the interatomic dipole-dipole interaction. The other listed contributions are classed as *induced* [1, 35].

The total magnetic anisotropy energy can be written as

$$E_{\text{ani}} = E_{\text{MCA}} + E_{\text{shape}} + E_{\text{surf}} + E_{\text{strain}} \tag{2.32}$$

where E_{MCA} is the magnetocrystalline energy contribution, E_{shape} is the energy provided by shape anisotropy, E_{surf} is energy of the surface anisotropy and E_{strain} is the energy introduced by strain in the magnetic film. A fuller description of these contributions is put forth in the following.

Magnetocrystalline Anisotropy

The magnetocrystalline anisotropy E_{MCA} is the anisotropy directed due to the structure and symmetry of the crystalline lattice. There are two sources of this anisotropy namely *single-ion anisotropy* and *two-ion anisotropy*. In the first case, this contribution originates from the presence of a crystal field generated by an electrostatic interaction of the orbitals containing magnetic electrons with the potential created at the atomic site by the crystal. This acts to stabilise a particular orbital, which through the spin-orbit interaction can then align the magnetic moment in a particular crystallographic direction. Two-ion anisotropy generally arises from the anisotropy of the dipole-dipole interaction, which acts to align magnetic moments into a lower energy configuration. In cubic lattices, this contribution vanishes, with it having a much greater impacts in the case of non-cubic lattices [1]. In the case of a uniaxial magnetic anisotropy, as seen in the work reported in Chapter 5 and 6, the energy density is expressed as

$$\mathcal{E}_{\mathrm{uni}} = \sum_{n} K_{u,n} \sin^{2n}\theta = K_{u,0} + K_{u,1}\sin^{2}\theta + ... \tag{2.33}$$

where $K_{u,0}$ is not relevant for anisotropic properties as it has no angular dependence [57]. The anisotropy constants ($K_{u,n}$) can take either positive or negative values, with this conventionally representing that the anisotropy energy is minimised when the magnetisation is aligned with the EA or HA respectively [65]. For later discussions, it is useful to express the form of the energy density of a uniaxial anisotropy in the $x-$direction as

$$\mathcal{E}_{\mathrm{uni}} = -K_u(\mathbf{e_x}\cdot\mathbf{m})^2. \tag{2.34}$$

where $\mathbf{e_x}$ is the unit vector in the $x-$direction [65] [72]. To relate these parameters to commonly used materials, cobalt at room temperature possesses $K_{u,1} = 4.1\times10^5$ J/m^3 and $K_{u,2} = 1.5\times10^5$ J/m^3 [57].

Surface Anisotropy

Surface anisotropy E_{surf} is an effect that arises due to the presence of interfaces. This results from the atoms experiencing a different magnetic environment due to the presence of dissimilar nearest-neighbor atoms in one direction and the broken symmetry this incurs. The overall anisotropy must therefore be considered as a bulk contribution K_{vol} and a surface contribution K_{surf}, where the surface term has an inverse dependence on the thickness of the film

$$K_{\text{tot}} = K_{\text{vol}} + 2\frac{K_{\text{surf}}}{t_{\text{FM}}} \tag{2.35}$$

where t_{FM} is the thickness of the film [1] [57]. An anisotropy of this kind was first hypothesised by Néel, where cobalt was predicted to have a K_{surf} an order of magnitude stronger per atom than K_{vol} [1, 73]. The energy density of this term is [40, 72]

$$\mathcal{E}_{\text{surf}} = -\frac{K_{\text{surf}}}{t_{\text{FM}}} m_z^2. \tag{2.36}$$

Common values for the magnitude are K_{surf} lie in the range 0.1-1 mJm^{-2} [1].

Strain Anisotropy

Strain anisotropy arises from mechanical strain or compression of a magnetic layer, arising from a lattice mismatch with adjacent layers, resulting in magnetoelastic energy. The magnetisation is associated with the strain due to the magneto-elastic coupling, with this stress generating an associated anisotropy given by

$$K_{\text{strain}} = \frac{3}{2}\sigma_{\text{stress}}\lambda_S \tag{2.37}$$

where σ_{stress} is the uniaxial stress and λ_S is the spontaneous magnetostriction. This effect is typically weak, with major contributions seen only in cases where the film is grown with a large lattice mismatch [1, 35].

2.5 Magnetic Domains

In the absence of external magnetic fields the magnetic configuration within FM and ferrimagnetic materials can form a domain structure. This results from the system seeking to minimise its free energy [1, 65]. Thus, the magnetic ordering breaks into

regions of local ordering, typically magnitudes smaller than the overall volume of material, with each region effectively acting as tiny magnets. The size of these domains range from 100 nm to 10 μm [1]. Upon the application of an external field of sufficient strength, these domains align leading to the annihilation of the domain structure and a homogeneous magnetisation across the system [7]. The first experimental evidence for domain structure was provided by Williams in 1949 regarding silicon iron single crystals [74], with domain theory subsequently becoming a central plank in the understanding of magnetisation processes [35].

The direction of magnetisation of each domain can vary region to region, with the alignment of these moments undergoing a transition across boundaries known as *domain walls* [1, 7, 35]. The first theoretical investigations into the structure of these walls was carried out by Bloch [75]. The width of a domain wall (δ_w) and its topology is governed by a competition between the exchange interaction and the magnetocrystalline anisotropy as at, or within, a wall the magnetisation must change direction from one crystallographic direction to another. As such, any abrupt changes in the direction of the spins is prevented by the exchange interaction due to the energy penalty this would incur.

There are two types of domain walls commonly encountered; referred to as *Bloch* or *Néel* walls. The reorientation of the spins in each case is shown schematically in Figure 2.4. Notably, in a Bloch wall the spins re-orientate perpendicular to the plane of the film whereas in the Néel case the magnetisation rotates within the plane of domain magnetisation. Of these two types of walls, the energy is greater in the Néel case due to the creation of a stray field from the divergence of the magnetisation generated, though there is no accompanying surface charge. Néel walls are only stable in films possessing a thickness comparable or thinner than the wall width [1, 35, 70]. In the case of hard magnetic materials with dominant crystalline anisotropy the wall is usually classified as being of the Bloch type [70]. The width of a freestanding Bloch domain wall is given by [1, 70]

$$\delta_w = \pi\sqrt{\frac{A_{\text{ex}}}{K_1}}. \tag{2.38}$$

In practice, the domain wall does not have a definitive width with the direction of the magnetisation approaching the new alignment asymptotically. The energy per unit domain wall area is defined as [1]

$$\varepsilon_w = 4\sqrt{A_{\text{ex}}K_1} \tag{2.39}$$

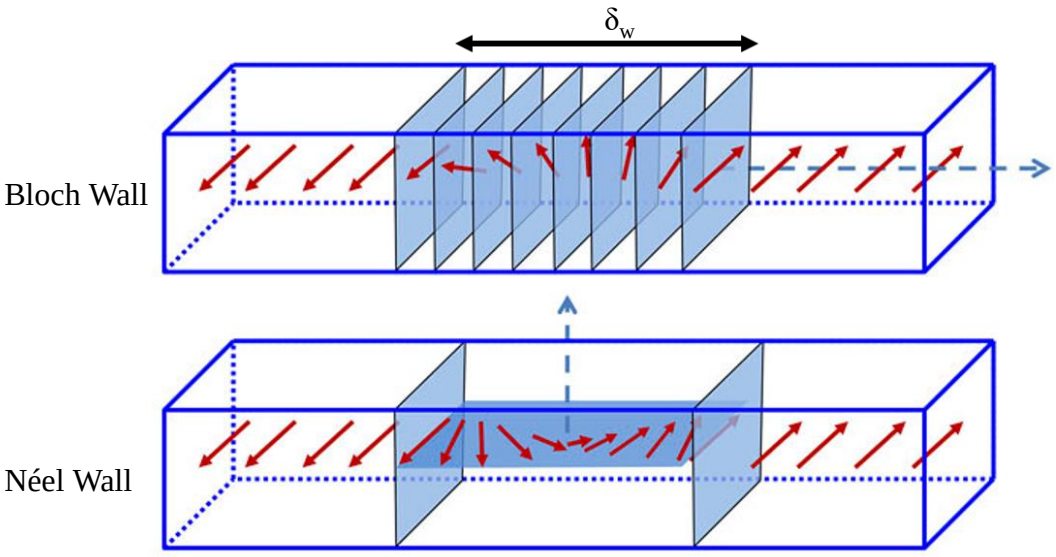

Figure 2.4: Schematic of the reorientation of spins in a Bloch or Néel type magnetic domain wall, adapted from [76]. The dashed line represents the axis of rotation of the the magnetisation with the red arrows representing the direction of the spins.

where K_1 is the first order anisotropy constant.

2.6 Magnetisation Reversal

2.6.1 Hysteresis

Spontaneous magnetisation, such as that seen in iron or magnetite, is usually accompanied with the phenomena of *hysteresis* as named by James Ewing in 1881 [1]. Indeed, the irreversible nonlinear response of the magnetisation to an externally applied magnetic field is a fundamental characteristic of any magnetic material. This *hysteresis loop*, as shown in Figure 2.5, can be used to determine many of the key parameters of magnetic materials. These include the saturation magnetisation (M_S), the remnant magnetisation (M_R) and the coercivity, also known as switching field, (H_c). The magnetic response of a material varies depending on a variety of extrinsic parameters including surface roughness, sample shape, defects along with the thermal history of the material [1]. Furthermore, the presence on an anisotropy within the system can result in vastly different hysteresis loops based on the direction of the applied field [57].

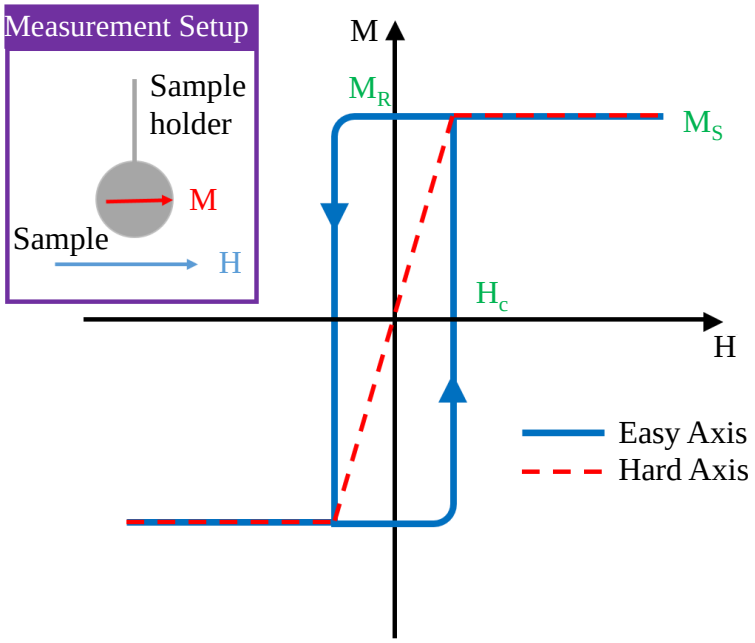

Figure 2.5: An example of a M-H hysteresis loop, where here *H* denotes external field. The major features of such a loop are labelled. Inset: Thin film measuring geometry for Vibrating Sample Magnetometry technique, detailed in section 4.2.3.

2.6.2 Stoner-Wohlfarth Model

Magnetic hysteresis was first understood through the Stoner-Wohlfath model developed by Stoner and Wohlfath in 1948 [77], where the switching of an ideal *Stoner-Wohlfarth (SW) particle* is described. Despite its restrictive conditions of coherent magnetisation reversal, where the direction of the magnetisation remains uniform throughout this process, and the lack of thermal activation (i.e. at 0 K temperature) it has proved a defining concept of this phenomena. Notably it is the simplest analytical model that displays hysteresis [1]. Furthermore, its applicability to real magnetic systems has been demonstrated [78].

The SW particle is a uniformly magnetised ellipsoid with uniaxial anisotropy of shape or magnetocrystaline origin. The externally applied field is applied at an angle α to the anisotropy axis as shown in Figure 2.6.

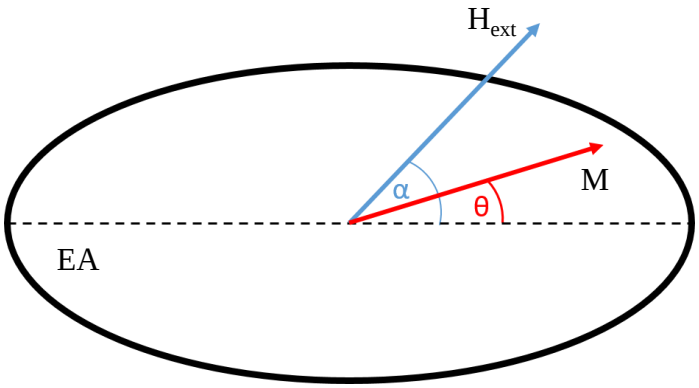

Figure 2.6: A schematic of the Stoner-Wohlfarth particle. The angle of the external field H_{ext} and the magnetisation M from the EA are denoted by α and θ respectively.

Its energy density is given by (in SI units) [35]

$$\mathcal{E}_{\text{tot,sw}} = K_u \sin^2\theta - \mu_0 MH\cos(\alpha - \theta) \tag{2.40}$$

where θ is the angle between the magnetisation vector and the easy axis. The effect of minimising $E_{\text{tot,sw}}$ leads to one of two energy minima, with the hysteresis phenomena present in the field range where the these minima are located. The switching event, occurring when $d^2E/d\theta^2 = 0$, is the result of an irreversible jump from one energy minima to another. This occurs when the condition that the switching field is equal to the coercivity of the system is satisfied [1]. Magnetisation curves of a SW particle where the external field is applied at a range of angles from the easy axis are shown in Figure 2.7.

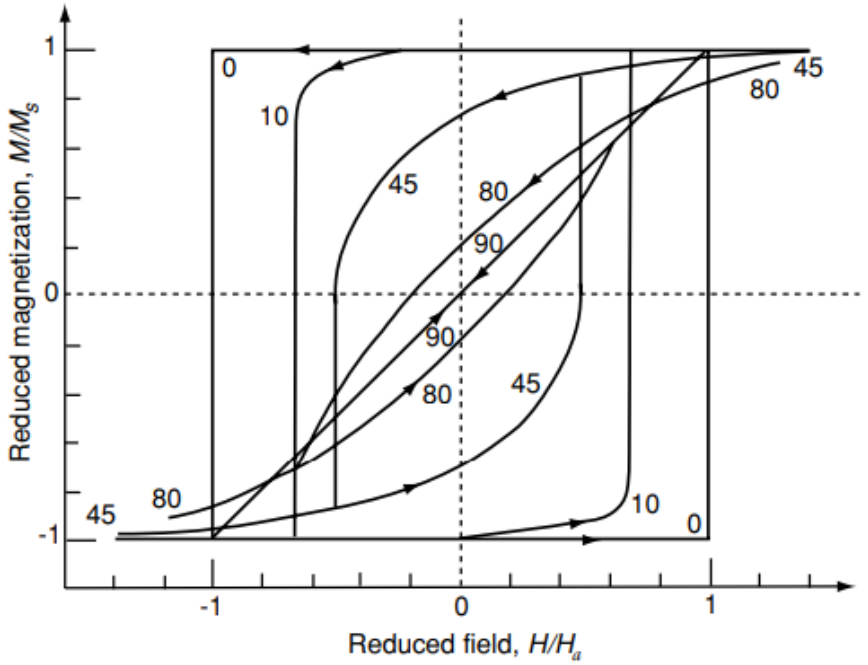

Figure 2.7: The magnetic reversal of a Stoner-Wohlfarth particle in the cases where the external magnetic field (here denoted H) is applied at a range of in-plane angles with respect to the easy axis (0^o). H is in units of the anisotropy field (here donated as H_a). This figure is reproduced from [1].

As shown in Figure 2.7, the switching field has strong dependence on the angle at which the external field is applied. In the case where $\alpha = 0$ the coercivity is equal to the anisotropy field [35, 57]

$$H_c = H_k = \frac{2K_u}{\mu_0 M_s}. \tag{2.41}$$

It is important to note that in real materials, with the exception of nanometer size particles, the magnetisation reversal is always incoherent. Thus, the physics of real systems is therefore significantly more complicated than the case of an SW particle. This is due to effects including the presence and movement of domain walls and thermal fluctuation due to a finite temperature [78]. This model can, however, be extended to the thin film case by considering a system as an array of SW particles. This provides an avenue for the exploration of polycrystalline films, for instance [1].

2.7 Interlayer Coupling

The case of interlayer coupling, which does not feature in the single layer materials discussed thus far, is now considered. This effect originates due to the artificial layering of magnetic materials to create magnetic multilayers, a key feature of the work reported in this thesis. There are two classes of mechanism through which this coupling can occur namely *exchange coupling* or *magnetostatic (dipolar) coupling* [1].

2.7.1 Exchange Coupling

Direct

Direct exchange coupling occurs between layers with different magnetic properties when they are in contact. In the case of two ferromagnets, a FM coupling forms which causes these individual layers to act as a single FM layer. This type of coupling can also occur between two FM layers separated by a NM spacer layer if pinholes are present. In this context, pinholes are breaks in the NM spacer layer such that the two magnetic layers are in contact. As coupling due to pinholes only exists over a small fraction of the interface area the strength of the coupling is typically of order $0.1\,\mathrm{mJm}^{-2}$. Further examples of direct exchange coupling include *exchange biasing*, which is present in structures where a ferromagnet is in direct contact with an antiferromagnet [1].

Indirect

The topic of interlayer coupling of FM layers through a NM metallic spacer layer (FM/NM/FM) has been a rich, widely studied area of material science. It is possible to achieve either a AF or FM coupling through such layering, the focus of the studies reported in Chapters 5 and 6 respectively, which has important ramifications for both the static and dynamic magnetic properties of the resultant thin film [40]. The first demonstrations of interlayer couplings took place in the mid-1980s independently by Fert [42] and Grünberg [43] where an AF exchange coupling between Fe layers separated by Cr was reported. The historical impact was profound, with these findings lauded as the beginnings of the fields of spintronics and nanomagnetism [29, 79, 80]. Indeed, this effect was crucial to the discovery of Giant Magnetoresistance (GMR), where the resistance of a multilayer stack is dependent on the magnetisation alignments of the metallic magnetic layers [38, 42, 81]. To elaborate, as presented schematically Figure 2.8, electrons of opposite spin to that of the majority in each FM layer face a greater

resistance than electrons of the same spin. This leads to a lower/higher resistance to electrons traversing magnetic layers with same/different magnetisation orientations. The greatest impact of the discovery of GMR is widely recognised to have been in recording technologies, where adoption of this effect is accredited with increases in recording densities of more than two orders of magnitude (from ca. 1 in 1997 to ca. 600 Gbit inch^{-2} in 2007) [9, 10].

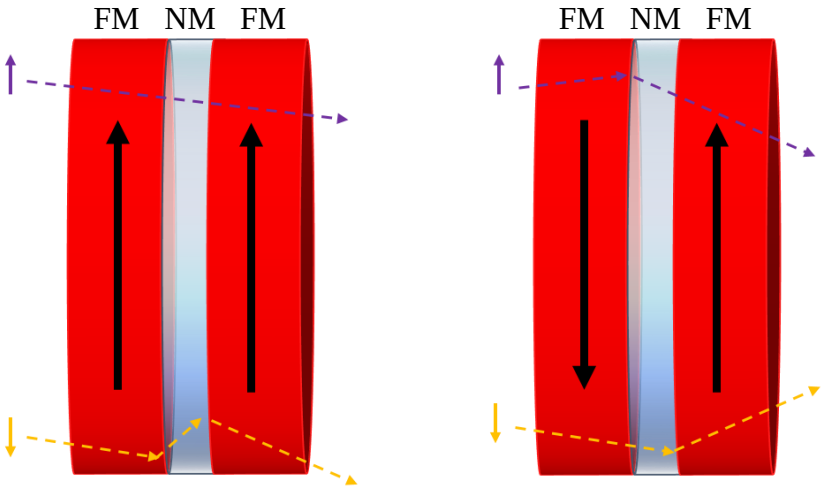

Figure 2.8: A schematic diagram of the GMR effect apparent in FM/NM/FM structures. The magnetisation of the FM layers are represented by the black arrows, with the path of a spin up (down) electron represented by the purple (orange) dashed lines. The antiparalel magnetisation arrangement possesses a higher resistance than the parallel arrangement.

The indirect exchange coupling of magnetic layers has physical origins closely linked to the RKKY (Ruderman–Kittel–Kasuya–Yosida) interaction between magnetic impurities [1, 82, 83] and was first theoretical addressed by studies performed by Bruno and Chappart [45]. A key consideration for the coupling between the FM layers is the NM spacer layer, due to this coupling being mediated by electrons within this layer. Ultimately, the properties of this layer is key and mandates the strength and type (either FM or AF) of the coupling manifested in the stack [1, 41, 45, 82]. Indeed, the RKKY interlayer exchange coupling strength (J_{IEC}) oscillates in both strength and sign (in a treatment analogous to the exchange integral discussed in section 2.4.1, a positive sign corresponds to FM coupling and a negative sign to AF coupling) as a function of NM spacer layer thickness [82]. This is shown schematically in Figure 2.9, where the

expected variation of J_{IEC} with NM spacer layer thickness is presented. It is seen that a number of instances of FM and AF coupling can be achieved, with the strength of the coupling decreasing as spacer layer thickness increases. Typically, and in the case of the material system reported in this thesis, strong AF or FM coupling is established when the NM spacer layer thickness is of order 1 nm with decoupling of the layers observed at approximately 3 nm [82]. The requirement that the NM layer is ultrathin hindered initial studies of these trilayers, with limitations in sample quality and the presence of pinholes screening any evidence of interlayer coupling until 1986.

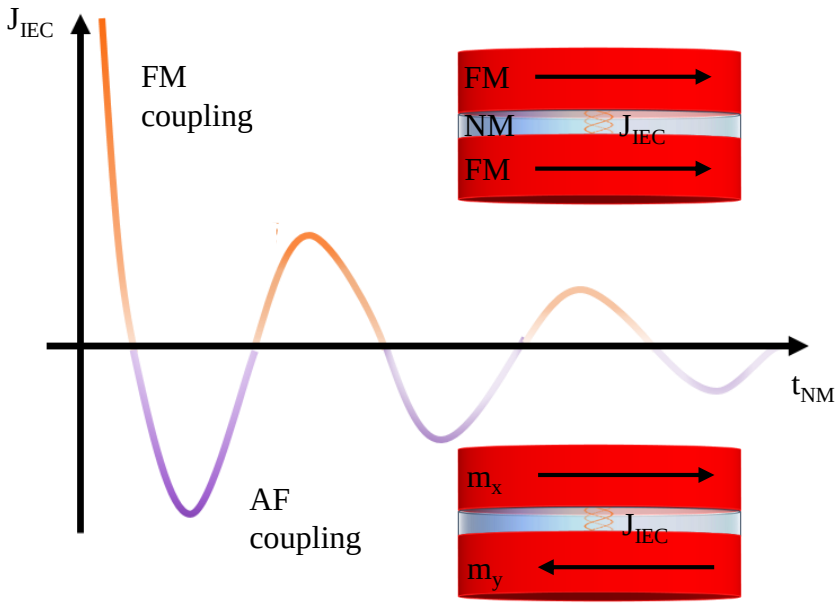

Figure 2.9: The variation of J_{IEC} with spacer layer thickness (t_{NM}) for a FM/NM/FM structure. The coupling oscillates between promoting a FM coupling and an AF coupling. The black arrows represent the direction of magnetisation of each FM layer, labelled m_x and m_y.

Ultimately, the strength and periodicity observed in the oscillation of RKKY coupling strength is dependent on the Fermi surface of the NM spacer layer. The interested reader can find additional information in the following excellent resources [84–86]. Here, we will limit discussion to the physics behind the periodicity of the coupling where *critical spanning vectors* play a key role. These are the vectors in the direction of the interface normal that connect two sheets of a Fermi surface arranged parallel to each other. The period of coupling is larger than initially expected due to the lattice

of the spacer layer. Specifically, as the spacer layer is comprised of a discrete number of monolayers (MLs), this periodicity may be screened in a phenomena known as the aliasing effect [87]. The period of these oscillations is known as the aliased period, defined as

$$\Lambda = \frac{1}{|\ \frac{2\pi}{\lambda_F} - n\frac{2\pi}{d_L}\ |} \tag{2.42}$$

where d_L is half the lattice parameter of the spacer material, λ_F is the Fermi wavelength and n is a positive integer satisfying the condition that $\Lambda = 2t_{\mathrm{NM}} = 2\mathrm{ML}$. In this relation, t_{NM} denotes the thickness of the NM spacer layer. It follows that the shortest possible oscillation period is $\Lambda = 2t_{\mathrm{NM}}$ [88]. The amplitude (strength) of the oscillatory coupling is a property of the nesting features encountered at the Fermi surface [89].

The simplest form of the energy density of the RKKY interlayer exchange coupling is given by

$$\frac{E}{A} = -J_1(\mathbf{m_x} \cdot \mathbf{m_y}) \tag{2.43}$$

where E is the energy, A the cross sectional area of the interface and J_1 is the bilinear coupling constant. The bilinear coupling constant and in later discussion the biquadratic coupling constant are indirect exchange coupling analogues of the exchange integral introduced in equation 2.19. The $\mathbf{m_x}$ and $\mathbf{m_y}$ terms are the unit magnetisation vectors of the first and second FM layers respectively, as shown in Figure 2.9. This is known as bilinear coupling as the energy per area is linear in the direction of both magnetisation. Analogous to the exchange interaction, in case of positive J_1 this coupling favors parallel alignment of the layer magnetisation, with antiparallel alignment promoted in the case of negative J_1 [87, 90]. There can also be the presence of a biquadratic coupling, which is attributed to extrinsic effects, such as disorder caused by interfacial roughness and manifestations of short period topological oscillations at the interfaces [87, 90–93]. In this case, the energy varies quadratically in both directions. Pinholes, can also lead to the generation of biquadratic coupling in cases where the bilinear coupling is antiferromagnetic [94]. In energy terms, biquadratic coupling is expressed as

$$\frac{E}{A} = -J_2(\mathbf{m_x} \cdot \mathbf{m_y})^2 \tag{2.44}$$

where J_2 is the biquadratic coupling constant [90]. In the case where J_2 is positive it favours a colinear alignment, with a negative value promoting a perpendicular layer magnetisation alignment. For completeness, when these two contributing energies are

considered, the total energy interlayer exchange coupling energy can be defined as

$$\frac{E}{A} = -J_1\cos(\Delta\psi) - J_2\cos^2(\Delta\psi) \tag{2.45}$$

where $\Delta\psi$ is the angle between magnetisation of the films on each side of the spacer layer [95]. This phenomenological model has been successful in interpreting the behaviour of a number of magnetic systems [87, 90]. Experimentally, it is found that the biquadratic coupling is typically magnitudes smaller than the bilinear coupling [96].

The strength of the interlayer exchange coupling in the case of AF coupling is often probed by investigating the magnetic field strength required to overcome this energy and force the layer magnetisations into a parallel arrangement (denoted H_{Sat}) . This relation is

$$J_{\mathrm{IEC}} = M_S H_{\mathrm{Sat}} \frac{t_x t_y}{t_x + t_y} \tag{2.46}$$

where t_x and t_y are the thicknesses of the individual magnetic layers [97].

This RKKY interaction can be realised with a range of materials acting as the NM spacer layers including Cu, Ir and Ru [1, 41, 93]. Of these, the latter is often utilized as the spacer layer material due to its ability to promote AF interlayer exchange coupling in a number of magnetic materials such as Co, Fe, Ni and various composites. In this project, Ru was used due to its proven ability to support strong interlayer exchange couplings [1, 41].

2.7.2 Dipolar Coupling

Magnetic multilayers can also experience a coupling due to magnetostatic effects arising both macro- and micro-scopically. These can manifest in the cases where the interlayer is comprised of a metallic or insulating material. The simplest form of magnetostatic coupling between two FM layers is through the interaction of the the stray fields of the layers, a phenomena detailed in section 2.4.2. This results in the FM layers exhibiting a preference to orientate antiferromagnetically in order to minimise this stray field. In contrast to the case of interlayer exchange coupling, this magnetostatic coupling is highly non-uniform at the edges of the film compared to the central region. This form of coupling becomes important in the case of devices possessing sub-micron lateral directions [98, 99]. Furthermore, if the sample is not uniformly magnetised, a further magnetostatic coupling can arise from the presence of Néel domain walls. Due to the stray field of this type of domain wall being out of the plane of the thin film, it acts to lower the energy required to nucleate a domain wall in another FM film in close

proximity [100].

Néel studied the magnetostatic coupling arising due to the stray field generated from the roughness present at the interfaces. In the ideal case of perfectly smooth, uniformly magnetised FM layers this effect does not occur. It is commonly referred to as the *orange peel effect* or as *Néel coupling* and was first studied in 1962 [101–104]. Essentially, this roughness results in the formation of magnetic charges on the surface of magnetic layers as presented in Figure 2.10. In the event that this occurs on both sides of the magnetic layers in a correlated fashion it can lead to the formation of a magnetostatic coupling between the layers [105]. Layer roughness has become a key concern to the development of many technologies, where interfacial effects are essential to the functionality of the material [1, 19].

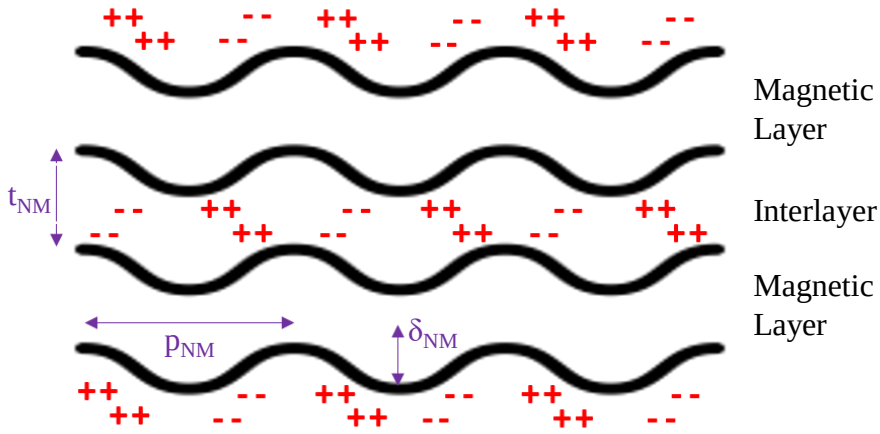

Figure 2.10: Schematic of the orange peel effect experienced by a FM/NM/FM multilayer with spacer layer thickness t_{NM}. The in-plane roughness has an amplitude δ_{NM} and period p_{NM} [102].

The magnitude of this dipolar coupling as a function of roughness, as calculated by Kools [103], is given by

$$\sigma_d = \frac{\pi^2}{\sqrt{2}} \frac{\delta_{\mathrm{NM}}^2}{p_{\mathrm{NM}}} \mu_0 M_S^2 \exp(-2\pi\sqrt{2} t_{\mathrm{NM}}/p_{\mathrm{NM}}) \tag{2.47}$$

where δ_{NM} is the amplitude of the surface roughness of the spacer layer and p_{NM} is the periodicity of the roughness. This interaction can modify the magnetic behaviour of a stack in various manners compared to a single film. For example, in multilayers with identical magnetic layers, it can alter the coercivity of the stack from the single layer

case [102, 105]. This effect can also weaken any interlayer exchange coupling, culminating in a dominating orange peel coupling. Notably, FM orange peel coupling, due to in-phase interface roughness, could partially negate AF exchange coupling resulting in the reduction of the net coupling [102, 106].

2.8 Chapter Summary

In this chapter, the origins of magnetism and its characteristic energies have been detailed. A discussion of effects observable only at the nanoscale have been described, with the phenomena of interlayer coupling in particular elucidated upon. The following chapter focuses on the dynamical behaviour of magnetic materials that occur when the magnetisation is perturbed from its equilibrium position. These effects comprise of the main focus of this thesis.

Chapter 3

Magnetisation Dynamics

The dynamics of magnetically ordered materials offers insights into the fundamental physics governing magnetic processes along with a plethora of device applications. This chapter introduces this rich area of magnetism, with a particular focus on the phenomena of magnetisation precession and its associated damping due to its central importance to the work reported in this thesis.

3.1 Magnetisation Precession

Key to the dynamical behaviour of magnetic materials is the concept of *precession*, where the moments in a magnetic material precess around their equilibrium position due to a perturbation by a small alternating external magnetic field ($\mathbf{h}_{\text{rf}}$) [7]. This physical phenomenon is analogous to a spinning top [7]. First, the case where an electron is constrained to move in an orbit, as outlined in section 2.2.1, and acts as an isolated moment is considered. The torque ($\boldsymbol{\Gamma}$) this moment experiences due to the application of an external magnetic field $\mathbf{H}_{\text{ext}}$ is given by

$$\boldsymbol{\Gamma} = \boldsymbol{\mu} \times \mathbf{H}_{\text{ext}} \tag{3.1}$$

where the symbol definitions are provided in Chapter 2. From Newton's law of angular momentum $\boldsymbol{\Gamma} = \frac{d\boldsymbol{\ell}}{dt}$ where ℓ is the angular momentum, we can obtain

$$\frac{d\boldsymbol{\mu}}{dt} = -\gamma_{\text{orb}}\, \boldsymbol{\mu} \times \mathbf{H}_{\text{ext}}. \tag{3.2}$$

where γ_{orb} is the orbital gyromagnetic ratio, as introduced in Chapter 2. In the case of an isolated moment, the precession around the applied field direction occurs at the Larmor frequency [1]

$$f_L = \frac{\gamma_{\text{orb}} H_{\text{ext}}}{2\pi}. \tag{3.3}$$

It is insightful that the Plank constant is not present in equation 3.3 meaning that through the correspondence principle this expression can be derived classically [2]. Notably, the precessional frequency has different values depending on the type of magnetic moment under consideration, as detailed in section 2.2. To repeat, in the case where only an orbital moment is considered $\frac{\gamma_{\text{orb}}}{2\pi} = 14\,\text{GHz/T}$ but for a spin moment $\frac{\gamma_{\text{spin}}}{2\pi} = 28\,\text{GHz/T}$ (also known as the cyclotron frequency) [1]. In reality, electrons possess a mixture of orbital and spin angular momentum, as presented in equation 2.8. In this case, the γ term as shown in equation 2.10 and restated here for clarity [7]

$$\gamma = g\frac{e}{2m_e}. \tag{3.4}$$

where g is the Landé g-factor and e and m_e are the magnitude of the electron charge and mass respectively. When we consider ferromagnetic (FM) materials the concept of Larmor precession is no longer a valid description of the system. This is due to a magnetic system being comprised of a complicated ensemble of strongly interacting electrons which generate a substantial magnetisation and consequently large internal magnetic field [2]. Therefore, we must once again introduce the concept of effective magnetisation $\mathbf{H}_{\text{eff}}$, defined in equation 2.16, to develop a thorough description of the magnetisation dynamics [107]. The most general statement for the precessional motion of the magnetisation is given by an equation of motion of the form [2, 7, 107]

$$\frac{d\mathbf{M}}{dt} = -\gamma\mathbf{M} \times \mathbf{H}_{\text{eff}}. \tag{3.5}$$

The presence of a negative sign in the equation of motion is required to describe the direction of the precessional motion [2] [7], for reasons outlined in section 2.2.1.

It is essential at this stage that we now highlight a key difference in the g-factor obtained using different magnetometry techniques. Discrepancies due to different measurement techniques became particularly apparent after the advent of Ferromagnetic Resonance (FMR) spectroscopy and the studies of the precessional motion of magnetisation. Put simply, the g-factor obtained from a FMR experiment has a different value to that performed through the use of a technique such as the Einstein-de Haas effect [108–110]. This is because, in the latter case, the measurement incorporates the influence of both spin and orbital angular momentum and derives a quantity known as the *Magnetomechanical g-factor (g')*. However, the FMR technique is only influenced by the spin angular momentum, and thus measures a quantity referred to as the *spectroscopic g-factor* [107, 111], denoted as g in the derivation put forth in section

3.2. This is a result of the orbital moment being *quenched* due to the crystal field of the lattice produced in surrounding atoms or ions in the solid. Specifically, the orbital moments are bound rather strongly to the lattice whereas the spins only experience weak coupling. Therefore, when a magnetic field is applied to a magnetic system the orbits, along with their corresponding moments, are bound to the lattice and do not contribute to these magnetic measurements with only spin contribution measured [35]. A description of the crystal fields responsible for this quenching is available in section 2.4.4.

Thus, g should have the value 2, with Fe, Co and Ni exhibiting room temperature g values of 2.10, 2.18 and 2.21 respectively [64]. An approximation to first order relates g and g' through the relation [112, 113]

$$g - 2 = 2 - g'. \tag{3.6}$$

Indeed, in the situation where the effective electronic orbital contribution to the magnetisation (M_{orb}) is much less than the saturation magnetisation (M_S) such that $\frac{M_{\text{orb}}}{M_S} \lll 1$, it can be shown

$$g' = 2 - 2\frac{M_{\text{orb}}}{M_S} \tag{3.7}$$

and that

$$g = 2 + 2\frac{M_{\text{orb}}}{M_S}. \tag{3.8}$$

It is therefore clear that g' and g deviate from 2 by twice the ratio $\frac{M_{\text{orb}}}{M_S}$, with opposite signs [110].

Hitherto, the descriptions of magnetisation precession have assumed that the motion is lossless with the system therefore incapable of achieving the lowest energy configuration with $\mathbf{M}$ parallel to $\mathbf{H}_{\text{eff}}$. This situation arises due to the lack of the incorporation of a magnetic damping, hence energy dissipating, mechanism into equation 3.5 [7]. However, in experimental observation the magnetisation returns to its equilibrium position in a finite time. This occurs through mechanisms including eddy currents and phonon excitations via the spin lattice coupling which act as energy dissipating channels [65], as detailed in later sections. To address this, Landau and Lifshitz altered the formulation of equation 3.5 to included damping as a phenomenological torque which slowly re-orientated the magnetisation towards the effective field direction [114]. This

Landau-Lifshitz (LL) formulation is given by

$$\frac{d\mathbf{M}}{dt} = -\gamma(\mathbf{M} \times \mathbf{H}_{\text{eff}}) - \frac{\lambda}{M_S^2}\mathbf{M} \times (\mathbf{M} \times \mathbf{H}_{\text{eff}}). \tag{3.9}$$

and contains a phenomenological damping constant $\lambda = 1/\tau$ which corresponds to the inverse of the relaxation time (τ) and possesses the dimension of frequency [65, 114]. A major issue with this model is the incorrect prediction of fast precession in large damping regimes. In 1955, Gilbert [115] introduced a much more successful viscous torque equation where damping is proportional to the time derivative of the magnetisation. The Landau-Lifshitz-Gilbert (LLG) formalism is

$$\frac{d\mathbf{M}}{dt} = \underbrace{-\gamma(\mathbf{M} \times \mathbf{H}_{\text{eff}})}_{\text{Precessional term}} + \underbrace{\frac{\alpha}{M_S}\left(\mathbf{M} \times \frac{d\mathbf{M}}{dt}\right)}_{\text{Damping term}} \tag{3.10}$$

where α is the *dimensionless phenomenological damping parameter* [1, 7, 35, 107]. To be clear, as shown schematically in Figure 3.1, the first term on the RHS represents the precessional motion whilst the last term represents the damping term. As a result of the damping term, the magnetisation relaxation follows a helical trajectory towards the equilibrium position. Furthermore, in both cases the length of the magnetisation is preserved [72]. It should be emphasised that the damping term is wholly phenomenological, made necessary to accurately unify the predictions of modelling with experimental observation. As discussed in section 3.4, the processes responsible for energy dissipation in a magnetic material are numerous and therefore can only be approximated by a single damping parameter.

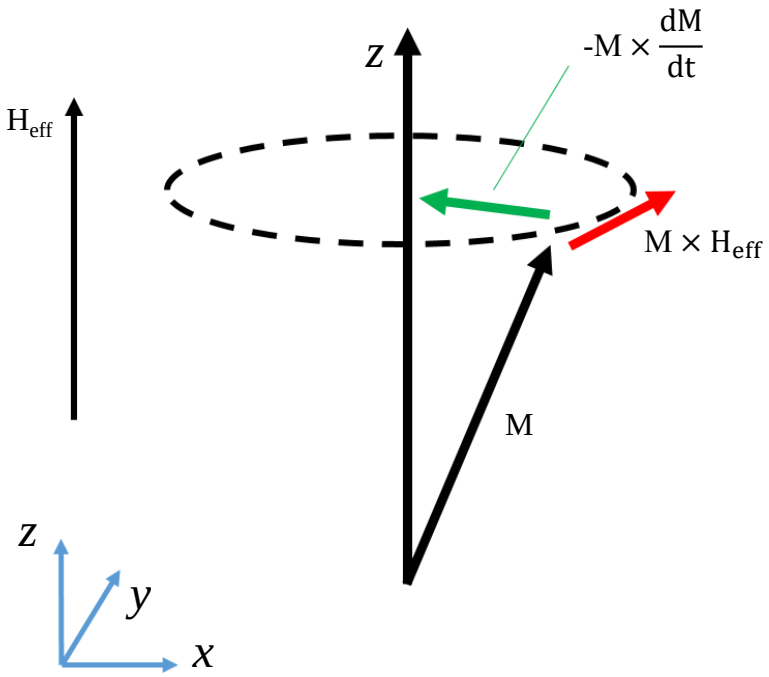

Figure 3.1: Schematic of damped magnetisation precession following LLG formalism presented in equation 3.10. From this model, it can be seen that the precesional motion of **M** is dissipated through the effects of damping resulting in **M** eventually aligning with $\mathbf{H}_{\text{eff}}$.

3.2 Dynamic Susceptibility

It is not feasible to obtain an analytical solution to the LLG equation (equation 3.10) in its general form. In the following, the approach of solving this equation for a special case is presented, guided by the work of Bilzer [72], Gurevich [116] and Neudecker [117]. This derivation will be carried out in SI, utilising the SI version of the magnetisation energies detailed in section 2.4, and consider the angular frequency $\omega = 2\pi f$ where f is frequency. The relevant equations to understand the work reported in Chapters 5, 6 and 7 will then be converted to CGS and stated in terms of f. To begin, we list the assumptions required for this derivation:

- The sample is a thin film (thus infinitely extended) in the $x-y$ plane. Therefore, as introduced in section 2.4.2, the demagnetising factors are $N_x = N_y = 0$ and $N_z = 1$.
- The presence of a uniaxial IP magnetocrystalline anisotropy ($H_{\text{uni}} \ll M_S$) with an EA along x.

- The presence of a uniaxial perpendicular anisotropy as a result of the two surfaces present. It is necessary to assume that it is weaker than the demagnetising field and that the effective magnetisation remains positive (eg. in-plane) .

- The magnetisation uniformly points in the direction of the externally applied homogeneous magnetic field $\mathbf{H}_{\text{ext}}$.

- The system possesses a low damping such that $\alpha \ll 1$.

- The magnetisation is treated in the macrospin model where no spatial variation of the magnetisation vector is permitted.

- The presence of a small uniform excitation field $\mathbf{h}_{\text{rf}}$ directed along the y-axis ie. perpendicular to $\mathbf{H}_{\text{ext}}$.

These assumptions adequately reflect the nature of the sample and experimental conditions of a FMR experiment as described in section 4.3. The interested reader is guided to section 4.3.1 where a discussion concerning the limitations of these assumptions is available. As $\mathbf{h}_{\text{rf}} \ll \mathbf{H}_{\text{ext}}$, the excitation field will generate a small angle precession of the magnetisation around the x-axis. Thus, we are able to separate the magnetisation components into static and dynamics contributions

$$\mathbf{M} = M_S\mathbf{m} \approx M_S\mathbf{e_x} + m_y\mathbf{e_y} + m_z\mathbf{e_x} \tag{3.11}$$

where m_y and m_z are the oscillating high frequency components of the magnetisation. The $\mathbf{e_x}$, $\mathbf{e_y}$ and $\mathbf{e_z}$ are unit vectors in the x, y and z directions respectively. The total energy density is comprised of the contributions described by the SI forms of equations 2.30, 2.31, 2.34, 2.36, and has the form

$$\mathcal{E}_{\text{tot}} = -\mu_0\mathbf{M}\cdot\mathbf{H}_{\text{ext}} + \frac{\mu_0}{2}(\mathbf{e_z}\cdot\mathbf{M})^2 - K_u(\mathbf{e_x}\cdot\mathbf{m})^2 - \frac{K_{\text{surf}}}{t_{\text{FM}}}(\mathbf{e_z}\cdot\mathbf{m})^2. \tag{3.12}$$

Under the perturbation of a small excitation field we find, after making use of equation 2.16,

$$\mathbf{H}_{\text{eff}} = \mathbf{H}_{\text{ext}} + \mathbf{h}_{\text{rf}} - \mathbf{e_z}(\mathbf{e_z}\cdot\mathbf{M}) + \frac{2K_{\text{surf}}}{t_{\text{FM}}\mu_0 M_S}\mathbf{e_z}(\mathbf{e_z}\cdot\mathbf{m}) + \frac{2K_u}{\mu_0 M_S}\mathbf{e_x}(\mathbf{e_x}\cdot\mathbf{m}) \tag{3.13}$$

To simplify this equation, we use introduce the term H_k representing the uniaxial

anisotropy and M_{eff} containing the demagnetising and perpendicular anisotropy contributions. As such

$$H_k = \frac{2K_u}{\mu_0 M_S} \tag{3.14}$$

and

$$M_{\text{eff}} = M_S - \frac{2K_{\text{surf}}}{t_{\text{FM}}\mu_0 M_S} \tag{3.15}$$

From equations 3.11, 3.14 and 3.15 being introduced into 3.13, we obtain

$$\mathbf{H}_{\text{eff}} = (H_{\text{ext}} + H_{\text{k}})\mathbf{e_x} + h_{\text{rf}}\mathbf{e_y} - \frac{M_{\text{eff}}}{M_S} m_z \mathbf{e_z}. \tag{3.16}$$

We now introduce the LLG formalism of magnetisation motion (equation 3.10) which shows

$$\begin{pmatrix} 0 \\ \frac{dm_y}{dt} \\ \frac{dm_z}{dt} \end{pmatrix} = -\gamma\mu_0 \begin{pmatrix} M_S \\ m_y \\ m_z \end{pmatrix} \times \begin{pmatrix} H_{\text{ext}} + H_k \\ h_{\text{rf}} \\ -\frac{M_{\text{Eff}}}{M_S} m_z \end{pmatrix} + \frac{\alpha}{M_S} \begin{pmatrix} M_S \\ m_y \\ m_z \end{pmatrix} \times \begin{pmatrix} 0 \\ \frac{dm_y}{dt} \\ \frac{dm_z}{dt} \end{pmatrix}. \tag{3.17}$$

We can now separate equation 3.17 into its individual components to obtain

$$0 = -\gamma\mu_0(-m_y \frac{M_{\text{eff}}}{M_S} m_z - m_z h_{\text{rf}}) + \frac{\alpha}{M_S}\left(m_y \frac{dm_z}{dt} - m_z \frac{dm_y}{dt}\right) \tag{3.18}$$

$$\frac{dm_y}{dt} = -\gamma\mu_0(m_z(H_{\text{ext}} + H_k) + M_{\text{eff}} m_z) - \alpha\frac{dm_z}{dt} \tag{3.19}$$

$$\frac{dm_z}{dt} = -\gamma\mu_0(M_S h_{\text{rf}} - m_y(H_{\text{ext}} + H_k)) + \alpha\frac{dm_y}{dt}. \tag{3.20}$$

We then linearise this set of differential equations in h_{rf} and m_i where $i = x, y, z$ by discounting the terms that contain a product of these as, due to the small angles of precession under consideration, $h_{\text{rf}} \ll H_{\text{ext}}$ and $m_i \ll M_S$ thus their product is negligibly small [117]. We now seek to describe the time dependence of the system by introducing the expected oscillating motion $m_i = Re(\tilde{m_i} e^{i\omega t})$ with an accordingly represented excitation field $h_{\text{rf}} = Re(\tilde{h_{\text{rf}}} e^{i\omega t})$. For ease, we introduce ω which represents the angular frequency of the perturbating field and $\tilde{h_{\text{rf}}}$ and $\tilde{m_i}$ that represent the amplitudes of the alternating field and magnetisation respectively. Whilst $\tilde{h_{\text{rf}}}$ is real, the $\tilde{m_i}$ are complex values where $\text{Re}(\tilde{m_i})$ is in-phase with $\tilde{h_{\text{rf}}}$ and $\text{Im}(\tilde{m_i})$ is out-of-phase. Through

inserting this notation into equations 3.18, 3.19 and 3.20 we find

$$0 = \tilde{m}_y(i\omega) + \tilde{m}_z(\omega_H + \omega_{\text{eff}} + i\omega\alpha) \tag{3.21}$$

$$\omega_M \tilde{h_{\text{rf}}} = \tilde{m}_y(i\omega\alpha + \omega_H) + \tilde{m}_z(-i\omega) \tag{3.22}$$

where

$$\omega_H = \gamma\mu_0(H_{\text{ext}} + H_k) \ ; \ \omega_M = \gamma\mu_0 M_s \ ; \ \omega_{\text{eff}} = \gamma\mu_0 M_{\text{eff}}. \tag{3.23}$$

This can be rewritten as a relation between $\mathbf{h}_{\text{rf}} = (\tilde{h_{\text{rf}}}, 0)$ and $\mathbf{m} = (\tilde{m}_y, \tilde{m}_z)$ as follows

$$\begin{pmatrix} \tilde{h_{\text{rf}}} \\ 0 \end{pmatrix} \omega_M = \begin{bmatrix} \omega_H + i\omega\alpha & -i\omega \\ i\omega & \omega_H + \omega_{\text{eff}} + i\omega\alpha \end{bmatrix} \begin{pmatrix} \tilde{m}_y \\ \tilde{m}_z \end{pmatrix}. \tag{3.24}$$

Following the approach of Polder [118], described by equation 2.13, we rearrange the equation as

$$\begin{pmatrix} \tilde{m}_y \\ \tilde{m}_z \end{pmatrix} = \mathbf{m} = \bar{\bar{\chi}}\mathbf{h}_{\text{rf}} = \begin{bmatrix} \chi_{yy} & \chi_{yz} \\ \chi_{zy} & \chi_{zz} \end{bmatrix} \begin{pmatrix} \tilde{h_{\text{rf}}} \\ 0 \end{pmatrix} \tag{3.25}$$

where $\bar{\bar{\chi}}$ is the susceptibility in its tensor form. Therefore, from rearranging equation 3.24

$$\begin{pmatrix} \tilde{m}_y \\ \tilde{m}_z \end{pmatrix} = \frac{\omega_M}{\omega_H(\omega_{\text{eff}} + \omega_H) - \omega^2 + i\omega\alpha(2\omega_H + \omega_{\text{eff}})} \begin{bmatrix} \omega_H + \omega_{\text{eff}} + i\omega\alpha & i\omega \\ -i\omega & \omega_H + i\omega\alpha \end{bmatrix} \begin{pmatrix} \tilde{h_{\text{rf}}} \\ 0 \end{pmatrix} \tag{3.26}$$

As we consider only low damping situations we can simplify this equation through the approximation that $1 + \alpha^2 \approx 1$. We measure the component χ_{yy} of the susceptibility tensor, with the real and imaginary parts $\chi'_{yy} - i\chi''_{yy}$ (negative sign following common usage) are

$$\chi'_{yy} = \frac{\omega_M(\omega_H + \omega_{\text{eff}})(\omega_{\text{res}}^2 - \omega^2)}{(\omega_{\text{res}}^2 - \omega^2)^2 + \alpha^2\omega^2(2\omega_H + \omega_{\text{eff}})^2} \tag{3.27}$$

$$\chi''_{yy} = \frac{\alpha\omega\omega_M[\omega^2 + (\omega_H + \omega_{\text{eff}})^2]}{(\omega_{\text{res}}^2 - \omega^2)^2 + \alpha^2\omega^2(2\omega_H + \omega_{\text{eff}})^2} \tag{3.28}$$

where ω_{res} represents the resonant frequency defined by

$$\omega_{\text{res}}^2 = \omega_H(\omega_{\text{eff}} + \omega_H). \tag{3.29}$$

Thus, in CGS,

$$f_r = \frac{\omega_{\text{res}}}{2\pi} = \frac{\gamma}{2\pi}\sqrt{(H_{\text{ext}} + H_{\text{k}})(H_{\text{ext}} + H_{\text{k}} + 4\pi M_{\text{Eff}})}. \tag{3.30}$$

The obtained solution presented in equation 3.30 is a special case of the well-known Kittel's equation [6]. A more general result for the resonant frequency for an ellipsoid sample is provided by (in CGS)

$$f_r = \frac{\gamma}{2\pi}\sqrt{(H_{\text{ext}} + H_{\text{k}} + (N_z - N_x)4\pi M_{\text{Eff}})(H_{\text{ext}} + H_{\text{k}} + (N_y - N_x)4\pi M_{\text{Eff}})} \tag{3.31}$$

To recover the case where the applied field is IP (equation 3.30) we consider a thin film such that $N_x = N_y = 0$ and $N_z = 1$ along with the presence of an additional surface anisotropy ($\omega_M \to \omega_{\text{eff}}$). Furthermore, we can see that in the case where there is the presence of an out-of-plane (OOP) field, the demagnetising factors are of form $N_z = 0$, $N_y = 0$ and $N_x = 1$ with the resonance described as (in CGS)

$$f_r = \frac{\gamma}{2\pi}(H_{\text{ext}} + H_{\text{k}} - 4\pi M_{\text{Eff}}). \tag{3.32}$$

This resonant mode is known as the fundamental or ferromagnetic resonance (FMR) mode where all spins precess with the same frequency and phase [6, 50].

We can now discuss the physical meanings that can be drawn from the obtained equations, particularly concerning ourselves with the dynamic susceptibility. The real part χ'_{yy} expresses the component of $\tilde{m}_y$ that is in-phase with $\tilde{h_{\text{rf}}}$ whereas χ''_{yy} expresses its component delayed by a phase angle of 90° (out-of-phase) from $\tilde{h_{\text{rf}}}$. Therefore, ω_{res} is the frequency at which $\tilde{m}_y$ and $\tilde{h_{\text{rf}}}$ are out of phase by 90° such that $\chi'_{yy}(\omega_{\text{res}}) = 0$. Indeed, in a lossless system ($\alpha = 0$) from equation 3.28 it can be seen that $\chi''_{yy} = 0$ and therefore $\chi_{yy} = \chi'_{yy}$ [72, 117]. The presence of the out-of-phase component χ''_{yy} results in the requirement of a supply of energy to maintain the alternating magnetisation [2, 119].

An example of the variation of the real and imaginary components of χ_{yy} is shown in Figure 3.2. The real part χ'_{yy} represents the dispersion and has the functional dependence of an asymmetric Lorentzian around ω_{res} reaching zero at this frequency. At the extremes

$$\chi_{\text{stat}} = \chi'_{\text{stat}} = \frac{\omega_M}{\omega_H} = \frac{M_S}{H_{\text{ext}} + H_k} \tag{3.33}$$

as expected from static measurements, reproducing the result presented in equation 2.13. Another important feature of χ'_{yy} is the antiresonance frequency ω_{antires} where

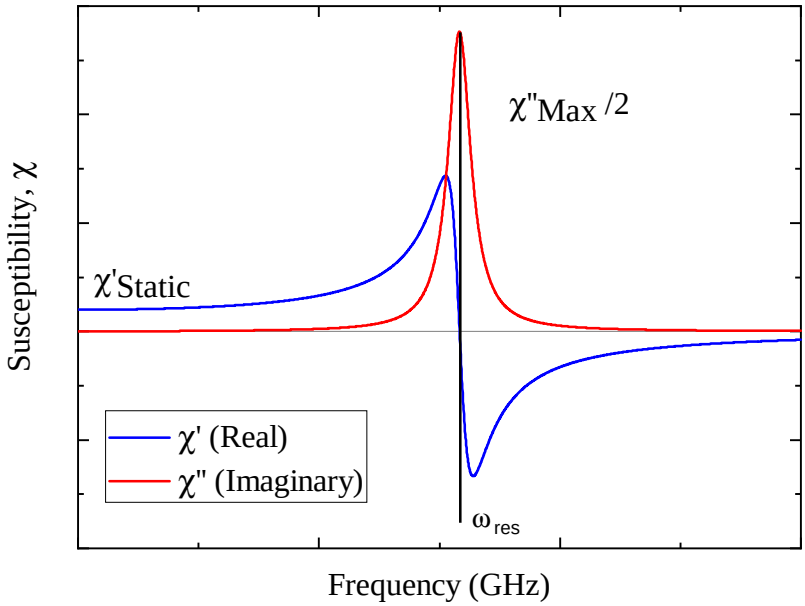

Figure 3.2: An example of the variation of the dynamic susceptibility χ_{yy} of a magnetic sample with excitation frequency as derived under the assumptions outlined at the start of section 3.2.

$\chi'_{yy} = -1$ and, following from equation 2.14, the permeability is equal to zero. At this resonance the skin depth (defined in equation 3.49) increases significantly thus maximising the perturbating field passing through the film and hence transmitted power [120]. The imaginary part of the permeability has a very small value at this point, with a minimum in the energy absorption seen. The condition for antiresonance is [72] [120]

$$\omega_{\text{antires}} = \sqrt{(\omega_{\text{eff}} + \omega_H)(\omega_M + \omega_H)} \approx \omega_{\text{eff}} + \omega_H. \tag{3.34}$$

The first observation of an antiresonance minimum was reported by Yager from investigations of surface impedance of a thin film of supermalloy [121]. The antiresonance frequencies are greater than that seen for the FMR mode [120].

As aforementioned, the imaginary part χ''_{yy} represents the absorption of energy by the magnetic system and is a symmetric Lorentzian around ω_{res} reaching a maximum at this frequency. A bound on the high frequency magnetic losses expected from a magnetic material can be stated in terms of its M_S, where the integral of the frequency

weighted χ''_{yy} is of the form

$$I = \int_0^{+\infty} f\chi''_{yy} df \approx \frac{\pi}{2}(2\gamma M_S)^2. \tag{3.35}$$

This relation is valid independently of the anisotropy field and the applied external field [122].

The linewidth of the resonance, the Full Width at Half Maximum (FWHM) of the imaginary part of the susceptibility χ''_{yy}, is related to the damping constant α through (in general form) [117]

$$\alpha = \frac{\Delta f}{2\omega_H + (N_z + N_y - 2N_x)\omega_M}. \tag{3.36}$$

It should be noted that χ'' is not precisely symmetric around ω_{res} and this is therefore a slight approximation. In terms of the IP static field discussed in this work, the linewidth is (in CGS) [123]

$$\Delta f = \gamma\alpha(2(H_{\text{ext}} + H_k) + 4\pi M_{\text{Eff}}). \tag{3.37}$$

For completeness, we introduce the relation of field swept linewidth ΔH which is measured when the field is swept at a constant frequency. This is a widely reported parameter in literature due to the dominance of field-swept FMR and cavity-based techniques in this research area. It is related to α through [124, 125]

$$\Delta H = 4\pi\frac{\alpha}{\gamma} f_{\text{res}}. \tag{3.38}$$

In this work, only frequency swept measurements were carried out and therefore only Δf is considered. The linewidth depends primarily upon the physical nature of the relaxation processes, which in turn are governed by the internal interactions in the magnetic system from which damping originates [2, 126, 127]. The direct correlation between the Gilbert damping constant, α, and the linewidth of the resonance peak leads to, as will be discussed in section 3.4, examinations of the linewidth being one of the main methods to investigate the relaxation mechanisms in thin films.

3.3 Spin Waves

The previous discussion has focused solely upon the uniform precession of the magnetisation, where the spins coherently precess at the same frequency and phase, referred to as the FMR mode. In this discussion, we will now consider higher order modes where the spins precess at the same frequency but different phases. These *spin waves* can be generated in real world conditions due to effects such as finite temperature, non-uniform excitation fields or sample defects. A schematic of the form of a spin wave is shown in Figure 3.3. Historically, these higher order spin waves were first theorized by Bloch in 1930 [75] with experimental evidence obtained by Seavey and Tannenwald in 1958 [128].

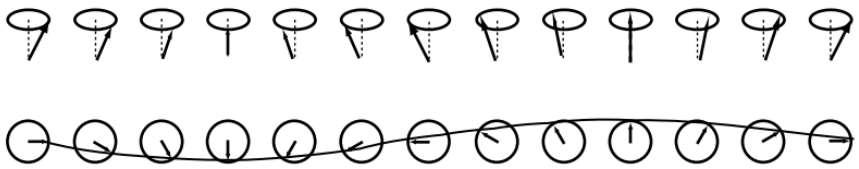

Figure 3.3: A schematic of a spin wave. The individual spins, represented through the black arrows, precess at the same frequency but at different phases. This figure was reproduced from [1].

It is common to treat spin waves as a type of quasiparticles called magnons, a quanta of collective excitations of moments, in an analogous treatment to that seen in the case of lattice vibration and phonons. Magnons hold great promise for nanoelectronics [129–131] with the nascent field of magnonics offering functionalities in RF applications beyond that possible through conventional electronics or surface acoustic waves [129]. These features include nonlinearity, reconfigurability, scalability to sub-100 nm and a wide operational frequency range from 1 GHz to 100s THz [27]. Moreover, a greater knowledge of spin wave phenomena is also sought to increase the understanding of magnetic processes in thin film magnetic recording heads [7].

A central plank to the understanding of spin wave phenomena is the *wavevector*, defined as

$$k = \frac{2\pi}{\lambda} \tag{3.39}$$

where λ is the wavelength [57]. This provides the criteria to classify the range of spin waves arising from exchange or dipolar effects. The FMR mode possesses wavevector

$k = 0$, and thus can be understood as a wave of infinite wavelength, with higher order excitations possess non-zero wavevector ($k \neq 0$). Short wavelength spin waves (high k) are dominated by the exchange interaction, and possess wavelength ($\lambda < 1\,\mu$m). In the case of long wavelength spin waves (small k) the exchange interaction is too short range to dominate with the longer range dipolar interactions instead governing these excitations. The general term *spin wave* is used to describe both dipolar and exchange dominated excitations. We use the terms *exchange spin wave* to describe situations where only the exchange interaction is important and *magnetostatic wave* or *dipolar spin waves* when magnetic dipolar interactions overcome electric and exchange interactions [7]. To date, the most significant application of magnons have been the use of magnetostatic waves for microwave signal processing due to the capability to excite and detect these spin waves in inductive antennas [132, 133]. Exchange spin waves are of increasing interest due to their suitability to nanometer sized structures and devices due to their shorter wavelength [129].

In the following, the different types of spin waves phenomena are introduced. In particular, Perpendicular Stationary Spin Waves (PSSWs), an exchange dominated spin wave which arises due to the thickness constraints of a thin film, are described in great detail due to their importance to the work reported in this thesis.

3.3.1 Magnetostatic Spin Waves

Magnetostatic Spin Waves (MSWs) arise from dipole-dipole interactions and are by nature long wavelength excitations. For the magnetostatic approximations, Maxwell's equations are

$$\nabla \times \mathbf{H} = 0 \tag{3.40}$$

$$\nabla \cdot \mathbf{B} = 0. \tag{3.41}$$

From consideration of the definition of the magnetic induction

$$\mathbf{B} = \mu_0(1 + \bar{\bar{\chi}})\mathbf{H} \tag{3.42}$$

it follows that we can derive the propagating wave equation for the spatial part of the magnetostatic scalar potential ψ

$$(1+\chi)\left[\frac{\partial^2\psi}{\partial x^2} + \frac{\partial^2\psi}{\partial y^2}\right] + \frac{\partial^2\psi}{\partial z^2} = 0 \tag{3.43}$$

where the excitation field is given by $\mathbf{h} = \nabla\psi$. This equation describes magnetostatic modes in homogeneous media and is known as the Walker's equation [134]. A detailed derivation is provided by Stancil [135]. In the case $\chi = -1$ the solution corresponds to the uniform precession frequency given by equation 3.31, whereas the solutions of $\chi \neq -1$ represent propagating magnetostatic spin waves.

MSWs are classified based upon on the angle between the spin wavevector **k** and the magnetisation vector **M**, resulting from the characteristic anisotropy of the dipolar interaction. Further demarcation is offered through consideration of its dispersion relation, that is the dependence of wavevector on the frequency. There are two types of MSWs which exhibit positive dispersion detailed. These are *Magnetostatic Surface Spin Waves* (or Damon-Eshbach (DE) waves named after their discoverer) where the magnetisation is IP but perpendicular to the direction of the wavevector and *Magnetostatic Forward Volume Waves* (MSFVWs) which occur when the magnetisation is aligned perpendicular to the plane and the wavevector direction. *Backward Volume Magnetostatic Waves* where the magnetisation is IP and parallel to the direction of the wavevector possess a negative dispersion. It follows that the *forward* and *backward* naming convention describes the dispersion relationship, where a positive or negative dispersion is seen respectively. A schematic of the wavevector and magnetisation vector direction for each of the different classes of MSWs is presented in Figure 3.4 [7, 129].

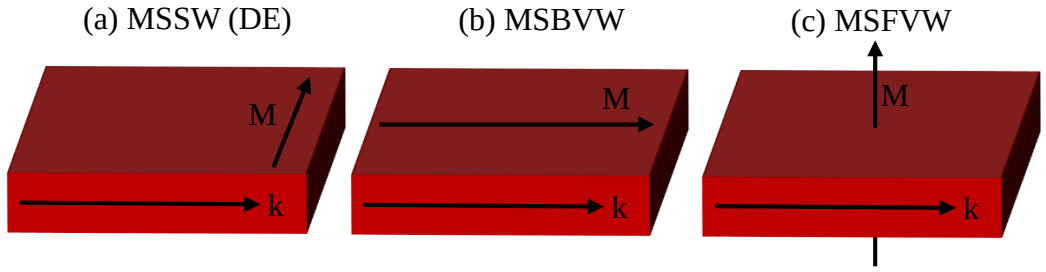

Figure 3.4: Schematics of the wavevector k and magnetisation M configuration for the different types of magnetostatic waves a) A Magnetostatic Surface Wave (MSSW) (also known as Damon-Eshbach (DE) waves) b) A Magnetostatic Backward Volume Wave (MSBVW) c) A Magnetostatic Forward Volume Wave (MSFVW).

3.3.2 Exchange Spin Waves

Exchange spin waves form when the exchange interaction dominates the contribution from the dipole-dipole interaction. This occurs when the magnon wavelength is of the order of the exchange length given by equation 2.25. As the exchange energy of the system is increased, the resonant frequencies of such waves is correspondingly enhanced. The description of the physics governing such waves can be obtained from the LGG equation [117].

In-plane Exchange Waves

In-plane exchange spin waves are described through a phenomenological theory known as the Herring-Kittel equation, which is of a similar form to the equations derived for the fundamental ($k = 0$) modes with a term to introduce the exchange energy introduced. It is given by

$$f_{\text{ex}} = \frac{\gamma}{2\pi}\sqrt{\left(H_{\text{ext}} + \left(\frac{2A_{\text{ex}}}{M_S}k_{\parallel}^2\right)\right)\left(H_{\text{ext}} + 4\pi M_{\text{Eff}}\sin^2\theta + \left(\frac{2A_{\text{ex}}}{M_S}k_{\parallel}^2\right)\right)} \tag{3.44}$$

where $k_{\parallel}$ is the IP wavevector and θ is its angle from the magnetisation vector [136]. To build on the success of this model, Arias developed a more general dispersion relationship accounting for arbitrary fields and pinning due to surface anisotropy [137].

Perpendicular Standing Spin Waves

Perpendicular Stationary Spin Waves (PSSWs) are higher order spin excitations which propagate in the direction of film thickness due to the nanometer scale confinement in this direction. They are widely studied due to the high wavevectors, hence high frequencies, they can possess. Figure 3.5 shows a schematic representation of PSSW modes. The efficiency of excitation of such modes is governed by the uniformity of the material properties throughout the volume of the material and the driving magnetic field. In the latter case, a non-uniform driving magnetic field can arise in the experimental realisation of the FMR technique in cases where the sample dimensions exceed that of the waveguide [50]. For further discussion of the FMR experiment, the reader is referred to section 4.3.

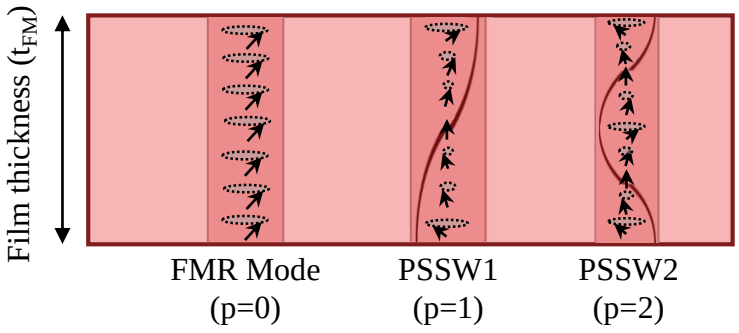

Figure 3.5: Schematic of the spin configuration of PSSWs of different mode number p, reproduced from [50]. The arrows represent the precessing spins with these profiles assume that the surface spins are unpinned.

The wave numbers of these resonant modes are given by

$$k_N = \frac{p\pi}{t_{\mathrm{FM}}} \tag{3.45}$$

where p is an integer denoting spin wave mode number and t_{FM} is the thickness of the thin film. In the case of an IP magnetised film, the frequency of the PSSWs is given by

$$f_{\mathrm{PSSW}} = \frac{\gamma}{2\pi}\sqrt{\left(H_{\mathrm{ext}} + \frac{2A_{\mathrm{ex}}}{M_s}\left(\frac{\pi p}{t_{\mathrm{FM}}}\right)^2\right)\left(H_{\mathrm{ext}} + 4\pi M_{\mathrm{Eff}} + \frac{2A_{\mathrm{ex}}}{M_s}\left(\frac{\pi p}{t_{\mathrm{FM}}}\right)^2\right)} \tag{3.46}$$

with the OOP magnetised film case having a similar form

$$f_{\mathrm{PSSW}} = \frac{\gamma}{2\pi}\left(H_{\mathrm{ext}} - 4\pi M_{\mathrm{Eff}} + \frac{2A_{\mathrm{ex}}}{M_s}\left(\frac{\pi p}{t_{\mathrm{FM}}}\right)^2\right) \tag{3.47}$$

where A_{ex} is the exchange constant as outlined in equation 2.21 in section 2.4.1 [7, 50].

Further scientific interest in PSSWs arises due to the potential to exploit this phenomena for the study of important magnetic parameters such as A_{ex} due to the highly exchange dominated nature of these waves [50, 123]. These PSSW modes have been observed in single magnetic layers and multilayers such as FM/NM/FM trilayers. Currently, there has been no practical application of these waves due to decreasing susceptibilities with increasing mode number.

There are two theories underlying the physics of PSSWs. Kittel theorised that there are rigidly pinned spins at the surface due to the effects of surface anisotropy [138]. It should be noted that the surface pinning this anisotropy generates can have a great

impact on the overall form of these resonances. Specifically, this anisotropy acts to prevent the spins at the surface precessing as freely as those in the bulk, with only small amplitude precession sufficient to ensure the minimisation of the exchange energy allowed. A consideration of the resulting form of these resonances is crucial for the experimental detection of these waves. For example, perfectly symmetric PSSWs defined as possessing an even mode number are unobservable when excited by a spatially uniform magnetic field. Therefore, this model predicts only the detection of PSSWs with an odd mode number. This is due to the non-vanishing interaction with a uniform RF field these mode possess due to the instantaneous transverse magnetic moment having a non-zero value when summed over the line. [7, 50, 128, 138]. A contrasting approach was proposed by Wigen et al. [139] and Portis [140] which introduced the concept of dynamic pinning to describe PSSW resonances. This pinning arises from small differences in the magnetisation of the film near the surface, which leads to slightly different resonant conditions than seen in the bulk of the film and thus an effective pinning in dynamic response. In this model, even mode number spins can be excited due to the asymmetry in pinning at the surface and substrate. Similar to the Kittel description, if the spins experience complete pinning or this asymmetry in pinning is not present then even modes cannot be excited. Further discussions of the physics underpinning PSSWs is available in Chapter 7, where a study of the PSSW modes exhibited by a series of NiFe thin films with varying thickness and capping layer is reported.

3.4 Damping

Damping of the precession of the magnetisation occurs through the transfer of the energy of the magnetic excitations into the microscopic thermal motion of the lattice, a process which is still not fully understood [141]. As aforementioned, the most common measure of damping is the Gilbert damping parameter introduced in equation 3.10 to model the eventual end of precessional motion. Studies of this parameter are motivated due to the crucial need to further understand the relaxation of magnetisation, a complicated process that can be impacted by spin interactions and sample quality [107].

Historically, damping has been of particular interest in the recording industry due to its impact upon device performance [35, 142]. These concerns are all the more pressing given device applications extending into the microwave frequency range [143], where

a rigorous understanding of the damping is crucial for future device development [107, 144, 145]. In the case of magnetisation switching, for example, the energy losses control the speed at which this can occur in a FM material. In the extreme cases where we consider a lossless system with zero damping, the magnetisation will precess and never achieve an equilibrium position parallel to the field; in the case of extremely large damping, the magnetisation relaxes to the field direction very slowly leading to long switching times. An intermediate level of losses, referred to as the critical damping, leads to the fastest switching [35, 146]. Beyond this application, damping also has ramifications for the critical current necessary to generate self-sustained oscillations [147] along with being a key metric for the suitability of materials for high frequency [29, 148] and nanomagnonic operations [131]. In particular, it is important for the realisation of emerging spintronic technologies such as STT-MRAM [149, 150] and Spin Torque Nano-Oscillators (STNOs) [151, 152].

Although damping is introduced as a single parameter, it is comprised of many different contributions. The variety of physical mechanisms that dissipate precessional energy are commonly divided into *intrinsic* and *extrinsic* processes. The *intrinsic* cases include mechanisms arising from fundamental physics of a material system such as the direct couplings of the magnons to the lattice via spin-orbit interaction and the eddy currents generated by free electrons in metallic layers. These excitations are termed Gilbert type, and exhibit a frequency dependence. *Extrinsic* contributions, non-Gilbert type [107, 141] channels that are invariant to the frequency, relate to secondary effects resulting from sample quality such as imperfections and inhomogeneities in the material system that give rise to magnon scattering [142, 153–155]. The identification and control of the sources of extrinsic damping is extremely relevant technologically, with this being one way to control damping through sample preparation [145].

Further physical properties of thin films that can affect the damping include parameters such as the thickness of the FM film, where it has been demonstrated that damping increases in very thin films due to the comparatively larger presence of defects and disorder [107]. Alloying also provides a way to alter the composition and can be used to control the damping of an FM film. In particular, it has recently been demonstrated that alloying can provide an ultralow damping of $\alpha \approx 10^{-4}$ in CoFe metallic films, postulated to be due to this resulting in changes to the density of states [148].

As aforementioned, the damping is intricately related to the linewidth of the resonance, as presented in equation 3.36. The intrinsic contribution is represented by

α whilst the extrinsic contributions necessitate the introduction of an inhomogeneous line broadening term (Δf_0) in such a way that the overall linewidth is represented by

$$\Delta f = \Delta f_0 + [\gamma\alpha(2(H_{\text{ext}} + H_{\text{k}}) + 4\pi M_{\text{Eff}}] \tag{3.48}$$

for the IP magnetised case, for example. No matter the dissipation channel, the final result is invariably the generation of microscopic thermal motion and the dissipation of energy into the lattice of the material. The mechanism may be described as either *direct* or *indirect* depending on the pathway to the final state with *fast* or *slow* descriptions applied respectively. In direct dissipation, there is a flow of energy from the uniform mode into the lattice vibrations. Indirect mechanisms utilise spin wave modes beyond that considered for a simple macrospin, necessitating the excitation of higher-order spin wave states as described in section 3.3. These processes involves the transition of energy from the uniform mode into spin waves and eventually into the lattice. In Figure 3.6, the dissipation channels are presented.

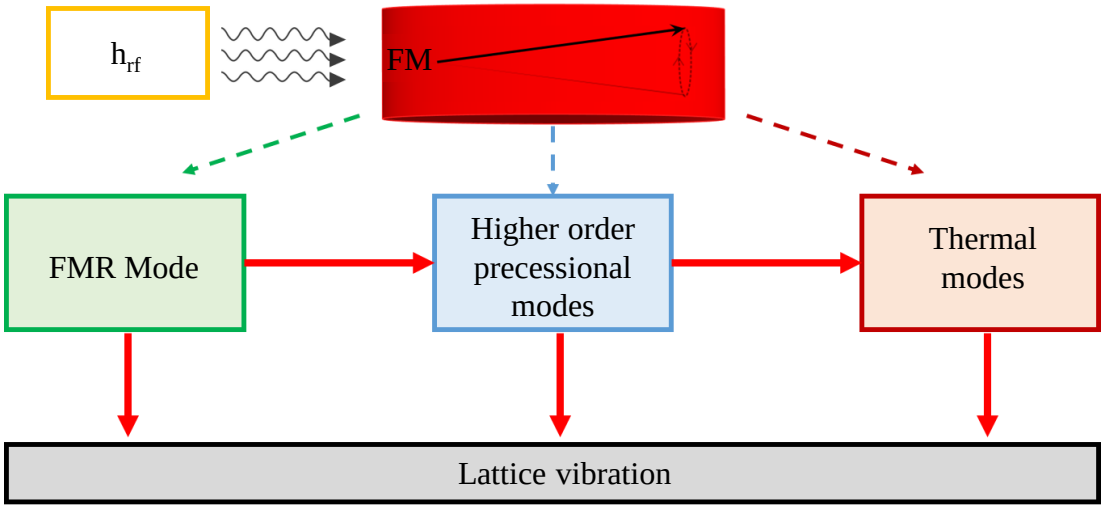

Figure 3.6: A diagram presenting the dissipative channels available for the energy of precessing magnetisation. The magnetisation dynamics is generated by an external perturbating magnetic field h_{rf} with the end-state in all cases being a transfer of energy into vibration of the lattice.

The different physical contributions to the damping process are elucidated in the following sections.

3.4.1 Eddy Currents

The generation of eddy currents, induced by the magnetisation precession, can screen the perturbating magnetic field. This contribution is designated as an intrinsic type of damping [145]. The effects of eddy currents are characterised by the skin depth defined as the depth below the surface of a conductor at which current density decays to $1/e$ of its value at surface. The skin depth, δ_{sd}, is given by [1]

$$\delta_{sd} = \sqrt{\frac{\rho}{\pi \mu_r \mu_0 f}} \tag{3.49}$$

where ρ is resistivity, μ_r is relative permeability, μ_0 is permeability of free space and f is frequency.

The contribution of eddy currents is important in cases where the film thickness is comparable to or greater than the skin depth. For transition metals the classical skin depth at 10 GHz is in the range of 1 μm [156]. However, as previously discussed in section 3.2, at the ferromagnetic resonance frequency the permeability increases thus reducing skin depth due to this increased permeability and susceptibility. For samples with thickness lower than the skin depth, the contribution to damping can be written as follows

$$\alpha_{eddy} = \frac{1}{6} M_S \gamma \left(\frac{4\pi}{c}\right)^2 \sigma t_{FM}^2. \tag{3.50}$$

where σ is the conductivity [145].

Due the dependence of this contribution on the square of the thickness, the effects of eddy currents is only significant in the case of thick films. It is notable that in this case, even in the absence of other damping contributions, eddy currents can generate a finite resonant linewidth through the exchange conductivity mechanism as described by Ament and Rado [157]. This is named such in reference to the impact of exchange interaction, where the damping contribution from this parameter is proportional to $\sqrt{D\sigma}$.

3.4.2 Two-magnon Scattering

Two-magnon scattering has been known for decades as a source of extrinsic, non-Gilbert type damping in FM insulators [155] and metals [158]. Two-magnon scattering involves the annihilation of a uniformly precessing magnon ($k = 0$) excited by

FMR and subsequent scattering into a higher order $k \neq 0$ magnon [145, 155, 159]. As this is a spin-spin process, the total number of magnons is unchanged. However, as a consequence of the higher order spin wave excitation $k \neq 0$, the length of the magnetisation is not conserved. This is due to dephasing of the spins in the magnon resulting in a reduced length of magnetisation. As such, the Bloch-Bloembergen (BB) model [160] is better suited to describe such behavior as it accounts for a changing length of magnetisation and is therefore more applicable to this damping than the LLG equation (equation 3.10).

This process requires that the spin wave dispersion permits degenerate states along with the presence of scattering centres, with the linewidth generated by this mechanism acting as a measure of the scattering rate present [141]. Indeed, the geometric separation of scattering sites is connected to the form of the final magnon states. For instance, long wavelength spin waves mean that the scattering sites are separated by several hundred of nanometers rather than on an atomic length scale. Importantly, Arias and Mills introduced this concept to the thin film case in 1999. They reported that lateral variations in the perpendicular uniaxial interface anisotropy field, resulting from the interfacial roughness, are the main source of the two magnon scattering in ultrathin films [153].

3.4.3 Spin Pumping

The phenomena of spin pumping was originally proposed by Berger [161]. It is seen in multilayers where the precessing uniform mode macrospin may dissipate angular momentum in the form of a *spin current* from the FM layer across an interface into adjacent layers, typically NM heavy metals. The spin-orbit interaction then causes relaxation of this non-equilibirum spin population in the NM layer. This process is considered intrinsic despite the role played by the presence of additional layers [107].

The net Direct Current (DC) spin current into the NM layer from the FM layer from this uniform precession generates a torque [162]

$$\Gamma_{\text{pump}} = \frac{h}{4\pi} g_{\text{eff}}^{\uparrow\downarrow} \left(\mathbf{m} \times \frac{d\mathbf{m}}{dt} \right). \tag{3.51}$$

The quantity $g_{\text{eff}}^{\uparrow\downarrow}$ is the *effective interfacial spin mixing conductance* [163]. It represents the ability of a spin current to traverse the interface into the adjacent NM layer, its ability to relax within NM layer, and the diffusion driven back-flow of unrelaxed spin-current in to the FM layer [164–168]. The damping of this contribution is given

by [169]

$$\alpha_s = g_{\text{eff}}^{\uparrow\downarrow} \frac{\gamma h}{A M_s t_{\text{FM}}} \tag{3.52}$$

where all symbols have been defined previously. The reader should note that in this relation the effect of back-flow into the FM layer is neglected. Spin pumping can play a key role in the damping of multilayers, as elucidated in the following section.

3.5 Dynamics of Multilayers

The phenomena of interlayer exchange coupling, introduced in section 2.7.1, can have a profound effect on the resonant dynamics of FM/NM/FM multilayers compared to that displayed by its constituent FM layers. It results in the coupling of the precessional motions of the two FM layers which generates an Optic Mode (OM) in addition to the conventional Acoustic (Kittel) Mode (AM). The AM and OM labelling refers to the magnetisation of each FM layer resonating either in-phase or out-of-phase in each case respectively. This labelling is analogous to the treatment of phonons [38, 40].

The modelling of the resonances of such structures is significantly more difficult than that of the single layer case where the analytical Kittel's equation (equation 3.30) can be applied. The resonant frequencies and intensities of the modes depend in a complicated fashion on the coupled Landau-Lifshitz equation of motion. Generally, the OM is only observable in FMR spectroscopy measurements under the condition that the individual layers have different resonance fields or magnetisations. It is found that the OM reduces in intensity compared to the AM as the magnetic properties of FM layers become more similar [40]. As detailed in section 4.4, numerical modelling using micromagnetics software offers one way to model the resonant dynamics of such systems.

The resonant dynamics differ based on whether the interlayer exchange coupling strength (J_{IEC}) promotes a FM coupling ($J_{\text{IEC}}>0$) or an AF coupling ($J_{\text{IEC}}<0$) as shown in Figure 3.7. These cases, as elucidated in section 2.7.1, are known as a Synthetic Ferromagnet (SFM) or Synthetic Antiferromagnet (SAF) respectively. Dynamically, a SFM supports both a lower frequency AM and a higher frequency OM at a range of applied fields. Similarly, in the case of a SAF, both an AM and OM are displayed though significant changes in the dynamical response can occur in these systems as the applied field is varied. Specifically, the strength of the external field can alter which mode displays the highest frequency and signal. In cases where the external field

strength is insufficient to overcome the interlayer exchange coupling and the magnetisation vectors possess an antiparallel alignment, the OM is higher frequency and higher signal than the AM; in situations where the external field is sufficient to align the magnetisation parallel the AM is greater in both frequency and signal than the OM [40]. Furthermore, even in regions where the static profile is invariant to alterations in the external field there can be significant changes to resonant linewidth [170]. We refer the reader to an excellent review by Heinrich [158] and reports by Wigen [171] and Rezende [172] concerning analytical models of the resonant modes of the SAF case. In chapter 5 and 6, the studies performed during this project concerning the dynamics of SAFs and SFMs respectively are available.

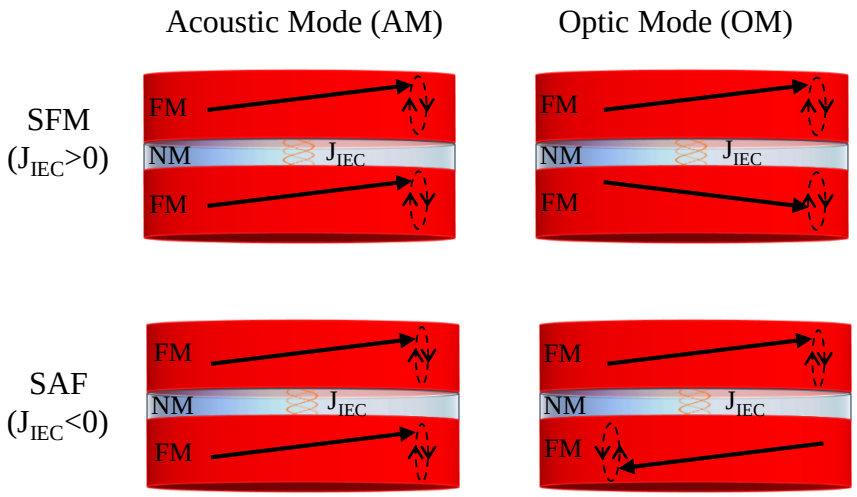

Figure 3.7: Resonant dynamics of a SFM and SAF. The J_{IEC} promotes either a FM or AF coupling between the FM layers through the NM spacer layer in each case respectively. In the case of the OM of a SAF, it is assumed that the applied field is lower than that required to align the magnetisation of the layers in parallel.

The origin of damping in multilayers is of a more complicated nature than that seen in single layer films, arising due to interface effects and spin transfer torques. It is not well described by the LLG equation (equation 3.10). A key contribution to the damping present in such structures is mutual spin pumping, a phenomena discussed in section 3.4.3, where a non-equilibrium interlayer spin current generates a sizable modification to the resonant behaviour of the system. This is due to the FM layers acting as both a source and receiver of spin waves [173]. Indeed even in the case of decoupled layers, thus no alterations to the displayed resonant frequencies, Heinrich

found that there remained significant linewidth broadening compared to that seen in the single layer case [159]. In the case of the presence of an interlayer exchange coupling, the impact of the spin pumping depends on whether the precession occurs in-phase or out-of-phase. For example, it has been demonstrated by Heinrich that there is a significant reduction in the resonant linewidth when the two FM layers precess in phase. This arises from the mutual spin pumping effect, where outflow of angular momentum is compensated from inflow from the other FM layer. In the case of out-of-phase precession, such as the OM of a SAF, the linewidth of the optic mode has been shown to be five times greater than the AM [174]. The effects of dipolar coupling and the damping this generates has, to the knowledge of the author, not been reported in the literature.

3.6 Chapter Summary

This chapter has introduced the physics of magnetisation dynamics. A plethora of spin wave excitations, ranging from the fundamental resonant mode to higher order, have been reported along with the damping that eventually returns the magnetisation to equilibrium. Importantly, a derivation of the high frequency response of the magnetic susceptibility in a special case is available which is extremely relevant for the results reported in later chapters. The dynamics of magnetic multilayers and the ramifications of this interlayer exchange coupling has also been discussed. In the following chapter, the experimental methods and techniques used to carry out the project are detailed.

Chapter 4

Experimental Methods and Techniques

This chapter encompasses the various experimental techniques required to fabricate and characterise the thin films studied throughout this project. These techniques include magnetron sputtering, X-ray Reflectivity (XRR), Atomic Force Microscopy (AFM), vector Vibrating Sample Magnetometry (VSM) and Vector Network Analyser-Ferromagnetic Resonance (VNA-FMR) spectroscopy. Due to the central focus of the project being upon high frequency magnetisation dynamics, an emphasis has been placed on the workings of the VNA-FMR method in particular. Numerical modelling has also been performed using the micromagnetics simulation software Mumax^3 to further investigate and understand the dynamic response of the studied samples.

4.1 Magnetron Sputtering

Sputtering is part of a class of fabrication techniques known as Physical Vapor Deposition (PVD), a methodology based upon the ejection of atoms from a source material (target) followed by condensation onto a substrate. Due to it yielding samples possessing a high purity and its easy scale-up to manufacturing, sputtering is generally considered the PVD technique of choice in the fabrication of thin films and has been the workhorse of industry since the 1970s [1, 24, 175–177]. In sputtering, the atoms are ejected from the target due to non-thermal transport based on momentum exchange between energetic ions and surface atoms. It follows that sputtering can occur irrespective of the physical properties of materials, such as melting point, meaning that a large range of materials including insulators, metals and semiconductors are able to be deposited by this process [175]. Sputtering offers many advantages compared to other PVD methods which promotes its use both in laboratory and industry settings. The key advantages of this technique includes the aforementioned versatility of material choice along with it permitting large coating area with high degree of uniformity and

strong adhesion [176, 177]. The films also possess nearly bulk-like properties which are predictable and stable. Importantly, sputtering also offers high deposition rates in the range 1 nm/s to 10 nm/s [175]. The samples fabricated from this technique also largely reflect the chemical composition of the targets which is a crucial consideration for film stoichiometry [178].

In this project, *magnetron sputtering* was utilised. A schematic of the magnetron sputtering setup is shown in Figure 4.1. This process entails the introduction of argon

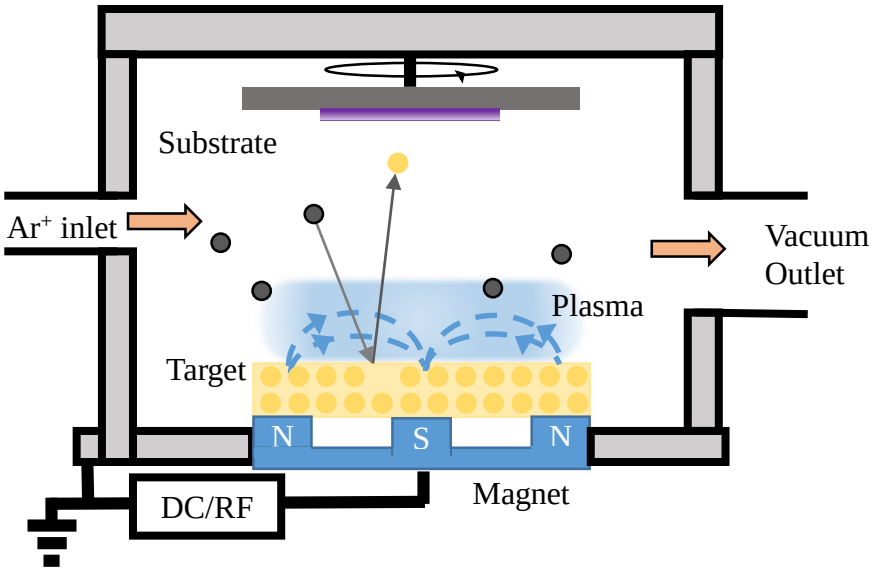

Figure 4.1: A schematic of the magnetron sputtering process.

gas into the chamber, with the Ar^+ accelerated towards the target material. Ar is typically used due to its nonreactive nature [1]. The incident ions are subjected to a complicated scattering process at the target, where collisions with the target atoms occur and transmit a fraction of the ion's momentum. This forms a cascade process which provides target atoms close to the surface with sufficient momentum for outward motion resulting in sputtering from the target and subsequent condensation onto the substrate. The sputter yield is defined as the ratio between the number of sputter-ejected atoms and the number of incident projectiles (ions) [23]. In production systems, to achieve uniformity over the wafer sized areas, large targets are used or planetary motion occurs throughout the deposition process [179]. Furthermore, cooling of the equipment involved is required as a large part of energy involved in this process is converted to heat. This is because the secondary electron yields, the ratio of electrons emitted compared to the primary incident electrons, of many typical sputtered materials are low

(usually 25 % for most materials) [177].

The *magnetron* is an arrangement of permanent magnets placed behind the target material which provides a magnetic field above the target surface [180]. This additional closed magnetic field parallel to the target surface acts to increase the plasma density as it causes the electrons to traverse a helical trajectory and thus increases the probability of collisions with argon atoms. This also has the effect of confining the secondary electrons to a specific area of the target surface, enhancing the ionisation efficiency and permitting a higher sputtering rate to be realised [24, 177, 180]. Furthermore, the sputtering process can be maintained at lower working pressures allowing the sputtered atoms to easily traverse the distance to the substrate with minimal collisions and scattering in the plasma [180]. The helical drift path forms a circle where preferential sputtering occurs, known as the racetrack, on the surface of the target material [177].

There are several techniques that can be used to perform the magnetron sputter deposition of materials. The simplest and most common is where a DC power source is utilised to power the magnetron. In this case, the sputtering occurs as described above. The magnetron can also be pulsed to reduce the accumulation of charge in the case of dielectric materials [175]. A variation of this technique is Radio Frequency (RF) sputtering, where an RF source is coupled to the target material. This can provide additional capabilities in the sputtering of thin films, notably permitting insulating materials such as oxides to be sputtered. This technique is also beneficial in the deposition of ultrathin films where lower sputtering rates may be required [177]. Due to the use of RF sputtering, in addition to DC sputtering, in this project a more detailed overview of this technique follows.

Throughout the RF sputtering process the electrons will oscillate between the target and substrate (acting as the two electrodes) with a frequency equal to that of the applied power. Typically, the RF power source operates at a frequency of 13.56 MHz [177]. The ion mobility, however, is too low at the applied frequency to experience similar high degrees of oscillation leading to inertial confinement. This results in the bulk of the ions essentially remaining at the centre of the plasma between the electrodes [181]. Therefore, throughout the positive half of the power cycle the target acts as an anode and will acquire many electrons but the counter electrode will not gain many ions and vice versa during the negative half of the cycle. Thus, both electrodes charge negatively. Due to its negative bias the target will eventually no longer capture as many electrons during the positive part of the cycle and will obtain enough ions during the negative half of the cycle to negate any of the electron gains [182]. At this

point, the target has a net DC bias, attracting the process gas ions and generating the sputtering of the target material [183]. The effect of this is that, for a part of the cycle, Ar^+ ions bombard the target whilst for the rest of the cycle electrons act to neutralise the collection of positive charges. For a successful sputtering process, an asymmetric arrangement must be utilised with the target and substrate being of different sizes or else a cathode/anode arrangement used where the chamber itself acts along with the substrate as the anode through electrically connecting the substrate to the chamber walls. In cases where the ratio between the substrate area and target area is high, the sputtering of the anode and chamber walls will be negligible [23].

Due to the applied power being split between the two electrodes, the effective power experienced at the anode is normally only 50 % of that delivered in DC sputtering [177]. Furthermore, as the magnetic field supplied by the magnetron opens up and closes throughout the RF cycle, electrons can escape this confinement. This forces electrons to cross magnetic field lines and hence reduces the power of the discharge which ultimately decreases the power available at the target when the trap is closed. Altogether, this leads to considerably lower deposition rates from RF sputtering processes than in the equivalent DC process [23, 177]. Due to the high frequency nature of the applied RF power, when setting up these circuits it is important to utilise appropriate matching networks to ensure reflected power remains low. This requires expensive power sources and circuitry which can make the scale-up of RF processes difficult and expensive [176].

The micro-structure of the thin film formed on the substrate is highly dependent on the growth conditions used throughout its deposition. In many cases, it is imperative to have precise control of the film structure to attain properties of practical importance such as intrinsic stress, surface roughness and electrical resistivity [23, 176]. In particular, the adatom mobility at the surface and near-surface environment is the dominant contribution to the resulting film structure, and mainly depends on the substrate temperature and particle bombardment. It is of importance as the sputtered atoms possess substantial kinetic energies, an order of magnitude or larger compared to bond energies, sufficient to greatly influence the formation of the thin film. Therefore, the control of energy loss mechanisms during transport in the gas phase, between the target and the substrate, is crucial. For example if the pressure in the chamber were low enough that target atoms arrived without having undergone a scattering event it may cause re-sputter of material from the forming film. Moreover, in the case where the atoms have too little energy when incident on the substrate, hence a low mobility, the formation

of a rough surface will occur [176]. Relevant growth parameters to control the fluxes and the energy per particle arriving at the substrate include the sputtering power, working pressures and temperature (where heat can be applied throughout the deposition or applied post deposition as an annealing step) [23]. Of particular concern in the science of thin film growth is the presence of defects, which can significantly impact the functional properties of the fabricated samples. The label *defects* encompass a range of features such as dislocations and grain boundaries along with growth related issues more specific to thin film fabrication such as roughness of interfaces and mixing of layers. Due to the ultrathin film growth required in this project, the primary concern was the roughness of the films for reasons outlined in sections 2.7.1 and 2.7.2.

In this project, the deposition system used for DC and RF magnetron sputtering was an 11 target AJA International ATC 2200-V DC magnetron sputtering system [184]. The microstructure of the films grown in this project were tailored by controlling deposition power, working pressure and substrate temperature. A base pressure of order 1×10^{-8} Torr was achieved in the deposition chamber when fabricating films. Due to the plasma confinement provided by the magnetron, low Ar pressures of 3 mTorr were used along with low target powers of 100 W or lower. A getter process was frequently used inside the chamber to reduce the base pressure. This involved sputtering metals such as Ti, which reduces out gassing and hydrogen leakage by absorption and chemical bonding [185]. The thicknesses of the deposited layers were controlled through deposition times, with a deposition rate (time and corresponding layer thickness) calibrated through X-ray Reflectivity (XRR) as introduced in section 4.2.1.

4.2 Characterisation Techniques

4.2.1 X-ray Reflectivity

X-ray Reflectivity (XRR) is a surface-sensitive characterisation technique notable for its versatility in the study of films with thickness in the nanometer regime [186–189]. A non-contact and non-destructive method, it is used to measure critical properties such as layer thicknesses, interfacial roughness and material densities. As the dimensions of thin films are reduced, these properties can differ significantly from the bulk case. Thus, the detailed characterisation of thin films is crucial to tailoring the functional properties of such materials [187, 189]. Key advantages of this technique include that it can provide information on structural features without special sample synthesis

[188] and that it possesses a high spatial sensitivity permitting the layer roughness to be resolved on a scale of 0.1 nm [187].

XRR harnesses the penetrative properties of X-rays that derive from their electromagnetic nature. Specifically, the orbiting electrons present in the thin films interact only weakly with incident electromagnetic field compared to the interaction with a particle of a fixed charge, such as an electron. Therefore, the X-rays are able to penetrate much further into a material than a charged particle, with penetration depths of a few millimeters seen in aluminium [190]. This large penetration depth is crucial for a thorough examination of film structure to take place.

In essence, the XRR technique analyses the intensity of X-rays which are incident upon and specularly reflected from a flat surface at a range of different incident angles, permitting the effects of charge scattering to be studied [104, 187]. Due to the specular nature of this scattering, the angle of incidence (θ_i) is equal to the angle of reflection (θ_f) and in the following will be referred to as θ. Therefore, in measurement, the total scattering angle is equal to as 2θ [187]. A schematic of this measurement geometry is shown in Figure 4.2.

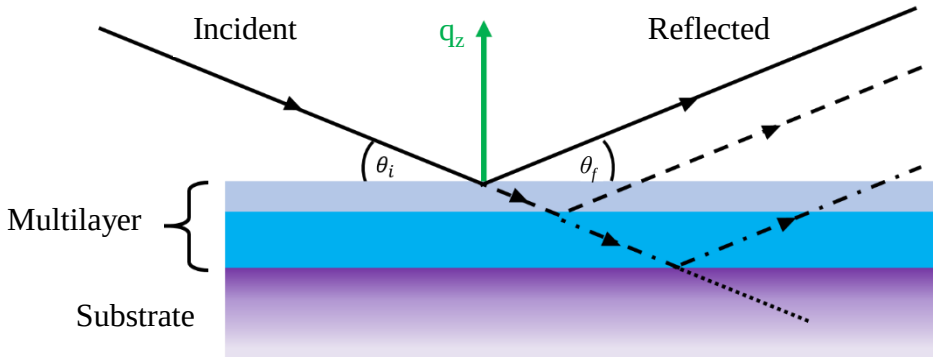

Figure 4.2: Schematic of the geometry of specular XRR measurement, adapted from [186]. The angle of incidence θ_i is equal to the angle of reflection θ_f thus only the momentum normal to the plane q_z changes.

As this technique considers specular reflections, it is only sensitive to the change in momentum in the direction normal to the film surface (q_z). This means that only the electron density profiles in the direction parallel to the thickness of the sample are probed [104, 191]. The scattering wavevector is $\mathbf{q} = \mathbf{k_f} - \mathbf{k_i}$, where $\mathbf{k_f}$ and $\mathbf{k_i}$ are the wavevectors of the outgoing and incoming wave respectively. The variation of $\mathbf{q}$ with differing θ is given by

$$\mathbf{q} = q_z = 4\pi \sin\left(\frac{\theta}{\lambda}\right) \tag{4.1}$$

where λ is the X-ray wavelength, typically of order 10^{-10} m [192]. It follows that no information in the lateral direction is obtained. In measurement, the typical angular range is 0.05 °-8 ° and samples of thickness of order 100 nm can be measured [192].

The crucial information provided by XRR is contained in the reflectively curve, with an example presented in Figure 4.3. On the length scale of X-rays, most fabricated films do not have perfect interfaces due to rough surfaces, diffuse interfaces, and grain boundaries in polycrystalline materials. This leads to deviations in the reflectivity curve from the case of ideal specular behaviour, detailed in equation 4.1. Thus, from analysis of the differences to the ideal specular reflection behaviour information concerning the structure of the thin films can be obtained [187].

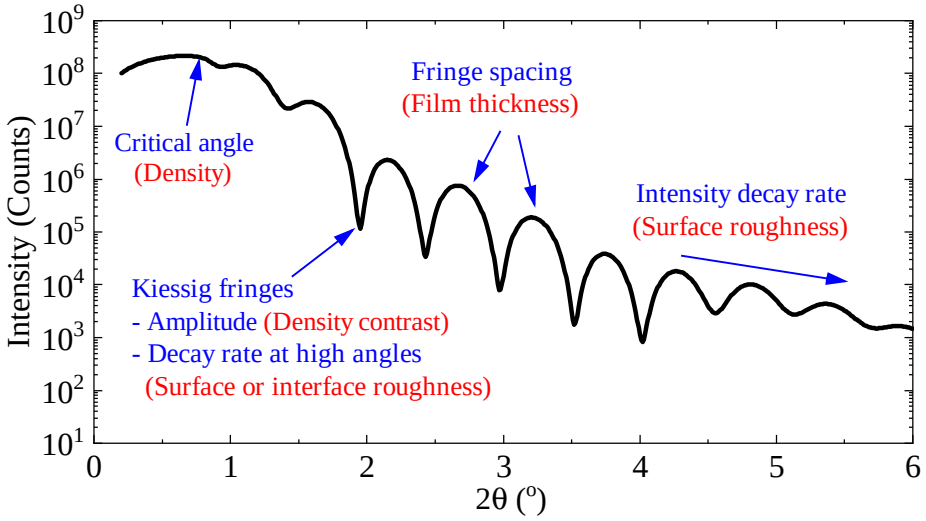

Figure 4.3: An example reflectivity curve presenting the variation of intensity with changes in angle 2θ. The important features of the curve (blue) and the physical attribute of the sample it relates to (red) are labelled [192].

A discussion of the key features of the reflectivity profile, as shown in Figure 4.3, follows. It is seen that intensity begins to reduce only after a critical angle (≈ 0.8 °), with total external reflection occurring at angles of incidence lower than this. This critical edge is sensitive to the densities of the uppermost layers of the film. The air-surface interface is responsible for the majority of the scattering due to the relatively large change in density between vacuum (or air) and solid matter. Therefore, the overall reduction in reflectively with increasing angle is dominated by top surface

roughness. If the bulk substrate is uniformly coated with a thin film of a different material, due to the variations in the electron density profile in the direction normal to the film plane, the X-rays reflected from the film surface will interfere with those from the film-substrate interface as shown in Figure 4.2. The presence of such buried interfaces leads to the formation of interference fringes, known as Kiessig fringes [186]. The spacing between the maxima of these fringes relates to film thickness, with smaller spacing observed as film thickness increases. The amplitude of the oscillation of these fringes is related to the density contrast of the layers, with higher density contrast leading to more pronounced oscillations. Furthermore, the relative phase of oscillations is dependent on the sign of the density change at the buried interfaces. The impact of buried interface roughness appears in a more subtle manner, usually through damping of the Kiessig fringes at high angles where a reduction in amplitude corresponds to a more damped case. The degree of damping of these fringes at high angles can also be related to the surface roughness of the film. In experimental data a beam footprint is present in the spectra at angles below $\approx 0.05\,^{\circ}$, considered a grazing angle. This is attributed to geometric effects and difficulties with the alignment of the sample with the beam. The misalignment of the beam and difficulties to contain it on the sample is one of the most significant challenges of XRR [187, 191].

Measurements were performed in a Rigaku SmartLab X-Ray diffraction system equipped with a 3 kW X-ray generator tube and operates at 40 kV and 45 mA producing CuK_{α} radiation at wavelength 0.154 nm [193]. A diagrammatic representation of source and detection optics in a general XRD system shown in Figure 4.4. Throughout the measurement, the source and detector are scanned together such that their angular positions are equivalent about the sample normal. XRR measurements require a well-collimated incident X-ray beam for high resolution measurements, necessitating the use of a series of X-ray optical equipment. This is a particular concern due to the wide range of intensities measured in XRR [192]. To control and manipulate the X-ray beam, adjustable slits are utilised to enable and optimise the measurement. A height limiting slit, in conjunction with an incident slit, determines the area which is illuminated by the X-rays. Furthermore, a vertical Soller slit (a multilayer mirror) is used to produce high intensity and parallel incident beam [192]. To receive the reflected X-rays, an additional Soller slit along with with two receiving slits shield the detector from scattered x-rays. Prior to each measurement, alignment of the instrument optics and the sample were performed. A $2\theta/\theta$ measurement geometry performed over angle range 0^{o}-8^{o} was used to collect the reflectivity spectra.

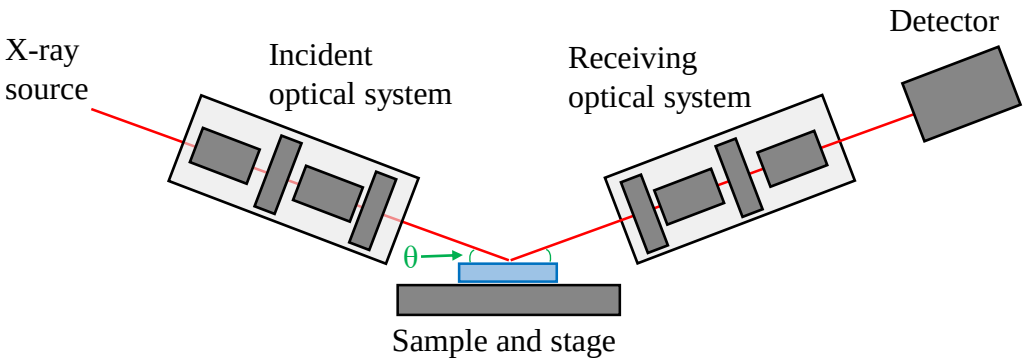

Figure 4.4: A schematic of the experimental setup of the XRR technique, after [187].

The collected data is analysed using GenX: X-ray and neutron reflectivity fitting software [189]. The program utilises the Parratt recursive algorithm [194] to simulate a specular reflectivity curve fit to the data, based upon a model of the structure defined by the user. A structural Scattering Length Density (SLD) profile, specifically the variation in the scattering length multiplied by the density as a function of distance from the substrate, is also provided. The simulated reflectivity curve determines the thin film structural parameters, including thickness, density and roughness. The roughness is assumed to have a guassian profile and is modelled according to the Nevot-Croce model [195]. Dynamic modelling is utilised in GenX software as opposed to kinematical scattering theory, which cannot model low angle specular reflectively due to a breakdown caused by effects such as refraction and multiple reflections [189]. The Storn and Price genetic algorithm, a differential evolution global optimisation program [196], performs iterations of the parameters space to optimise the fit until the Figure Of Merit (FOM) plateaus. The FOM is the function which determines how well the simulation reflects the measured data. There are multiple FOMs available to optimise different parts of the reflectivity profile. The FOM generally used in this project were *log*, which is the average of the difference between logarithms (base 10) of the data and simulation given by

$$\mathrm{FOM}_{\log} = \frac{1}{N-p} \times \Sigma_i \mid \log_{10}(Y_i) - \log_{10}(M_i) \mid \tag{4.2}$$

and the *logR2* which results in more similar weighting of high intensity and low intensity data which can aid fits spanning several orders of magnitude in intensity

$$\mathrm{FOM}_{\mathrm{logR2}} = \frac{\Sigma_i(\log_{10}(Y_i) - \log_{10}(M_i))^2}{\Sigma_i(\log_{10}(Y_i))^2}. \tag{4.3}$$

In these definitions Y represents the data, M represents the simulation and i represents each data point. The values of N and p are the number of data points and free parameters respectively [197]. The interested reader is guided to the following resources for more information regarding the functionality of GenX and its operating principles [189, 198].

A limitation of this analysis software is that it requires the input of reasonable estimates of the parameters along with appropriate bounds to the fitting algorithm. It is found that the program requires initial values close enough to the real structure for the optimisation to converge and to prevent the program optimising to a local FOM minima as opposed to the global minimum [189]. The initial user inputs can be informed from the use of other characterisation techniques such as AFM and VSM, as discussed in later sections.

4.2.2 Atomic Force Microscopy

Atomic Force Microscopy (AFM) was introduced in 1986 [199] and has since become a standard tool in nanotechnology. The operating principle of an atomic force microscope is shown in Figure 4.5a. Essentially, a probe is brought into close proximity to

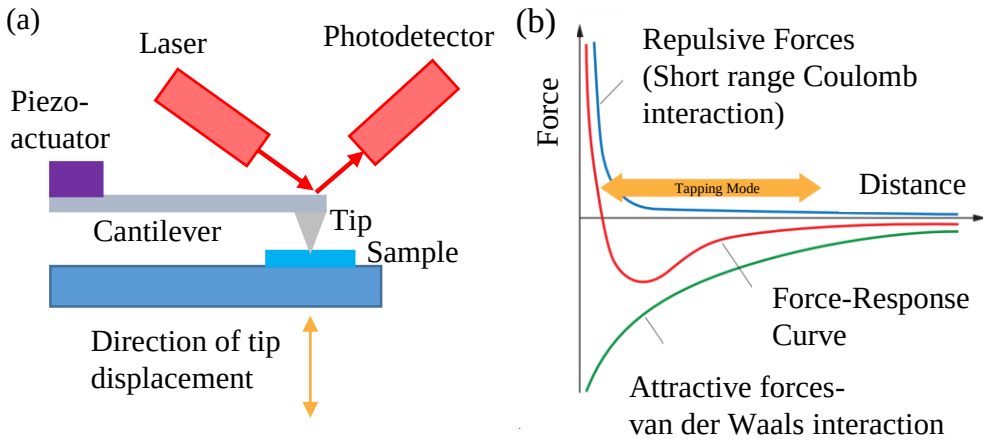

Figure 4.5: The operating principles of AFM, adapted from from [200]. a) A schematic of the experimental setup of AFM. b) A Force-Distance curve presenting the motion of the oscillating cantilever when operated in tapping mode.

a sample, with probe and sample moved relative to each other in a raster-like manner. The probe consists of a cantilever and a sharp tip. The interaction between the tip of the probe and the sample surface can be monitored by measuring the displacement of

the free end of the attached cantilever. Thus, certain quantities can be measured at discrete locations with an image (pixels) obtained. The most common method to measure cantilever deflection is a beam-bounce scheme. This uses a laser focused onto a spot at the back of the cantilever and reflected into a 4-quadrant photodetector which measures the deflection. Small movements of the cantilever are magnified at the photodetector, meaning that the system is highly sensitive to relatively small deformations. Hence, this setup has the capability to detect extremely low interaction forces. Throughout operation of this equipment, it is necessary to realign of the laser onto the back of the cantilever each time the probe is changed [200, 201].

The cantilever and tip are usually one unit which consist of silicon, with the length of the cantilever typically 100 μm and the radius of the tip less than 10 nm respectively [200]. The tip can have different coatings to enable sensitives to certain interactions, such as a magnetic coating to allow magnetic force microscopy to take place [64]. It should be noted that the images taken by the AFM are a convolution of shape of the tip and the sample surface. As such, the quality of the measurement is dependent upon the quality of the tip used. For instance, a dull tip does not map the surface morphology as well as a sharp tip giving rise to lower surface heights and shallower holes than actually present. An important consideration is that over time or through misuse the quality of a tip can degrade (becoming duller). Thus, care must be taken to monitor image quality and replace degraded probes tips to ensure high standard measurements are taken [201].

There are three main AFM modes utilised to study the sample surface; namely contact, non-contact and tapping (intermittent contact). Of these tapping mode is the dominant imaging technique as it avoids exerting large lateral forces on the sample seen in contact mode, which can potentially result in sample damage, whilst maintaining a high lateral resolution [200]. As this AFM mode was utilised in this project a more detailed overview follows. Tapping mode is where the imaging is carried out by having the probe tip in contact with the sample surface for only a short amount of time. This is realised through the cantilever oscillating at or near its resonant frequency, normal to the sample surface, using a piezoelectric element. The usual amplitudes of the oscillation are of the order 10 nm, which is small in comparison to the cantilever length. A force-distance curve is shown in Figure 4.5b, and the region that tapping mode operates in is highlighted. To elaborate, as the oscillating tip is moved into the vicinity of the sample surface there is a change to the oscillation arising from the interaction between the probe and the field from the sample. This interaction can be either

attractive, due to the van der Waals interaction, or repulsive, due to to the Coulomb interaction, depending on the distance of the tip from the surface. Overall, the effect is a damping of the cantilever motion that results in the reduction of the frequency and amplitude of the oscillation. The oscillation is monitored by a setup such as the aforementioned beam-bounce scheme, with adjustments to the distance between the tip and the sample surface via a feedback loop carried out to maintain the probe at a fixed distance from the sample [201]. The degree of probe height correction is taken to be the sample topography. It should be noted that tapping mode does not measure direct forces. Instead, as the cantilever oscillates back and forth only an average response of the the many interactions is measured through a lock-in amplifier [200], which is adequate to allow the sample topography to be studied.

In this project, a Bruker Dimension FastScan atomic force microscope with a dimension FastScan head was used. Fast scan A tips [202] were used which had a nominal resonant frequency of 1400 KHz and a nominal tip radius of 5 nm. For measurement, low scan speeds of 0.5-2 Hz were used to obtain high resolution topographical images. This was sufficient to analyse surface roughness of the thin films studied in this project, as will be discussed in section 5.1.1.

4.2.3 Vibrating Sample Magnetometry

The Vibrating Sample Magnetometer was proposed by Foner in 1959 [203], with the technique of Vibrating Sample Magnetometry (VSM) since becoming a standard measurement to examine fundamental properties of magnetic materials. It is known for its versatility, accuracy and ease of use [204]. A schematic of the measurement setup is shown in Figure 4.6 [205].

This technique involves magnetising a sample in a uniform magnetic field with the sample then sinusoidally vibrated at a fixed amplitude, usually 1-3 mm, by driving an oscillator at a known frequency usually between 50-100 Hz. A voltage is induced in the pickup coil as the sample is displaced, which is independent of the applied magnetic field but proportional to the samples magnetic moment [204]. This small induced voltage is then amplified by a lock-in amplifier which is sensitive to only signals at the vibration frequency. The lock-in amplifier must be provided with the reference signal of the vibration, which is is determined by the reference magnet and pick-up coil arrangement [35]. As the VSM technique measures the stray field from a sample it does not offer spatial resolution. The operating principle of the VSM can be understood through Faraday's Law of magnetic induction which dictates that the

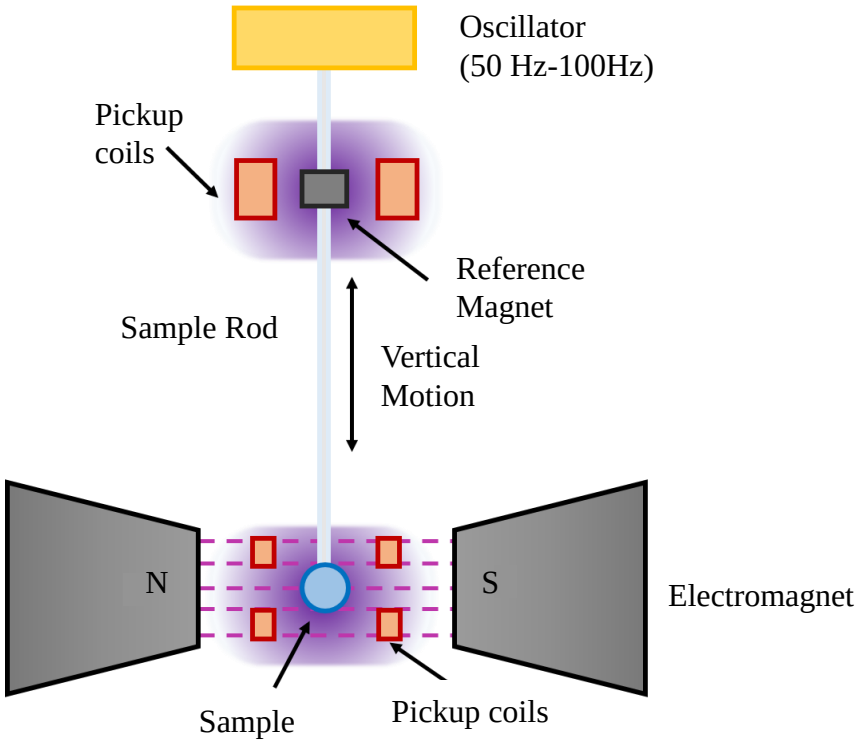

Figure 4.6: A schematic of vector vibrating sample magnetometer showing its key components [35].

resulting change in flux (ϕ) generates an electromotive force (V_{EMF}) in the pickup coils [1] [206]

$$V_{\text{EMF}} = -N\frac{d\phi}{dt} \tag{4.4}$$

where N is the number of turns of the coil. The design of the pickup coil ensures a linear response over the region of vibration and enables the signal generated from the applied DC field to be removed [35].

In this project, a MicroSense Vector Magnetometer Model 10 VSM was used. This VSM can support a magnetic field of up to 20 kOe at an arbitrary direction to the sample. In addition to being able to characterise the field dependence of a sample, it is also possible to measure the sensitivity of a sample to different temperatures. All in all, this instrument allows the magnetisation vector to be determined to an accuracy of more than 1.5% and 1.5°. Averaging allows the noise in the vector signal to be reduced below 0.5 μemu. Using this instrument, field noise as low as 5 mOe can be attained [207]. A calibration sample of similar size and shape to the sample with known saturation magnetisation must be measured to allow correct readings of the sample magnetic moment to be taken. The samples were prepared using a Southbay disc cutter [208] to

provide an 8 mm diameter disk for the measurement. A hysteresis loop as described in section 2.6.1 can be measured by sweeping the magnetic field from -20 kOe to 20 kOe allowing the saturation magnetisation, coercivity, remnant magnetisation along with the anisotropy field of the sample to be obtained [204]. The theory underpinning these parameters is detailed in section 2.6. In the data analysis stage, it is necessary to remove the diamagentic contributions from the substrate and sample rod by performing linear background subtractions. To perform this subtraction, a first order polynomial was fit to a linear region of hysteresis curve where the sample is saturated. The parameters from this linear fit could then be used to subtract the diamagnetic background from the measured hysteresis loop. For the interested reader, further information regarding the proper treatment of hysteresis data is available at [209].

4.3 Ferromagnetic Resonance Spectroscopy

The technique of Ferromagnetic Resonance (FMR) spectroscopy is one of the oldest and most established methods to characterise magnetic materials. It is an indispensable tool allowing the study of the (small) angle dynamics of magnetisation motion [3, 6, 50]. It has been used to determine fundamental magnetic properties including anisotropies, damping parameters, g-factors and exchange couplings [40]. In chapter 3, the underlying physics of FMR arising due to perturbating magnetic fields has been discussed, with the following discussion now focusing on the experimental realisation of this technique. The reader should note that the important RF aspects of this technique namely the Vector Network Analyser (VNA), S-parameters and transmission lines are discussed at the end of this section.

At this point, it is important to bring to the reader's attention that there are a range of additional techniques available for the study of magnetisation dynamics in thin films, such as Magneto-Optic Kerr Effect (MOKE) [210] and Brillouin Light Scattering (BLS) [211]. In this project, FMR spectroscopy was utilised due to the ready availability of the experimental setup and also the many advantages offered. As aforementioned, FMR is one of the most powerful techniques in the study of magnetisation of thin films. It offers the study of all the essential magnetic parameters along with possessing a high sensitivity, high field and frequency resolution and a deep knowledge base in literature for the interpretation of the dynamics measured [3]. An additional major advantage of this method is that it allows the determination of the magnetisation without the need to know the sample volume [1]. Furthermore, it has a relatively easy

setup, with the required equipment being available and standard. The limits of this methodology include its lack of surface and lateral sensitivity, along with measurements including the contributions of imperfections in the waveguide and the substrate along with the magnetic thin film. Moreover, large magnetic fields may be required to observe a resonance, which has the drawback of potentially influencing the measurement due to effects such as force magnetostriction for instance [3]. The reader is guided to an excellent review by Farle where further highly relevant information regarding a range of techniques for the study of magnetisation dynamics can be found [3].

The first experimental measurements of FMR were performed by Griffiths in 1946 [5]. This technique has historically involved using a microwave resonant cavity placed between the poles of an electromagnet together with a source and a detector of microwave power, a technique which here we will refer to as cavity-FMR. The intensities of the microwaves propagating within the cavity are measured as the applied field is varied with a reduction of the signal detected when the resonant frequency of the sample and the cavity frequency are equal [50]. Due to cavity enhancement factors, specifically a high quality factor [50], this technique exhibits a high sensitivity and a maximum detection capability in the range $10^{10} - 10^{14}\,\mu_B$ [3]. The reader should note that detection limits are often discussed in terms of the number of electron spins detected, or equivalently, as the moment of the sample expressed in units of Bohr magnetons (μ_B as defined in equation 2.4). The main disadvantage of this cavity-FMR method is the dependence of the electromagnetic (EM) waves supported on the dimensions of the cavity which severely limits the frequency regions that can be probed. Typically, mm-waves in the X-band region (around 9.4 GHz) have been employed for these systems with a transverse electronic resonant mode, usually TE_{102}, exploited due to its high spatial uniformity in the middle of the cavity where the sample is placed. A further disadvantage of this method is the use of a swept magnetic field which can cause perturbations to the magnetic state of the sample [50].

The first reports of a Vector Network Analyser-Ferromagnetic Resonance (VNA-FMR) setup emerged in the 1990s [212–214]. This technique was a significant development in the study of magnetisation dynamics offering numerous functionalities that are not achievable through the use of the more traditional cavity-FMR. Advances in this area originated due to breakthroughs with waveguide technology, which is central to the VNA-FMR technique [215–217]. Crucially, in VNA-FMR it is possible to explore a broad frequency range which permits a greater insight into key dynamic

properties [218]. For example, as outlined in section 3.2, it allows important parameters such as the Landé g-factor and Gilbert damping parameter to be measured [50]. The study of magnetic damping, in particular, is a topic which attracts great research interest due to its importance to the mechanisms of spin transfer, spin Hall effect and spin pumping. These phenomena are critical to future technologies to enable next generation devices [29] [50]. The VNA-FMR technique with appropriate calibration can also provide phase information meaning that insights to both the real and imaginary parts of the susceptibility, detailed in section 3.2, can be obtained [50].

4.3.1 Experimental Setup

In Figure 4.7a, a schematic showing the experimental realisation of this technique is presented. The magnetisation dynamics of a sample are probed by this technique as follows. The sample is subject to a small perturbing RF magnetic field (h_{rf}) generated by a microwave current propagating through a waveguide in close proximity. When the frequency of h_{rf} is equal to the resonant frequency of the sample, as described in equation 3.28, a resonant absorption of the rf energy from the waveguide into the magnetic sample will take place, detected as a reduction in the energy traversing the waveguide [50]. An electromagnet can then used to apply a range of static magnetic fields to further characterise the dynamics at different field hence frequencies. The underlying physics of this resonant absorption is described in section 3.2. In this experimental realisation of FMR, it is important that the reader notes that there are several deviations from the assumptions made in the provided derivations of the dynamic susceptibility. These include that the sample dimensions exceed that of the waveguide (leading to the application of a nonuniform perturbating field), the measurements are carried out at room temperature and that the sample may possess a multidomain state at low fields.

A photograph of the setup used in this project is provided in Figure 4.7b, with the key components labelled. This setup was designed and constructed by N.A.B. Johansson and further details pertinent to the design, construction and specification of this instrument are detailed in his PhD thesis [219]. The main components of this setup include a GMW 5403 electromagnet, which applies the static magnetic field of strength up to 15 kOe. The power supplies used to control the electromagnet are two Kepco BOP 36-28MG connected in series, which provided a maximum current of 50 A. This was sufficient to saturate the samples studied in this work to a known state. The field takes approximately 2 s to stabilise. It is important to ensure the sample is correctly positioned in the centre of the pole pieces to minimise the effects of field inhomogeneity.

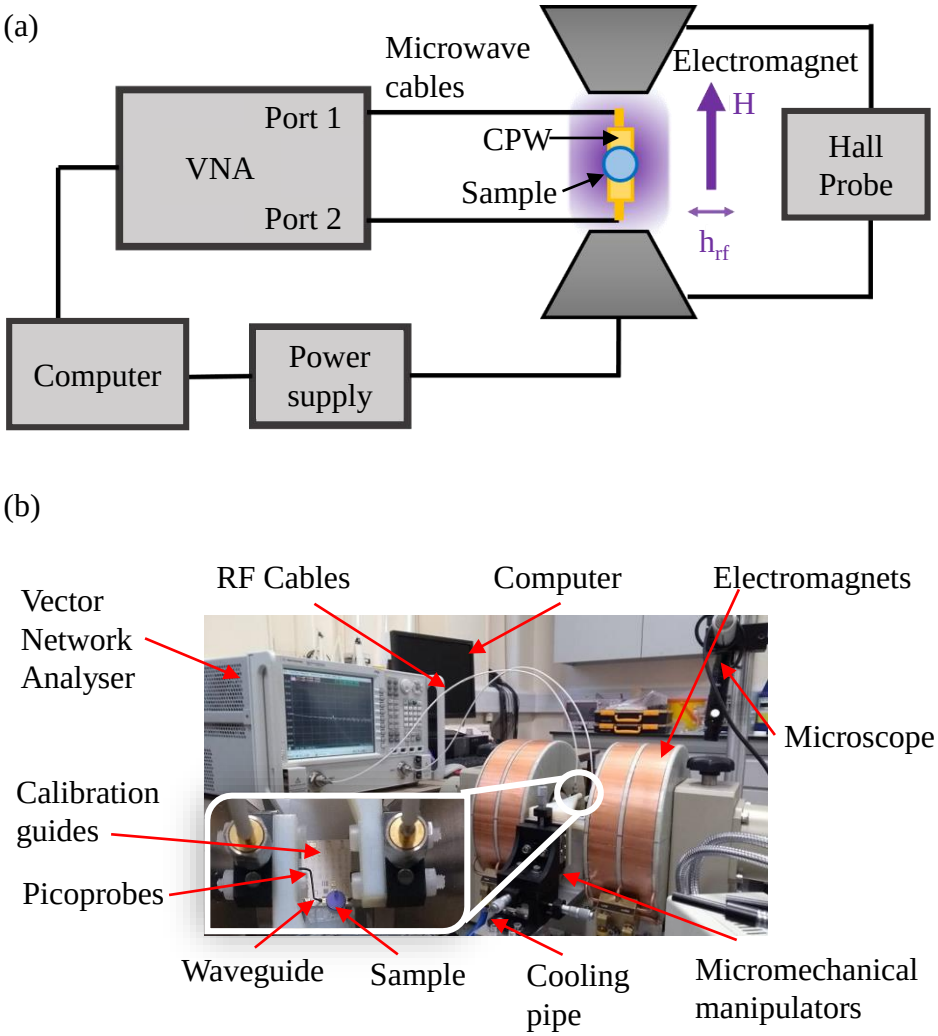

Figure 4.7: The VNA-FMR setup, as used in the project. (a) Schematic diagram of the experimental setup where the static field is applied IP. (b) A photograph of VNA-FMR spectrometer.

This static field can be applied either IP or OOP, based on the choice of sample holder used. For clarity, in Chapters 5 and 6 the reported dynamic measurements utilise only a IP field whilst in Chapter 7 measurements of both the cases where the static field is applied IP or OOP are presented. A Lakeshore gaussmeter [220] was used to calibrate the static field. The electromagnets also required water cooling to prevent overheating at high fields. To generate and measure the RF signals a Keysight PNA N5224A [221] was used in conjunction with a Picoprobe CS-9 calibration substrate which supported the traversing EM waves. The selected coplanar waveguide (CPW) on the calibration substrate possessed a length of 6.6 mm and had a central conductor of width 50 μm

[222]. The planar structure of these striplines makes them highly useful in the study of thin films and planar nanostructures, with their broadband nature allowing measurements in the frequency range of several hundred MHz to approximately 50 GHz. The calibration substrate also possesses a set of known standard waveguides for calibration. This allowed contributions to the full signal path from the source to the probe tips to be subtracted from the total signal measured. To connect the VNA to the waveguide, semi-rigid coaxial cables provided by RF coax were used along with microwave probes (Picoprobes) designed in-house and produced by GGB Industries Inc. to connect the coaxial geometry to the coplanar geometry. In this project, two sets of Picoprobes were available to permit the measurement of the sample with the sample positioned so that the applied field was IP (as shown in Figure 4.7b) or OOP. In the latter case, the use of a different sample holder to position the sample vertically between the electromagnets was necessary. A microscope was used to ensure accurate placement of the Picoprobe tips upon the waveguide. To ensure high sensitivity of the instrument, it is essential that the microwave components of the setup consist only of NM materials to eliminate parasitic magnetic contributions to the background signal [50].

The film is placed in a flip-chip manner against the waveguide and positioned so that it covers the central conductor. The accessibility of the waveguide and ease of sample placement is an advantage of this setup. This necessitates the film to be cut to into a circle of diameter 5 mm using a Southbay disc cutter, as outlined above in section 4.2.3. As the sample is not perfectly flat, an air gap is present which provides a sufficient insulating layer to prevent a short between the ground and signal lines. The high frequency current supplied by the VNA creates a small oscillating magnetic field above the central conductor of the waveguide. As outlined above, in operation the microwave absorption as a function of externally applied magnetic field is measured by the VNA. When resonant absorption is achieved, a lorentzian absorption in the trace of the RF energy transmitted through the waveguide is observed. This is parameterised through the use of the scattering parameters (S-parameters) of the system, which are discussed later [50]. An example of the data collected from the FMR experiment is shown in Figure 4.8, where the resonant absorption of a thin film as a function of applied field and frequency applied by the VNA is measured.

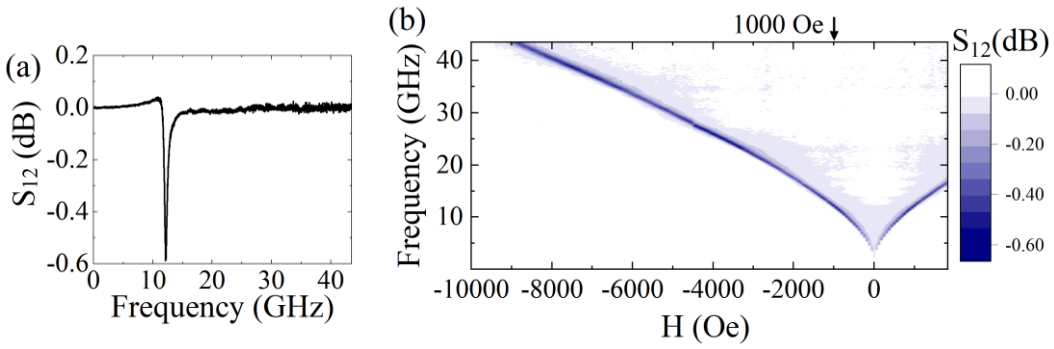

Figure 4.8: An example of the data collected from a VNA-FMR experiment. a) S_{12} absorption profile at an externally applied field of 1000 Oe. b) 2D maps of the resonant spectra obtained from sweeping the external field. The blue areas if the 2D map indicate resonant absorption. In the analysis stage each S_{12} profile, as shown in (a), is fitted using equation 4.5, as discussed later.

This instrument has a detection limit $7 \times 10^{13} \mu_B$, sufficient to measure a film with thickness of order 1 nm. MatLab and LabView software developed by N.A.B. Johansson is used to control this instrument throughout the measurement [219]. The reproducibility of this VNA-FMR measurement technique was also investigated by N.A.B. Johansson, with it found that the uncertainties in frequency of 1-2 % and linewidth of 20 % (especially in the case of high linewidth resonances) can be expected. Further discussions on this aspect of the measurement can be found in his thesis [219]. This measurement setup (denoted as the Picoprobe setup in later chapters) was used in the studies the magnetic dynamics reported in Chapters 5 and 6 and in section 7.4.

It is important that the magnetisation angle remains small with respect to the equilibrium direction so that the dynamics of the magnetisation remain in the linear regime. This is necessary to ensure that assumptions made in the derivation of Kittel's equation in section 3.2 remain valid. In a standard measurement, a power of 10 dbm was used which was chosen as it corresponds to a perturbating magnetic field of magnitude 1 Oe (as shown by HFSS simulations of the waveguide carried out by Mr Danielius Banys). In practice, the actual field experienced by the sample will be slightly reduced due to the aforementioned air gap along with the signal attenuation that occurs within the CPW and cables. For similar material sets and frequency ranges, it has been shown that the skin depth, as defined by equation 3.49, is of the order 100 nm [35, 40] and for our material set ≈ 500 nm [223]. Instrumentation upgrades were performed throughout this work to augment the setup with an IP rotational capability. This was motivated by a desire to characterise the dynamics responses at a range of angles between the IP and

OOP film directions. This stage of the project along with a summary of the enhanced capabilities of this setup is detailed in later discussions.

The complete calibration procedure as outlined by Bilzer [224], requiring reference measurements that can only be taken by rotating the IP angle of the static field with respect to the waveguide, could not be performed for this experimental setup. This is due to difficulties associated with maintaining the placement of the Picoprobes upon the waveguide. Therefore, in this project, we measure only the magnitude of the S_{12} parameter to characterise the transmission. This involved a calibration process following the SOLT procedure; where a Short, Open, Load possessing $50\,\Omega$ impedance and Through circuit are measured by connecting the Picoprobes. This allowed the contribution of the electrical equipment up to the Picoprobe tips to be accounted for. A further step was then taken where a reference measurement of the transmission through the waveguide was subtracted from the experimental data to remove the contribution of the waveguide. The reader is guided to N.A.B. Johansson's thesis for a more comprehensive overview of the calibration process for the VNA-FMR setup [219]. As discussed by Bilzer, this procedure can introduce an asymmetry into the line-shapes of the measured absorption spectra resulting from a mixture of the real and imaginary components of the complex susceptibility contributing to the measurement. It is reported that deviations in the measured frequency between our method and the method detailed by Bilzer are less than 1 %. However, there is a greater impact on the linewidth, particularly at low applied field with deviations of up to 10 % reported [224]. A multitude of sources can contribute to these discrepancies. The greatest contribution is the imperfect nature of the stripline, causing it to act as an inhomogeneous mm-wave source. These imperfections include difficulties in impedance matching within the electrical circuit in addition to the fact that the excitation field as experienced by the sample has some small components in the two other orthogonal directions to the principal field direction. Furthermore, we must consider that the measured response includes both the sample along with the substrate and is also susceptible to misalignment of the sample positioning on the CPW [50, 225]. It has also been reported that in the case of FM/NM bilayers eddy currents in the sample arising from components of the driving the field perpendicular to plane can contribute to this asymmetry even in cases where we consider a film with thickness less than the skin depth of the material [226].

In these measurements, a frequency-swept method as opposed to a field-swept method was performed. A key advantage of this approach is the lack of disturbances to the magnetic configuration of the film that can be generated from sweeping the field

[227]. However, drawbacks include a lower sensitivity than a field-swept method and the introduction of effects such as the frequency dependence of the impedance of the setup. The impacts of this can mitigated by performing suitable background removals and calibration methods [50].

The collected S_{12} data, as shown in Figure 4.8, for each static applied field was fitted through Python software developed throughout the PhD project. Following literature [44, 50, 224, 225, 228], the analysis procedure accounted both for the real and imaginary components that influence the line-shape of the resonance. The fitting equation used was

$$y = y_0 + bf + \cos(\xi)P\frac{(\frac{\Delta f_{\mathrm{dB}}}{2})^2}{(f-f_r)^2+(\frac{\Delta f_{\mathrm{dB}}}{2})^2} + \sin(\xi)P\frac{(\frac{\Delta f_{\mathrm{dB}}}{2})(f-f_r)}{(f-f_r)^2+(\frac{\Delta f_{\mathrm{dB}}}{2})^2}. \tag{4.5}$$

where y_0 is the baseline, b is the linear background, ξ is the mixing parameter, P is the peak amplitude, f and f_r are the frequency and resonant frequency respectively with Δf_{dB} is the linewidth (Full Width at Half Max) of the fit in the dB scale. In such a way, the important features of the real and imaginary components of the dynamic susceptibility of the samples, as introduced in equations 3.27 and 3.28, could be extracted. The resonant linewidth Δf as introduced in section 3.2 was assessed by determining the peak-to-peak linewidth (Δf_{pp}) of the differentiated lorentzian fit. This parameter is related to Δf by the relation [229]

$$\Delta f_{\mathrm{pp}} = \frac{1}{\sqrt{3}}\Delta f. \tag{4.6}$$

At this stage, the variation of the extracted parameters over the range of applied static fields could be analysed with the use of equations presented in section 3.2 to extract the important characteristic magnetic properties. In the remaining part of this section details of the upgrades required to the VNA-FMR system for the study reported in Chapter 7 are provided. Subsequent discussions of the key high frequency components and physics underpinning the VNA-FMR technique are then put forth.

4.3.2 VNA-FMR Upgrades

Instrumentation upgrades to the VNA-FMR were required to allow the magnetisation dynamics at a range of angles between the IP direction and OOP direction to be characterised. This was not possible using the previously discussed Picoprobe setup (which

permitted only measurements in the cases where the external field was applied IP or OOP) due to difficulties maintaining the connection of the probe to the waveguide throughout the rotation. The following improvements were required:

1. The electromagnet placed upon a turntable.
2. A bracket to enable to sample to be held vertically between the pole-pieces of the electromagnet.
3. A waveguide with coaxial connectors. This was motivated due to the operational difficulties of connecting the installed Picoprobes upon the waveguide correctly and then maintaining the contact in the configuration required for rotational measurements.
4. A new sample holder to allow the sample to be positioned vertically against the waveguide.

To this end, a NanOsc. waveguide capable of supporting frequencies from 2 GHz to 50 GHz [230] was incorporated. This waveguide could be connected to the VNA-FMR through coaxial connectors, a great simplification of the Picoprobe arrangement. A photograph of the augmented setup is presented in Figure 4.9. A custom made sample holder, presented in Figure 4.9(inset), was 3D printed to position the sample at suitable proximity to the waveguide. As in the case of the calibration substrate discussed above, a sufficient natural air insulating gap to prevent shorting of the ground and signal lines of the waveguide was present.

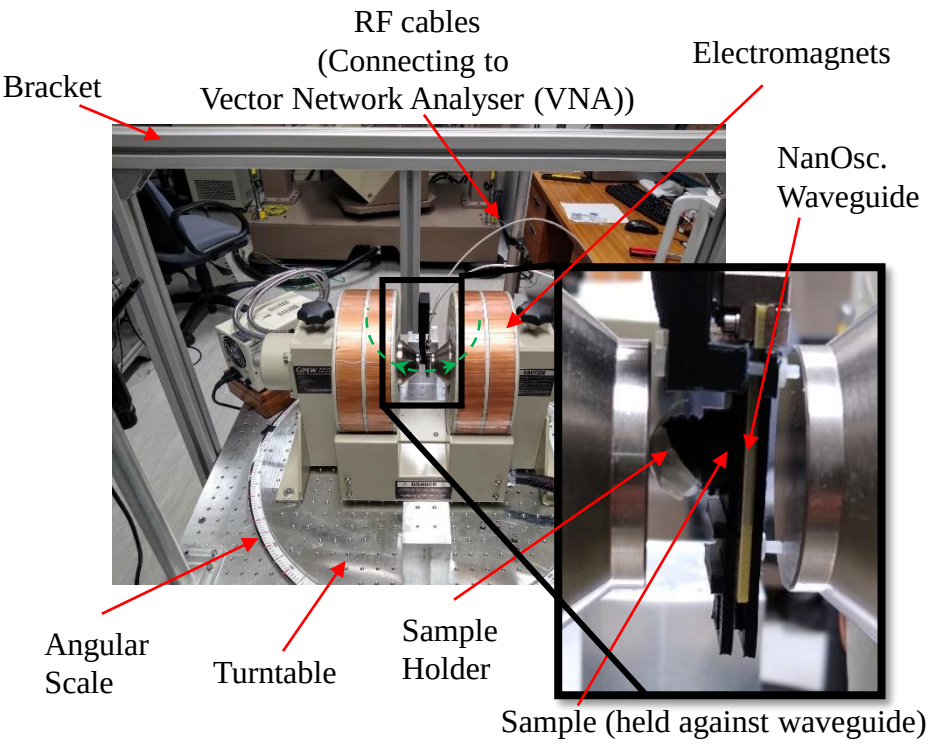

Figure 4.9: Instrumentation upgrades for the VNA-FMR system. The sample is held in a fixed vertical position against the NanOsc. waveguide with it now possible to rotate the electromagnet from applying the field in the OOP direction, as shown, up to 15^{o} to the IP direction. A green dashed line is provided as a guide of the motion of the electromagnets. The other possible configuration of this instrument is shown in Figure 4.7. Inset: A magnified view of the sample holder and waveguide arrangement.

A limitation of the improved setup is that the sample holder only permitted rotation of the electromagnet (hence external field) of up to 15^{o} from the OOP direction. This was deemed sufficient for the investigation exploring PSSW dynamics reported in Chapter 7. The waveguide was calibrated by taking a reference measurement that could be subtracted from subsequent sample readings. This procedure enabled the instrument to have the sensitivity required to measure a NiFe film of thickness of approximately 4.5 nm.

4.3.3 RF Components and Concepts

Vector Network Analyser

The Vector Network Analyser (VNA) is the key component of the VNA- FMR setup used in this project. It enables the RF properties of magnetic materials and devices to be characterised in terms of S-parameters [231, 232], discussed later. It possesses two or more ports each capable of being a source and receiver of a RF current and can measure the transmission and reflection of this current over a broad frequency range. The *vector* naming denotes its ability to determine not only the amplitude of oscillation, but also its phase.

The VNA possesses several sources of error that must be minimised to enable low signal to noise ratios to be achieved. These include issues with the matching of the ports of the VNA and deviations from the ideal 50 Ω impedance paradigm. Moreover, imperfect directivity of the bridges and couplers utilised to keep the incident and reflective signals isolated from each other can lead to additional uncertainty. Further errors arise from the differing frequency response of the multiple receivers and issues with the isolation between the ports. Ideally, the VNA would have infinite isolation between the ports but this cannot be achieved practically as the bidirectional couplers will not have perfect directionality, leaking some incident signal to the reflected receiver. This leakage manifests as sharp ripple effects in the data and is often referred to as 'cross-talk'. As these errors are repeatable and systematic, the effects of the internal components of the instrument on the measurement can be removed or compensated by calibrating against known standards. In this project calibration was carried out through the SOLT procedure; where a Short, Open, Load possessing 50 Ω impedance and Through circuit are measured. After the system has been calibrated, a degree of drift from this calibration is expected due to temperature change for instance or loosening of connections in day-to-day use. Therefore, frequent calibration is advisable [231, 233].

As previously mentioned, this measurement procedure relies on connecting to a CPW to transmit RF current with low loss and little distortion into proximity with the sample. An overview of the physics underlying transmission lines such as CPWs is given in section 4.3.3.

S-parameters

S-parameters are used to describe the magnitude and phase relationships between incident and reflected waves from the two ports of the VNA, which act as both source

and receivers of RF current. They are widely used in the area of high frequency electronics as the high speed nature of the measurement renders transient quantities such as voltage or current insufficient to describe the system [50, 232]. In this formalism, the S_{mn} is the transmission coefficient for a wave sourced at port n and received at port m [234]. They are calculated as

$$S_{mn} = \frac{b_m}{a_n} \tag{4.7}$$

where b and a are the power at the respective ports. From transmission line theory, S_{11} is defined as

$$S_{12} = \frac{Z_0 + Z}{Z + 2Z_0} \tag{4.8}$$

where Z is the impedance and Z_0 is the characteristic impedance of the line. The general form of these waves are directly measured as a function of frequency by the VNA [235].

Transmission Lines

The presence of a perturbating microwave magnetic field is required to excite resonant precession of the sample magnetisation. Therefore, a transmission line, a structure designed to support the propagation of RF voltages and currents, is required. In the absence of magnetic materials, the propagation of microwaves through the waveguide is governed through the telegrapher's equations [236]. A more detailed overview of this physics and its application in VNA-FMR can be found in [224]. The key properties of a waveguide for wave propagation are the resistance, inductance, shunt capacitance, and conductance. Crucially, these parameters are highly susceptible to the environment and material properties surrounding the transmission line [216].

In VNA-FMR, a type of planar transmission line known as a Coplanar Waveguide (CPW) is used. Introduced by Wen in 1969 [215], this consists of a central signal line with wider grounding lines on either side as shown in Figure 4.10. This structure supports a quasi-transverse electromagnetic (quasi-TEM) propagation where the dominant mode consists of the electric and magnetic fields propagating perpendicular to the current direction [237]. The ground strips act to keep the field in close proximity to the waveguide. This design is widely used in electronics, mainly due to the low cross leakage allowing high current densities, low losses and ease of fabrication. Their application to VNA-FMR derives from the oscillating magnetic field produced at the surface of the waveguide ensuring that the propagating signal is sensitive to the external environment, particularly the relative permeability μ_r and relative permittivity ε_r

of materials in close proximity. The coupling between these properties and the waveguide was first outlined by Barry [216]. When the resonant condition of a magnetic sample is satisfied, the permeability of the sample (hence the external environment of the waveguide) alters with this impacting the S-parameters [216]. It should be noted, however, that CPW geometry can also lead to a broadening of the resonant line-width due to the excitation of higher-order spin wave excitations [39].

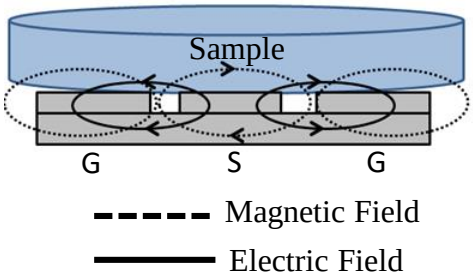

Figure 4.10: A schematic of the Coplanar Waveguide (CPW) setup, the electric and magnetic fields generated along with sample positioning. The labels G and S correspond to the ground and signal lines respectively. This schematic is reproduced from [50].

4.4 Ferromagnetic Resonance Simulations

Micromagnetics simulation software is an indispensable tool of modern magnetic research [238]. It is vital to the study of magnetisation dynamics in particular due to the rarity of analytical solutions to the central equation of motion for most magnetic systems, the Landau-Lifshitz-Gilbert equation (equation 3.10) introduced in section 3.1 [65]. Of the multitude of simulation platforms available, Mumax^3 [239] was used in this project as it is an open-source general purpose micromagnetics simulation software designed for high performance calculations and typically utilised for large simulations. Furthermore, I had direct experience with this simulation software during a secondment carried out at Thales Research and Technology with it also being widely utilised in my research group. A key advantage of this software is that it is utilises the Graphical Processing Units (GPUs) to accelerate the simulation to running times beyond that achievable by the sole use of the Central Processing Units (CPUs) [65, 239]. The motivation for this is that GPUs are capable of performing calculations in parallel, minimising the time required to run detailed simulations compared to CPU based

software [65]. Mumax^3 operates through solving the classical Landau-Lifshitz equation and can model the effects of exchange and magnetostatic interactions, anisotropy, thermal effects and spin transfer torque. However, it is limited to only considering the case of perfect interfaces with zero roughness [239].

Mumax^3 utilises the Finite-Difference Methods (FDM), a class of element solvers which are the most direct way of discretising space employing a 2D or 3D grid of orthorhombic cells to solve partial differential equations (PDE). In such a way relevant magnetic parameters can be assessed in different areas of the grid. Specifically, volumetric quantities such as magnetisation and effective field are solved in the centre of each cell whereas coupling quantities such as the exchange interaction are considered on the outer faces of each cell [239]. The dominant PDE is solved for a predetermined set of regions with the boundary conditions applied at the nodes. The framework connecting the nodes, known as the grid or mesh, must have dimensions comparable or smaller than half the exchange length (defined in equation 2.25) [239]. The continuous PDE is discretised on a regular grid to permit efficient solution methods, making large scale simulations accessible. This makes FDM particularly applicable for the modelling of uniform geometries such as thin films. FDM solves the PDE in its original form, thereby by increasing the accuracy of solution, with it therefore assumed that the underlying physical conservation laws are satisfied [65, 240]. As FDM solves the PDE by satisfying it at all nodes and the boundary conditions it is referred to as the *strong form* of the solution. This means that the governing PDE is not modified prior to its discretisation or solution [240].

An alternate approach is the Finite Element Methods (FEM), where the simulation domain is discretised into finite elements. The solution to the governing equations is evaluated at the nodes connecting the elements and the spatial variation within elements is estimated using polynomial interpolation. FEM are considered to be more mathematically strict than FDM thus allowing the use of adaptive meshes that can simulate complex geometries. This represents a significant advantage over FDM modelling. The underlying operation of adaptive meshes are that for each time-step the initial mesh is refined into areas where the magnetisation is non-uniform whereas areas with uniform magnetisation experience a coarsening (a removal of cells). This dynamic alteration of the mesh reduces the computational expense of these simulations. An important divergence of this approach from FDM is that it solves the weak form of a differential equation, whereby the equation is not required to hold for the entire region. Instead, the residual of a suggested solution is measured. In cases where the

residual is zero, the weak solution is considered to be equivalent to the strong classical solution [240] [241].

Today, the prominent GPU-accelerated micromagnetic solvers are predominantly based upon FDM as opposed to FEM techniques. This is likely due to the computational complexity and higher memory requirements of the FEM approach resulting in only relatively simple problems being solvable on a reasonable time scale. To further examine the adoption of numerical simulation techniques by the magnetism community, the reader is guided to an excellent review by Leliaert [65].

4.4.1 FMR Simulation Techniques

Transverse Oscillating Field

It is possible to simulate FMR experiments through directly reproducing the physical processes underlying this measurement. This involves modelling a time dependent periodic sinusoidal microwave magnetic field at a fixed frequency perturbating the magnetisation of a sample, with its dynamic response then recorded. However, despite the conceptual simplicity of this approach, this technique is computationally expensive [242] [243]. This is because in order to get a complete frequency-field heatmap the sweeping both the oscillating field frequency and static magnetic field at each data point is required.

Ringdown Method

The Ringdown method is an efficient method to determine the eigen-modes of a system. It operates through applying a short-lived and sufficiently weak excitation field to the sample, with its magnetisation dynamics then recorded as the system relaxes to equilibrium. It is necessary to perform a Fourier Transform to convert the time domain output of the evolution of the magnetisation to the frequency-domain [244].

Fast Fourier Transform

For the simulations performed in this project it was necessary to Fourier transform the time-domain outputs to the frequency domain for further analysis to take place. It was not possible to carry out a Fourier Transform analytically thus a discrete method known as the Fast Fourier Transform (FFT) was utilised [245, 246]. The Power Spectral Density (PSD) is given by

$$S_x(f) = \mid F_x(f) \mid^2 \tag{4.9}$$

where

$$F_x(f) = \sum_{k\equiv 1}^{N} \langle M_x \rangle \langle t_k \rangle e^{-i2\pi f t_k} \tag{4.10}$$

where f is the frequency, M_x indicates the macroscopic magnetisation in the x-direction and $t_k = k\Delta t$ and $k = 1, 2, ..., N$ where N is the number of time steps Δt [243]. The amplitude spectrum can also be analysed which is given by $\mid F_x(f) \mid$. When using this protocol, it is important to consider the information lost in the discretising process. FFT has a property where the maximum frequency that may be calculated is the Nyquist frequency, given by

$$f_{\max} = \frac{f_s}{2} \tag{4.11}$$

where f_s is the sampling frequency [247]. In a highly varying power spectrum, the f_s needs to be much higher than periodicity for a smoother spectrum to recreate it. Otherwise, an aliasing of the signal would occur meaning that a high frequency waveform would appear low frequency [246, 248].

Chapter 5

Synthetic Antiferromagnetic Dynamics

This chapter reports a comprehensive investigation on the fabrication and characterisation of a series of Ferromagnetic (FM)/Nonmagnetic (NM)/FM trilayers coupled through the RKKY interaction. The underlying physics of such trilayer structures and the ramifications of this interlayer exchange coupling on the exhibited magnetic properties are described in section 2.7 and section 3.5 for the static and dynamic cases respectively. The investigation reported in the following has recently been published in Physical Review Applied [51].

This chapter is structured in the following way. In section 5.1 a discussion of the fabrication and characterisation of a series of Ta/CoFeB/Ru/CoFeB stacks with either Pt or Pd capping layers (dependent on the availability of Pt or Pd in the sputtering system) is given. The choice of $Co_{0.2}Fe_{0.6}B_{0.2}$ as the FM element of the structure was motivated due to its widespread use as a magnetic thin film for spintronic devices including STT-MRAM [44], future write heads and wireless inductors [223]. The alloys of CoFeB have a range of desirable properties including a large saturation magnetization [49, 249], high resistivity [223], and high tunnel magnetoresistance values [123, 250, 251]. Ru was selected as the NM spacer layer material due to the high interlayer exchange couple strength J_{IEC} supported by this element [41]. For comparison purposes, the properties of a single CoFeB layer (SL), structure Ta(2 nm)/CoFeB(9 nm)/Pt(4 nm), are also discussed. In section 5.2, the chapter proceeds to focus solely on the Synthetic Antiferromagnet (SAF) form of these structures with the investigations on their Synthetic Ferromagnet (SFM) counterparts reported in Chapter 6.

To date, much attention has focused upon SAFs, where an antiparallel arrangement of the layer magnetisations occurs due to a negative interlayer coupling strength ($J_{\mathrm{IEC}}<0$) [38] [41, 97]. In particular, these structures exhibit significantly different resonant properties than those displayed by their constituent layers. In such systems,

the resonance frequency is intermediate between natural ferromagnetically and antiferromagnetically ordered systems, with a high frequency optic mode (OM) introduced [26, 40, 51]. This optic mode has been studied by several groups due to its potential to significantly enhance self-biased ferromagnetic resonances towards the 100 GHz range [48, 49]. In recent works, high OM frequencies (f_r^o) were demonstrated by S. Li et al. [48] where a zero field OM resonance of 11.32 GHz was reported. In Figure 5.1, a schematic illustration of the resonant OM of a SAF is presented alongside the standard acoustic (Kittel) mode (AM) exhibited by the SL case. The J_{IEC} present in the SAF system allows higher frequency dynamics to be supported than seen in the SL case.

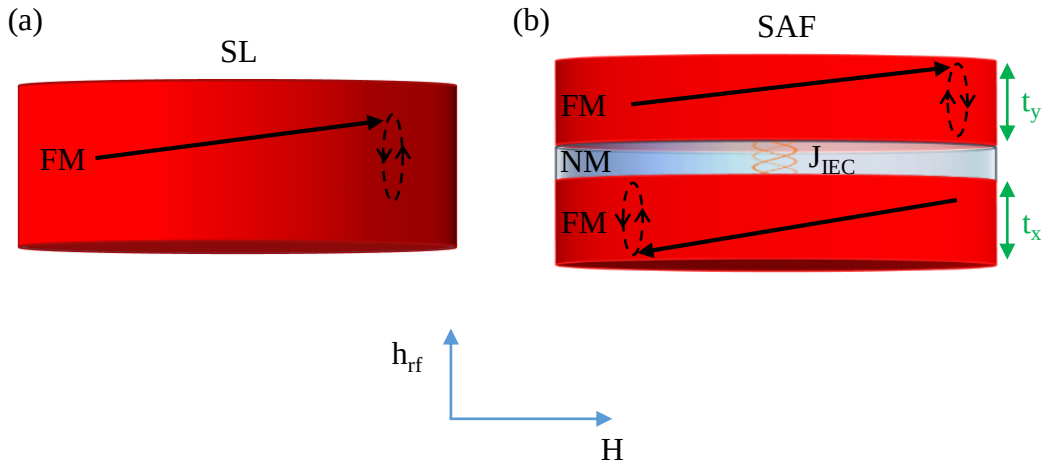

Figure 5.1: Magnetic precession due to a perturbation field h_{rf} of a) a single FM layer b) a SAF, with structure FM/NM/FM where the J_{IEC} promotes an antiferromagnetic layer magnetisation alignment and OM precession is supported. The thickness of the FM layers are represented by t_x and t_y respectively. The red coloured layers are ferromagnetic, whilst the blue is the NM spacer layer.

The OM frequency has a contribution from the interlayer coupling, as discussed in Chapter 3, which modifies the Kittel equation (equation 3.30) to the form

$$f_r^o = \frac{\gamma}{2\pi}\sqrt{(H + H_{\text{ex}} + H_k)(H + H_{\text{ex}} + H_k + 4\pi M_s)}, \tag{5.1}$$

where H_{ex} is related to J_{IEC} by the relation

$$H_{\text{ex}} = \frac{2J_{\text{IEC}}}{M_S(t_x + t_y)} \tag{5.2}$$

where t_x and t_y are the thickness of the FM layers [48].

5.1 Sample Series

5.1.1 Sample Fabrication

The sample fabrication was accomplished using an AJA ATC 2200-V magnetron sputtering system detailed in section 4.1. The substrates employed were Si/SiO_2, where the oxide layer was of thickness 290 nm. No deliberate substrate heating was used either during the deposition or as an annealing step. The full structure of the samples was $Ta(2\,nm)/Co_{0.2}Fe_{0.6}B_{0.2}$ (5 nm)/$Ru(t_{Ru})/Co_{0.2}Fe_{0.6}B_{0.2}(5\,nm)/Pt(4\,nm)$ or $Pd(4\,nm)$ where t_{Ru} is the thickness of the Ru layer. The CoFeB layer thickness was selected to be approximately one exchange length, defined in equation 2.25, where each layer could be regarded as a macrospin which simplified the interpretation of the data allowing the measurements to modelled analytically (as carried out in section 5.4). The structure of the trilayers is shown schematically in Figure 5.2.

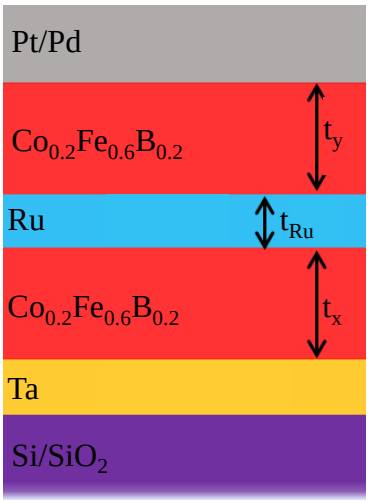

Figure 5.2: A schematic of the CoFeB trilayer stack with layer structure $Ta(2\,nm)/Co_{0.2}Fe_{0.6}B_{0.2}(5\,nm)/Ru(t_{Ru})/Co_{0.2}Fe_{0.6}B_{0.2}(5\,nm)/Pt(4\,nm)$ or $Pd(4\,nm)$. The thicknesses of FM layers and the NM Ru spacer layer are denoted as t_x, t_y and t_{Ru} respectively.

The purpose of the Ta was to act as an adhesion layer and Pt or Pd was used as a capping layer to inhibit oxidisation of the films. The deposition of the Ta, CoFeB, Pt and Pd layers was carried out using DC magnetron sputtering from either elemental or, in the case of CoFeB, alloy targets. The motivations underlying the choices of sputtering powers described in the following are discussed in section 5.1.1. The deposition times of the layers were decided upon through a deposition rate calibration using X-ray

Reflectivity (XRR), as discussed in section 4.2.1. The Ta and CoFeB layers were deposited at a power of 20 W, with the capping layer deposited at 100 W. The deposition time for the Ta was 125 s and for the CoFeB layers 1100 s. The Ru layer was deposited through a Radio Frequency (rf) sputtering at a power of 75 W. The deposition time for the Ru layer was varied from 0 to 200 s to explore a t_{Ru} ranging from 0 nm to 3 nm. This allowed the full range of RKKY phenomena to be explored. The base pressure prior to deposition was less than 5×10^{-8} Torr, with no in-situ magnetic fields applied. The working pressure of the Ar^{+} gas was between 3-4 mTorr for the CoFeB layers (variation due to experimentally unavoidable plasma instabilities due to the magnetic nature of the target) and set as 3 mTorr for the Ta, Ru and Pt layers.

Roughness Investigations

An investigation regarding the sputtering parameters that would provide the lowest surface roughness for the Ta and CofeB underlayers was carried out using Atomic Force Microscopy (AFM) as discussed in section 4.2.2. This study was motivated due to the quality of the Ta and CoFeB underlayers being paramount concern due to the fact that roughness in these layers could propagate into the Ru layer, with a subsequent deleterious impact on the attainable interlayer coupling [252]. In this process, a range of Ta and Ta/CoFeB films, with nominally identical thicknesses respectively, were fabricated with differing sputtering powers ranging from 20 W to 50 W. The minimum sputtering power investigated was 20 W as below this threshold a plasma could not be maintained. The potential to further reduce layer roughness using substrate heating was also explored, though ultimately this was not used to fabricate the studied samples as explained below. The roughness (σ_{film}) was characterised through determining the standard deviation of the height distribution of the obtained AFM image.

In Tables 5.1 and 5.2 the impacts of reducing the sputtering power along with substrate heating on the roughness of the Ta and CoFeB layers are presented. It was found that as the sputtering power was reduced the layer roughness was correspondingly lowered with smoother layer growth seen. Insightfully, it can be seen that the roughness of the CoFeB is highly dependent on the properties of the Ta underlayer. The data also demonstrate that increase of substrate temperature to 100 °C during deposition does not provided any significant additional reduction in roughness. This motivates the use of the lowest possible sputtering power (in this case 20 W) that will sustain a stable plasma for the sputtering of these layers and a room temperature deposition.

Further investigation was not deemed necessary to further optimise this stage of sample growth as the film roughness was comparable with that of the Si/SiO_2 substrate at (0.211 ± 0.002) nm.

Deposition Time (s)	Deposition Temperature (^{o}C)	Sputtering Power (W)	σ_{film} (nm)
49	0	50	0.569 $\pm$0.005
125	0	20	0.1808 $\pm$0.0005
125	100	20	0.1562 $\pm$0.0003

Table 5.1: An investigation into the impacts of sputtering parameters on Ta layer roughness.

Deposition Time (s)			Sputtering Power (W)		
Ta	CoFeB	Deposition Temperature (^{o}C)	Ta	CoFeB	σ_{film} (nm)
125	1100	0	50	20	0.576 $\pm$0.002
125	1100	0	20	20	0.1411$\pm$0.0003
125	1100	100	20	20	0.390 $\pm$0.003

Table 5.2: An investigation exploring the impacts of sputtering parameters on CoFeB layer roughness.

The Ru layer was deposited through RF sputtering, made necessary by the requirement that this layer possess a high quality yet be ultrathin ($\lesssim 1$ nm) . In particular, it was found through vector Vibrating Sample Magnetometry (VSM) measurements (see section 4.2.3) that DC sputtering, even in the case where the power was reduced to the minimum limit to maintain plasma, was unable to create a sufficient quality of interlayer to establish AF interlayer coupling. In order to determine the optimal sputtering power, a range of conditions between 15 W and 75 W were investigated. From VSM measurements, a magnetometry technique discussed in section 4.2.3, it was demonstrated that AF coupling was established between the FM layers only in the 75 W case. The reader is referred to Figures 5.4a, 5.11 and 6.3 for examples of the hysteresis loop of SL and trilayers with AF coupling (SAF) and FM coupling (SFM) respectively. Given the relatively large deposition times required to create ultrathin Ru layers, up to 200 s for the deposition of a Ru layer with thickness 3 nm, the use of a sputtering power of 75 W was chosen as the most appropriate optimisation between the following criteria i) a reduction in sputtering power could introduce contaminants to this ultrathin

layer ii) an increase to sputtering power to reduce deposition time would result in an increase of layer roughness.

5.1.2 Sample Characterisation

In this section, a report of the characterisation undertaken on the properties of the layers of the stack is given. Firstly, a discussion of the characterisation performed on a single layer CoFeB thin film, stack structure Ta(2 nm)/$Co_{0.2}Fe_{0.6}B_{0.2}$(9 nm)/Pt(4 nm), is provided. As the selected ferromagnetic element of the trilayers it was crucial to characterise the fundamental magnetic properties of this material. The latter part of the discussion presents the variation of the properties of the Ru layer of the stacks with deposition time.

CoFeB Characterisation

The layer structure of SL was determined using XRR. The data were fitted to a Fresnel model using the GenX software package as outlined in section 4.2.1. All measurements were performed over a 2θ range of 0.1^{o}–8.0^{o} with a step size of 0.01^{o}. The fitting was performed until the reduced χ^2 figure of merit was optimised. The results of this analysis can be seen in Table 5.3 and Figure 5.3. In particular, the variation of the SLD throughout the film thickness is presented in Figure 5.3b showing the expected trilayer structure. It is seen that the Ta, CoFeB and Pt densities are in agreement with literature values [253] with low layer roughness also achieved. The roughness of the layers are also similar to that reported in other literature reports concerning CoFe alloys [252, 254].

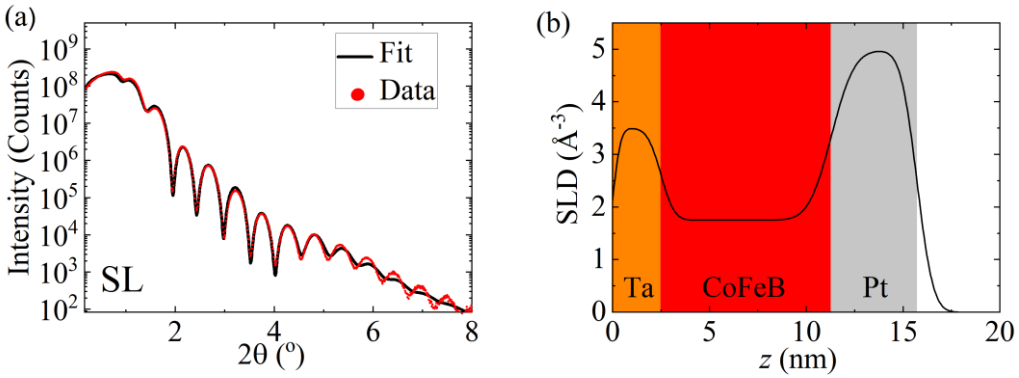

Figure 5.3: Structural characterisation of single layer CoFeB thin film with nominal structure Ta(2 nm)/ CoFeB(9 nm)/Pt(4 nm), referred to as SL in the main text. a) XRR measurement b) SLD profile as derived from the model fit to the XRR measurement as a function of distance from the substrate z. The overlaying colours represent the different layers corresponding to the colouring in Figure 5.2. The FOM_{Log} of the displayed fits were of order $\times 10^{-2}$.

Layer	Thickness (nm)	Roughness (nm)	Density (Å^3)
Ta	2.5	0.5	0.052
CoFeB	8.8	0.9	0.017
Pt	4.4	0.7	0.068

Table 5.3: Layer properties of the single CoFeB layer with structure Ta(2 nm) /CoFeB(9 nm)/Pt(4 nm) referred to as SL in the main text, as characterised by XRR and modelled using GenX.

The static magnetic properties of SL were explored using VSM. Figure 5.4 shows that the CoFeB possessed a M_S of 1300 emu/cm^3, as expected from literature [48, 51]. For the range of layer thickness studied in this project, CoFeB possessed an IP magnetisation. In addition to the expected magnetic properties it was noted that an IP uniaxial anisotropy was present in all SL samples. In Figure 5.4a, the uniaxial anisotropy is demonstrated where an EA and HA is exhibited with IP rotation by VSM measurement at room temperature. Furthermore, Figure 5.4b displays the variation of the coercivity with IP rotation due to this uniaxial anisotropy. This uniaxial anisotropy was found despite no deliberate conditions being employed to induce a preferential magnetisation direction. Indeed, as the sample holder was rotated throughout the deposition the formation of any anisotropy induced by the deposition process should have been suppressed, though may not have been eliminated entirely [255, 256]. The uniaxial anisotropy H_k was found to be (58 ± 2) Oe by an analysis of the anisotropy field

as detailed in section 2.4.4. It can therefore be concluded that this is likely to be an intrinsic property of the material, as previously reported by Hindmarch et al. [257]. In his report, the origin of this anisotropy is ascribed to an interfacial anisotropy that propagates throughout the bulk of the material during film growth.

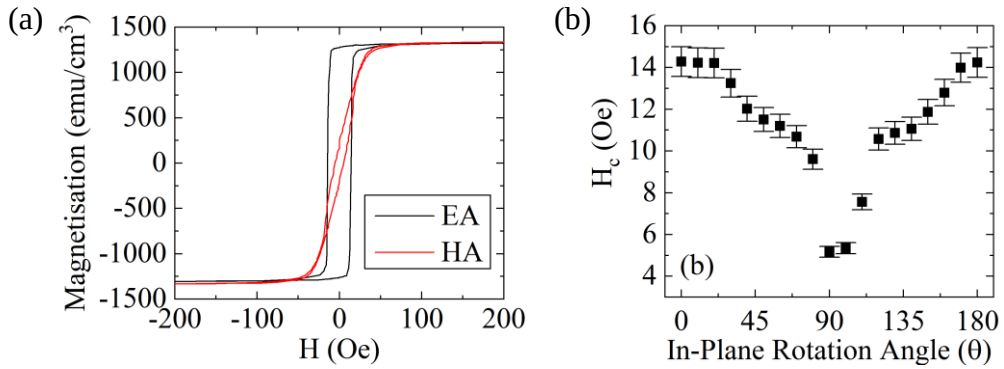

Figure 5.4: IP uniaxial anisotropy of a single layer CoFeB thin film, referred to as SL in main text. (a) M-H loops taken at room temperature with the the external field applied IP along the EA and the HA (b) Variation of H_c with IP rotation angle.

The dynamic properties of SL were investigated through VNA-FMR spectroscopy at room temperature with the magnetic field applied in the plane of the samples. The VNA-FMR measurement procedure is described fully in section 4.3 and the reader should note that for the measurements reported in this chapter the Picoprobe setup was utilised. The resonant properties of the sample can be seen in Figure 5.5, where the S_{12} profiles at a range of applied fields are shown along with 2D maps of the resonant fields as a function of applied field and frequency provided by the VNA source. It is seen that an AM resonance is excited across the field range, as expected, which was fitted using equation 3.30. From use of equation 3.37, the Gilbert damping parameter was extracted as (0.01 ± 0.001). This compares well with literature expectations [250].

Due to presence of the IP uniaxial anisotropy, it is also of interest to study the impact of IP rotation with respect to the applied field upon the dynamics of the CoFeB film. This involved observing the peak amplitude and linewidth of the resonant spectra in cases where the external magnetic field was applied along the EA and HA of the uniaxial anisotropy. The rotation was carried out by re-positioning the sample on the waveguide, with respect to the marked EA direction. The impacts of this investigation upon the resonant dynamics is shown in Figure 5.6.

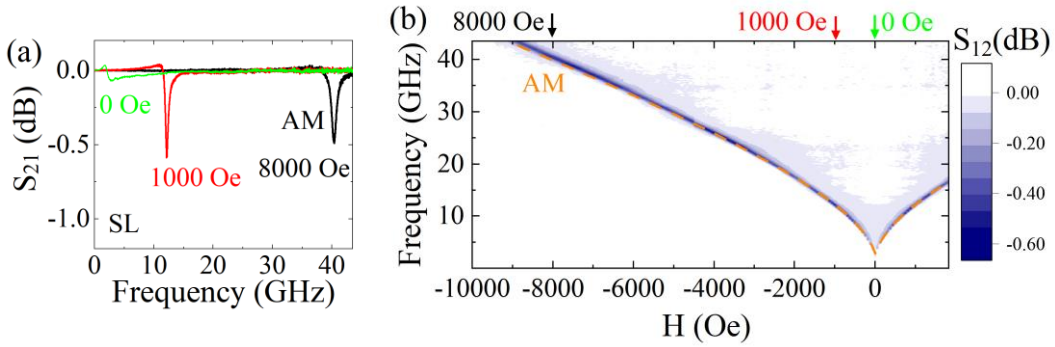

Figure 5.5: The resonant dynamics of a single layer CoFeB thin film, referred to as SL in main text. a) S_{12} absorption profiles for different applied fields b) 2D maps of the resonant spectra and modelled behaviour of the AM which, as expected, is the only mode excited.

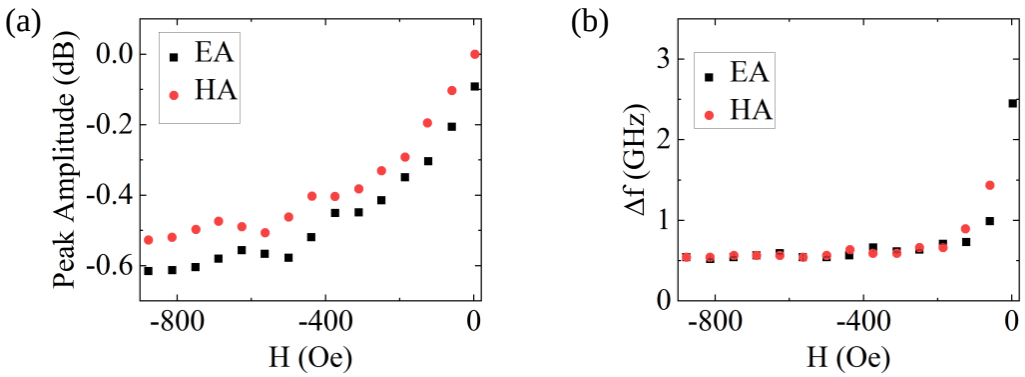

Figure 5.6: Impacts of the IP uniaxial anisotropy on the resonant dynamics of a single layer CoFeB film, referred to as SL in main text. In these cases, the external field is applied in-plane along the EA or the HA. The impact of effect of negative field only is shown, with the effect replicated in positive field. a) The peak amplitude of the resonance with applied field. b) The variation of the linewidth Δf with applied external field. The HA value at 0 Oe is not shown as in this configuration there is no measured resonance. The error bars are within the symbols for some data.

The resonant frequency was found to be invariant to the IP rotation. Due to the focus of this chapter on the SAF OM dynamics which are only realised at low fields and the comparatively small value of the anisotropy field we consider only a field range up to 900 Oe (in magnitude). From Figure 5.6(a), it can be seen that the magnitude of the peak amplitude of the resonance decreases slightly when the applied field is directed along the HA as opposed to the EA. This effect is most stark at zero applied field, as expected, where no resonance signal is exhibited when the applied external

field is directed along the HA. This can easily be understood, as outlined in section 3.2, as the perturbation field $\mathbf{h}_{rf}$ must be applied perpendicular to the direction of magnetisation of the sample for ferromagnetic resonance to occur. Therefore, when the sample HA is aligned along the applied field direction, by definition the EA is parallel to the direction of $\mathbf{h}_{rf}$. Thus, in the absence of a biasing magnetic field capable of realigning the magnetisation perpendicular to $\mathbf{h}_{rf}$, ferromagnetic resonance cannot be achieved and no signal will be measured. It is also clear from Figure 5.6(b) that the linewidth is largely invariant to the angle of applied field, excepting the zero applied field case. Furthermore, in both cases the linewidth increases at low field, consistent with literature reports [224].

Ru Layer Characterisation

The layer structure of the fabricated trilayer series was determined using XRR. The deposition parameters of the stacks are provided in section 5.1.1, and it is restated for clarity that t_{Ru} was varied between 0 nm to 3 nm. The properties of the Ru layer were of particular interest due its central importance to the interlayer exchange coupling achievable in the trilayers. Figure 5.7 presents the variation of t_{Ru} and the corresponding roughness of the Ru layer (σ_{Ru}) with Ru layer deposition time. It can be seen that two distinct growth regimes are observed as Ru layer thickness increases. These data support a hypothesis of an initial island growth stage which subsequently coalesces to form a continuous Ru film at $\approx$1 nm thickness. These findings concur with that reported by Li et al. for a similar material system [258]. The roughness of the Ru layer decreases with deposition time as expected from this growth model. The average roughness in the island growth regime is 1.1 nm and in the continuous regime it is 0.6 nm.

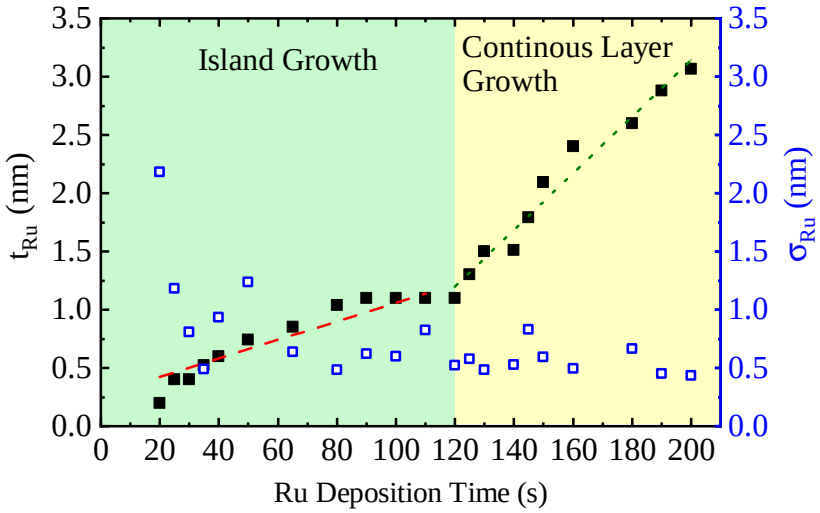

Figure 5.7: The variation of t_{Ru} and associated σ_{Ru} of the Ru layer as derived from XRR for a range of deposition times. The dashed lines are a guide to the eye.

5.2 Synthetic Antiferromagnets

In this section, the properties of samples with a t_{Ru} which supports an AF interlayer exchange coupling are investigated. As can be seen in the given spectra (Figure 5.8), a number of high frequency zero field optic modes were observed as t_{Ru} was varied. This data was produced from fitting the zero field S_{12} measurements obtained using the VNA-FMR. The exhibited zero field resonant frequencies of the sample series range from (2.8 ± 0.1) GHz for the SL case to (21.13 ± 0.01) GHz, the highest frequency optic mode observed in the studied sample range. Notably this is the highest zero field optic mode observed in a SAF to date [51], approximately twice that of the previous record at 11.32 GHz [48]. The importance of high frequency resonances at zero applied field, as explained in Chapter 1, arises from the need to remove the requirement of large magnetic fields for fast operational speed to allow high density, energy efficient and low cost next generation devices.

Furthermore, the various J_{IEC} exhibited by the samples as a function of t_{Ru} were explored and is presented in Figure 5.9. This parameter was investigated through use of equation 2.46 restated here as equation 5.3 for clarity

$$J_{IEC} = M_S H_{Sat} \frac{t_x t_y}{t_x + t_y}. \tag{5.3}$$

This method is only a valid assessment of the strength of the AF coupling and cannot

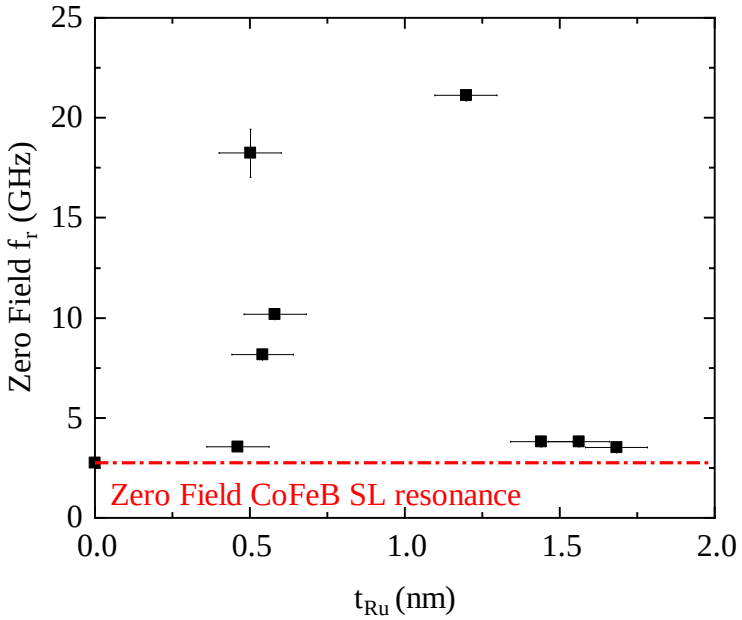

Figure 5.8: Zero field optic mode resonant frequencies (f_r) achieved in synthetic antiferromagnets with different Ru layer thickness t_{Ru}. The dashed red line represents the zero field f_r achieved in the case of a single layer CoFeB thin film, referred to as SL in main text. The frequency error bars are within the marker size for some data.

be used to determine the strength of FM coupling, as it considers only the variation of the saturating field which does not alter to a great extent in the case of FM coupling.

As expected, the evolution of J_{IEC} with t_{Ru} mirrors the zero field optic mode frequencies presented in Figure 5.8. Furthermore, it can be seen that the first and second AF peaks of RKKY interaction observed at t_{Ru}= 0.6 nm (Ru deposition time 30 s) and t_{Ru}= 1.1 nm (Ru deposition time 120 s). Contrary to expectations, where the RKKY interaction is anticipated to be strongest at the first AF coupling peak [41], these data show that J_{IEC} is only slightly reduced at the second AF coupling peak. This is ascribed to the smoother Ru interface, as shown in Figure 5.7, possessed by the sample at the second RKKY coupling peak. This finding suggests that improvements in film growth could further enhance AF coupling strength. Moreover, the measured oscillation period shown in Figure 5.9 compares well with literature expectations [259], where the theoretical period is calculated to be ≈ 0.5 nm using equation 2.42 and the experimentally determined value is $\Lambda \approx 0.7$ nm. The discrepancies in these values is most likely a result of the interfacial roughness which can have the effect of broadening the interlayer coupling peaks along with introducing an asymmetry [45].

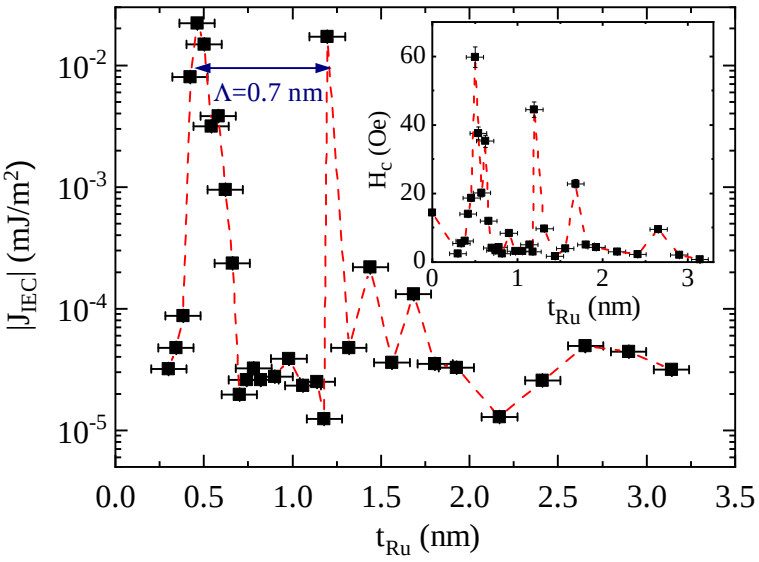

Figure 5.9: The magnitude of J_{IEC} of the trilayers with varying thicknesses of Ru t_{Ru} acting as the NM spacer layer. The experimentally measured wavelength Λ of the RKKY interaction is shown. Inset: Evolution of H_c of the trilayers with varying t_{Ru}.

The variation of H_c, a concept of introduced in section 2.6. with t_{Ru} is plotted in the inset of Figure 5.9 shows that the AF coupling is correlated with an variations in H_c. This behaviour is readily understood as AF coupling provides an additional energy term (J_{IEC}) which must be overcome to align layer magnetisation of the structure with an applied magnetic field.

In the following, a discussion of the samples displaying maximum AF coupling on the first and second AF peaks is available. Specifically, as aforementioned, this was found in the case of Ta(2 nm)/$Co_{0.2}Fe_{0.6}B_{0.2}$ (5 nm)/Ru(0.6 nm)/$Co_{0.2}Fe_{0.6}B_{0.2}$(5 nm)/Pt(4 nm) and Ta(2 nm)/$Co_{0.2}Fe_{0.6}B_{0.2}$ (5 nm)/Ru(1.1 nm)/$Co_{0.2}Fe_{0.6}B_{0.2}$(5 nm)/Pd(4 nm), referred to as SAF1 and SAF2 in the following respectively. As stated earlier, different capping layers are used due to availability in the sputtering system at the time of fabrication and do not impact the presented measurements.

5.2.1 Structural Characterisation

The structural analyses provided by XRR specific to SAF1 and SAF2 are shown in Figure 5.10. For comparison, the XRR analysis of the SL is available in Figure 5.3. From Figures 5.10(c-d), it can be seen that the values of the SLDs of the constituent

layers of the SAFs are in agreement with that determined from XRR analysis of the SL case. However, there is a clear evolution in the SLD profile derived for SAF1 and SAF2. Specifically, it is clear that the Ru layer is continuous in the case of SAF2 with the presence of a noticeable change of SLD compared to the adjacent CoFeB layers in addition to a linear gradient presented at the transition between the layers. Furthermore, the SLD of the two CoFeB layers present in SAF2 are similar. In the case of SAF1, however, the SLD does not change for the Ru layer compared to the underlying CoFeB layer and the CoFeB layer grown on the Ru layer possesses a significantly decreased SLD, roughly half than that of the lower CoFeB layer. This is postulated to be due to the island growth nature of the Ru layer in SAF1, and these differences between SAF1 and SAF2 are in accordance with the two regimes of Ru growth postulated in section 5.1.2 and evidenced in Figure 5.7. The impact of this roughness, specifically the linewidth and peak amplitude on the resonant dynamics of SAF1 and SAF2, is discussed in section 5.6. The reader should note that the slight differences in Ta layer thickness shown in Figure 5.10(c-d) is not expected to have impacted the findings due to this material only acting as a seed layer to promote adhesion of the CoFeB to the Si/SiO_2 substrate.

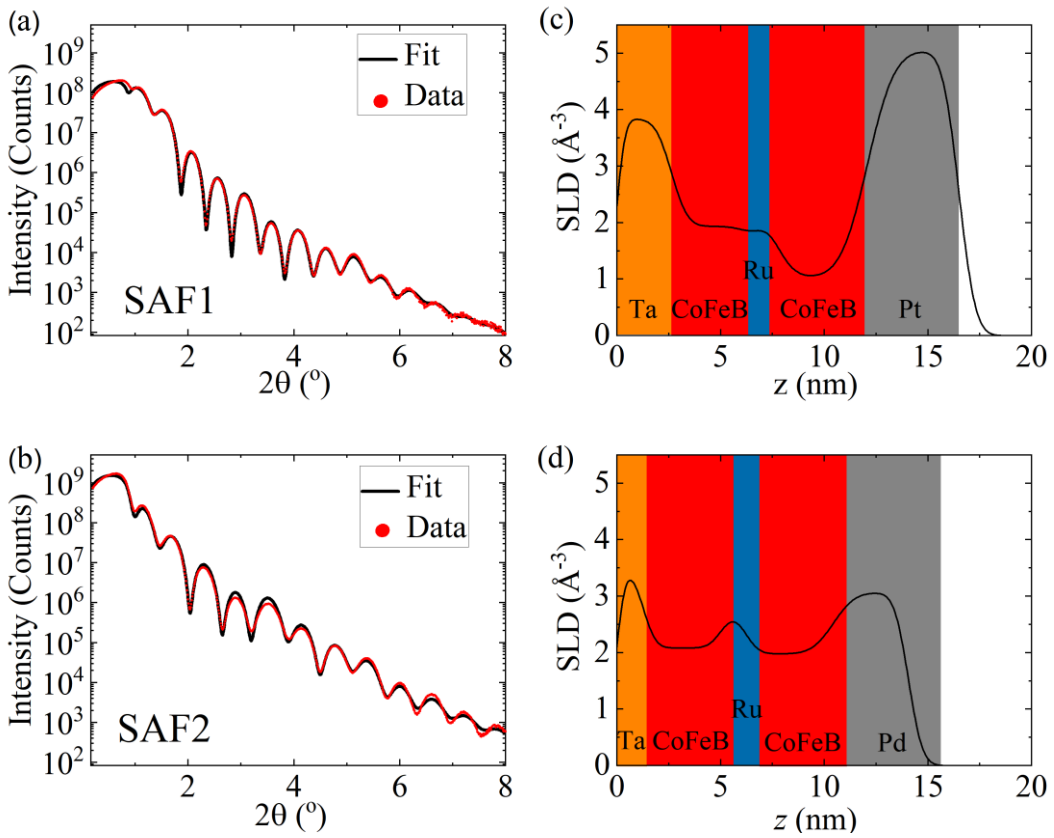

Figure 5.10: Structural characterisation of the SAF thin films using XRR for Ru layer thickness t_{Ru} (a) t_{Ru} = 0.6 nm (SAF1) (b) t_{Ru} = 1.1 nm (SAF2). (c-d) Corresponding SLD plots as a function of distance from the substrate z as derived from fitting the XRR measurement to the structure shown in Figure 5.2. The FOM_{Log} of the displayed fits were of order $\times 10^{-2}$.

5.2.2 Static Properties

The static magnetic properties of the SAF samples were investigated using IP VSM measurements at room temperature. The IP M-H hysteresis loops for SAF1 and SAF2 samples are presented in Figure 5.11, which presents the evolving magnetic profiles of the films with increases in Ru thickness. For comparison, the M-H hysteresis loop exhibited by SL is available in Figure 5.4.

In the case of SAF1 and SAF2, the presence of an AF coupling between the FM layers has a dramatic impact on the static properties of the films compared to the SL case. In particular, in the SAF case the net magnetisation reduces as the external field is decreased from saturation until a plateau is reached where an antiparallel alignment

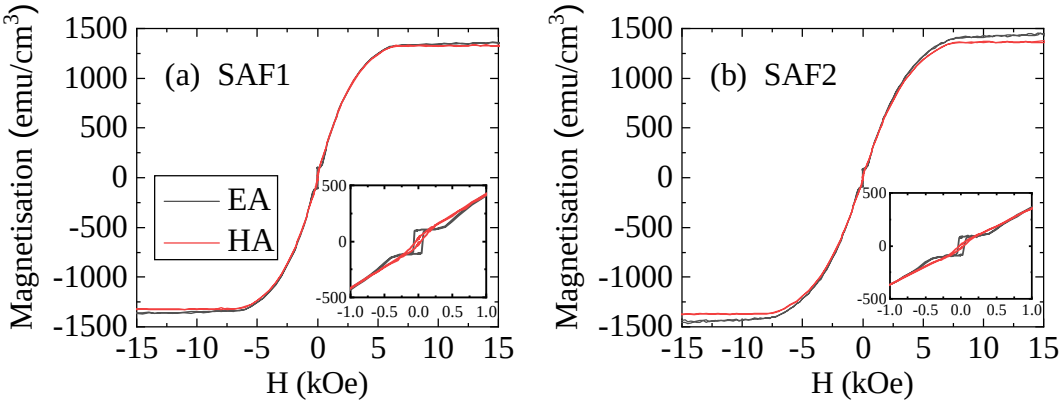

Figure 5.11: M-H hysteresis loops of the SAF thin films taken at room temperature with the external field applied along the EA or HA. The Ru layer thickness (t_{Ru}) of the SAFs are (a) t_{Ru} = 0.6 nm (SAF1) (b) t_{Ru} = 1.1 nm (SAF2). Inset: Magnified view of the hysteresis loop with the same axes labels as used on larger graphs.

of the layers is established. The finite value of the magnetisation in this anti-parallel state is due to small differences of the magnetisations of the two FM layers which is experimentally unavoidable. The saturating field for SAF1 is $\approx$ 5 kOe whilst for SAF2 it is $\approx$ 6.5 kOe. This is significantly larger than $\approx$ 2 kOe reported in previous works [48], leading to the supposition that these samples also have large J_{IEC}, and possibly the highest H_{ex} demonstrated to date [254].

5.3 Dynamic Characterisation

The dynamic properties of the samples were measured using VNA-FMR at room temperature with the static magnetic field applied along the plane of the samples. The resonance was characterised using the VNA S_{12} absorption parameter. Figure 5.12(a-b) present examples of individual spectra measured using applied magnetic fields of 0 Oe, 1 kOe and 8 kOe for each SAF sample investigated with corresponding 2D resonant spectra as a function of frequency and field shown in Figure 5.12(c-d). These applied magnetic field values were chosen to display the dynamic properties of each of the magnetic configurations achievable in these SAF structures. From measurements of the SL shown in Figure 5.5, it is seen that only the conventional AM is excited as expected, whilst in the case of SAF1 and SAF2 shown in Figure 5.12 both AM and OM are exhibited. These measurements present the range of frequencies over which both the AM and the OM occur, and exhibit a zero field OM of (18.2 $\pm$ 1.2) GHz in the

case of the first AF maxima (SAF1) and (21.13 ± 0.01) GHz at the second AF maxima (SAF2), contrasting with the zero field SL resonance of (2.8 ± 0.1) GHz which is due to the presence of a finite H_k.

It is clear that for the SAF samples there are three regions of distinct dynamic behaviour which are determined by the applied magnetic field. In the high field (region I) of SAF1 and SAF2 and at all fields in the SL case only the conventional AM resonance is excited. As the applied field is reduced (in magnitude) the magnetisation vectors undergo a reoriention from a parallel to antiparallel alignment (region II) and a dual mode is exhibited, whilst for low applied fields only the OM associated with antiparallel alignment is obtained (region III). An AM is not excited in the AF configuration due to the magnetisation vectors resonating in-phase but in opposite direction thus cancelling out any experimentally measurable response (essentially antiferromagnetically phase locked) [48] [260]. It is also shown that the OM persists at much higher fields than has been previously reported, with the OM extinguished at an applied field of ≈ 1400 Oe in the case of SAF2 as opposed to the 300 Oe field value seen in other literature reports [261].

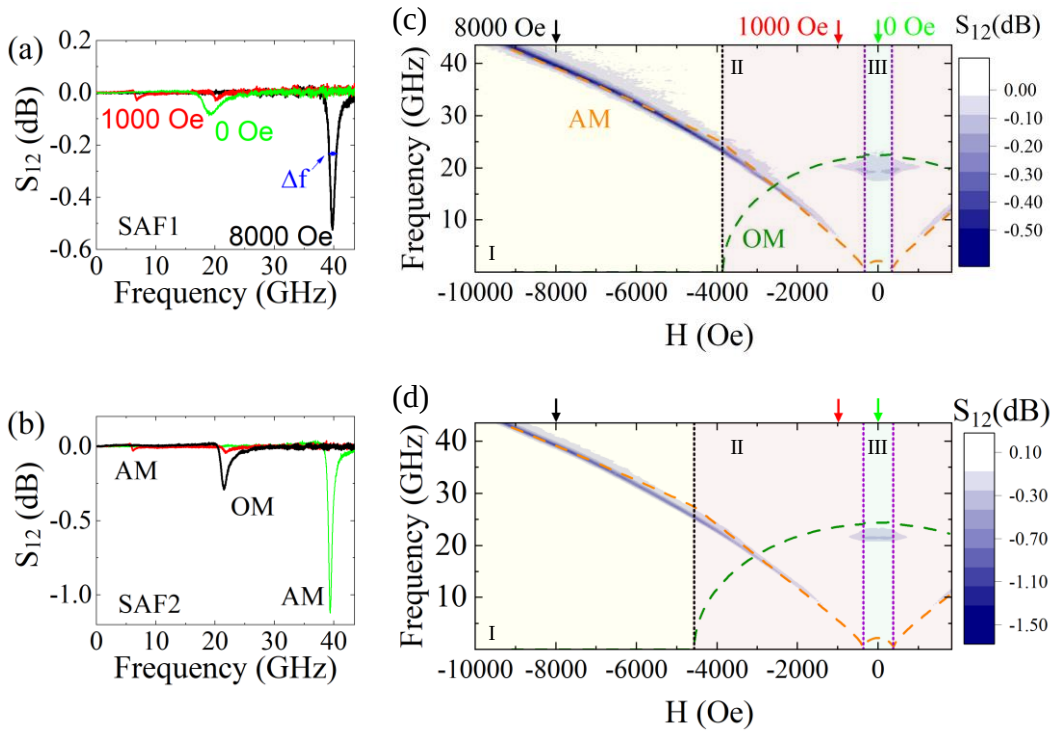

Figure 5.12: S_{12} absorption profiles for different applied fields for SAF possessing t_{Ru} (a) t_{Ru} = 0.6 nm (SAF1) (b) t_{Ru} = 1.1 nm (SAF2). The resonant linewidth Δf is highlighted. 2D maps of the resonant spectra and modelled behaviour of the AM (orange dashed line) and OM (green dashed line) are displayed for (c) SAF1 (d) SAF2. The three magnetisation regimes are highlighted: region I where the magnetisations of the layers are ferromagnetically aligned, region II where the magnetisation of each layer are undergoing a spin flop reorientation and region III where the magnetisations are in an antiferromagnetic configuration.

5.4 Analytical Modelling

To allow the study of the resonant frequencies of the SAF samples an analytical model for coupled magnetic thin film trilayers developed by Rezende et al. [172] and Wigen et al. [171] was utilised. Consistent with the dynamic behaviour displayed in these data, the model describes the resonant modes of a SAF structure undergoing a spin flop process from an AF to FM alignment. Mathematically, for increasing field, the spin flop regime (region II) where the magnetic vectors begin to reorient from antiparallel (region III) to parallel alignment commences at

$$H_{SF} = \sqrt{H_k(2H_{ex} + H_k)} \tag{5.4}$$

where H_k is the uniaxial anisotropy field and H_{ex} has been defined previously in equation 5.2. The field required to align the magnetisation of each layer in parallel is defined as

$$H_{Sat} = 2H_{ex} - H_k. \tag{5.5}$$

The angle of the magnetisation vectors during the reorientation from AF to FM alignment with increasing field is defined as

$$\sin\theta = \frac{H_{ext}}{2H_{ex} - H_k} \tag{5.6}$$

where θ is the angle of the magnetisation vectors from the EA of the IP anisotropy, which in this model is assumed to be along the direction along which H_{ext} is applied. In the case of the antiferromagnetically coupled regime ($H<H_{SF}$), the resonant frequencies of the resonant modes are given by

$$f_{\pm} = \frac{\gamma}{2\pi}\sqrt{H_{ext}^2 - H_k^2 + (H_k + H_{ex})(2H_k + 4\pi M_S) \pm [H_{ext}^2(2H_k + 4\pi M_s)} \overline{(2H_k + 4\pi M_S + 4H_{ex}) + H_{ex}^2(4\pi M_S)^2]^{\frac{1}{2}}} \tag{5.6}$$

where f_+ (f_-)is the OM (AM) resonant frequency. In the spin flop region ($H_{SF}<H_{ext}<H_{Sat}$), the resonant frequencies are modelled as

$$f_{\pm} = \frac{\gamma}{2\pi}\sqrt{[2H_{ex}^2 + H_k(H_{ex} + 4\pi M_S)]\sin^2\theta + (H_{ex} + 4\pi M_S)(H_{ex} - H_k) - H_{ex}^2} \overline{\pm H_{ex}[(2H_{ex} + 8\pi M_S + H_k)\sin^2\theta - (H_k + 4\pi M_S)]} \tag{5.7}$$

where, conversely, f_+ (f_-)is the AM (OM) resonant frequency. In the saturated regime ($H_{ext}>H_{Sat}$), the acoustic mode is described by equation 3.30 with an OM resonance having the form

$$f_r^o = \frac{\gamma}{2\pi}\sqrt{(H_{ext} + H_k - 2H_{ex})(H_{ext} + H_k - 2H_{ex} + 4\pi M_S)}. \tag{5.8}$$

As shown in Figure 5.12, this analytical model successfully reproduces the major features of the experimentally measured resonances; with parameter optimisation performed using a least squares fitting procedure between the measured and modelled AM present in the saturated and spin flop regime. The parameters obtained from the model are presented in Table 5.4. The values for H_k and H_{ex} can be extracted by this approach, a notable feat given the similar effects that H_{ex} and H_k can have on static

measurements and OM frequencies meaning that these parameters are typically difficult to deconvolute.

	Magnetic Parameters				
Sample	g	M_S (emu/cm^3)	H_k (Oe)	FMR: H_{ex} (Oe)	VSM: H_{ex} (Oe)
SL	2.03	1300	58	-	-
SAF1	2	1300	30	1950	1980
SAF2	2	1300	30	2300	2580

Table 5.4: Parameters extracted from fitting the FMR data to the analytical model put forth by Rezende et al. [172]. The effective coupling from VSM measurement was obtained from use of equations 5.2 and 5.3.

However, the modelled OM frequency is greater than that measured for both SAF1 and SAF2, specifically 22.4 GHz and 24.4 GHz respectively. The model also does not capture the behaviour of the OM throughout the spin flop phase (region II) with a field insensitive resonance with diminishing intensity observed experimentally. The discrepancies between the experimental measurements could be due to the presence of additional contributions in the spin flop and antiparallel regimes that are unaccounted for in the model. These include effects such as the role of lateral spin transport due to local variations in the interfaces present within the system and spin pumping [262, 263].

The fitted FMR data shows that two characteristics are needed to achieve enhanced OM resonant frequencies: namely an IP uniaxial anisotropy and RKKY coupling between the two FM layers. The effective interlayer coupling H_{ex} extracted from modelling the FMR data are in good agreement than those obtained from VSM measurement and among the highest seen to date [48]. This supports the analytical extraction of H_{ex} from the static and dynamic measurements. The closer agreement between these two values for SAF1 compared with SAF2 could possibly be due to dynamical effects that may influence higher frequency dynamic behaviour to a greater degree, such as spin transport related phenomena. The model also predicts the presence of a small IP uniaxial anisotropy, which has been experimentally observed from rotational VSM measurements, as shown in Figure 5.4. The model of the AM for SAF1 and SAF2 indicates that H_k is approximately half the value of that was found for the SL. Analysis of the g-factor shows that a value of 2.03 provides a better fit to the SL dynamics whereas a value of 2.00, the lower boundary, is optimum in the case of the SAF systems. Further impacts of the effects of this uniaxial anisotropy on resonant dynamics of the SAFs are outlined in section 5.6.

5.5 Gilbert Damping

The Gilbert damping parameter, α, of the SAF samples have also been extracted using the Δf, as shown in Figure 5.12, and equation 3.37. The α of SAF1 was found to be (0.011 ± 0.001) and for SAF2 it was (0.008 ± 0.001). This parameter was evaluated only for the AM, as the OM occurs at roughly the same linewidth for the narrow range of fields where it is observed. Hence, the determination of the damping from the OM mode using this method is not possible. It is interesting that the α of SAF1 is greater than that of SAF2, a finding possibly related to the island grown nature of the Ru layer in the prior case. More detailed discussions regarding this finding are available in section 5.6.

5.6 Impact of Uniaxial Anisotropy on Optic Mode Dynamics

The effects of the uniaxial anisotropy on the resonant dynamics of the OM, specifically the peak amplitude and linewidth, exhibited by SAF1 and SAF2 samples has also been explored. Similarly to the SL case, the resonant frequencies displayed were found to be invariant to the IP rotation. For this investigation, similarly to the examination of SL presented in Figure 5.6, the IP externally applied static magnetic field was applied along the EA and HA of the SAF samples. In Figure 5.13, the effects of this uniaxial anisotropy on the peak amplitude and Δf of the OM resonances of SAF1 and SAF2 are presented.

It is evidenced that there is a significantly greater impact of IP rotation on the resonant dynamics in the SAF cases than the SL case. Interestingly, it is demonstrated that the dependence of both the peak amplitude and linewidth on the IP rotation increases as the applied field reduces. The behaviour of the peak amplitudes of the resonances of the SAFs is consistent with that exhibited by SL with the peak amplitude reducing (in magnitude) when the applied field is directed along the HA as compared to the EA. Furthermore, the variation of the peak amplitude in each SAF case is broadly consistent in the two applied field directions.

From an examination of Figure 5.13(c-d) it is seen that the linewidth of SAF1 is much more dependent on the direction of the external field and its magnitude than SAF2. The linewidths of SAF1 and SAF2 can also be compared from a consideration of the external field directed along the EA only. It is clear that whilst in the spin

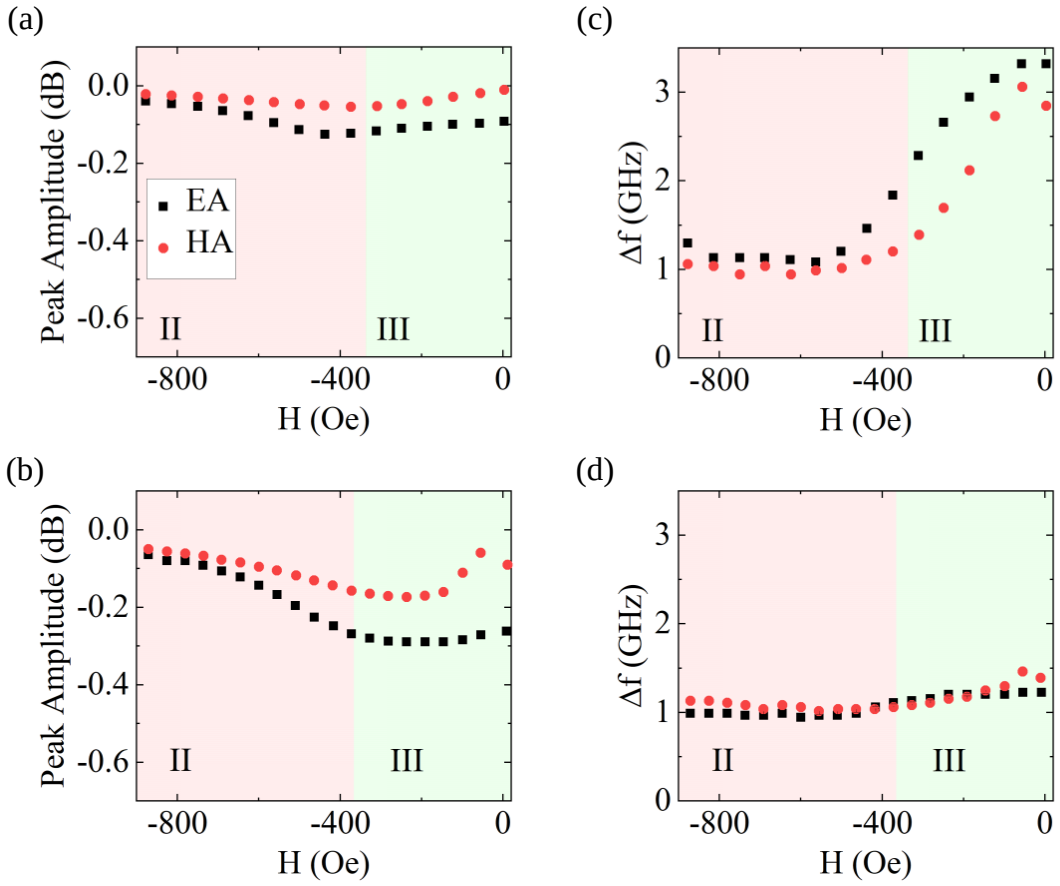

Figure 5.13: Impacts of the IP uniaxial anisotropy on the resonant dynamics of the SAF films with Ru layer thickness 0.6 nm (SAF1) and 1.1 nm (SAF2). In these cases, the external field is applied IP along the EA or the HA. The variation of the peak amplitude with applied external field H of a) SAF1 and b) SAF2. (c-d) The corresponding variation of the linewidth Δf with applied external field. The two magnetization regimes where an optic is present are highlighted: region III where the magnetisations of the layers are antiferromagnetically aligned, and region II where the magnetisation of each layer is undergoing a spin-flop reorientation. The error bars are within the symbols for some data.

flop phase (region II) the linewidths of the optic modes of SAF1 and SAF2 are similar as the layer magnetisations of the SAFs enter the antiferromagnetically aligned regime (region III) the OM exhibited by SAF1 has a much greater linewidth than that presented by SAF2. It is of particular interest that this should be the case when the interlayer coupling is the dominant energy of the system, due to the applied field and its associated Zeeman energy being low in this region. It is likely that the difference in resonant linewidth exhibited by SAF1 and SAF2 is correlated to the observed change

in Ru growth mode and layer roughness from SAF1 to SAF2, as demonstrated by Figure 5.7. However, to verify this hypothesis more detailed simulations than the simple analytical models reported here are necessary.

5.7 Chapter Summary

In summary, in this chapter the fabrication and characterisation of CoFeB/Ru/CoFeB multilayers along with a characterisation of the constituent layers is reported. Importantly, it has been shown that the CoFeB material has a natural uniaxial anisotropy, which impacts its static and dynamic magnetic response. It has been shown, as expected, that the OM frequencies supported by SAFs varies with Ru layer thickness. This presents one way to fabricate advanced tailored materials capable of supporting a range of zero field high frequency dynamics. Furthermore, this work has demonstrated the highest OM resonant frequencies in SAFs at zero applied magnetic field reported to date [51]. The measured resonant frequencies at zero field were (18.2 ± 1.2) GHz and (21.13 ± 0.01) GHz for samples on the first and second AF peaks of the RKKY interaction respectively. This is approximately an order of magnitude increase compared to the resonance frequency of a single CoFeB layer (2.8 ± 0.1) GHz. Furthermore, it has been shown that smoother CoFeB/Ru interfaces offers a route to enhancement of frequencies attainable from SAF structures. Indeed, the correlation of structural, static and dynamic characterisations that has been presented highlights the exploitation of the second, and possibly also higher order, AF RKKY peaks to enhance the zero field resonant frequency of synthetic antiferromagnetic systems into the 10s GHz range.

An analytical model can successfully reproduce all the major features of the dynamic response of the SAF samples on the first and second AF RKKY peaks. The parameters obtained from the model are in good agreement with the data though there are small differences between the model and static (VSM) measurements. Furthermore, there are slight changes in the modelled g-factors, with SAF1 and SAF2 displaying a g-factor of 2 in contrast of the 2.03 displayed by SL. This reduction could be attributed to the intermixing of FM layer with the NM Ru layer or the breaking of inversion symmetry [264]. The importance of a uniaxial anisotropy to the OM dynamics has also been explored, with the impact of IP rotation on the resonant dynamics detailed.

Chapter 6

Synthetic Ferromagnetic Dynamics

This chapter details an investigation of the dynamical properties of Synthetic Ferromagnets (SFMs). These structures possess the same
Ferromagnetic (FM)/Nonmagnetic (NM)/FM structure as the widely studied Synthetic Antiferromagnets (SAFs), but describe the case where the NM layer thickness promotes a parallel alignment of the layer magnetisations. By definition in this case the interlayer exchange coupling strength is positive ($J_{\mathrm{IEC}}>0$). The studied films are of the same series as that described in Chapter 5, specifically the cases where FM coupling is observed with an Ru deposition time of 90 s, 100 s and 110 s, with a discussion of the fabrication and characterisation processes performed available in section 5.1. Furthermore, the magnetic properties of a single CoFeB layer (SL) are also reported in Chapter 5. The study presented in this chapter has recently been published in Physical Review B [52].

Despite having been widely utilised in quasi-static spintronic devices [44, 265, 266], key aspects of the resonant dynamics of SFMs remain unexplored. It has been reported that in the case where there is the presence of a weak FM interlayer exchange coupling along with a difference in layer magnetisation (ΔM) a double resonance is exhibited [40, 44, 265]. This double resonance consists of a lower frequency Acoustic Mode (AM) and a higher frequency Optic Mode (OM), with a schematic of the resonant dynamics of each case presented in Figure 6.1. The AM and OM labelling refers to the phase relationship between the two precessing magnetic layers where for the AM the layer magnetisation precess in-phase (phase difference $\Delta\phi = 0^{\mathrm{o}}$) and for the OM the layer magnetisation precess out-of-phase ($\Delta\phi = 180^{\mathrm{o}}$) [40]. A thorough description of the dynamics of multilayers subject to interlayer coupling is available in section 3.5.

There remains a severe deficiency in the understanding of SFM dynamics beyond these observations, however. Specifically, the effect of varying (i) the J_{IEC} and ii) the ΔM on the two resonant modes of the SFM system has not been investigated systematically. Moreover, the impacts of these parameters on the phase difference of the two resonances remains to be explored. It has been previously reported that for the

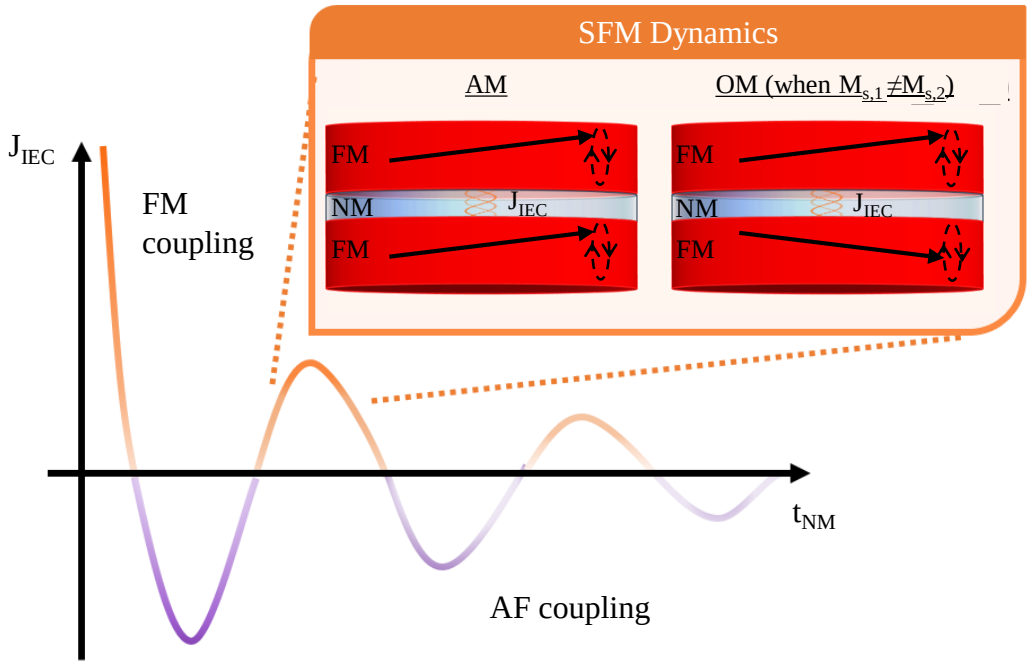

Figure 6.1: The evolution of J_{IEC} for a FM/NM/FM trilayer with NM layer thickness (t_{NM}). J_{IEC} oscillates between promoting a FM or an AF layer magnetisation alignment. Usually, the first FM maxima occurs close to 1 nm with the magnetic layers decoupled at approximately 3 nm. The inset shows the resonant dynamics supported by a SFM. An OM is seen in addition to the AM only in cases where there is a difference in the layer magnetisation of the FM layers.

manifestation of an OM in a SFM to occur the constituent FM layers must possess significantly different magnetic properties [44], thus hampering the range of experiments that can be performed. This has been a significant impediment to the study of SFM dynamics, especially in the case where the desired system must possess similar FM layers. This is a key technological requirement for a range of devices such as the free layer in Spin Orbit Torque (SOT-) or STT-MRAM [44, 267].

Here, the dynamic properties of Ta/$Co_{0.2}Fe_{0.6}B_{0.2}$/Ru/$Co_{0.2}Fe_{0.6}B_{0.2}$/Pd stacks exhibiting magnetic properties consistent with interlayer exchange coupling on the first FM RKKY peak are reported. The physics of the SFM resonances are elaborated upon with the interlayer coupling strength and the magnetisation difference of the ferromagnetic layers extracted. Additionally, the developed methodology permits the phase relations between the resonant modes of the individual layers to be accurately quantified. This work was aided by a collaboration with Mr Y. Li, who contributed significantly

to the simulation aspects of the investigation.

6.1 Structural Characterisation

The structure of the SFM samples was examined using X-ray Reflectivity (XRR) as outlined in section 4.2.1. The reader is referred to section 5.1 for further characterisation of the constituent layers of the stacks. SFMs exhibiting magnetic properties consistent with a positive J_{IEC} on the first FM coupling peak, that is a FM hysteresis behaviour, a double resonance exhibited in dynamic measurements and a Ru layer thickness between that of the samples displaying the first and second instances of AF coupling as discussed in Chapter 5, were found in the case of where Ru layer was deposited for 90 s, 100 s and 110 s and are referred to as SFM1, SFM2 and SFM3 respectively. As there is no discernible difference in the Ru layer thickness of these stacks from XRR measurement, the Ru layer thicknesses was instead determined from a calibration of thickness and Ru layer deposition time, as presented in Figure 5.7. From this analysis, SAF1, SAF2 and SAF3 were found to have t_{Ru}= 1.03 nm, 1.07 nm and 1.10 nm respectively. The XRR measurements of the SFM samples and the corresponding structural SLDs can be seen in Figure 6.2. From the presented SLD plots (Figures 6.2(d-f)) it can be seen that the structure of the SFM samples are consistent with similar SLD profiles obtained. Importantly, well defined layers are evidenced. From comparisons with the XRR measurements of SL (Figure 5.3(b)) and SAF cases (Figure 5.10(c-d)) it can be seen similar SLD values for each constituent layer has been derived, as expected.

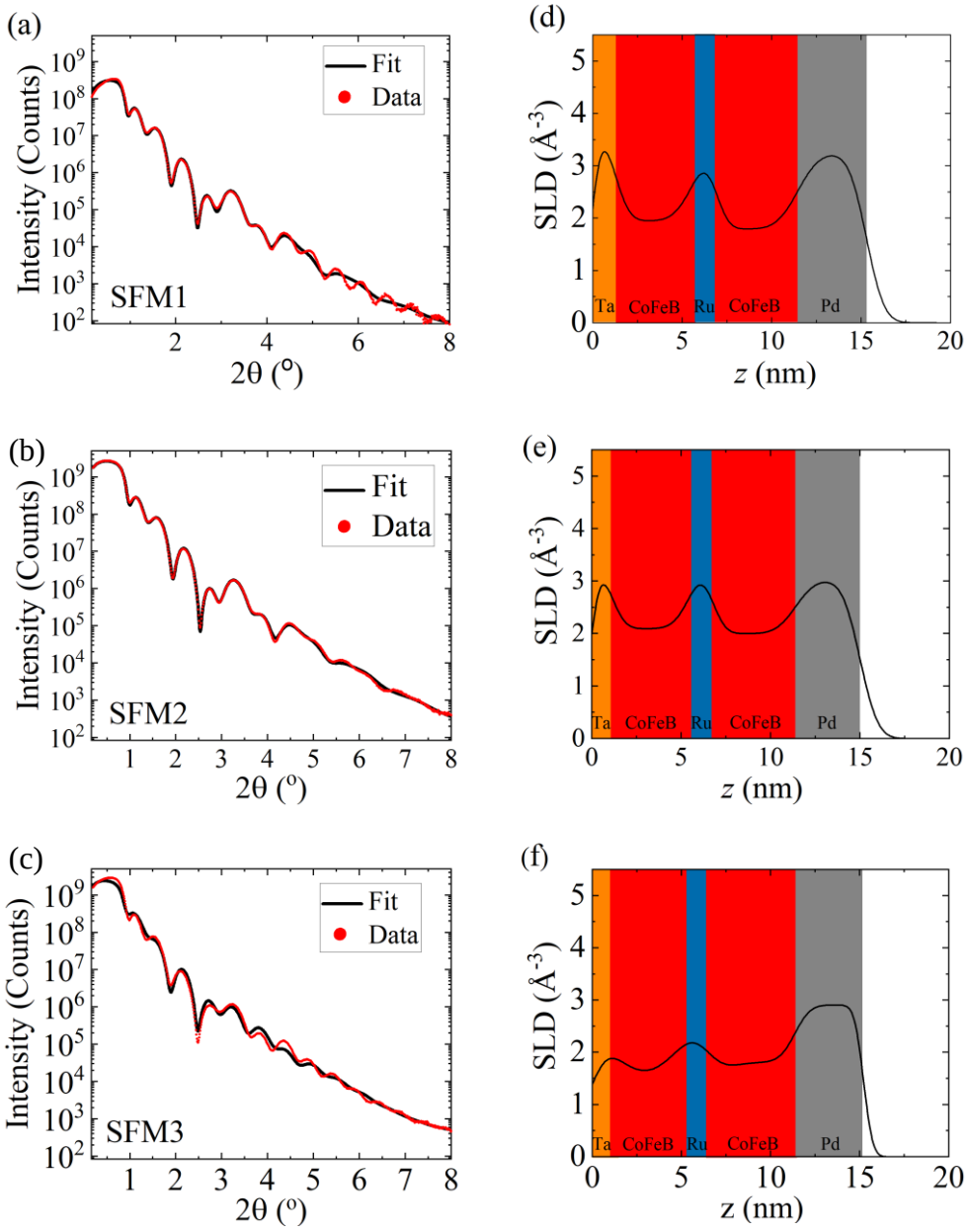

Figure 6.2: Structural characterisation of the SFM samples using XRR for a) t_{Ru}= 1.03 nm (SFM1) b) t_{Ru}=1.07 nm (SFM2) and c) t_{Ru}=1.10 nm (SFM3). Corresponding SLD plots as a function of distance from the substrate z, as derived from fitting the XRR measurement to the structure shown in Figure 5.2 for d) SFM1 e) SFM2 f) SFM3. The FOM_{Log} of the fits is of order 10^{-2} in all cases.

6.2 Static Characterisation of SFMs

Static magnetic measurements were performed on the samples using vector Vibrating Sample Magnetometry (VSM), as described in section 4.2.3. Figure 6.3 shows the IP hysteresis loops for the three SFM samples and two reference single layer films. Table 6.1 summarises the saturation magnetisation values obtained from measurements. The two single layer CoFeB films measured reflected both the thickness of an individual layer (5 nm) and the total SFM magnetic layer thickness (9 nm). These single layer films show a value of saturation magnetisation consistent with literature [48] and that the changes in CoFeB thickness does not affect the saturation magnetisation, as expected. These data demonstrate that the SFMs possess a reduced saturation magnetisation compared to SL, particularly in the case of SFM3. This reduction in saturation magnetisation is significant in that it provides the conditions that allow both AM and OM resonances to form. We hypothesise that the reduction in magnetisation is due to the difference in the two seed layers (Ta and Ru for each respective FM layer) where small differences in relatively thin layers are not physically unreasonable. However, further evidence is needed before a definitive conclusion can be made on this point.

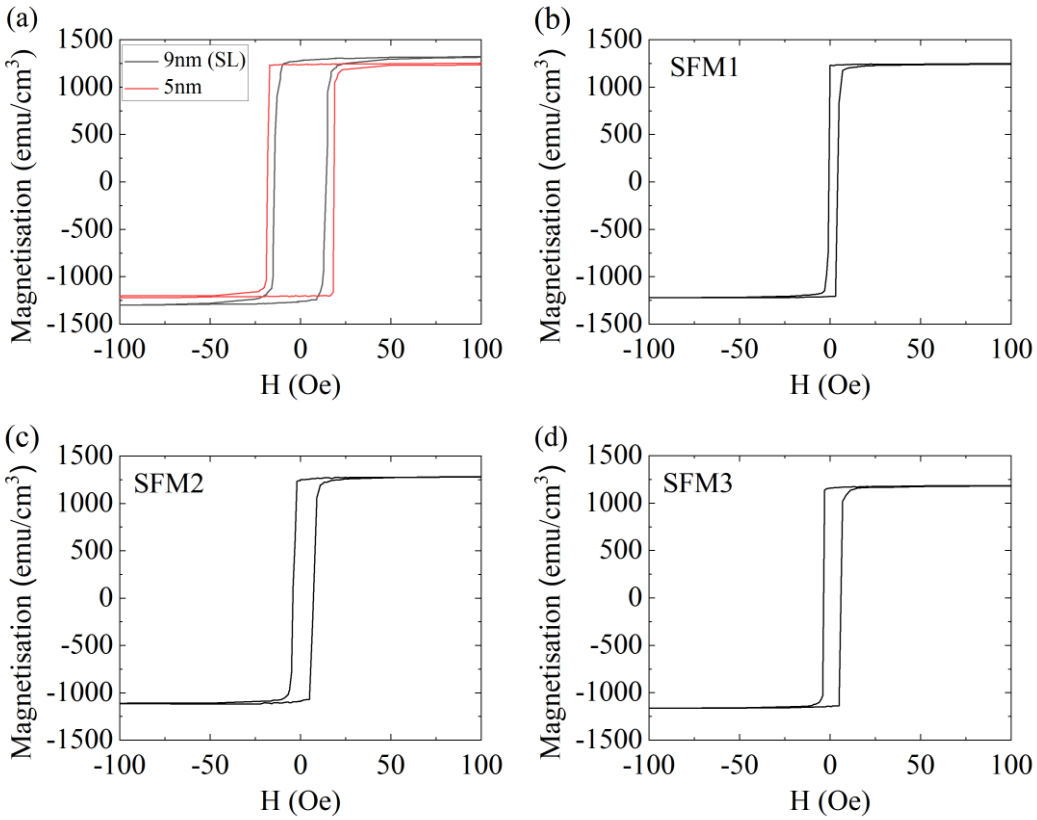

Figure 6.3: In-plane M-H hysteresis loops of the samples taken along the EA at room temperature. (a) Measurements of single layer CoFeB films with film thickness 9 nm (SL) and 5 nm. SFM thin films possessing (b) t_{Ru}=1.03 nm (SFM1) (c) t_{Ru}=1.07 nm (SFM2) (d) t_{Ru}=1.10nm (SFM3).

Sample	M_S (emu/cm^3)
SL	1320 ±70
SFM1	1240 ±60
SFM2	1230 ±60
SFM3	1180 ±60

Table 6.1: The M_S of the SL and SFM samples.

6.3 Dynamic Characterisation

The magnetisation dynamics of the samples were characterised through Vector Network Analsyer-Ferromagnetic Resonance (VNA-FMR) using the VNA S_{12} absorption parameter at room temperature. The VNA-FMR measurement procedure is described fully in section 4.3 and the reader should note that for the measurements reported in this chapter the Picoprobe setup was utilised with the external field applied IP. Figure 6.4(a-c) presents examples of individual spectra measured at externally applied magnetic fields of 1 kOe, 4 kOe and 7 kOe for the three samples investigated. In Figure 6.4(d-f) a series of S_{12} spectra are combined to create 2D maps of the resonance spectra as a function of applied field and frequency. The resonant properties of the SL are presented in Figure 5.5.

These data demonstrate that both the lower frequency AM and the higher frequency OM manifest at a range of applied fields. It is notable that the OM and AM resonances are clearly separated, especially given the near identical properties of the two magnetic layers comprising the SFMs. The data also show that the dependence of the resonant frequencies of the samples with field is consistent. For example, as the applied field is reduced (in magnitude) in all cases the OM reduces in amplitude compared to the AM. Furthermore, from a detailed examination of the resonant spectra, it can be seen that the AM and OM differ for SFM1-3 despite the only sub-atomic changes in Ru layer thickness. This demonstrates the expected sensitivity of the RKKY interaction to the Ru layer thickness and shows the high sensitivity of the measurement. This extraordinary sensitivity to Ru layer thickness is a key challenge in the fabrication of such samples, with the presented data showing that a high degree of control over the SFM structure has been accomplished. The origins of the observed increase in peak amplitude of the OM exhibited by SFM3 at higher fields is unclear, though as in the following we only consider resonant frequencies this does not impact study reported.

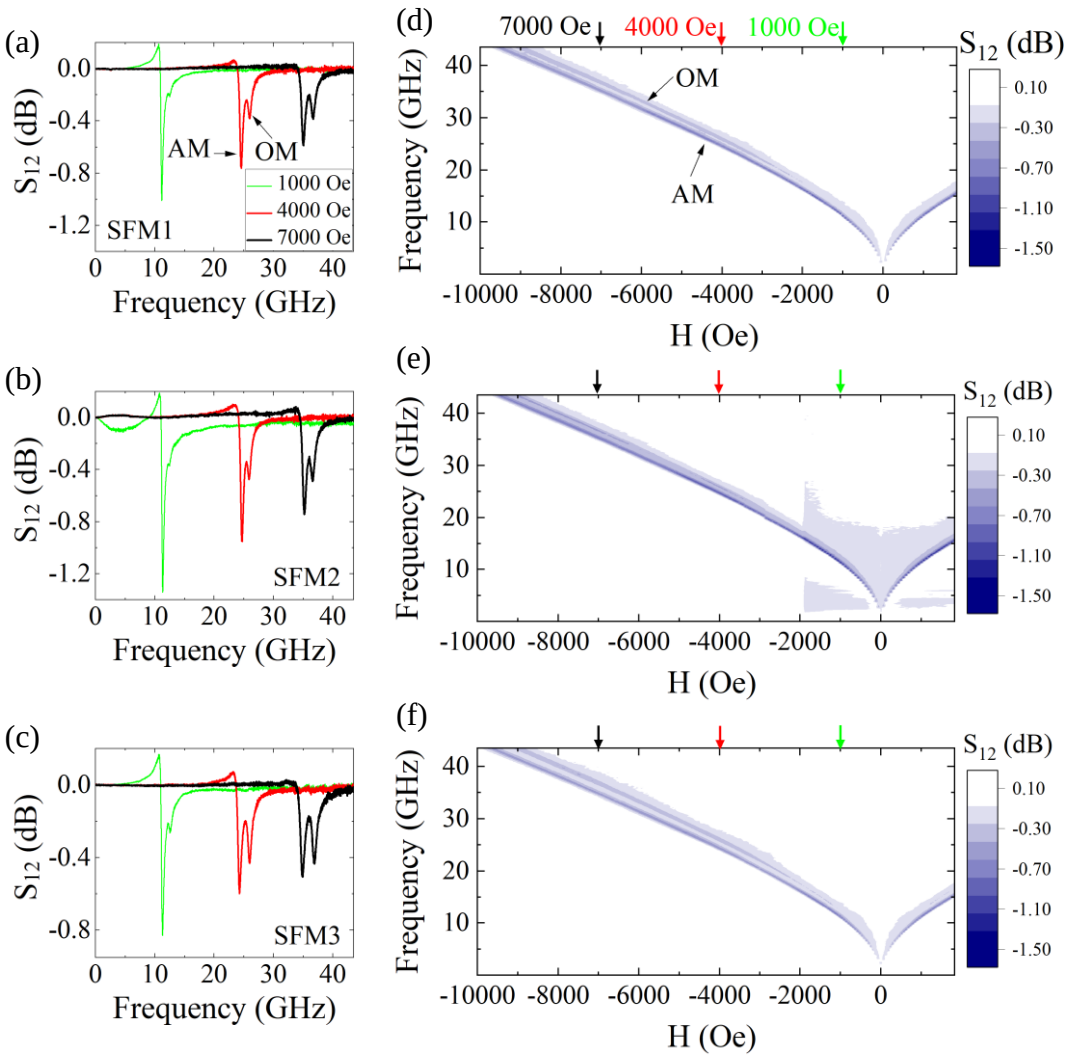

Figure 6.4: Resonant AM and OM dynamics displayed by the SFMs. S_{12} absorption profiles at varying applied field strength in the case of (a) t_{Ru}=1.03 nm (SFM1) (b) t_{Ru}=1.07 nm (SFM2) (c) t_{Ru}=1.10 nm (SFM3). (d-f) Corresponding 2D maps of the resonant spectra as a function of applied field and frequency.

6.4 Micromagnetic Simulation of SFM Resonant Dynamics

To study the effects of varying the interlayer exchange coupling and difference in the layer magnetisation on the dynamics of the SFMs, namely resonant frequencies and phases, the FM_1/NM/FM_2 structure of the samples was reproduced with a micromagnetic model as shown in Figure 6.5(a). The FM_1 and FM_2 labels represent the FM

layers grown on the Ta layer and Ru layer respectively. For this simulation part of the reported work I collaborated with a fellow PhD student, Mr Y. Li, who made a significant contribution. The method detailed is based upon a comprehensive series of simulations where the resonant frequencies and phases of the system are systematically determined as a function of the relative layer magnetisation and the interlayer exchange coupling and compared to the measured resonances of the samples.

The numerical simulations were executed using the micromagnetic modelling package Mumax^3 which is a finite-difference GPU-accelerated simulation program [239], as introduced in section 4.4. The magnetic parameters utilised in this numerical simulation were chosen to permit direct comparison with the SFM samples. The damping parameter was set to $\alpha = 0.001$, a magnitude lower than measurements presented for CoFeB discussed in section 5.1.2, to increase signal to noise ratio. It was verified that the lower damping value did not affect the output resonant frequencies or phase. The exchange constant (A_{ex}) was input as $A_{\mathrm{ex}} = 1 \times 10^{-6}$ erg/cm, close to the value reported in literature for a CoFeB alloy [251]. The saturation magnetisation of FM_1 ($M_{S,1}$) was set as $M_{S,1}$= 1300 emu/cm^3, equal to that of $Co_{0.2}Fe_{0.6}B_{0.2}$ [51]. This was further supported by Figure 6.3(a), which shows the static measurement of a 5 nm thick single layer CoFeB film. The saturation magnetisation of FM_2 ($M_{S,2}$) was investigated for a range of values between 500 emu/cm^3 and 1200 emu/cm^3, as required to generate OM dynamics, with the J_{IEC} range explored of similar magnitudes to literature reports for a CoFeB trilayer systems [44]. In order to minimise the demagnetisation effects from the physical edge periodic boundary conditions were applied in the plane. The overall system is discretised into 1 nm x 1 nm x 0.5 nm cuboid cells with the dimension in the *xy*-plane set to 128 nm x 128 nm. The ringdown method, as introduced in section 4.4.1, was used to obtain the free inductive decay of the magnetisation which was then Fourier transformed to obtain the ferromagnetic resonance signal. The phase information of the system is determined by applying a time-dependent sinusoidal excitation h_{rf}(t) with frequency f: $h_{\mathrm{rf}}(t) = \tilde{h}\sin(2\pi ft)$ where $\tilde{h}$ is the amplitude of the excitation, and t is time. The time-resolved magnetisation in each FM layer was recorded. Subsequently, a fast Fourier Transform (FFT), described in section 4.4.1, is used to obtain the amplitude spectrum of the averaged magnetisation, and the characteristic frequencies then extracted from the measured time-domain. Examples of the Mumax^3 simulation scripts used within this investigation are presented in Appendix B.1.

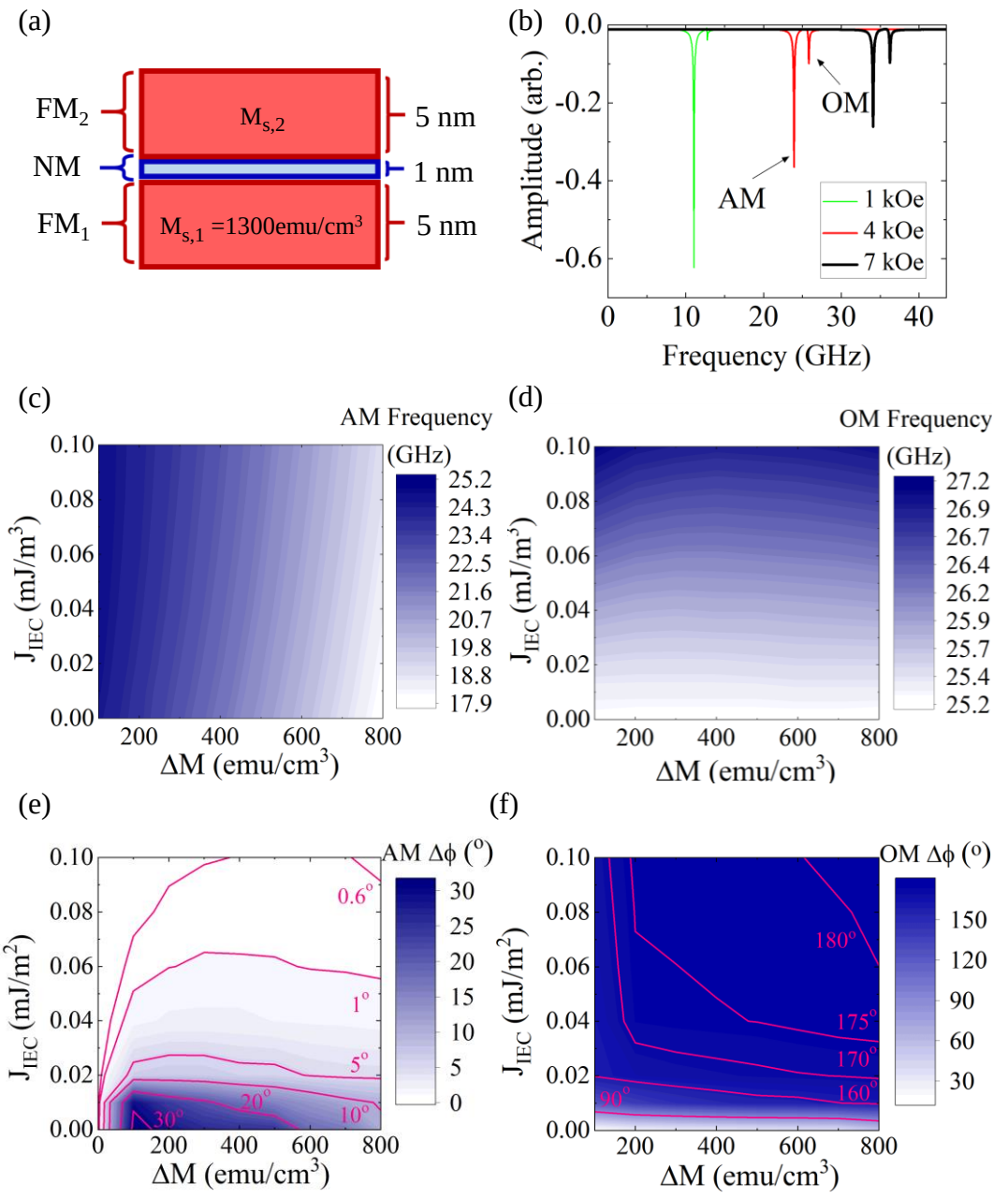

Figure 6.5: Simulated dynamics of the SFM films. (a) The SFM structure, consisting of a FM_1/NM/FM_2 trilayer. The layer magnetisation of FM_1 ($M_{S,1}$) is fixed whilst the layer magnetisation of FM2 ($M_{S,2}$) is varied. (b) An example of a simulated absorption spectrum of a SFM where $\Delta M (= M_{S,1} - M_{S,2})$ is 100 emu/cm^3 and J_{IEC} is 0.1 mJ/m^2 at a range of different fields. (c-f) Impact of J_{IEC} and ΔM at an externally applied field of 4 kOe on the resonance frequency of the (c) AM (d) OM; and on the $\Delta\phi$ in the case of the (e) AM and (f) OM.

To treat this numerical simulation as representative of the SFM samples, it must be assumed that $M_{S,1}$ is identical to that obtained from measurement of the SL case whilst $M_{S,2}$ is reduced. This is a reasonable assumption but differences in the magnetic properties of FM_1 to the SL case may exist due to mechanisms such as interdiffusion with the Ru layer [268, 269]. From the static measurements presented in Figure 6.3 it is indicated that the the saturation magnetisation of the SFM samples are reduced compared to the SL case, especially in the case of SFM3. Furthermore, it is known that for an OM to form a difference in layer magnetisation is required [40]. This supports the modelling of a structure containing a FM layer with a reduced magnetisation. Further verification of the suitability of the simulation developed is offered by comparisons with the measured resonances. Specifically, Figure 6.5b shows that the key features of the resonance behavior exhibited by the samples can be reproduced by the simulation with i) the formation of a double resonance observed and ii) a notable diminishment of the OM intensity as the applied field is reduced (in magnitude).

From Figure 6.5(c-f), a general assessment of the impact of varying the interlayer coupling strength and difference in the layer magnetisations on SFM dynamics can be made. Strikingly, it is shown that the resonant frequencies have orthogonal dependencies on J_{IEC} and ΔM. In particular, as shown in Figure 6.5(c-d), the AM resonance is highly influenced by ΔM whilst the OM resonance is governed mainly by J_{IEC}. Indeed, the greatest reduction in the AM frequency and enhancement in OM frequency is seen in cases where there is a greater J_{IEC} and a higher ΔM respectively.

The phase behavior, the phase difference between the two resonating magnetic layers, of each mode can also be explored. In Figure 6.5(e-f) the simulations demonstrate that the phases are impacted by both J_{IEC} and ΔM which contrasts with the dependence shown by the resonant frequencies. In particular, the simulations reveal that that the conventional in-phase and out-of-phase understanding of the AM and OM respectively does not fully describe the abundance of the dynamics achievable in a SFM system where a range of $\Delta\phi$ between 0^{o} and 180^{o} can be supported. From an examination of Figure 6.5(e-f) it is instead shown that the resonances would be better understood through acoustic-like/optic-like labels. It should be noted that in all simulated cases we do not achieve a truly out-of-phase (180^{o}) OM. Furthermore, it is seen that the phase differences vary starkly from the AM/OM description in cases where the SFMs possess similar layer magnetisations and an extremely weak J_{IEC} (0 - 0.04mJ/m^2). The simulations clearly demonstrate that the OM has a significantly greater dependence on these parameters than the AM. This is especially evident in the weak coupling limit

(≈ 0.01 mJ/m^2), where $\Delta\phi$ transitions from a high phase difference ($\approx 180^o$) quasi-OM to a low phase difference ($<90^o$) acoustic-like mode.

6.5 Parameter Extraction

From comparisons of the resonant frequencies of the AM and OM as obtained from the experimental data and simulations, the J_{IEC} and ΔM corresponding to the studied SFM samples could be extracted. Specifically, this was carried out through an optimisation process where the residual of the measured and simulated AM and OM was minimised. The J_{IEC} and ΔM required to simulate the resonances of each experimentally measured SFM are presented in Figure 6.6(a) and Table 6.2.

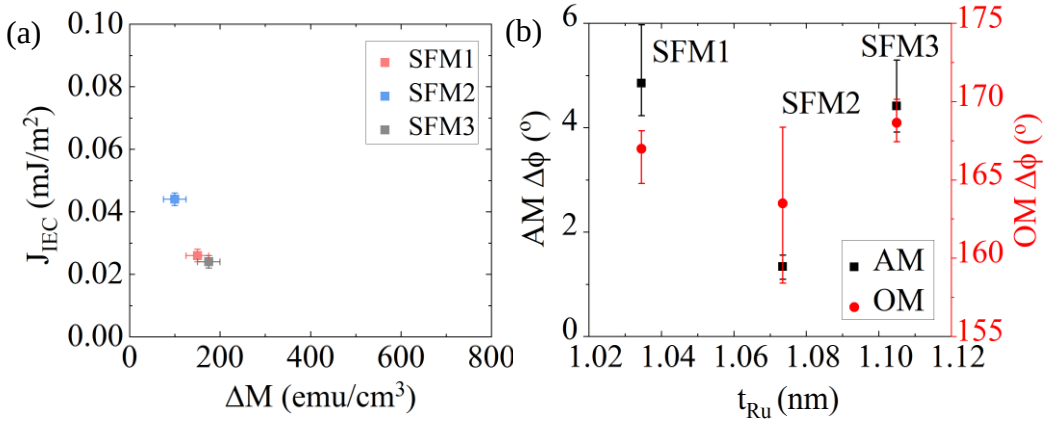

Figure 6.6: Extracted parameters of the SFMs with differing t_{Ru} labelled as i) SFM1: t_{Ru} =1.03 nm ii) SFM2: t_{Ru}=1.07 nm iii) SFM3: t_{Ru}=1.10 nm. (a) The J_{IEC} and ΔM as extracted from fitting to the measured and simulated resonances. This figure is plotted on the same scale as Figure 6.5(c-d) to permit direct comparison with the numerical simulation. (b) $\Delta\phi$ for each sample in the AM and OM case, as extracted from the numerical simulation.

Sample	t_{Ru}	ΔM (emu/cm^3)	J_{IEC} (mJ/m^2)
SFM1	1.03	150 $\pm$25	0.026 $\pm$0.002
SFM2	1.07	100 $\pm$25	0.044 $\pm$0.002
SFM3	1.10	175 $\pm$25	0.024 $\pm$0.002

Table 6.2: Parameters extracted from the numerical simulation for the studied synthetic ferromagnets.

Figure 6.6(a) demonstrates that the ΔM required to simulate the resonances of each

SFM corresponds to the reduction in saturation magnetisation measured by VSM (Figures 6.3(b-d) and Table 6.1). The fact that the saturation magnetisation for SFM3 is lower than SFM1 and SFM2 is reflected in the fact that the ΔM for this sample is greater than for the other samples. The success of this methodology is particularly noteworthy in light of the similar magnetisation the two FM layers possess. For example, the extracted ΔM values are significantly lower than that reported by McKinnon et al. [44]. The magnitudes of the extracted J_{IEC} (0.02-0.04 mJ/m^2) are similar to their reports, however. It is seen that the obtained J_{IEC} also displays a behavior with Ru layer thickness that is in accordance with that expected of the first FM coupling peak. Specifically, SFM2 exhibits the highest J_{IEC} thus indicating that it is close to the maximum of the first FM peak with SFM1 and SFM3 to either side of the this maxima. Furthermore, comparisons with Figure 5.9, show that the J_{IEC} obtained for the samples on the first FM peak is a magnitude lower than that present in samples on the first and second AF peaks.

The extracted J_{IEC} and ΔM values can be utilized to determine the phase behavior of the AM and OM mode for each SFM sample. The extracted $\Delta\phi$ for each mode as a function of t_{Ru} is presented in Figure 6.6(b). It is seen in the case of SFM2 that although a higher J_{IEC} is displayed, the $\Delta\phi$ of the OM is lower compared to that seen in SFM1 and SFM3. This is a direct result of the lower ΔM possessed by SFM2. The extraction of the phases of the resonant modes using lab-based instrumentation and simulation is a notable success of this methodology, with techniques such as XFMR [270] or X-ray reflectometry FMR [271] typically required for such measurement.

6.6 Chapter Summary

In conclusion, the experimental observation and numerical simulation of the resonant dynamics of SFMs has been demonstrated. It is notable that a well separated double resonance was observed in the studied SFM samples given the similar properties of the FM layers present in the structure. The simulations have elucidated on hitherto unexplored dependence of the supported AM and OM on the difference in magnetisation of the FM layers and the RKKY interlayer exchange coupling. It is shown that an orthogonal dependence exists, where the AM exhibits a greater dependence to the magnetisation difference whilst the OM is more sensitive to the coupling strength. Thus, by comparison of the measured resonance frequencies with simulations the interlayer exchange coupling in these structures, a property that is difficult to obtain experimentally,

can be determined.

Furthermore, using these extracted parameters, the phase behavior of the magnetic layers at each resonant mode can be determined from the numerical simulation. It is clear that the conventional acoustical and optical description of these resonant modes does not fully capture the intricacy of the dynamics exhibited by these structures. The measurement and analysis can be carried out using laboratory based VNA-FMR equipment and is thus complimentary to developing synchrotron techniques.

Finally, this report presents an accessible and convenient methodology for the determination of parameters that have hitherto required challenging experimental measurements. As such, this work is of potential value to the development of future exchange coupled spintronic materials with tailored their properties for desired device applications, such as STT- or SOT-MRAM [44, 266, 267].

Chapter 7

Perpendicular Stationary Spin Waves

This chapter reports a comprehensive investigation on the fabrication and characterisation of a series of series of NiFe thin films with different capping layers. The ultimate motivation was the study of the exchange constant (A_{ex}), as introduced in section 2.4.1, through Ferromagnetic Resonance (FMR) spectroscopy and micromagnetic simulations. A manuscript detailing the study presented in this chapter is currently in preparation.

The exchange constant together with the saturation magnetisation (M_S), Curie temperature (T_C) and the anisotropy are the four fundamental properties of magnetically ordered materials [204]. These parameters determine the nature of this ordering, thus a proper understanding and control is crucial to the development of advanced materials with specific properties. In particular, as material characteristics at the nanoscale can vary significantly from that of the bulk material, suitable measurement techniques to determine these parameters in nanoscale thin films are essential [272].

It is possible to accurately determine M_S, T_C and the anisotropy directly from magnetometry measurements provided suitable temperature ranges and magnetic fields can be applied. However, A_{ex} cannot be as readily ascertained, necessitating measurement through indirect means. A thorough description of A_{ex} is available in section 2.4.1. The development of an accurate and precise measurement technique for this quantity is imperative for the advancement of both fundamental understanding and the technological application of magnetic materials. For example, a more complete understanding of A_{ex} is necessary to advance research fields such as magnonics by increasing the understanding of spin wave propagation in magnetic systems [68, 273]. A greater control of A_{ex} is also crucial to permit further reduction in the size of the read heads due to spin wave noise related difficulties [274]. Moreover, A_{ex} is required as an input parameter for atomistic and micromagnetic modelling, thus an accurate determination of this value in real materials is vital for the proper simulation of magnetic processes [275].

Typically, A_{ex} is estimated through the study of spin phenomena such as thermal magnons [276–278], with common setups involving exploring the variation of M_S at

low temperatures. This technique is only valid in low temperature regions due to thermal effects [69]. These measurements are also potentially influenced by internal magnetic fields which are governed by crystal anisotropies and M_S. Thus, it is desirable to use methodologies which require minimal knowledge of other magnetic properties due to their associated uncertainties resulting in significant experimental difficulties in obtaining sufficient accuracy [68].

In recent times, there has been an increasing interest in the use of FMR spectroscopy to ascertain A_{ex} [1, 68, 69, 123]. This method relies on the observation of exchange dominated higher order spin wave resonances that manifest in the direction perpendicular to the plane of the film due to the constraints of film thickness. Such excitations are known as Perpendicular Stationary Spin Waves (PSSWs) [50]. The physics of PSSWs is elaborated in section 3.3.2, with a schematic of the form of PSSWs shown in Figure 3.5. For clarity, the standard theory of the frequency of PSSWs for a thin film dominated by shape anisotropy given by equation 3.47 is restated as equation 7.1

$$f_{\text{PSSW}} = \frac{\gamma}{2\pi}\left(H_{\text{ext}} - 4\pi M_{\text{Eff}} + \frac{2A_{\text{ex}}}{M_S}\left(\frac{\pi p}{t_{\text{FM}}}\right)^2\right) \tag{7.1}$$

where γ is the gyromagnetic ratio, H_{ext} is the externally applied magnetic field, M_{Eff} is the effective magnetisation, p is mode number and t_{FM} is thickness of ferromagnetic (FM) layer. Kittel first considered the case where it is assumed the modes experience a rigid surface pinning at the two boundaries of the film [50, 279].

PSSW resonances were originally predicted by Kittel [138], with experimental detection demonstrated by M. H. Seavey et al. [128]. A notable advantage of the extraction of A_{ex} using PSSWs is that this is possible at a range of temperatures [69]. However, a significant limitation of this technique arises from the comparatively low intensities exhibited by these higher order resonances, as many measurement systems lack the sensitivity required to detect higher than first order ($p>1$) PSSWs. This has led to studies to extract A_{ex} focusing only upon the properties of the first PSSW mode [123, 251, 280]. However, there are reports that the A_{ex} determined from different PSSW resonances can vary [279, 281–283]. Indeed, the literature surrounding this area from the initial studies of PSSW are confused and in some cases contradictory [128, 139, 283, 284] with different theoretical backgrounds for the physics underpinning PSSWs put forth but no firm conclusions able to be drawn [279]. Recently, a summary of the current understanding of PSSWs has been included in a review by

Maksymov et al. [50]. In their review, it is stated that the efficiency of excitation of PSSWs is governed by concerns such as the uniformity of the driving magnetic field, variation in the magnetic parameters over the volume of the thin film and pinning due to surface anisotropies. The impact of the latter case and subsequent deformation of PSSW modes, hence deviations from equation 7.1, are also discussed. A more detailed insight regarding the influence of the magnetic properties of thin films on the PSSW resonances and the effects upon the determined A_{ex}, in particular, is currently lacking.

In this chapter, the observation of multiple PSSW modes in a series of $Ni_{0.8}Fe_{0.2}$ samples of varying thickness is reported. NiFe was chosen as the FM material as its magnetic properties have been extensively characterised and it is a technologically useful material [285–288]. NiFe also has the advantage that the field required to saturate this material out-of-plane (OOP) is within the field range that could be applied using our VNA-FMR system. The aim of this investigation is to explore the variation of A_{ex} extensively as a function of mode number and film thickness through both experiment and numerical simulation. The use of modern micromagnetics software offers great opportunity to probe the behaviour of PSSWs beyond that possible in earlier investigations and an investigation of this kind is, to the best knowledge of the author, currently lacking in literature.

Since the layers immediately adjacent to the magnetic layer are important in creating PSSW modes, this investigation also explored the impact that different capping layers can exert on the magnetic properties of the NiFe thin film. This is a crucial concern due to the ramifications that interface effects can have upon the high frequency response and precessional frequency of a magnetic thin film. A proper understanding of the impact of these adjacent layers is key for the engineering of high frequency magnetic devices such as recording heads with very thin magnetic layers [264]. In this study, the effects of no capping layer (referred to as uncapped), Pt and Ta capping layers were explored. These were selected to allow the study of the impact of a range of interfacial effects.

7.1 Sample Fabrication

The sample fabrication was accomplished using an AJA ATC 2200-V magnetron sputtering system as detailed in section 4.1. The substrates employed were Si/SiO_2 where the oxide layer was of thickness 290 nm. No deliberate substrate heating was used either during the deposition or as an annealing step. The structure of the samples studied

is shown schematically in Figure 7.1. In this study, sample series with no capping layer (uncapped), Pt capping layer and Ta capping layer were investigated.

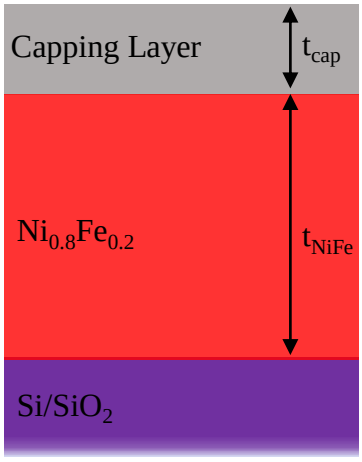

Figure 7.1: A schematic diagram of the overall NiFe stack layer structure. The NiFe and capping layer thickness is denoted as t_{NiFe} and t_{cap} respectively. The capping layers investigated were the case of no capping layer (uncapped), Pt capping layer of nominal thickness 4 nm and a Ta capping layer with nominal thickness 5 nm.

The deposition of the $Ni_{0.8}Fe_{0.2}$, Ta and Pt layers was carried out using DC magnetron sputtering from either elemental, or in the case of NiFe alloy, targets. The base pressure prior to deposition was less than 5×10^{-8} Torr with the working pressure of the Ar^{+} gas set at 3 mTorr. The NiFe and capping layers were deposited at a power of 100 W with the exception of Ta which was deposited at 20 W. These powers were chosen due to prior experience sputtering these materials with these parameters along with a consideration of time constrains placed upon the project. No in-situ magnetic fields were applied throughout deposition. A self terminating oxide layer formed in the uncapped case, as expected [287]. The NiFe thickness (t_{NiFe}) was explored between 23 nm to 102 nm to allow a range of PSSW spectra to be measured. The NiFe layer thickness was controlled via a calibrated deposition rate determined using X-ray Reflectivity (XRR). For further details the reader is directed to section 7.2.

7.2 Structural Properties

The layer structure of the films was determined using XRR where the data were fitted to a Fresnel model using the GenX software package as detailed in section 4.2.1. All measurements were performed over a 2θ range of 0.1–6.0 ^{o} with a step size of 0.01^{o}. The fitting was performed until the reduced χ^2 figure of merit was optimised. In Figure 7.2, XRR measurements and fits to models for samples possessing $t_{\mathrm{NiFe}} = 55\,\mathrm{nm}$ for each capping layer case are presented. The important structural parameters of the stack (namely layer thickness, roughness and density) as extracted from the XRR measurement are presented in Table 7.1.

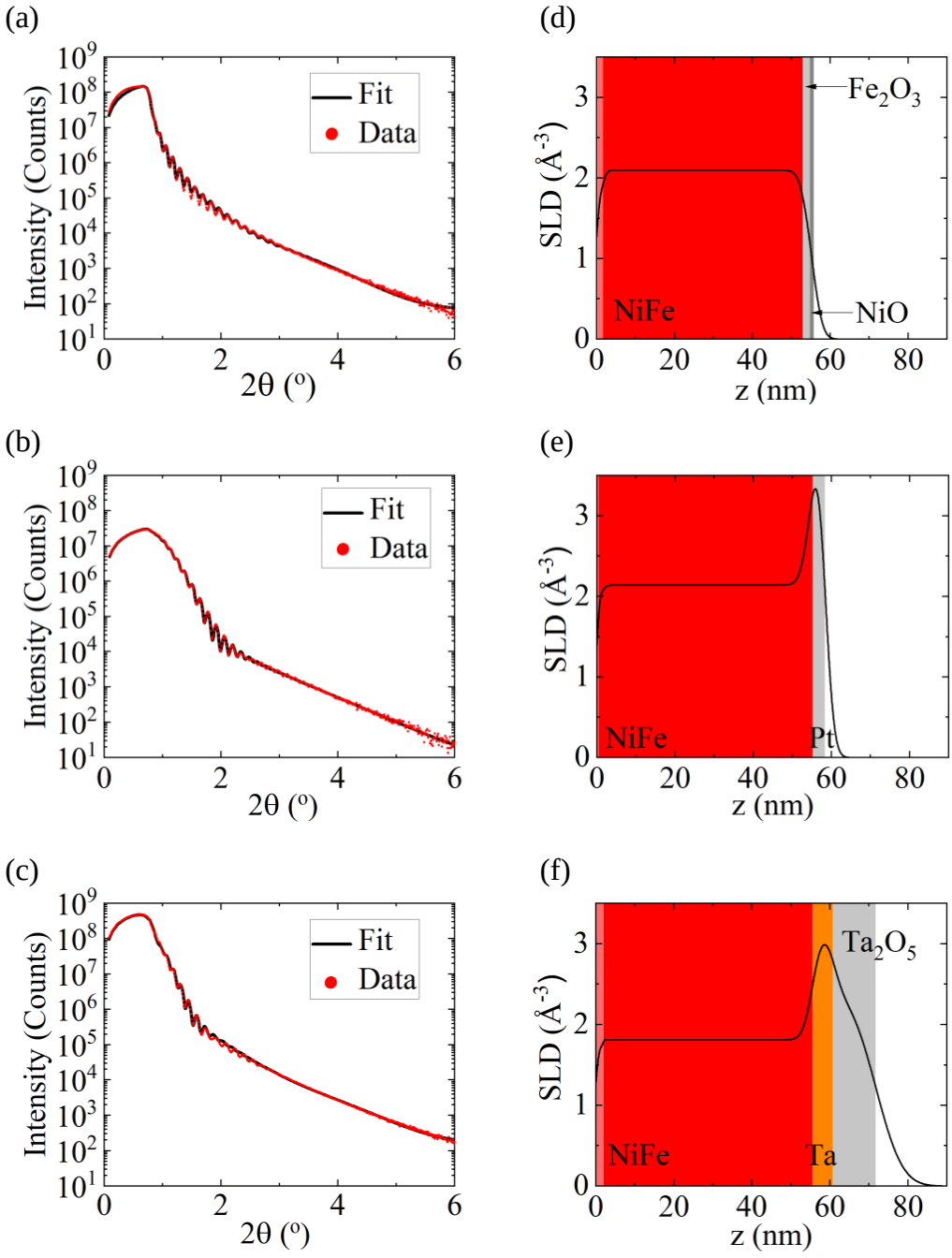

Figure 7.2: XRR measurements of the NiFe stacks possessing $t_{\mathrm{NiFe}} = 55\,\mathrm{nm}$. The fitted data in the case where the capping layer is a) No capping layer (uncapped) b) Pt c) Ta. (d-f) Corresponding SLDs as derived from the model fits to the XRR measurement as a function of distance from substrate z. The $\mathrm{FOM_{Log}}$ of the displayed fits were of order $\times 10^{-2}$.

		Structural Parameters		
Capping layer	Layer	Thickness (nm)	Roughness (nm)	Density ($Å^{-3}$)
Uncapped	NiFe	1.6	0.8	0.070
	NiFe	51.4	1.6	0.085
	Fe_2O_3	1.9	1.1	0.024
	NiO	0.7	2.0	0.056
Pt	NiFe	0.4	1.2	0.071
	NiFe	54.8	2.2	0.086
	Pt	3.0	1.8	0.066
Ta	NiFe	1.8	3	0.070
	NiFe	53.8	2.1	0.073
	Ta	5.2	2.2	0.048
	Ta_2O_5	11.0	5.3	0.014

Table 7.1: Important structural parameters of the NiFe films possessing $t_{\mathrm{NiFe}} = 55\,\mathrm{nm}$, as derived from XRR measurements.

The fit of the XRR data shown in Figure 7.2 required the modelling of a few atomic layers at the interface between the NiFe and the substrate. This initial layer could be due to initial growth processes and possibly increased contamination. The uncapped and Ta capped cases formed self-terminating oxide layers. It was found that for the uncapped case the most suitable model to reflect the XRR data was obtained for an oxide layer consisting of a Fe_2O_3/NiO bilayer, which is in agreement with the work of Fitzsimmons [287]. However, it was found that the oxide layer incorporated a thinner NiO layer at 0.7 nm than the 1.5 nm layer reported by Fitzsimmons. The presence of other iron oxides, such as FeO, in some cases has also been reported [287]. In this work, however, a model incorporating a FeO layer could not simulate the XRR data leading to the conclusion than an FeO layer was not present in the uncapped sample series. In the case of Ta capping layer, the Ta oxidised into a self-terminating Ta_2O_5 layer at the top of the film stack.

The t_{NiFe} extracted from the XRR measurements were used as a deposition rate calibration for NiFe layer thickness. XRR analysis was only possible for samples where $t_{\mathrm{NiFe}}<55\,\mathrm{nm}$ due to the lack of density contrast in thicker samples resulting in the reflectivity curves possessing insufficient features to allow a meaningful analysis. For greater explanation of the relevance of density contrasts to the XRR technique the reader is referred to section 4.2.1. The deposition rate calibration of the NiFe layer is shown in Figure 7.3. The linear fit was extrapolated to determine the thickness of samples with $t_{\mathrm{NiFe}}>55\,\mathrm{nm}$. The errors were assigned from an analysis of the residual

sum of squares of the linear fit where the standard deviation was determined to be 1.3 nm.

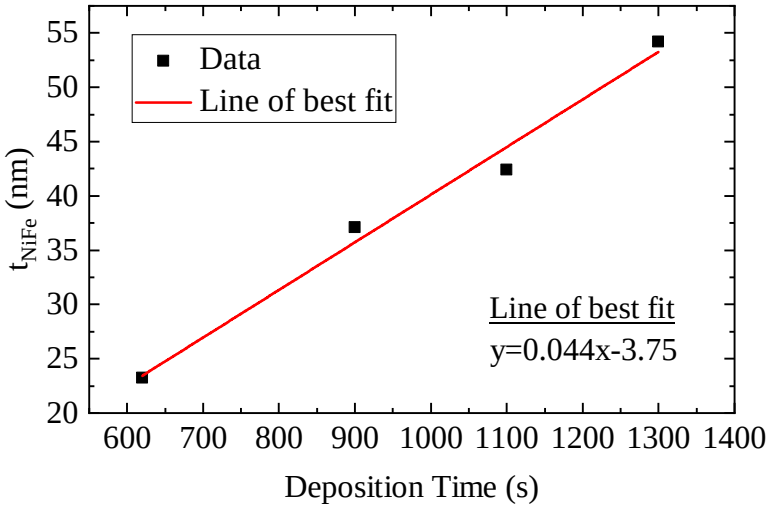

Figure 7.3: The calibrated rate t_{NiFe}, as extracted from XRR, against deposition time. The red line is a line of best fit to the measured data.

7.3 Static Properties

The static properties of the NiFe thin films were studied using vector Vibrating Sample Magnetrometry (VSM), as described in section 4.2.3. As expected, the films possessed an in-plane (IP) magnetisation with no uniaxial anisotropy present. In Figure 7.4, hysteresis loops for the IP and OOP directions of the Ta capped NiFe film of thickness t_{NiFe}=65 nm are presented. It can be seen that the exhibited M_S is in agreement with literature and that the films also possess small coercivities, as expected [1]. Furthermore, the external field required to saturate the sample in the OOP direction is within the range of the FMR electromagnet, as discussed in section 4.3, which is crucial for the OOP dynamic characterisation reported in section 7.4.2.

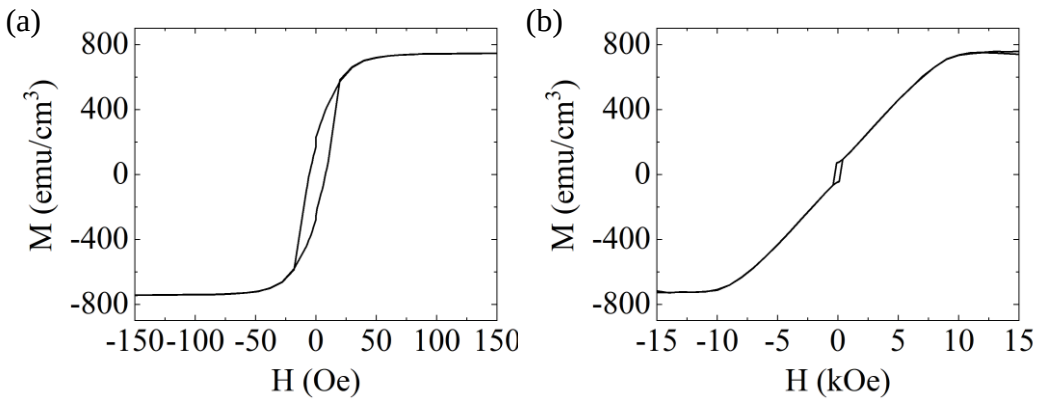

Figure 7.4: M-H hysteresis loops for an uncapped NiFe film possessing t_{NiFe}=65 nm at room temperature. The case where the external magnetic field is applied a) IP b) OOP.

In Figure 7.5 the extracted M_S values for the samples across the thickness range in each capping layer case are presented, with the average value for each capping layer case given in Table 7.2. The averaged M_S is consistent in each capping layer case and in agreement with literature expectations [1].

Capping layer	M_S (emu/cm^3)
Uncapped	720 ± 30
Pt Capped	700 ± 50
Ta Capped	720 ± 50

Table 7.2: The average M_S of the samples in each capping layer case.

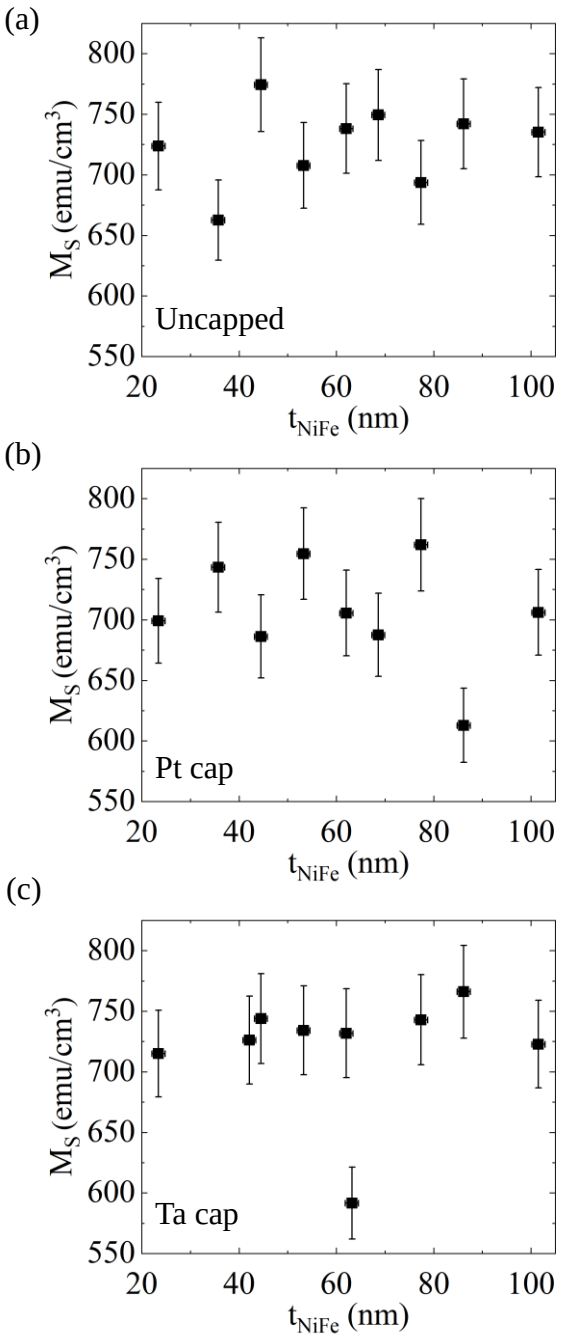

Figure 7.5: M_S as a function of t_{NiFe} in the a) uncapped case b) Pt capped case c) Ta capped case.

7.4 Dynamic Characterisation

The dynamic properties of the samples were investigated using the Vector Network Analyser-Ferromagnetic Resonance Spectrometer (VNA-FMR) at room temperature. The VNA-FMR measurement procedure is described fully in section 4.3 and the reader should note that the measurements reported in this section were performed using the Picoprobe setup in the cases where the external field applied both IP and OOP. In section 7.6.1, the magnetisation dynamics are studied with the external field applied at a range of angles from the OOP direction using the upgraded setup and the NanOsc. waveguide (further details of this experimental setup can be found in section 4.3.2).

7.4.1 In-Plane

The dynamics of the NiFe thin films were investigated with a static field applied IP to verify that a conventional Acoustic Mode (AM) resonance was present. The studied sample was an uncapped NiFe layer with t_{NiFe}=65 nm and the resonance spectra is shown in Figure 7.6. From equation 3.37, the Gilbert damping parameter, α, is determined to be (0.010 ± 0.001), in agreement with literature expectations [288]. A similar set of results were observed for the other t_{NiFe} investigated, with the expected AM resonance measured in all cases.

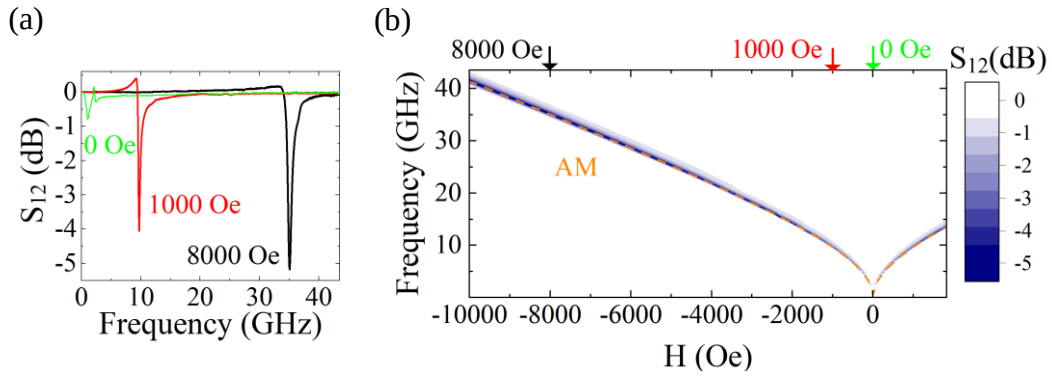

Figure 7.6: The resonant dynamics of an uncapped NiFe layer with thickness t_{NiFe}= 65 nm a) S_{12} absorption profiles for different applied fields b) A 2D map of the resonant spectra as a function of applied field and frequency. The orange dashed line represents the fit to the AM.

7.4.2 Out-Of-Plane

The OOP dynamic properties of the samples were investigated and the obtained spin wave spectra studied. For this experiment, it was necessary for the static field to be applied out of the sample plane. This required, as discussed in section 4.3, a different sample holder to permit the sample to be held vertically and the use of different Picoprobes to allow connections to the waveguide to be made. The spin wave spectra measured for the case of a Ta capped NiFe layer with $t_{\mathrm{NiFe}} = 77\,\mathrm{nm}$ are presented in Figure 7.7 where a fundamental resonance (FMR) mode along with higher order PSSWs are observed. The relevant background theory underlying PSSWs was introduced in section 3.3.2. The measurements show that the peak amplitudes of the PSSWs reduces with mode number, as expected [50]. The detected PSSWs were designated as PSSW1 for $p = 1$ and PSSW2 for $p = 2$. This approach is supported by numerical modelling of the dynamics of the samples, as discussed in section 7.5. The formation of PSSW resonances at an external field of magnitude greater than $\approx 10\,\mathrm{kOe}$ is consistent with the field required to saturate the NiFe film in OOP direction in static measurements as shown in Figure 7.4.

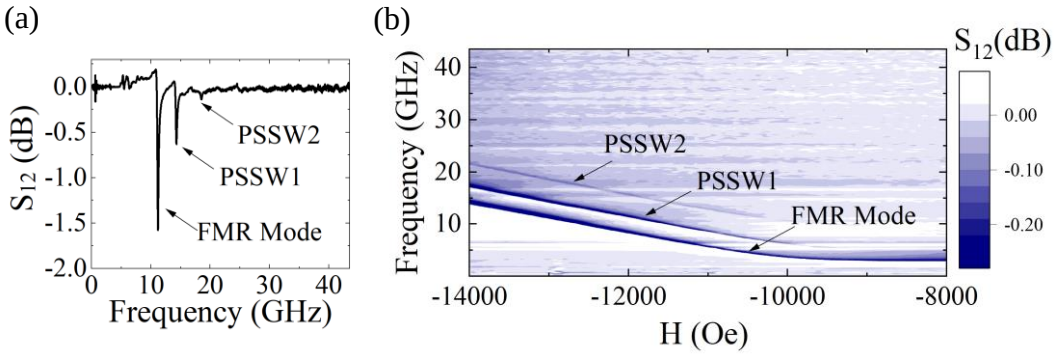

Figure 7.7: The spin wave spectra of a Ta capped NiFe layer with thickness $t_{\mathrm{NiFe}} = 77\,\mathrm{nm}$. The FMR label denotes the the fundamental mode, whilst the PSSW1 and PSSW2 labels refer to the order of the higher order PSSW excitations. a) S_{12} spectra at an applied field of 13 kOe. b) A 2D map of the resonant spectra as a function of applied field and frequency.

In our sample series, PSSW modes were observed only in the cases where NiFe thickness was greater than 40 nm. We also observe that in cases where the NiFe layer thickness is greater than 90 nm the peak amplitude of the PSSW1 resonant modes became comparable with that of the fundamental mode. This contrasts with the expectation that PSSW peak amplitude reduces with mode number [50]. Therefore, in the

PSSW investigation reported here only samples with t_{NiFe} between 40 nm to 90 nm are detailed.

In section 7.4.3 an assessment of the fundamental magnetic properties g and M_{Eff} is provided. A study of the effect the different capping layers have upon these magnetic properties is of interest due the impact this can have on the high frequency response of the material. Specifically, the g-factor sets the proportionality of angular momentum and magnetic moment for the individual spins precessional motions whilst M_{Eff} characterises an internal demagnetising field which acts to greatly accelerate these dynamics [264]. In section 7.4.4, the impacts of these capping layers on A_{ex} as extracted from the spin wave spectrum using equation 7.1 are detailed.

7.4.3 g-factor and Effective Magnetisation

The g-factor and M_{Eff} determined from FMR measurements for each capping layer case over the NiFe thickness range are shown in Figure 7.8. These values were extracted from the dynamic measurements through use of equation 3.32 using the OOP FMR mode. From consideration of the determined g-factors, it is seen that this is well described by a value between 2 and 2.13 across NiFe thickness range and with different capping layers, which is similar to measurements obtained by Shaw et al. [289]. Table 7.3 shows the g-factor determined by averaging the values across all thicknesses for a particular capping layer and it is seen these averaged values are consistent within errors. Notably, the g-factor exhibits much greater consistency across the t_{NiFe} range in the Ta capping layer case than displayed in the other capping layer cases. These determined g-factors provide evidence that the effects of orbital moments arising from interfaces are not present. Thus, these measurements are in agreement with previous reports which state that interfacial effects and the lack of orbital quenching only potentially become significant at thickness below ≈ 10 nm [264].

Capping layer	g	M_{EFF} (emu/cm^{-3})	VSM: M_S (emu/cm^3)
Uncapped	2.07 $\pm$0.03	690 $\pm$30	720 $\pm$30
Pt Capped	2.06 $\pm$0.04	700 $\pm$30	700 $\pm$50
Ta Capped	2.07$\pm$0.01	720$\pm$30	720 $\pm$50

Table 7.3: The averaged magnetic parameters of the NiFe thin films in each capping layer case, as extracted from dynamic measurements. The M_S as determined from VSM are also shown for comparison.

The obtained M_{Eff} values are presented in Figure 7.8(d-f) with the averaged values for each particular capping layer case also displayed in Table 7.3. Importantly, it was found that the averaged M_{Eff} obtained from each capping layer case was in agreement and also consistent with the M_S values determined from VSM measurements (presented in Figure 7.5 and Table 7.2) and literature [1]. This is consistent with expectations that no significant surface anisotropy exists in the films which would result in M_{eff} being reduced compared to M_S. For a thorough description of the relationship between M_{Eff} and M_S, the reader is referred to section 3.2. However, there is a notable deviation in the M_{Eff} and M_S in the case of the Ta capped NiFe thin film possessing $t_{\mathrm{NiFe}} = 63\,\mathrm{nm}$. This may suggest that the thickness of the NiFe layer is incorrect in this case due to fabrication issues unique to this particular sample.

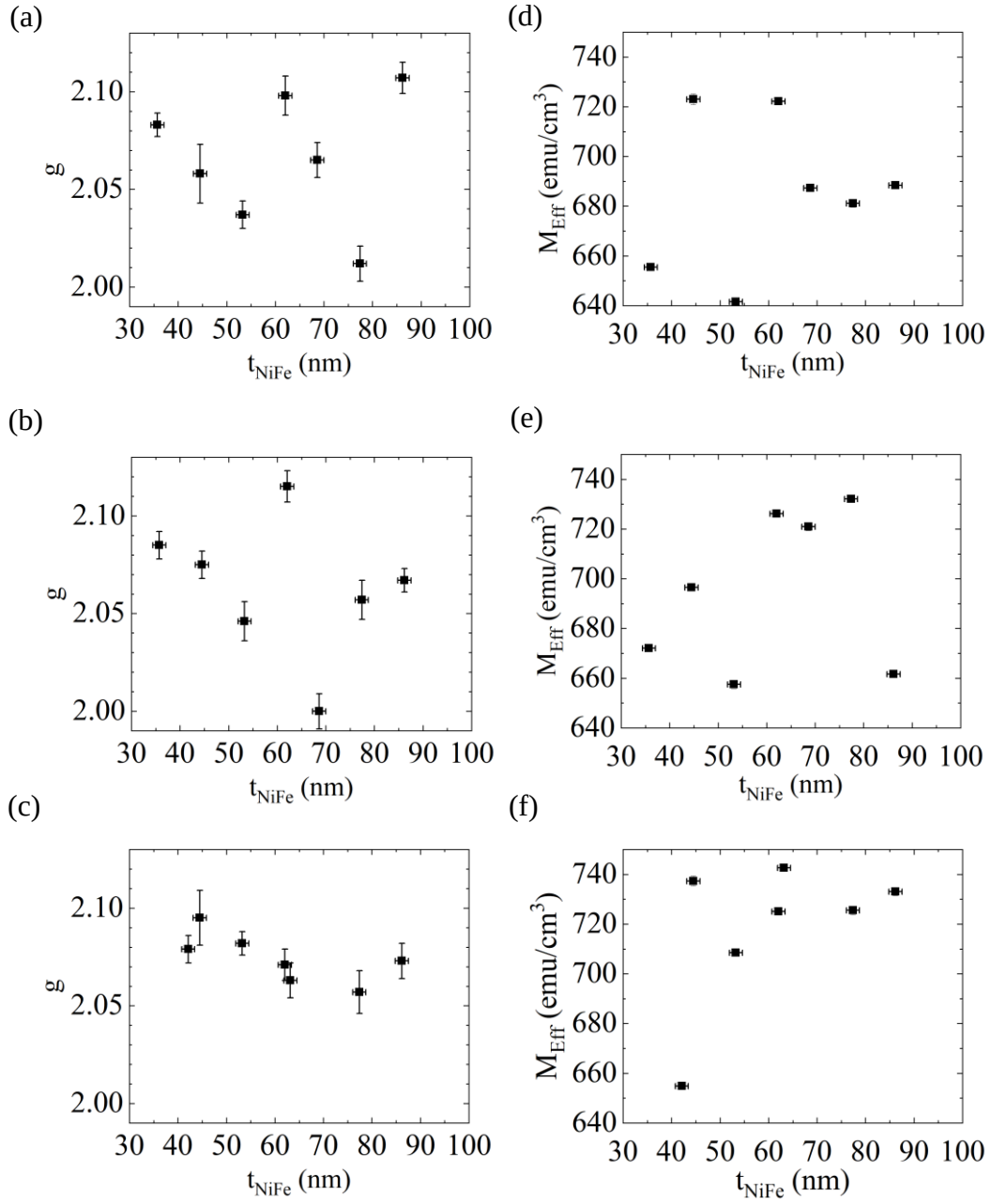

Figure 7.8: The variation of parameters governing the high frequency behaviour of magnetic materials, as determined from a study of the FMR mode when the applied field is applied OOP, with t_{NiFe} for each capping layer case. The g-factor in the capping layer case a) Uncapped b) Pt capped c) Ta capped. (d-f) Corresponding values of M_{Eff} in each capping layer case. The error bars are with the symbols in some cases.

7.4.4 Exchange Constant

The PSSW modes exhibited by each NiFe thin film were studied to examine the variation of A_{ex} with t_{NiFe}, p and capping layer material through use of equation 7.1. This was performed through fitting the variation of the resonant frequency of each PSSW mode with the external field with A_{ex} examined as the free parameter. The determination of other relevant physical properties, such as t_{NiFe}, g and M_{Eff}, required for this fitting has been detailed in earlier sections. As will be discussed, a single A_{ex} could not describe all the measured data. Thus, we refer to the value extracted from dynamics measurement as the effective exchange constant $A_{ex,eff}$ as the determination of A_{ex} is not necessarily straight forward. The extracted $A_{ex,eff}$ as a function of t_{NiFe} for each capping layer case is shown in Figure 7.9(a-c).

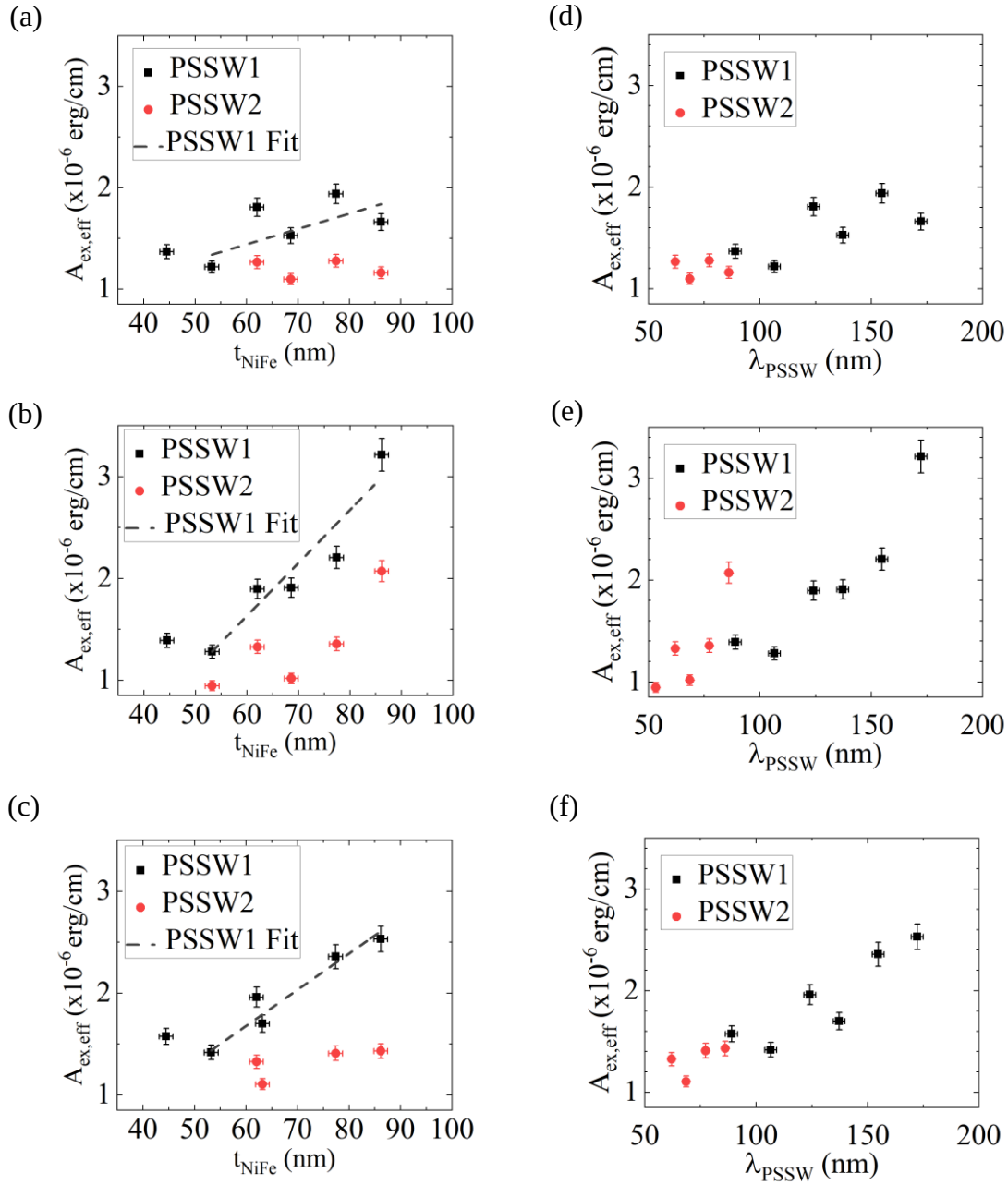

Figure 7.9: The variation of $A_{ex,eff}$, determined using equation 7.1 from a study of the PSSW modes, with t_{NiFe} and p for each capping layer case a) Uncapped b) Pt capped c) Ta capped. The corresponding variation of $A_{ex,eff}$ with PSSW wavelength (λ_{PSSW}) for each capping layer case d) Uncapped e) Pt cap f) Ta cap. The PSSW1 and PSSW2 labels denote the order of the PSSW excitations used to extract $A_{ex,eff}$. The dashed line is a linear fit to the PSSW1 data which shows an increase of $A_{ex,eff}$ with t_{NiFe}. The error bars are within the symbols for some data.

It is clear that the $A_{ex,eff}$ extracted for each sample is dependent on the capping layer material, t_{NiFe} and p as shown in Figure 7.9(a-c). For example, it is seen that the Pt capped samples are able to support the higher order PSSW2 mode at a lower t_{NiFe} than seen in the uncapped or Ta capped cases. This variation in $A_{ex,eff}$ is clearly inconsistent with the normal assumption that A_{ex} has a single value reported as 1×10^{-6} erg/cm for NiFe [1].

From consideration of PSSW1, it is observed that in all capping layer cases there is the presence of two regimes of the variation of $A_{ex,eff}$ as t_{NiFe} increases. At layer thicknesses lower than $\approx$ 55 nm it is seen that $A_{ex,eff}$ is roughly constant. However, at thicknesses greater than this, the extracted $A_{ex,eff}$ has steadily increasing values. Similar variations have been reported by Belmeguenai et al. [280], though attributed lack of precision in their work, and by Samantaray [281]. Furthermore, in the case of the Pt and Ta capped layers, $A_{ex,eff}$ increases linearly with t_{NiFe} with greater increases seen in the Pt capped case. From consideration of the $A_{ex,eff}$ extracted from the PSSW2 mode, which is only observed for $t_{NiFe}>50$ nm, it is clear that in all cases the $A_{ex,eff}$ is lower than that determined from the corresponding PSSW1 mode. Furthermore, the $A_{ex,eff}$ extracted from PSSW2 shows no significant dependence on t_{NiFe}, apart from in a singular case at the greatest t_{NiFe} examined in the Pt capped sample series. Moreover, it is notable that the $A_{ex,eff}$ extracted from PSSW2 is similar to that extracted from the PSSW1 modes of films with t_{NiFe} less than 60 nm. This finding could potentially indicate that the $A_{ex,eff}$ extracted from PSSW1 modes for samples with $t_{NiFe}<55$ nm and PSSW2 modes is more indicative of the exchange constant of the thin films. This suggests that as film thickness reduces the value of $A_{ex,eff}$ reaches an asymptotic value. The reasons underlying this finding are not fully explained. However, it is possible to hypothesise that the angle between the adjacent spins in the $z-$ direction is important and work is ongoing to resolve this question.

The variation of $A_{ex,eff}$ with PSSW wavelength (λ_{PSSW}) has also been explored and is shown in Figure 7.9(d-f). The wavelength of the spin waves are described by

$$\lambda_{PSSW} = \frac{2t_{FM}}{p} \tag{7.2}$$

where all symbols have been defined previously. It is seen that greater wavelength spin excitations lead to a larger $A_{ex,eff}$, with a linear trend seen in all capping layer cases.

7.5 Simulation Using a Single Exchange Constant

From the experimental findings reported in section 7.4.4, it is clear that the behaviour of the A_{ex} as determined through use of equation 7.1 is different from that expected from current understanding [1, 50, 138]. Specifically, it is not possible to describe the measured spin wave spectra with a single A_{ex}, with variations apparent with both t_{NiFe} and p. There are a small number of reports of this variation in literature, with similar experimental findings reported by Samantaray et al. [281], BenYoussef et al. [282] and Kooi et al. [279]. This suggests that the equation 7.1 does not fully describe the complexities of PSSWs leading to the extraction of an effective exchange constant as opposed to the exchange constant of the FM material.

Historically, the spin wave resonance in thin magnetic films has been described on the basis of two models [279]:

- *Kittel's model of surface pinning (SP model)*: The film possesses uniform properties throughout the bulk except at the surface where the spins are assumed to rigidly pinned, as proposed by Kittel [138]. The surface pinning could be provided by a interaction with an antiferromagnetic surface layer [290] or a Néel surface anisotropy [73].

- *Wigen's model of dynamic pinning (DP model)*: In this model, the surface of the thin film consists of a few atomic layers where the internal field differs by a small amount from that of the bulk. This results in the phenomena of *dynamic pinning*, as detailed later. Such an effect can arise from a number of mechanisms including a change in the anisotropy field perpendicular to the film, a different state of strain for these surface layers due to the magnetoelastic effect or a difference in the magnetisation of the surface layer resulting in an altered demagnetisation field [139, 291].

Numerical modelling has been performed to elaborate on the measured spin wave resonances in the context of these models to examine which better reflects the experimentally measured spin wave spectra. To be clear, this has involved the simulation of thin NiFe films subject to pinning generated from either the SP or DP model to examine which case better describes the experimental data using a single A_{ex}. This part of the investigation was carried out in collaboration with Mr Y. Li, who contributed significantly to the numerical modelling aspect of this investigation.

The numerical simulations were executed using the micromagnetic modelling package Mumax^3 which is a finite-difference GPU-accelerated simulation program [239],

as discussed in section 4.4. The central aim of this part of the investigation was to reconcile the physically required concept of a single A_{ex} with the experimentally measured resonances. The magnetic parameters input to the model were chosen to be consistent with NiFe to allow direct comparison of the simulation results with the experimental measurement. Specifically, the damping parameter was set to $\alpha = 0.001$, an order of magnitude lower than that extracted from measurements of the NiFe thin film discussed in section 7.4.1, to allow the simulations to achieve a higher signal to noise ratio. The exchange constant varied between $A_{ex} = 1 \times 10^{-6}$ erg/cm and $A_{ex} = 1.6 \times 10^{-6}$ erg/cm in order to investigate which case more fully reflected the experimental results. The saturation magnetisation was set as the corresponding M_{Eff} values measured from dynamic measurements (as reported in section 7.4.3) for each sample. In order to minimise the demagnetisation effects from the physical edge, periodic boundary conditions were applied in the plane. The overall system is discretised into 2 nm x 2 nm x 1 nm cuboid cells and the dimension in the *xy*-plane set to 128 nm x 128 nm. The ringdown method, as introduced in section 4.4.1, was used to obtain the free inductive decay of the magnetisation which was then Fourier transformed to obtain the ferromagnetic resonance signal. Information regarding the waveform of the PSSWs, as discussed in section 7.5.1, was determined by applying a time-dependent sinusoidal excitation $h_{rf}(t)$ with frequency f: $h_{rf}(t) = \tilde{h}\sin(2\pi ft)$ where $\tilde{h}$ is the amplitude of this excitation and t is time. The time-resolved magnetisation in each FM layer was recorded.

The SP model did not allow the PSSW resonant frequencies of each sample to be reproduced using a single A_{ex}, as might be expected from a consideration of the physics involved. Thus, this model was unable to account for the measured alteration of $A_{ex,eff}$ with both t_{NiFe} and p shown in Figure 7.9. Therefore, the applicability of the DP model and the ramifications of the introduced dynamic pinning on the PSSWs was explored. *Dynamic pinning* describes the case where there are different resonant conditions for a region of a few atomic layers at the surface of the film compared to the bulk. Therefore, whilst the surface spins are not rigidly pinned and can precess they cannot support a uniform precession mode at the same external field or frequency required for that of the bulk of the film [139]. This leads to a pinning which only becomes apparent during measurement to determine the dynamic response of the film. The dynamic pinning was introduced to the structure by modelling the thin film as two regions of magnetisation satisfying the following conditions [139]

1. The bulk layer possessing a magnetisation set to that extracted as M_{Eff} (see section 7.4.3). The thickness of this layer was set as the measured t_{NiFe}.

2. The presence of a thinner surface layer with a reduced magnetisation. The expectation of DP model is that the difference in layer magnetisation is small.

Examples of the Mumax^3 simulation scripts used within this investigation are presented in Appendix B.2.The investigation proceeded by using the experimentally obtained spin wave spectra for each film to determine the value of the reduced magnetisation layer and its thickness. Thus, a series of simulations were performed varying these parameters and comparing the modelled resonances with the experimentally measured values. For this step, the literature value of exchange constant for NiFe (A_{ex}= 1×10^{-6} erg/cm) was used [1]. The optimal parameters to reproduce the measured resonances are shown in Table 7.4. In the uncapped case, due to the AF nature of the self-terminating Fe_2O_3/NiO bilayer formed due to oxidisation of the NiFe surface, the approach of modelling antiferromagnets with Mumax^3 outlined by De Clercq [292] was utilised. Specifically, the reduced layer was initialised with an M_S value equal to that of the bulk layer with an AF coupling ($A_{\mathrm{ex}}<0$) input. It is seen that the Pt capped case satisfies the requirement that the surface layer has a slightly reduced magnetisation, though a much more significant difference from the bulk magnetisation is seen in the Ta capped case. The larger value of the reduced layer magnetisation for the Pt capped case compared with the Ta capped case is consistent with expectation of proximity magnetisation of a Pt layer adjacent to a FM layer. It should be noted that the difference between the magnetisation of the reduced layer compared to that of the bulk is found to be large, especially in the Ta capped case, which is not in agreement with the DP model as put forth by Wigen.

	Reduced Magnetisation Layer	
Capping Layer case	Thickness (nm)	Ms (emu/cm^3)
Uncapped	2	Bulk M_{Eff}
Pt	5	500
Ta	5	200

Table 7.4: The parameters of the reduced magnetisation layer required to reproduce the resonant frequencies of the measured spin wave spectra. In the uncapped case, the M_{Eff} of the bulk was used to represent the magnetic moment of the idealised layer of atoms adjacent to the bulk which provided an AF coupling contribution.

The case of two reduced magnetisation layers on either side of the bulk layer was investigated in a similar manner in the case of a FM reduced magnetisation layer. Similarly to the aforementioned case, the reduced layer magnetisation and its thickness was varied with the modelled resonances then compared with the experimentally measured values. Importantly, it was found that the measured resonances produced by such a model could not be reproduced for any arrangement of reduced layer thickness or magnetisation.

7.5.1 PSSW Waveform

The numerical simulations allowed the PSSW waveform supported by the samples to be investigated. The proper labelling of PSSW modes and the corresponding p is a crucial concern to the study of PSSWs due to the importance of this parameter to equations 3.45 and 7.1. Examples of the waveforms of the OOP spin wave spectra supported by our simulated structure are presented in Figure 7.10 for the case of a Ta capped NiFe layer of thickness $t_{\mathrm{NiFe}} = 86\,\mathrm{nm}$. This t_{NiFe} was selected to explore PSSW mode waveform as this should present the highest signal to noise ratio by virtue of the film thickness. Examples of the Mumax^3 simulation scripts used for this aspect of the investigation are presented in Appendix B.2.2.

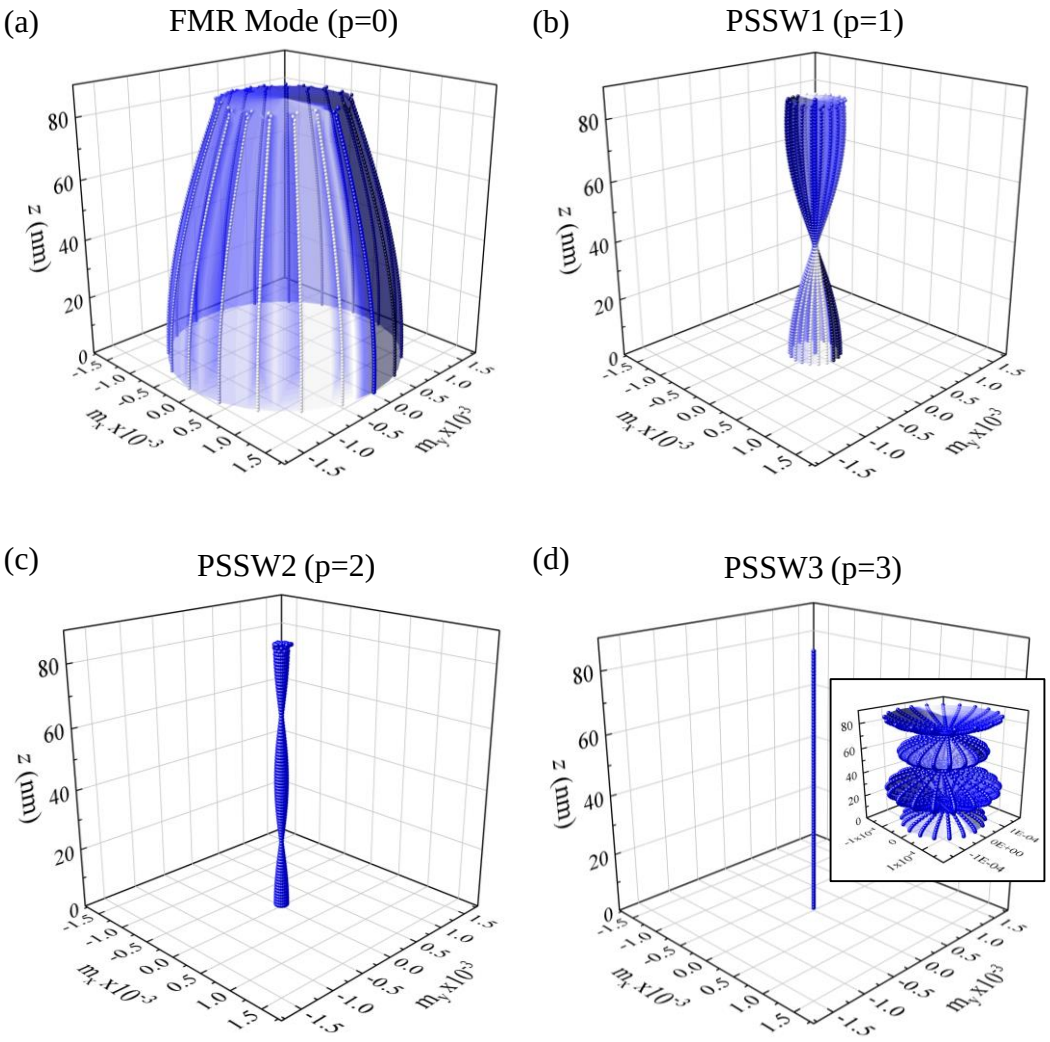

Figure 7.10: Simulated waveforms of PSSWs supported by a Ta capped NiFe thin film possessing t_{NiFe} =86 nm. In this simulation, the exchange constant was set as $A_{\mathrm{ex}} = 1.3 \times 10^{-6}$ erg/cm. a) FMR mode (p=0) b) PSSW1 (p=1) c) PSSW2 (p=2) d) PSSW3 (p=3) inset: Zoomed-in figure with same axis labels. The symbols z denotes distance from the substrate and m_x and m_y represents the reduced magnetisation in the x and y directions respectively.

From an examination of Figure 7.10, it can be seen that the evolution of the PSSW modes are consistent with expectations. Specifically, as p increases the wavelength λ_{PSSW} of the spin waves decreases. Furthermore, the displacements of the reduced magnetisation in the $x-$ and $y-$ directions (m_x and m_y respectively) decreases significantly with mode number. This corresponds to the reduced resonant peak amplitude of the PSSW modes with p observed experimentally and shown in Figure 7.7. It can be seen that the PSSW1 and PSSW2 resonances possess waveforms consistent with that

expected for the $p = 1$ and $p = 2$ modes. This is in agreement with the expectations of the DP model where, due to the presence of an asymmetric dynamic pinning and lack of surface pinning, even modes can be supported [50, 139].

These simulations also allow the impact of dynamic pinning on the configuration of the spins comprising the resonant modes to be examined. All modes show that the presence of the reduced magnetisation layer and the subsequent dynamic pinning results in a deformation of the spin wave modes in the near-surface region. This is especially insightful in the case of the FMR mode where its typical description as a wave of infinite wavelength no longer applies. This observation may offer an explanation for the experimentally observed differences in the evolution of $A_{\mathrm{ex,eff}}$ with thickness (Figures 7.9), as extracted from PSSW1 and PSSW2. It is hypothesised that as a greater proportion of the wavelength of PSSW1 occurs in the reduced magnetisation layer this mode is more affected by the dynamic pinning than the PSSW2 mode.

7.5.2 Modelling Resonances

The resonant frequencies of both the simulated resonances along with the experimentally measured values are presented in Figure 7.11. It is seen that, as expected, the FMR mode frequency is invariant to changes in A_{ex}, whilst the PSSW mode frequency increases with greater A_{ex}. Furthermore, in all capping layer cases the resonant modes are well described by the simulated model, thus supporting the DP model and demonstrating that these PSSWs are affected by a genuine change in magnetisation in the film, as opposed to the presence of a rigid surface pinning, and the emergence of dynamic pinning. The simulations also model the formation of higher order PSSW modes than can be detected in measurement, with PSSW3 ($p = 3$) shown. The lack of this mode in the experimentally obtained spectra is most likely due to the peak amplitude of this PSSW resonance being below the detection limits of the VNA-FMR used in measurement.

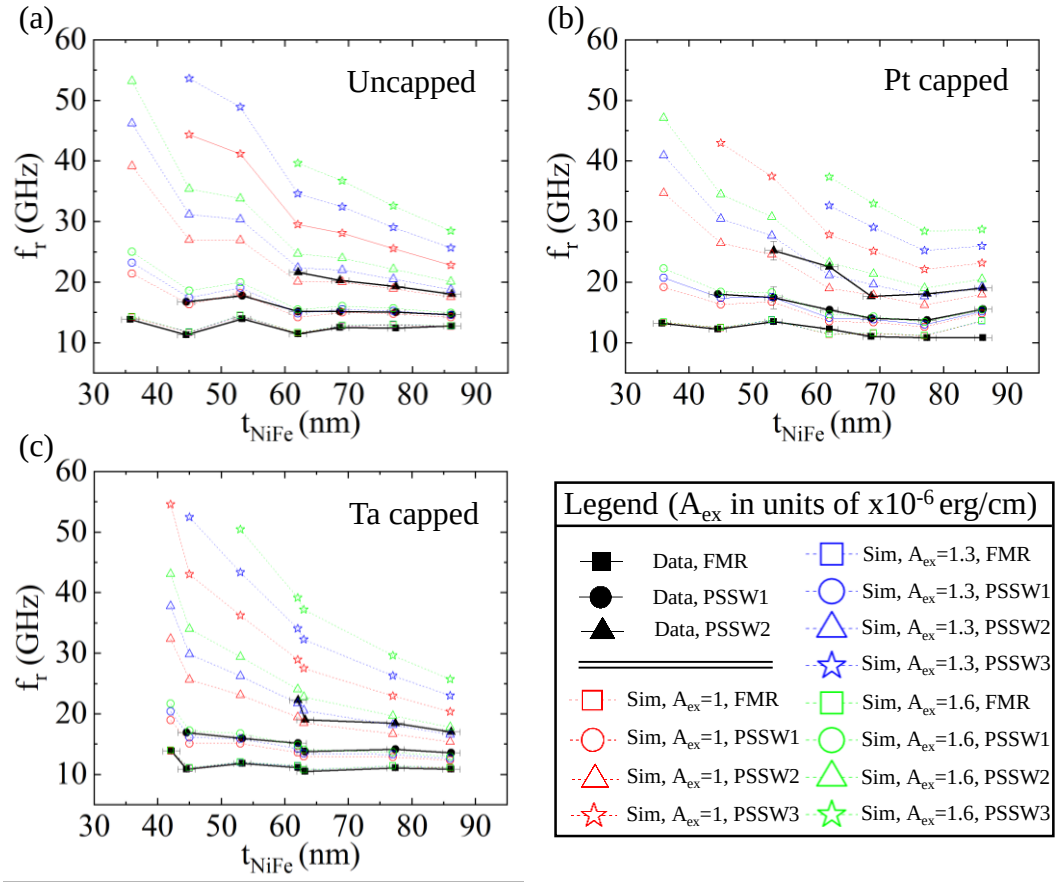

Figure 7.11: Measured and simulated resonant frequencies of the spin wave spectra exhibited for different t_{NiFe} and a range of A_{ex} in the following capping layer cases a) uncapped b) Pt capped c) Ta capped. The legend of the symbols is shown in lower-right panel.

The sensitivity of the simulated structures to A_{ex} is investigated by varying this parameter between $A_{\mathrm{ex}} = 1 \times 10^{-6}$ erg/cm and $A_{\mathrm{ex}} = 1.6 \times 10^{-6}$ erg/cm. The optimal parameter for each capping layer case was found by performing a linear fit to the simulated resonant frequency and corresponding A_{ex} for each PSSW mode. From this fit, the A_{ex} required to obtain each experimentally measured PSSW mode was then determined. The results of this analysis are presented in Table 7.5 where the A_{ex} extracted from an different appraisals of the measured PSSWs is presented.

	A_{ex} ($\times 10^{-6}$ erg/cm)			
Capping Layer	PSSW1 (t_{NiFe}<55 nm)	PSSW1	PSSW2	All modes
Uncapped	1.0 ±0.2	1.2 ±0.2	1.1 ±0.1	1.12 ±0.16
Pt Capped	1.4 ±0.2	1.6 ±0.3	1.2 ±0.2	1.4 ±0.2
Ta Capped	1.4 ±0.1	1.7 ±0.3	1.3 ±0.2	1.5 ±0.2

Table 7.5: The optimal A_{ex} for the studied sample series in each capping layer case, as extracted from comparisons between experimental measurement and simulation.

Notably, it can be seen from a consideration of all the modes, the PSSW1 mode and the PSSW1 mode of films with t_{NiFe}<55 nm that there is a dependence of the extracted A_{ex} upon the utilised capping layer. This appraisal of the data is a significant result which demonstrates that the structure in which the layers where the exchange constant is being investigated can influence the results obtained. An assessment of the PSSW2 modes only provides an A_{ex} that is consistent across capping layer cases and, within errors, in agreement with the generally accepted value for NiFe [1]. This supports the hypothesis that PSSW2 modes provide a more reliable method of determining the exchange constant in FM materials irrespective of capping layer material.

7.6 Angular Dependence of PSSWs

In this section, the evolution of the PSSW spectra with rotation of the external field from the perpendicular direction is reported. This investigation was motivated by the prediction of the DP model that at a certain critical angle the spin wave spectra collapses into a single FMR resonant mode [139, 279, 291]. At this critical angle, it is hypothesised that the precession condition in all regions of the film is equivalent leading to the excitation of a single FMR mode. The disappearance of higher order modes with these small rotations from the perpendicular is evidence that the film is comprised of a surface region of a few atomic layers possessing a reduced magnetisation exchange coupled to the bulk of the film [139].

7.6.1 Experimental Measurements

The evolution of the spin wave spectra as the applied external field was rotated from the OOP direction (denoted 0^o) to the IP direction up to an angle of 15^o was measured. To be clear, this investigation involved, as in the study reported in section 7.4.2, the sample held vertically so that the external field can be applied OOP to the sample, with the external field was then rotated with the sample position fixed. The details of the experimental setup and upgrades required to the VNA-FMR system to enable this study to take place are given in section 4.3.2. The reader should note that for this part of the study, the NanOsc. waveguide was used as opposed to the Picoprobes. For this investigation, an angular increment of 1^o was selected, consistent with previous reports [291]. In literature, this critical angle has been experimentally measured at angles between 2^o to 17^o [139, 279, 291] for a range of FM films including Co, Ni, and $Ni_{0.8}Fe_{0.2}$.

For this investigation the samples possessing t_{NiFe} = 86 nm were studied for each capping layer case, motivated by these samples exhibiting resonant modes with greater peak amplitudes. This was particularly important to ensure detection of the PSSWs due to the lower sensitivity of the NanOsc. waveguide employed in this study. In Figure 7.12, a selection of spin wave spectra for the Ta capped sample with rotation of the external field are shown. As expected, the limited detection capability of the NanOsc. waveguide resulted in lower peak amplitudes of the detected resonances than seen from the Picoprobe measurements (presented in Figure 7.7).

From an examination of the spin wave spectra presented in in Figure 7.12, it is clear that PSSW2 is extinguished by any rotation of the external field. Moreover, the resonant frequencies of the FMR mode and PSSW1 increase with increasing angle from the perpendicular. Whilst PSSW1 is detected at each of the studied angles, its peak amplitude decreases significantly with respect to the FMR mode as the angle of the field direction to the perpendicular increases. Whilst a critical angle where the PSSW modes collapse into a single FMR mode resonance is not observed, the evidence does show a reduction of the PSSW1 mode and a corresponding increase in the FMR mode. This is clear from an examination of Figure 7.12(a) and (d) where the peak amplitude FMR mode approximately doubles in magnitude in the case the field is applied at an angle of 15^o to the perpendicular as opposed to applied OOP. In this angular range the peak amplitude of PSSW1 decreases by roughly 40 %. An analysis of the peak amplitude of the PSSW1 mode compared to that of the FMR mode also presents a stark diminishment of PSSW1 over the angular range studied. It is measured

that the peak amplitude of PSSW1 decreases from roughly 60 % of the peak amplitude of the FMR mode when the applied field is applied at OOP direction to approximately 20 % when it is applied at 15^{o} to perpendicular. Thus, these findings suggest that the critical angle phenomena might be observed at higher angles than those accessible in this project [139]. Although a critical angle of 10^{o} has previously been reported in a similar material system [139] other reports have shown a critical angles as high as 17^{o} [279]. Therefore, it is likely that the determination of a critical angle depends on the sensitivity of the experimental apparatus, basically the angle at which the signal to noise ratio reduces to the noise floor. In all cases, a substantial reduction of the signal from the PSSW mode is observed as is the case here.

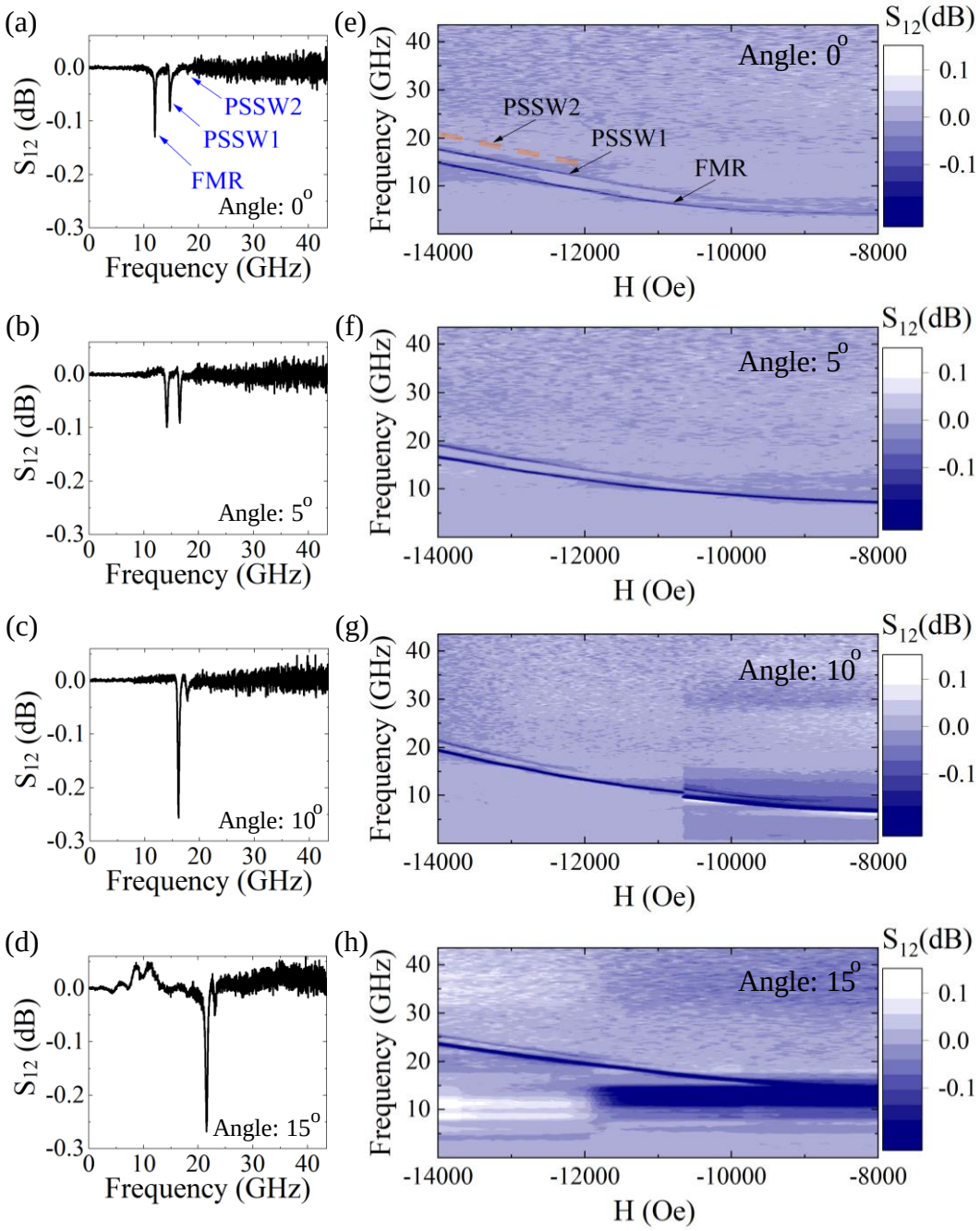

Figure 7.12: The spin wave spectra exhibited by a Ta capped NiFe thin film with t_{NiFe}= 86 nm as the external field is rotated from an OOP configuration to 15° with respect to the OOP direction. S_{12} spectra at an external field of 13 kOe applied at the following angles to the OOP direction a) 0° b) 5° c) 10° d)15°. (e-h) The corresponding 2D map of the resonant spectra as a function of applied field and frequency. In (e) the orange dashed line is a guide to the eye of the evolution of PSSW2 with changes of the external field.

7.6.2 Simulation of the Angular Dependence of PSSWs

Numerical simulation was also used to explore the evolution of the resonances with rotation of the applied field from the perpendicular direction. The angular range explored in the simulation was 0^{o} to 16^{o}, a similar range to that measured in the experimental results reported in section 7.6.1, with an angular increment of 2^{o}. The case of a Pt capped NiFe layer possessing an $A_{ex} = 1 \times 10^{-6}$erg/cm only was simulated to at an angular increment of 1^{o}. A higher angular resolution for this case was motivated due to the lower difference of the reduced layer magnetisation from the bulk exhibited by Pt capped films (Table 7.4), thus a greater alignment with the expectations of the DP model. The simulated cases all possessed $t_{NiFe} = 86$ nm, selected to be consistent with the samples investigated in section 7.6.1.

In Figure 7.13 the evolution of the simulated spin wave spectrum for the Pt capped sample is presented. Importantly it is shown that, in agreement with experiment, the frequencies of the modes increase when the external field is applied at increasing angle from the perpendicular direction. Furthermore, it is demonstrated that, consistent with experimental findings, PSSW1 is supported at all angles in the range $0^{o} - 16^{o}$. The simulation also reveals that higher order PSSW modes ($p>1$), not detected in experiment, also persist. The continuation of PSSW2 is in marked contrast to experiment where it was found to be extinguished with any rotation of the external field. This is readily explained by examining the peak amplitude of PSSW2 which decreased below the sensitivity of the VNA-FMR instrument. Similar to experiment, it can also be seen in Figure 7.13 that the prominence of the PSSWs reduce with increasing angle to the perpendicular direction. This is shown most clearly in the case where the external field is applied at a angle of 16^{o}.

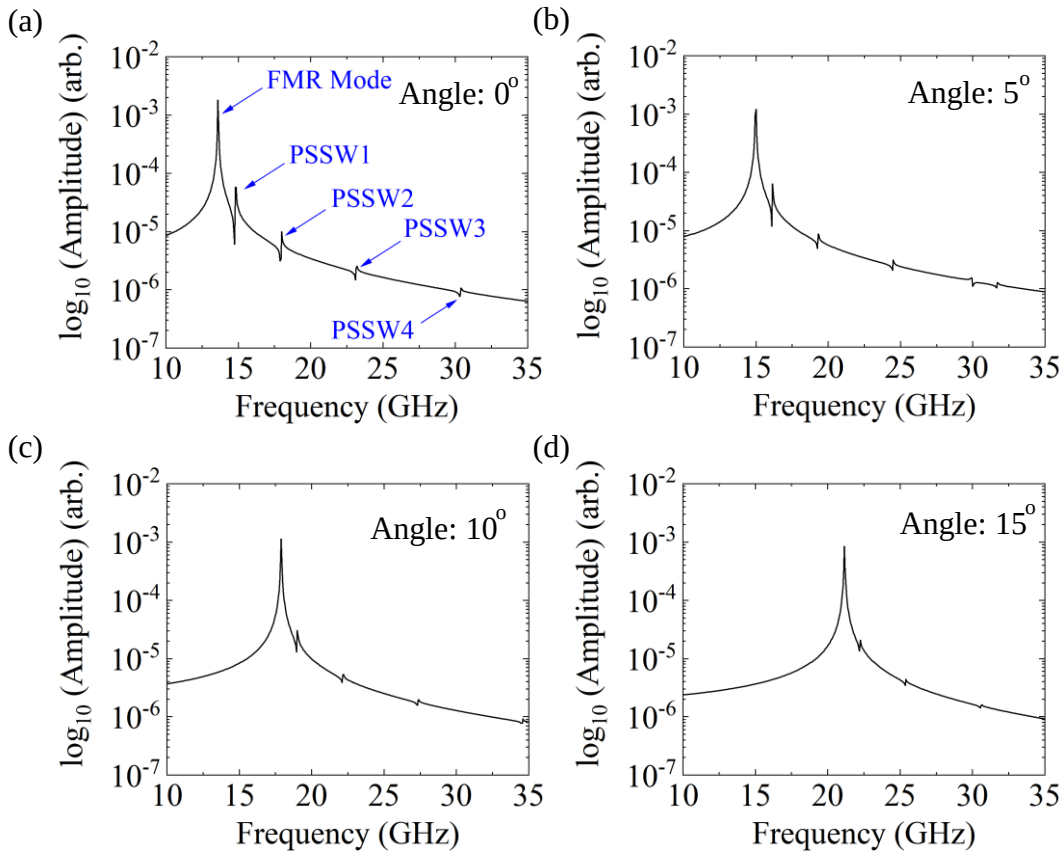

Figure 7.13: Simulated absorption spectra for evolution of the spin wave spectra of the Pt capped NiFe film with $t_{\mathrm{NiFe}} = 86$ nm and $A_{\mathrm{ex}} = 1 \times 10^{-6}$erg/cm, as the external field is rotated from the OOP direction by a) 0° b) 5° c) 10° d) 15°. The FMR label denotes the fundamental resonance mode whilst PSSW1, PSSW2, PSSW3, PSSW4 refer to the higher order PSSW excitations. The y-axes required a log scale to distinguish the higher order PSSW modes.

In Figure 7.14, the variation of the ratio of the peak amplitude of PSSW1 to the peak amplitude of the FMR mode with angle is shown for both the measurements and simulations. Two observations can be made. Firstly the peak amplitude of the PSSW1 peak reduces by a similar relative amount in both the experiments and simulation which is consistent with theory for dynamic pinning. Secondly, the amplitude ratios are different between the experimental results and the simulation by approximately a factor of 10. This likely reflects the difference between the idealised structure of the simulation, where a small region of reduced magnetisation is used to model dynamic pinning, and real samples where potentially several physical effects can contribute.

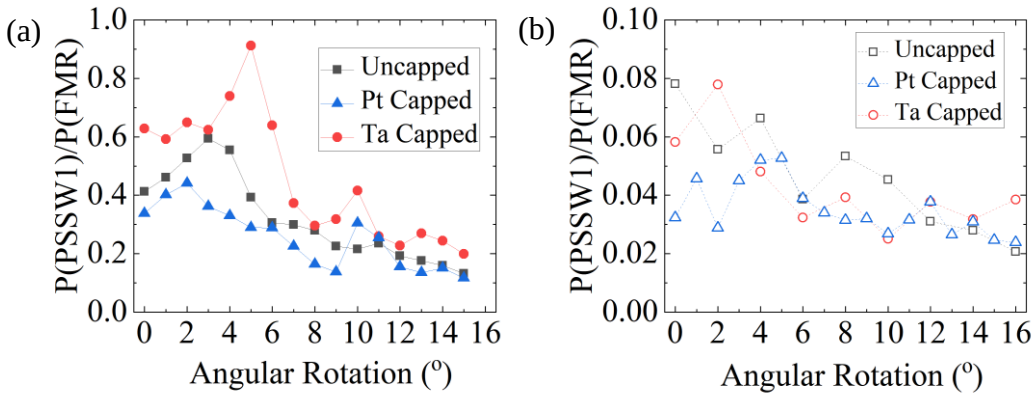

Figure 7.14: The ratio of the peak amplitude of PSSW1 to that of the FMR mode, as the external field is rotation from the OOP direction. For this measurement, a NiFe film with $t_{\mathrm{NiFe}} = 86\,\mathrm{nm}$ is considered. a) Experimental measurements b) Simulation results. The y-axis label P(PSSW1) and P(FMR) refer to the peak amplitude of the PSSW1 and FMR mode respectively.

A comparison of the simulated resonant frequencies of the NiFe films with $t_{\mathrm{NiFe}} = 86\,\mathrm{nm}$ in all capping layer cases with the experimental data is shown in Figure 7.15. The results of the numerical simulations and the experimental findings are in agreement, with similar increases in resonant frequencies with IP rotation exhibited. As expected, it is seen that a higher A_{ex} results in a greater increase of the frequencies of the modes [291].

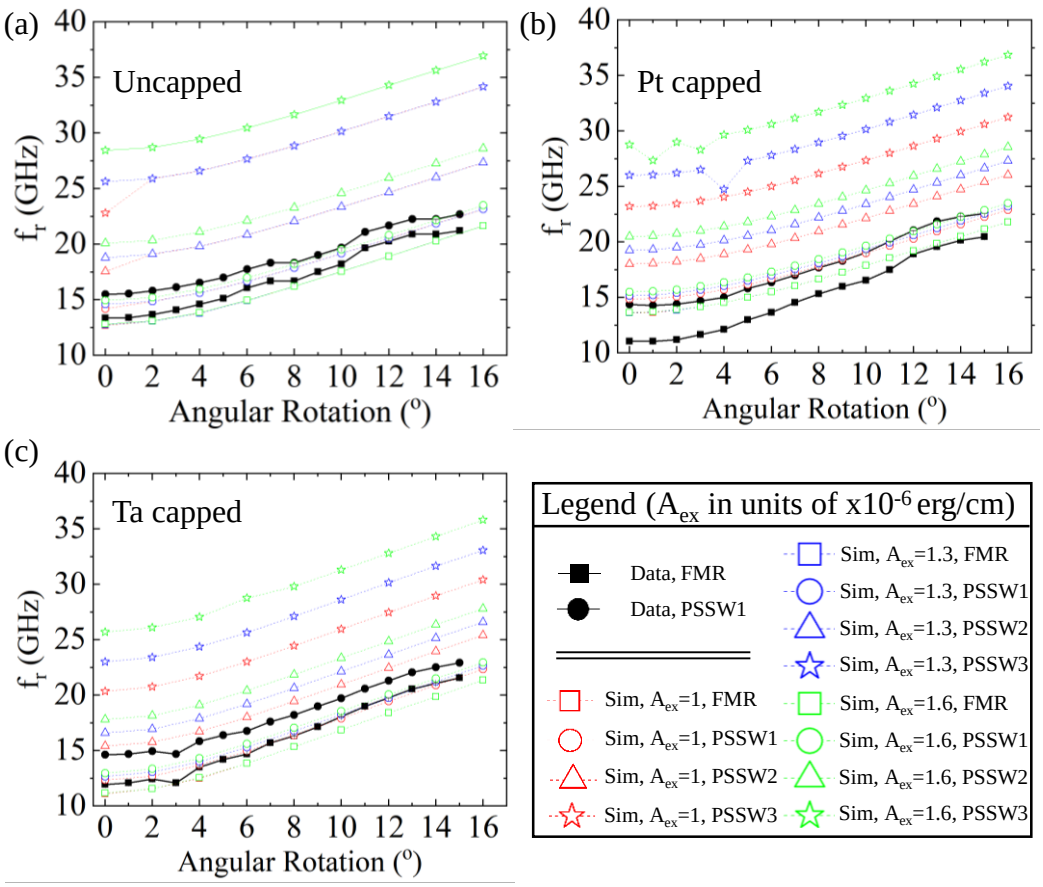

Figure 7.15: Measured and simulated resonant frequencies of the spin wave spectra exhibited by the films with $t_{\mathrm{NiFe}} = 86\,\mathrm{nm}$ with rotation of the external field from the OOP direction in the following capping layer cases a) Uncapped b) Pt capped c) Ta capped. A range of A_{ex} are explored in the simulation.

7.7 Chapter Summary

In summary, the dynamic properties of a series of NiFe thin films with differing layer thickness and capping layers have been explored. The data demonstrate that the magnetisation and g-factor are consistent across the range of thicknesses and different capping layer studied. The data also demonstrates that a simple analysis to extract a single value of the exchange constant, based on the surface pinning model of Kittel (equation 7.1), is unable to describe the resonant frequencies of the measured PSSWs. This is clearly inconsistent with the normal assumption that the measured A_{ex} is single valued. In order to address this physical inconsistency the data are first analysed in terms of an effective exchange constant.

The data show that there are similarities in the variation of the effective exchnage constant with NiFe layer thickness for samples with three different capping layers; uncapped, Pt and Ta. Specifically, for all films where the NiFe layer is thinner than ≈ 55 nm, the effective exchange constant is found to be roughly constant. At greater NiFe film thicknesses, the effective exchange constant obtained from the first PSSW mode (PSSW1) is larger and increases with thickness in the case of Pt or Ta capping layers. In all cases, the value extracted from corresponding second order PSSW mode (PSSW2) is approximately invariant to film thickness and exhibits a similar value to that extracted from PSSW1 for thin layers (thickness less than $\approx$55 nm). Additionally, it is seen that in all capping layer cases there exist an approximately linear dependence of the effective exchange constant on PSSW wavelength.

Numerical modelling has been performed to reconcile the concept of a single A_{ex} with the measured resonances. Attempts to reproduce the experimental data using the Kittel surface pinning mode failed. However, the simulations support the Dynamic Pinning (DP) model proposed by Wigen [139] by demonstrating that the measured resonances can be reproduced using a single A_{ex} by using a simulated structure that is comprised of a thin layer of reduced magnetisation at the film surface/interface in addition to the bulk layer. This model introduces the concept of dynamic pinning where the resonant condition of a thin layer close to the surface is different to that of the bulk of the film. Using this model, we are able to accurately simulate the experimentally measured PSSW data using a single value of the exchange constant. This finding supports the work of Kooi et al. [279], who concluded that evidence available in the 1960s tended to support a dynamic pinning (DP). However the magnetisation differences between the bulk and reduced layer required is greater than that assumed in the original DP model.

The DP model predicts that for small rotations of the applied magnetic field from the perpendicular, the spin wave spectra collapses into a single resonant mode. This is a key component of this model, which gives support to the dynamic pinning originating from a difference in magnetisation at the surface compared to the bulk. In order to test this prediction the dynamical response of the samples with rotation of the external field with respect to the OOP direction has been studied. Through both experiment and simulation, it has been observed that the prominence of the PSSW modes reduce significantly with respect to the fundamental mode at higher angles, but do not completely vanish above 10^{o} [139]. Due to the large reduction of the peak amplitudes of the PSSWs, it is likely that experimental measurement of this angle is dependent on the

sensitivity the experimental apparatus which is supported both by reports of a critical angle of 17^o [279] and by the fact that the simulations show a non-vanishing PSSW mode above 10^o [279].

Chapter 8

Conclusions

In summary, the work reported in this thesis has detailed the fabrication, comprehensive characterisation and analytical modelling or numerical simulation of a range of magnetic multilayer systems. The central research strand has been the investigation of the dynamic properties of thin magnetic films with the overall aims of

1. Increasing the understanding of the dynamic responses attainable in a range of multilayered materials comprised of ultrathin magnetic films.

2. The development of new methodologies to characterise the important parameters governing the resonant dynamics exhibited by such magnetic multilayers.

In the following, the conclusions of each investigation are presented along with potential areas for further investigation.

8.1 Synthetic Antiferromagnetic Dynamics

8.1.1 Conclusions

The work reported in Chapter 5 detailed the fabrication of a number of synthetic antiferromagnetic thin films displaying a range of low field Optic Mode (OM) dynamics. From this sample series, the highest OM resonant frequencies in Synthetic Antiferromagnets (SAFs) at zero applied magnetic field observed to date is exhibited. The measured resonant frequencies at zero field were (18.2 ± 1.2) GHz and (21.13 ± 0.01) GHz for samples on the first and second antiferromagnetic (AF) peaks of the RKKY interlayer exchange coupling respectively. This is approximately an order of magnitude increase compared to the resonance frequency of a single CoFeB layer (2.8 ± 0.1) GHz, and twice as great as that previously recorded [48]. An analytical model developed by Rezende et al. [172] that can successfully reproduce all the major features of the high frequency response of the SAFs has been used to extract key magnetic parameters including uniaxial anisotropies and effective exchange couplings. The parameters

obtained from the model are consistent with the data with only small differences compared with the values expected from static measurements. A key finding of this work is the demonstration that smoother CoFeB/Ru interfaces offers one route to achieving higher frequency zero field resonances. The reported structural, static and dynamic characterisations demonstrates the use of the second RKKY, and possibly also higher order, AF peaks to enhance the zero field resonance frequency of synthetic antiferromagnetic systems up to the high 10s GHz range.

8.1.2 Further Work

There is significant potential for additional studies in this area to further enhance the zero field resonant frequencies of SAF structures. These investigations center around the optimisation of the SAF structure to maximise all the physical parameters that contribute to the OM frequency. In particular, the study of the material parameters (both magnetic properties and the morphology of the ultrathin layers) is paramount. Specifically, the relevant properties are the saturation magnetisation (M_S), the uniaxial anisotropy (H_k) and the RKKY interlayer exchange coupling strength (J_{IEC}) [51]. As CoFeB alloys already possess a high M_S [223], the potential enhancement of the OM frequency from increasing this property is small and should not be a major focus. Instead, attempts should be made to increase the H_K possessed by the ferromagnetic (FM) layers either by applying in-situ magnetic fields throughout deposition or through the use of materials naturally possessing these higher anisotropy values. For example, materials possessing a perpendicular magnetic anisotropy, such as FePt [293] or MnAl [294], could be explored. Additional investigations to attain a greater J_{IEC} are also recommended. This work could build upon the insights regarding the importance of layer roughness and interface quality reported in this chapter. Such a research program could involve varying the sputtering parameters used to fabricate the Ru layer to a much greater extent than studied in this project. For example, the parameter space of different sputtering powers, working pressures and temperatures, either throughout deposition or as an annealing step, should be explored. The impact on the achievable J_{IEC} through the use of exchange decoration layers, consisting of a high moment material such as Co or CoFe, employed at the Ru interface could also be assessed due to the significant increases this approach has generated in other works [295–297].

8.2 Synthetic Ferromagnetic Dynamics

8.2.1 Conclusions

In this work, reported in Chapter 6, the experimental observation and numerical simulation of the resonant dynamics of Synthetic Ferromagnets (SFMs) has been detailed. Though widely utilised in quasi-static devices [44, 265, 266], such as STT-MRAM and magnetic sensors, until now there is very little literature on comprehensive investigations carried out regarding the high frequency response of such systems. The studied SFM samples exhibited magnetic properties consistent with possessing a J_{IEC} on the first FM RKKY coupling peak. Numerical simulations utilising Mumax^3 [239] have been performed to explore the dependence of the Acoustic Mode (AM) and OM supported by SFMs on the difference in layer magnetisation of the FM layers (ΔM) and J_{IEC}. These simulations have revealed that an orthogonal dependence exists, where the AM exhibits a greater sensitivity to ΔM whilst the OM is more dependent on J_{IEC}. Thus, a precise method to determine these parameters through comparisons of the measured resonance frequencies and simulations is provided. From application of this methodology to the SFM samples, it can be determined that they possess a much lower ΔM than reported in other works, whilst the J_{IEC} is consistent with literature expectations [44]. Furthermore, using these extracted parameters, the phase behavior of the magnetic layers at each resonant mode can be obtained by numerical simulation. Notably, it is demonstrated that the conventional acoustical and optical description of the precession of these modes does not capture the intricacy of the dynamics exhibited by these structures. This work is of potential use in the development of future exchange coupled spintronic materials and offer is complementary to developing synchrotron techniques.

8.2.2 Further Work

The additional investigations that could be carried out in this area include‘ the application of the developed methodology to SFMs comprised of a different material sets. The overall aim of such a work plan would be to assess the J_{IEC} attainable in various SFM structures. This would aim to address previous difficulties in extracting the J_{IEC} present within SFMs, a long-standing problem in the study of such systems. Furthermore, the reported investigation has refined the understanding of the phase differences of the magnetic layers possessed by each resonant mode beyond the conventional AM

and OM labelling. Using the developed methodology, experimental demonstration of the control of the rich resonant dynamics supported in such SFM structures could be performed. This would be an important step to highlight the potential to exploit the resonant phase of SFM dynamics for tailored spintronic devices. Furthermore, beyond the SFM case, this methodology could also be applied to their SAF counterparts. Such an approach could build upon the analytical modelling already performed on the SAF samples studied, further enriching our understanding of the dynamics of the high frequency zero field OM exhibited by such structures.

8.3 Perpendicular Stationary Spin Waves

8.3.1 Conclusions

The study reported in Chapter 7 concerns an investigation into the dynamic properties of a series of NiFe thin films with varying thickness and capping layer materials. It was found that the g-factor and magnetisation of the films were consistent across the range of capping layer and thicknesses studied. However, the data demonstrates that a single value of the exchange constant (A_{ex}), based on the surface pinning model of Kittel (equation 7.1) [138], is unable to describe the resonant frequencies of the measured Perpendicular Stationary Spin Waves (PSSWs). In order to quantify this effect the data is analysed first in terms of an effective exchange constant ($A_{\mathrm{ex,eff}}$), with it found this value decreased with mode number and, above a certain NiFe layer thickness, steadily increased with layer thickness.

To address this physical inconsistency, the micromagnetics simulation software Mumax^3 [239] was used to provide further insights. The two models historically used to describe PSSWs were investigated; namely the surface pinning (SP) model developed by Kittel [138] and the dynamic pinning (DP) model put forth by Wigen et al. [139]. Notably, it was found that the SP model failed to reproduce the measured spin-wave spectra. Instead by modelling the the structure as inspired by the DP model, specifically as a bilayer consisting of a few surface atomic layers of reduced magnetisation exchange-coupled to the bulk of the film, the full range of experimental data was able to be reproduced. It was noted that the magnetisation differences between the reduced layer and the bulk is greater than that assumed in the original DP model.

Furthermore, the critical angle predicted by the DP model, specifically that for

small rotations of the applied magnetic field from the perpendicular direction the spin-wave spectra collapses into a single resonant mode, was tested. Through both experiment and simulation, it has been observed that the prominence of the PSSW modes reduce significantly with respect to the fundamental mode at higher angles but do not completely vanish above 10^{o} [139]. Due to the large reduction of the peak amplitudes of the PSSWs, it is likely that experimental measurement of this angle is dependent on the sensitivity the experimental apparatus which is supported both by reports of a critical angle of 17^{o} [279] and by the fact that the simulations show a non-vanishing PSSW mode above 10^{o}.

8.3.2 Further Work

There are a plethora of further investigations that could expand upon the presented study. Such investigations would be motivated by the desire to achieve a more thorough understanding of A_{ex} for fundamental science, micromagnetic simulations and device applications. For example, an additional study of the evolution of PSSWs as the external field is applied at larger angles to perpendicular direction than explored here is warranted. This would allow a complete verification of the critical angle phenomena beyond that possible in this work. As the presence of a critical angle supports the hypothesis that dynamic pinning arises from a difference in magnetisation of a few atomic surface layers [139] this would be particularly insightful to elaborating on this mechanism.

Furthermore, investigations similar to this study utilising different material sets could be performed. This would permit further comparisons of the applicability of the SP and DP model to PSSWs across a range of material systems along with providing insights into an accurate method for the determination of A_{ex} from spin-wave spectra. An assessment of the critical angle of these systems would also be particularly insightful to study the mechanism responsible for dynamic pinning. As PSSWs can be observed at a range of temperatures, the methodologies discussed in this report could also be applied to characterise the variation of A_{ex} with temperature.

Lastly the experimental findings have indicated that as film thickness reduces the value of $A_{ex,eff}$ reaches an asymptotic value. The applicability of such measurements to determine the exchange constant of films too thin to support measurable PSSWs should therefore be tested. This would necessitate the use of other methods to determine A_{ex}, such as analysis of thermal magnons [1] for example, for comparative purposes. The findings of an investigation of this kind could be of crucial importance to a range of

developing technologies incorporating ultrathin magnetic layers such as STT-MRAM and STNOs [27].

Appendix A

Presentations and Publications

A.1 Awards

- *Best Student Speaker Finalist*, Magnetism and Magnetic Materials (MMM), 2020.
- *IEEE Magnetics Summer School*, Quito, Ecuador, 2018.

A.2 Presentations

A.2.1 Oral Presentations

- *Characterizing Interlayer Coupling in Synthetic Ferromagnetic Thin Films*, Intermag, 2021.
- *Zero field optic mode beyond 20 GHz in a Synthetic Antiferromagnet*, Magnetism and Magnetic Materials (MMM), 2020.
- *Zero field optic mode beyond 20 GHz in a Synthetic Antiferromagnet*, Magnetism and Magnetic Materials (MMM), 2020.
- *Zero field optic mode beyond 20 GHz in a Synthetic Antiferromagnet*, Current Research in Magnetism (CRIM), 2020.

A.2.2 Poster Presentations

- *Zero field optic mode beyond 20 GHz in a Synthetic Antiferromagnet*, Magnetism, Sheffield, UK, 2020. (Cancelled Due to Covid Pandemic)
- *Synthetic Antiferromagnets*, Magnetism, Leeds, UK, 2019.
- *Characterisation of Perpendicular Stationary Spin Waves in Thin Permalloy Films Using VNA-FMR*, International Conference for Microwave Magnetic Materials (ICMM), Exeter, UK, 2018.

- *Ferromagnetic Resonance Modes in Coupled Magnetic Thin Films*, IEEE Magnetics Summer School, Quito, Ecuador, 2018.
- *Ferromagnetic Resonant Modes of Magnetic Thin Film Structures*, Magnetism, Manchester, UK, 2018.

A.3 Publications

- Waring H.J., Johansson N.A.B., Vera-Marun I.J. and Thomson T., Zero-field Optic Mode Beyond 20 GHz in a Synthetic Antiferromagnet. Physical Review Applied, 13(3), p.034035. 2020.
- Waring H.J., Li Y., Johansson N.A.B., Moutafis C. and Thomson T., Exchange Constant Determination using Multiple-Mode FMR Perpendicular Standing Spin Waves. (Physical Review Letters: Manuscript In Preparation).
- Waring H.J., Li Y., Moutafis C., Vera-Marun I.J. and Thomson T., Magnetization Dynamics in Synthetic Ferromagnetic Thin Films, Physical Review B, 104(1), p.014419. 2021.
- Li Y., Waring H.J., Moutafis C., Vera-Marun I.J. and Thomson T., Simulating exchange-coupling/magnetisation FMR phase space of exchange coupled layers. (Physical Review Applied: Manuscript In Preparation).

Appendix B

Mumax^3 simulation code

The Mumax^3 code developed by Mr Yu Li for the investigations reported in Chapter 6 and 7 is presented.

B.1 Synthetic Ferromagnet Investigation

The Mumax^3 code utilised for the study of the synthetic ferromagnets (SFMs), as reported in Chapter 6 is available in this section.

B.1.1 Resonant Frequencies

The resonant frequencies of the SFMs were simulated using the following script. This method relied on the Ringdown method, as outlined in section 4.4.1. The current parameter inputs are for example purposes only.

```
//Magnetic Parameters
RKKY:=0.04e-3
M_sat0:=1100e3
M_sat2:=1300e3
alpha =0.001
Aex =1e-11
Msat =(M_sat0+M_sat2)/2

//Geometry
cellX:=1e-9
cellY:=1e-9
cellZ:=0.5e-9
setGridSize(128,128,22)
setCellSize(cellX,cellY,cellZ)
setPBC(16,16,0)
```

```
setgeom(layers(0,10).add(layers(12,22)))
t_spacer := cellZ*2

//Initialise RKKY coupling
F_I:=RKKY*t_spacer/(cellZ*cellZ*(M_sat0+M_sat2)/2)
Li:=layer(9)
B_i:=Madd(m,shifted(m, 0, 0, -3), -F_I, F_I)
Li3:=layer(12)
B_i3:=Madd(m,shifted(m,0,0,3),-F_I,F_I)
B_ex:=Add(Masked(B_i, Li),Masked(B_i3,Li3))
E_ex:=Mul(Mul(Const(-0.5), Msat),Dot(m, B_ex))
AddFieldTerm(B_ex)
AddEdensTerm(E_ex)

//Define regions (ie. create FM/NM/FM structure)
for ii:=100;ii<122;ii+= 1{
Defregion(ii, layer(ii-100))
}
for ii := 100; ii < 110; ii += 1 {
Msat.setregion(ii, M_sat0)
}
for ii := 112; ii < 122; ii += 1 {
Msat.setregion(ii, M_sat2)
}
EnableDemag = true
m = uniform(1, 1, 1)

//Setup external field
degree := 30       //Angle of external field
radDeg := degree * pi / 180
B_mag := 0.4      //External field strength
B_ext = vector(B_mag*cos(radDeg), B_mag*sin(radDeg), 0)
relax()
minimize()
B_ext = vector(B_mag*cos(radDeg+0.001), B_mag*sin(radDeg+0.001), 0)
```

```
// Run simulation
tableautosave(1e-13)
run(50e-9)
```

B.1.2 Resonant Phases

The resonant phases of the SFMs was simulated using the following script. The current parameter inputs are for example purposes only.

```
//Magnetic Parameters
Aex = 13e-12
alpha = 0.0010
RKKY := 0.026e-3
alpha = 0.001
M_sat0 := 1125e3
M_sat2 := 1300e3
Msat = (M_sat0 + M_sat2) / 2

//Set excitation frequency
freq_exc := 24.01e9  //Frequency of mode under consideration

//Geometry
cellX := 1e-9
cellY := 1e-9
cellZ := 0.5e-9
setGridSize(64, 64, 22)
setCellSize(cellX, cellY, cellZ)
setPBC(16, 16, 0)
t_spacer := cellZ * 2
setgeom(layers(0, 10).add(layers(12, 22)))
for ii := 100; ii < 122; ii += 1 {
Defregion(ii, layer(ii-100))
tableadd(m.comp(2).region(ii))
}
```

```
//Initialise RKKY coupling
F_I := RKKY * t_spacer / (cellZ * cellZ * (M_sat0 + M_sat2) / 2)
Li := layer(9)
B_i := Madd(m, shifted(m, 0, 0, -3), -F_I, F_I)
Li3 := layer(12)
B_i3 := Madd(m, shifted(m, 0, 0, 3), -F_I, F_I)
B_ex := Add(Masked(B_i, Li), Masked(B_i3, Li3))
E_ex := Mul(Mul(Const(-0.5), Msat), Dot(m, B_ex))
AddFieldTerm(B_ex)
AddEdensTerm(E_ex)

//Define regions (ie. create FM/NM/FM structure)
for ii := 100; ii < 110; ii += 1 {
Msat.setregion(ii, M_sat0)
}
for ii := 112; ii < 122; ii += 1 {
Msat.setregion(ii, M_sat2)
}
EnableDemag = true
m = uniform(1, 1, 1)

//Setup external fields
degree := 30       //Angle of external field
radDeg := degree * pi / 180
B_mag := 0.4      //External field strength
B_ext = vector(B_mag*cos(radDeg), B_mag*sin(radDeg), 0)
relax()
minimize()

B_exc := 0.1e-4      //Excitation field strength
B_ext = vector(B_mag*cos(radDeg)-B_exc*sin(radDeg)
*sin(2*pi*freq_exc*t),B_mag*sin(radDeg)
+B_exc*cos(radDeg)*cos(2*pi*freq_exc*t), 0)

// Run simulation
```

```
tableautosave(1e-13)
run(10e-9)
```

B.2 Perpendicular Stationary Spin Waves Investigation

The Mumax^3 code utilised for the study of the Perpendicular Stationary Spin Waves (PSSWs), as reported in Chapter 7, is presented.

B.2.1 Resonant Frequencies

The resonant frequencies of the spin-wave spectra were simulated using the following script. This method relied on the Ringdown method, as outlined in section 4.4.1. Due to the capping layers under consideration, two versions of this code was developed to simulate the ferromagnetic reduced magnetisation layers (present in Pt and Ta capped cases) and the antiferromagnetic layer (present in the uncapped case). The current parameter inputs are for example purposes only.

Ferromagnetic reduced layer case

```
//Magnetic Parameters
//Global parameters
Aex = 13e-12
alpha = 0.0010
//Bulk layer
Ms_NiFe := 661.7e3  //Set equal to effective magnetisation
                   //(as measured from VNA-FMR measurements)
Thick_NiFe := 86    //Thickness of bulk layer
//FM reduced magnetisation layer (at surface)
Ms_reduced := 500e3   //Reduced magnetisation layer
Thick_Reduced := 5    //Thickness of reduced
                     //magnetisation layer

//Geometry
Thick_total := Thick_NiFe + Thick_Reduced
SetCellSize(2e-9, 2e-9, 1e-9)
SetGridSize(64, 64, 48)
```

```
setpbc(16, 16, 0)
SetGridSize(128, 128, Thick_total)

//Define regions (ie. create Bulk layer/Surface
//layer structure)
DefRegion(1, Layers(Thick_NiFe, Thick_total))
DefRegion(2, Layers(0, Thick_NiFe))
Msat.setregion(1, Ms_reduced)
Msat.setregion(2, Ms_NiFe)
angle := 9 * pi / 180
m = uniform(0.01, 0.1, 1)

//Setup external field
B_mag := 1.3      //External field strength
B_deg := 5       //Angle of external field
tableadd(B_ext)
tableaddvar(B_deg, "Bdeg", "deg")
B_ext = vector(0, B_mag*sin(angle), B_mag*cos(angle))
relax()
minimize()
B_ext = vector(0, B_mag*sin(angle+0.0015), B_mag*cos(angle+0.0015))

//Run
tableautosave(1e-13)
run(20e-9)
```

Antiferromagnetic reduced layer case

```
//Magnetic Parameters
//Global parameters
alpha = 0.0010
//Bulk layer
Ms_NiFe := 688.4e3
Thick_NiFe := 86
A_FM := 13e-12
//AF layer (at surface)
```

```
Thick_Reduced := 2  // AF layer thickness
A_AFM := A_FM * -0.5
Cz := 1e-9
J_I := A_AFM / Cz
J_I_FM := A_FM / Cz

//Geometry
Thick_total := Thick_NiFe + Thick_Reduced + 1
SetCellSize(2e-9, 2e-9, 1e-9)
SetGridSize(128, 128, Thick_total)
setpbc(16, 16, 0)
setgeom(layers(0, Thick_total-2).add(layer(Thick_total - 1)))

//Define regions (ie. create Bulk layer/Surface
//layer structure)
defregion(0, layers(0, Thick_NiFe)) //Bulk FM layer
defregion(1, layer(Thick_total-3))  // AF layer
defregion(2, layer(Thick_total-1))  // AF layer
Msat = Ms_NiFe
Aex.setregion(0, A_FM)
Aex.setregion(1, A_FM)
Aex.setregion(2, A_FM)
NoDemagSpins.SetRegion(2, 1)  // No demag effects
NoDemagSpins.SetRegion(1, 1)  // No demag effects

// Setup AF layer interfacial effects
F_I := J_I / (Cz * Ms_NiFe)
Li := layer(Thick_total - 3)
B_i := Madd(m, shifted(m, 0, 0, -2), -F_I, F_I)
Li3 := layer(Thick_total - 1)
B_i3 := Madd(m, shifted(m, 0, 0, 2), -F_I, F_I)
B_ex := Add(Masked(B_i, Li), Masked(B_i3, Li3))
E_ex := Mul(Mul(Const(-0.5), Msat), Dot(m, B_ex))
AddFieldTerm(B_ex)
AddEdensTerm(E_ex)
```

```
F_I_2 := J_I_FM / (Cz * Ms_NiFe)
Li_2 := layer(Thick_total - 4)
B_i_2 := Madd(m, shifted(m, 0, 0, -3), -F_I_2, F_I_2)
Li3_2 := layer(Thick_total - 1)
B_i3_2 := Madd(m, shifted(m, 0, 0, 3), -F_I_2, F_I_2)
B_ex_2 := Add(Masked(B_i_2, Li_2), Masked(B_i3_2, Li3_2))
E_ex_2 := Mul(Mul(Const(-0.5), Msat), Dot(m, B_ex_2))
AddFieldTerm(B_ex_2)
AddEdensTerm(E_ex_2)
tableadd(m.comp(1).region(0))

//Setup external field
tableadd(B_ext)
B_mag := 1.3      //External field strength
B_deg := 5        //Angle of external field
tableaddvar(B_deg, "Bdeg", "deg")
angle := 2 * pi / 180
m = uniform(0.01, 0.1, 1)
B_ext = vector(0, B_mag*sin(angle), B_mag*cos(angle))
relax()
minimize()
B_ext = vector(0, B_mag*sin(angle+0.0015), B_mag*cos(angle+0.0015))

//Run
tableautosave(1e-13)
run(20e-9)
```

B.2.2 PSSW Waveform

The code required to simulate the waveform of the spin-wave spectra, as detailed in section 7.5.1, is presented. As these waveforms were only simulated in the case of a ferromagnetic reduced layer, only code considering this case was developed.

```
//Magnetic Parameters
//Global parameters
Aex = 13e-12
```

```
alpha = 0.0010
//Bulk layer
Ms_NiFe := 661.7e3
Thick_NiFe := 86
//FM Reduced layer
Thick_Reduced := 5
Ms_reduced := 500e3

//Set excitation frequency
freq_exc := 13.6e9  //PSSW mode frequency

//Geometry
Thick_total := Thick_NiFe + Thick_Reduced
SetCellSize(2e-9, 2e-9, 1e-9)
SetGridSize(64, 64, 48)
setpbc(16, 16, 0)
SetGridSize(128, 128, Thick_total)

//Define regions (ie. create Bulk layer/surface
//layer structure)
Msat = Ms_NiFe
for ii := 0; ii < Thick_total; ii++ {
defregion(ii, layer(ii))
tableadd(m.comp(0).region(ii))
tableadd(m.comp(1).region(ii))
}
for ii := 0; ii < Thick_NiFe; ii++ {
Msat.setregion(ii, Ms_NiFe)
}
for ii := Thick_NiFe; ii < Thick_total; ii++ {
Msat.setregion(ii, Ms_reduced)
}
tableadd(B_ext)
tableadd(E_total)
```

```
m = uniform(0.01, 0.1, 1)

//Set up external fields
B_mag := 1.3        //External field strength
B_ext = vector(0, B_mag*sin(angle),B_mag*cos(angle))
angle := 0 * pi / 180  //Angle of external field
relax()
minimize()
B_exc := 1e-6     //Excitation field strength
B_ext = vector(B_exc*sin(2*pi*freq_exc*t), B_mag*sin(angle)
-B_exc*cos(angle)*cos(2*pi*freq_exc*t),B_mag*cos(angle)
+B_exc*sin(angle)*cos(2*pi*freq_exc*t))

//Run
tableautosave(1e-13)
run(20e-9)
```

References

[1] J. Coey, *Magnetism and magnetic materials*. Cambridge university press, 2010.

[2] S. Vonsovskii, *Ferromagnetic Resonance*. Oxford: Pergamon Press, 1966.

[3] M. Farle, "Ferromagnetic resonance of ultrathin metallic layers," *Reports on Progress in Physics*, vol. 61, no. 7, p. 755, 1998.

[4] R. Hitchcock, *Radio-frequency and microwave radiation*. AIHA, 2004.

[5] J. Griffiths, "Anomalous high-frequency resistance of ferromagnetic metals," *Nature*, vol. 158, no. 4019, pp. 670–671, 1946.

[6] C. Kittel, "On the theory of ferromagnetic resonance absorption," *Physical Review*, vol. 73, no. 2, p. 155, 1948.

[7] D. Stancil and A. Prabhakar, *Spin waves*. Springer, 2009, vol. 5.

[8] A. Barman and A. Haldar, "Time-domain study of magnetization dynamics in magnetic thin films and micro-and nanostructures," *Solid State Physics*, vol. 65, pp. 1–108, 2014.

[9] J. Fullerton E.E.and Childress, "Spintronics, magnetoresistive heads, and the emergence of the digital world," *Proceedings of the IEEE*, vol. 104, no. 10, pp. 1787–1795, 2016.

[10] A. Fert, "Origin, development, and future of spintronics (Nobel lecture)," *Angewandte Chemie International Edition*, vol. 47, no. 32, pp. 5956–5967, 2008.

[11] A. Hirohata, K. Yamada, I. Nakatani Y.and Prejbeanu, B. Diény, and B. Pirro P.and Hillebrands, "Review on spintronics: Principles and device applications," *Journal of Magnetism and Magnetic Materials*, vol. 509, p. 166 711, 2020.

[12] S. Wolf, A. Chtchelkanova, and D. Treger, "Spintronics—A retrospective and perspective," *IBM Journal of Research and Development*, vol. 50, no. 1, pp. 101–110, 2006.

[13] J. Daughton, "Spin-dependent sensors," *Proceedings of the IEEE*, vol. 91, no. 5, pp. 681–686, 2003.

[14] D. Heim, R. Fontana, C. Tsang, V. Speriosu, B. Gurney, and M. Williams, "Design and operation of spin valve sensors," *IEEE Transactions on Magnetics*, vol. 30, no. 2, pp. 316–321, 1994.

[15] P. Braganca, B. Gurney, B. Wilson, J. Katine, S. Maat, and J. Childress, "Nanoscale magnetic field detection using a spin torque oscillator," *Nanotechnology*, vol. 21, no. 23, p. 235 202, 2010.

[16] M. Pardavi-Horvath, "Microwave applications of soft ferrites," *Journal of Magnetism and Magnetic Materials*, vol. 215, pp. 171–183, 2000.

[17] V. Harris, "Modern microwave ferrites," *IEEE Transactions on Magnetics*, vol. 48, no. 3, pp. 1075–1104, 2011.

[18] J. Adam, L. Davis, G. Dionne, E. Schloemann, and S. Stitzer, "Ferrite devices and materials," *IEEE Transactions on Microwave Theory and Techniques*, vol. 50, no. 3, pp. 721–737, 2002.

[19] R. Camley, Z. Celinski, and R. Stamps, *Magnetism of surfaces, interfaces, and nanoscale materials*. Elsevier, 2015.

[20] W. Palmer, D. Kirkwood, S. Gross, M. Steer, H. Newman, and S. Johnson, "A bright future for integrated magnetics: Magnetic components used in microwave and mm-wave systems, useful materials, and unique functionalities," *IEEE Microwave Magazine*, vol. 20, no. 6, pp. 36–50, 2019.

[21] A. Barman, S. Mondal, S. Sahoo, and A. De, "Magnetization dynamics of nanoscale magnetic materials: A perspective," *Journal of Applied Physics*, vol. 128, no. 17, p. 170 901, 2020.

[22] S. Swann, "Magnetron sputtering," *Physics in technology*, vol. 19, no. 2, p. 67, 1988.

[23] P. Martin, *Handbook of deposition technologies for films and coatings: science, applications and technology*. William Andrew, 2009.

[24] P. Kelly and R. Arnell, "Magnetron sputtering: A review of recent developments and applications," *Vacuum*, vol. 56, no. 3, pp. 159–172, 2000.

[25] I. Žutić, J. Fabian, and S. Sarma, "Spintronics: Fundamentals and applications," *Reviews of modern physics*, vol. 76, no. 2, p. 323, 2004.

[26] C. Li, G. Chai, C. Yang, W. Wang, and D. Xue, "Tunable zero-field ferromagnetic resonance frequency from S to X band in oblique deposited CoFeB thin films," *Scientific Reports*, vol. 5, no. 1, pp. 1–7, 2015.

[27] B. Dieny, I. Prejbeanu, K. Garello, P. Gambardella, P. Freitas, R. Lehndorff, W. Raberg, U. Ebels, S. Demokritov, J. Akerman, and A. Deac, "Opportunities and challenges for spintronics in the microelectronics industry," *Nature Electronics*, vol. 3, no. 8, pp. 446–459, 2020.

[28] G. Akpakwu, B. Silva, G. Hancke, and A. Abu-Mahfouz, "A survey on 5G networks for the Internet of Things: Communication technologies and challenges," *IEEE Access*, vol. 6, pp. 3619–3647, 2017.

[29] A. Hirohata and K. Takanashi, "Future perspectives for spintronic devices," *Journal of Physics D: Applied Physics*, vol. 47, no. 19, p. 193 001, 2014.

[30] R. Macêdo, K. Livesey, and R. Camley, "Using magnetic hyperbolic metamaterials as high frequency tunable filters," *Applied Physics Letters*, vol. 113, no. 12, p. 121 104, 2018.

[31] M. Jungfleisch, W. Zhang, and A. Hoffmann, "Perspectives of antiferromagnetic spintronics," *Physics Letters A*, vol. 382, no. 13, pp. 865–871, 2018.

[32] T. Jungwirth, X. Marti, P. Wadley, and J. Wunderlich, "Antiferromagnetic spintronics," *Nature Nanotechnology*, vol. 11, no. 3, pp. 231–241, 2016.

[33] D Sander, S. Valenzuela, D. Makarov, C. Marrows, E. Fullerton, P. Fischer, J. McCord, P. Vavassori, S. Mangin, P. Pirro, and B. Hillebrands, "The 2017 magnetism roadmap," *Journal of Physics D: Applied Physics*, vol. 50, no. 36, p. 363 001, 2017.

[34] E. Gomonay and V. Loktev, "Spintronics of antiferromagnetic systems," *Low Temperature Physics*, vol. 40, no. 1, pp. 17–35, 2014.

[35] B. D. Cullity and C. Graham, *Introduction to magnetic materials*. John Wiley & Sons, 2011.

[36] R. Khan, H. Nembach, J. Ali M.and Shaw, C. Marrows, and T. Moore, "Magnetic domain texture and the Dzyaloshinskii-Moriya interaction in Pt/Co/IrMn and Pt/Co/FeMn thin films with perpendicular exchange bias," *Physical Review B*, vol. 98, no. 6, p. 064 413, 2018.

[37] J. MacNeill D.and Hou, D. Klein, P. Zhang, P. Jarillo-Herrero, and L. Liu, "Gigahertz frequency antiferromagnetic resonance and strong magnon-magnon coupling in the layered crystal $CrCl_3$," *Physical Review Letters*, vol. 123, no. 4, p. 047 204, 2019.

[38] R. Duine, K. Lee, S. Parkin, and M. Stiles, "Synthetic antiferromagnetic spintronics," *Nature Physics*, vol. 14, no. 3, pp. 217–219, 2018.

[39] B. Kuanr, R. Camley, and Z. Celinski, "Extrinsic contribution to Gilbert damping in sputtered NiFe films by ferromagnetic resonance," *Journal of Magnetism and Magnetic Materials*, vol. 286, pp. 276–281, 2005.

[40] B. Heinrich and J. Cochran, "Ultrathin metallic magnetic films: Magnetic anisotropies and exchange interactions," *Advances in Physics*, vol. 42, no. 5, pp. 523–639, 1993.

[41] S. Parkin and D Mauri, "Spin engineering: Direct determination of the Ruderman-Kittel-Kasuya-Yosida far-field range function in ruthenium," *Physical Review B*, vol. 44, no. 13, p. 7131, 1991.

[42] M. Baibich, J. Broto, A. Fert, F. Van Dau, F. Petroff, P. Etienne, G. Creuzet, A. Friederich, and J. Chazelas, "Giant magnetoresistance of (001)Fe/(001)Cr magnetic superlattices," *Physical Review Letters*, vol. 61, no. 21, p. 2472, 1988.

[43] P. Grünberg, R. Schreiber, Y. Pang, M. Brodsky, and H. Sowers, "Layered magnetic structures: Evidence for antiferromagnetic coupling of Fe layers across Cr interlayers," *Physical Review Letters*, vol. 57, no. 19, p. 2442, 1986.

[44] T. McKinnon, P. Omelchenko, B. Heinrich, and E. Girt, "FMR study of interlayer exchange coupling in FeCoB—Ta—FeCoB trilayers with in-plane anisotropy," *Journal of Applied Physics*, vol. 123, no. 22, p. 223 903, 2018.

[45] P. Bruno and C. Chappert, "Oscillatory coupling between ferromagnetic layers separated by a nonmagnetic metal spacer," *Physical Review Letters*, vol. 67, no. 12, p. 1602, 1991.

[46] S. Byeon, A. Misra, and W. Doyle, "Synthetic antiferromagnetic soft underlayers for perpendicular recording media," *IEEE Transactions on Magnetics*, vol. 40, no. 4, pp. 2386–2388, 2004.

[47] S. Ikegawa, F. Mancoff, J. Janesky, and S. Aggarwal, "Magnetoresistive random access memory: Present and future," *IEEE Transactions on Electron Devices*, vol. 67, no. 4, pp. 1407–1419, 2020.

[48] S. Li, Q. Li, J. Xu, S. Yan, G. Miao, S. Kang, Y. Dai, J. Jiao, and Y. Lü, "Tunable optical mode ferromagnetic resonance in FeCoB/Ru/FeCoB synthetic antiferromagnetic trilayers under uniaxial magnetic anisotropy," *Advanced Functional Materials*, vol. 26, no. 21, pp. 3738–3744, 2016.

[49] S. Li, G. Miao, D. Cao, Q. Li, J. Xu, Z. Wen, Y. Dai, S. Yan, and g. Lu, "Stress-enhanced interlayer exchange coupling and optical-mode FMR frequency in self-bias FeCoB/Ru/FeCoB trilayers," *ACS Applied Materials & Interfaces*, vol. 10, no. 10, pp. 8853–8859, 2018.

[50] I. Maksymov and M. Kostylev, "Broadband stripline ferromagnetic resonance spectroscopy of ferromagnetic films, multilayers and nanostructures," *Physica E: Low-dimensional Systems and Nanostructures*, vol. 69, pp. 253–293, 2015.

[51] H. Waring, N. Johansson, I. Vera-Marun, and T. Thomson, "Zero-field optic mode beyond 20 GHz in a synthetic antiferromagnet," *Physical Review Applied*, vol. 13, no. 3, p. 034 035, 2020.

[52] H. Waring, Y. Li, C. Moutafis, I. Vera-Marun, and T. Thomson, "Magnetization dynamics in synthetic ferromagnetic thin films," *Physical Review B*, vol. 104, no. 1, p. 014 419, 2021.

[53] J. Coey, "Magnetism in future," *Journal of Magnetism and Magnetic Materials*, vol. 226, pp. 2107–2112, 2001.

[54] J. Coey, "Permanent magnetism," *Solid State Communications*, vol. 102, no. 2-3, pp. 101–105, 1997.

[55] W. Gilbert, *De magnete*. Courier Corporation, 1958.

[56] J. Maxwell, *A treatise on electricity and magnetism*. Clarendon press, 1873, vol. 1.

[57] R. O'handley, *Modern magnetic materials: Principles and applications*. Wiley, 2000.

[58] J. Stewart, "The moment of momentum accompanying magnetic moment in iron and nickel," *Physical Review*, vol. 11, no. 2, p. 100, 1918.

[59] W. Gerlach and O. Stern, "Der experimentelle nachweis der richtungsquantelung im magnetfeld," *Zeitschrift für Physik*, vol. 9, no. 1, pp. 349–352, 1922.

[60] G. Uhlenbeck and S. Goudsmit, "Ersetzung der hypothese vom unmechanischen zwang durch eine forderung bezüglich des inneren verhaltens jedes einzelnen elektrons," *Naturwissenschaften*, vol. 13, p. 953, 1925.

[61] P. Kusch and H. Foley, "The magnetic moment of the electron," *Physical Review*, vol. 74, no. 3, p. 250, 1948.

[62] N. Bohr, "Studies on the electron theory of metals," Ph.D. dissertation, University Of Copenhagen, 1911.

[63] H. van Leeuwen, "Doctoral thesis," Ph.D. dissertation, University Of Leiden, 1911.

[64] C. Kittel and P. McEuen, *Introduction to solid state physics*. Wiley New York, 1976, vol. 8.

[65] J. Leliaert, M. Dvornik, J. Mulkers, J. De Clercq, M. Milošević, and B. Van Waeyenberge, "Fast micromagnetic simulations on GPU-recent advances made with Mumax^3," *Journal of Physics D: Applied Physics*, vol. 51, no. 12, p. 123 002, 2018.

[66] C. Stefanita, *Magnetism: Basics and applications*. Springer Science & Business Media, 2012.

[67] R. Cardias, A. Szilva, A. Bergman, I. Di Marco, M. Katsnelson, A. Lichtenstein, L. Nordström, A. Klautau, O. Eriksson, and Y. Kvashnin, "The bethe-slater curve revisited; new insights from electronic structure theory," *Scientific Reports*, vol. 7, no. 1, pp. 1–11, 2017.

[68] S. Klingler, A. Chumak, T. Mewes, B. Khodadadi, C. Mewes, C. Dubs, O. Surzhenko, B. Hillebrands, and A. Conca, "Measurements of the exchange stiffness of YIG films using broadband ferromagnetic resonance techniques," *Journal of Physics D: Applied Physics*, vol. 48, no. 1, p. 015 001, 2014.

[69] H. Nosé, "Exchange integral in Ni and its alloy film from spin wave resonance," *Journal of the Physical Society of Japan*, vol. 16, no. 12, pp. 2475–2481, 1961.

[70] G. Abo, Y. Hong, J. Park, J. Lee, W. Lee, and B. Choi, "Definition of magnetic exchange length," *IEEE Transactions on Magnetics*, vol. 49, no. 8, pp. 4937–4939, 2013.

[71] G. Woltersdorf, "Spin-pumping and two-magnon scattering in magnetic multilayers," Ph.D. dissertation, Simon Fraser University, 2004.

[72] C. Bilzer, "Microwave susceptibility of thin ferromagnetic films: Metrology and insight into magnetization dynamics," Ph.D. dissertation, 2007.

[73] L. Néel, "Anisotropie magn etiquesuperficielle et surstructures d'orientation.," *Journal de Physique et le Radium*, vol. 15, no. 4, 225–239, 1954.

[74] H. Williams, R. Bozorth, and W. Shockley, "Magnetic domain patterns on single crystals of silicon iron," *Physical Review*, vol. 75, no. 1, p. 155, 1949.

[75] F. Bloch, "Zur theorie des ferromagnetismus," *Zeitschrift für Physik*, vol. 61, no. 3-4, pp. 206–219, 1930.

[76] E. Bhatia, Z. Barber, I. Maasilta, and K. Senapati, "Domain wall induced modulation of low field ht phase diagram in patterned superconductor-ferromagnet stripes," *AIP Advances*, vol. 9, no. 4, p. 045 107, 2019.

[77] E. Stoner and E. Wohlfarth, "A mechanism of magnetic hysteresis in heterogeneous alloys," *Philosophical Transactions of the Royal Society of London. Series A, Mathematical and Physical Sciences*, vol. 240, no. 826, pp. 599–642, 1948.

[78] C. Tannous and J. Gieraltowski, "The Stoner–Wohlfarth model of ferromagnetism," *European Journal of Physics*, vol. 29, no. 3, p. 475, 2008.

[79] H. Zabel, "Progress in spintronics," *Superlattices and microstructures*, vol. 46, no. 4, pp. 541–553, 2009.

[80] Y. Tian and S. Yan, "Giant magnetoresistance: History, development and beyond," *Science China Physics, Mechanics and Astronomy*, vol. 56, no. 1, pp. 2–14, 2013.

[81] G. Binasch, P. Grünberg, F. Saurenbach, and W. Zinn, "Enhanced magnetoresistance in layered magnetic structures with antiferromagnetic interlayer exchange," *Physical Review B*, vol. 39, no. 7, p. 4828, 1989.

[82] S. Parkin, N. More, and K. Roche, "Oscillations in exchange coupling and magnetoresistance in metallic superlattice structures: Co/Ru, Co/Cr, and Fe/Cr," *Physical Review Letters*, vol. 64, no. 19, p. 2304, 1990.

[83] M. Ruderman and C. Kittel, "Indirect exchange coupling of nuclear magnetic moments by conduction electrons," *Physical Review*, vol. 96, no. 1, p. 99, 1954.

[84] M. Stiles, "Interlayer exchange coupling," *Journal of Magnetism and Magnetic Materials*, vol. 200, no. 1-3, pp. 322–337, 1999.

[85] D. Mills and J. Bland, *Nanomagnetism: ultrathin films, multilayers and nanostructures*. Elsevier, 2006.

[86] J. de Vries, "Interlayer exchange coupling in magnetic multilayers: A systematic experimental study.," Ph.D. dissertation, 1998.

[87] M. Stiles, *Ultrathin Magnetic Structures III: Fundamentals of Nanomagnetism*. Wiley, 2005.

[88] R. Coehoorn, "Period of oscillatory exchange interactions in Co/Cu and Fe/Cu multilayer systems," *Physical Review B*, vol. 44, no. 17, p. 9331, 1991.

[89] P. Bruno, "Theory of intrinsic and thermally induced interlayer magnetic coupling between ferromagnetic films separated by an insulating layer," *Physical Review B*, vol. 49, no. 18, p. 13 231, 1994.

[90] S. Demokritov, "Biquadratic interlayer coupling in layered magnetic systems," *Journal of Physics D: Applied Physics*, vol. 31, no. 8, p. 925, 1998.

[91] J. Slonczewski, "Fluctuation mechanism for biquadratic exchange coupling in magnetic multilayers," *Physical Review Letters*, vol. 67, no. 22, p. 3172, 1991.

[92] S. Demokritov, E. Tsymbal, P. Grünberg, W. Zinn, and I. Schuller, "Magnetic-dipole mechanism for biquadratic interlayer coupling," *Physical Review B*, vol. 49, no. 1, p. 720, 1994.

[93] H. Zabel and S. Bader, "Magnetic heterostructures: Advances and perspectives in spin structures and spin transport," 2007.

[94] J. Bobo, H. Kikuchi, O. Redon, E. Snoeck, M. Piecuch, and R. White, "Pinholes in antiferromagnetically coupled multilayers: Effects on hysteresis loops and relation to biquadratic exchange," *Physical Review B*, vol. 60, no. 6, p. 4131, 1999.

[95] Q. Leng, V. Cros, R. Schäfer, A. Fuss, P. Grünberg, and W. Zinn, "Interlayer coupling across noble metal spacers," *Journal of Magnetism and Magnetic Materials*, vol. 126, no. 1-3, pp. 367–373, 1993.

[96] P. Bloemen, "Interlayer exchange coupling and giant magnetoresistance in magnetic multilayers," *Acta Physica Polonica A*, vol. 89, pp. 277–300, 1996.

[97] P. Bruno, "Theory of interlayer exchange interactions in magnetic multilayers," *Journal of Physics: Condensed Matter*, vol. 11, no. 48, p. 9403, 1999.

[98] Y. Lu, R. Altman, A. Marley, S. Rishton, P. Trouilloud, G. Xiao, W. Gallagher, and S. Parkin, "Shape-anisotropy-controlled magnetoresistive response in magnetic tunnel junctions," *Applied Physics Letters*, vol. 70, no. 19, pp. 2610–2612, 1997.

[99] K. Moon, R. Fontana Jr, and S. Parkin, "Exchange-biased magnetic tunnel junctions: Dependence of offset field on junction width," *Applied Physics Letters*, vol. 74, no. 24, pp. 3690–3692, 1999.

[100] H. Fuller and D. Sullivan, "Magnetostatic interactions between thin magnetic films," in *Proceedings of the Seventh Conference on Magnetism and Magnetic Materials*, Springer, 1962, pp. 1063–1064.

[101] L. Néel, "Sur un nouveau mode de couplage entre les aimantations de deux couches minces ferromagnétiques," *Comptes rendus de l'Académie des Sciences*, vol. 255, p. 1676, 1962.

[102] J. Zhang and R. White, "Topological coupling in magnetic multilayer films," *Journal of Applied Physics*, vol. 79, no. 8, pp. 5113–5115, 1996.

[103] J. Kools, W Kula, D. Mauri, and T. Lin, "Effect of finite magnetic film thickness on Néel coupling in spin valves," *Journal of Applied Physics*, vol. 85, no. 8, pp. 4466–4468, 1999.

[104] J. Langer, R. Mattheis, B. Ocker, W. Maaß, S. Senz, D. Hesse, and J. Kräußlich, "Microstructure and magnetic properties of sputtered spin valve systems," *Journal of Applied Physics*, vol. 90, no. 10, pp. 5126–5134, 2001.

[105] E. Hill, S. Tomlinson, and J. Li, "The role of dipole coupling in multilayers," *Journal of Applied Physics*, vol. 73, no. 10, pp. 5978–5980, 1993.

[106] M. Parker, S. Hossain, D. Seale, J. Barnard, M. Tan, and H. Fujiwara, "Low-field giant magnetoresistance in Co/Cu, CoFe/Cu and CoNiFe/Cu multilayer systems," *IEEE Transactions on Magnetics*, vol. 30, no. 2, pp. 358–363, 1994.

[107] S. Azzawi, A. Hindmarch, and D. Atkinson, "Magnetic damping phenomena in ferromagnetic thin-films and multilayers," *Journal of Physics D: Applied Physics*, vol. 50, no. 47, p. 473 001, 2017.

[108] A. Meyer and G. Asch, "Experimental g' and g values of Fe, Co, Ni, and their alloys," *Journal of Applied Physics*, vol. 32, no. 3, S330–S333, 1961.

[109] G. Scott, "Magnetomechanical determination of gyromagnetic ratios," *Journal of the Physical Society of Japan*, vol. 17, pp. 372–375, 1962.

[110] R. Reck and D. Fry, "Orbital and spin magnetization in Fe-Co, Fe-Ni, and Ni-Co," *Physical Review*, vol. 184, no. 2, p. 492, 1969.

[111] M. Singh, J. Callaway, and C. Wang, "Calculation of g and g' for iron and nickel," *Physical Review B*, vol. 14, no. 3, p. 1214, 1976.

[112] C. Kittel, "On the gyromagnetic ratio and spectroscopic splitting factor of ferromagnetic substances," *Physical Review*, vol. 76, no. 6, p. 743, 1949.

[113] J. Van Vleck, "Concerning the theory of ferromagnetic resonance absorption," *Physical Review*, vol. 78, no. 3, p. 266, 1950.

[114] L. Landau and E. Lifshitz, "On the theory of the dispersion of magnetic permeability in ferromagnetic bodies," in *Perspectives in Theoretical Physics*, Elsevier, 1992, pp. 51–65.

[115] T. Gilbert, "A phenomenological theory of damping in ferromagnetic materials," *IEEE Transactions on Magnetics*, vol. 40, no. 6, pp. 3443–3449, 2004.

[116] A. Gurevich and G. Melkov, *Magnetization oscillations and waves*. CRC press, 1996.

[117] I. Neudecker, "Magnetization dynamics of confined ferromagnetic systems," Ph.D. dissertation, 2006.

[118] D. Polder, "On the quantum theory of ferromagnetic resonance," *Physical Review*, vol. 73, no. 9, p. 1116, 1948.

[119] S. Chikazumi, "Magnetism-from fundamentals to nanoscale dynamics," *New York: Oxford University Press,*, 1999.

[120] A. Rinkevich, D. Perov, and O. Nemytova, "Magnetic antiresonance in nanocomposite materials," *Advanced Magnetic and Optical Materials*, pp. 47–79, 2016.

[121] W. Yager, "Additional ferromagnetic resonance absorption measurements on supermalloy," *Physical Review*, vol. 75, no. 2, p. 316, 1949.

[122] O. Acher and A. Adenot, "Bounds on the dynamic properties of magnetic materials," *Physical Review B*, vol. 62, no. 17, p. 11 324, 2000.

[123] C. Bilzer, T. Devolder, J. Kim, G. Counil, C. Chappert, S. Cardoso, and P. Freitas, "Study of the dynamic magnetic properties of soft CoFeB films," *Journal of Applied Physics*, vol. 100, no. 5, p. 053 903, 2006.

[124] T. Rossing, "Resonance linewidth and anisotropy variation in thin films," *Journal of Applied Physics*, vol. 34, no. 4, pp. 995–995, 1963.

[125] S. Kalarickal, P. Krivosik, M. Wu, C. Patton, P. Schneider M.L.and Kabos, T. Silva, and J. Nibarger, "Ferromagnetic resonance linewidth in metallic thin films: Comparison of measurement methods," *Journal of Applied Physics*, vol. 99, no. 9, p. 093 909, 2006.

[126] W. Platow, A. Anisimov, G. Dunifer, M. Farle, and K. Baberschke, "Correlations between ferromagnetic-resonance linewidths and sample quality in the study of metallic ultrathin films," *Physical Review B*, vol. 58, no. 9, p. 5611, 1998.

[127] J. Fermin, A. Azevedo, F. De Aguiar, B. Li, and S. Rezende, "Ferromagnetic resonance linewidth and anisotropy dispersions in thin Fe films," *Journal of Applied Physics*, vol. 85, no. 10, pp. 7316–7320, 1999.

[128] M. Seavey Jr and P. Tannenwald, "Direct observation of spin-wave resonance," *Physical Review Letters*, vol. 1, no. 5, p. 168, 1958.

[129] A. Chumak, V. Vasyuchka, A. Serga, and B. Hillebrands, "Magnon spintronics," *Nature Physics*, vol. 11, no. 6, pp. 453–461, 2015.

[130] V. Demidov, S. Urazhdin, G. De Loubens, O. Klein, V. Cros, A. Anane, and S. Demokritov, "Magnetization oscillations and waves driven by pure spin currents," *Physics Reports*, vol. 673, pp. 1–31, 2017.

[131] H. Yu, O. Kelly, V. Cros, R. Bernard, P. Bortolotti, A. Anane, F. Brandl, R. Huber, I. Stasinopoulos, and D. Grundler, "Magnetic thin-film insulator with ultra-low spin wave damping for coherent nanomagnonics," *Scientific Reports*, vol. 4, no. 1, pp. 1–5, 2014.

[132] J. Owens, J. Collins, and R. Carter, "System applications of magnetostatic wave devices," *Circuits, Systems and signal processing*, vol. 4, no. 1-2, pp. 317–334, 1985.

[133] J. Adam, "Analog signal processing with microwave magnetics," *Proceedings of the IEEE*, vol. 76, no. 2, pp. 159–170, 1988.

[134] L. Walker, "Magnetostatic modes in ferromagnetic resonance," *Physical Review*, vol. 105, no. 2, p. 390, 1957.

[135] D. Stancil, "Propagation characteristics and excitation of magnetostatic waves," in *Theory of Magnetostatic Waves*, Springer, 1993, pp. 119–153.

[136] C. Herring and C. Kittel, "On the theory of spin waves in ferromagnetic media," *Physical Review*, vol. 81, no. 5, p. 869, 1951.

[137] R. Arias, "Spin-wave modes of ferromagnetic films," *Physical Review B*, vol. 94, no. 13, p. 134 408, 2016.

[138] C. Kittel, "Excitation of spin waves in a ferromagnet by a uniform rf field," *Physical Review*, vol. 110, no. 6, p. 1295, 1958.

[139] P. Wigen, C. Kooi, M. Shanabarger, and T. Rossing, "Dynamic pinning in thin-film spin-wave resonance," *Physical Review Letters*, vol. 9, no. 5, p. 206, 1962.

[140] A. Portis, "Low-lying spin wave modes in ferromagnetic films," *Applied Physics Letters*, vol. 2, no. 4, pp. 69–71, 1963.

[141] K. Zakeri, J. Lindner, I. Barsukov, R. Meckenstock, M. Farle, U. Von Hörsten, H. Wende, W. Keune, J. Rocker, S. Kalarickal, and K. Lenz, "Spin dynamics in ferromagnets: Gilbert damping and two-magnon scattering," *Physical Review B*, vol. 76, no. 10, p. 104 416, 2007.

[142] H. Suhl, "Theory of the magnetic damping constant," *IEEE Transactions on Magnetics*, vol. 34, no. 4, pp. 1834–1838, 1998.

[143] A. Azevedo, A. Oliveira, F. De Aguiar, and S. Rezende, "Extrinsic contributions to spin-wave damping and renormalization in thin $Ni_{50}Fe_{50}$ films," *Physical Review B*, vol. 62, no. 9, p. 5331, 2000.

[144] P. Kuświk, H. Głowiński, E. Coy, J. Dubowik, and F. Stobiecki, "Perpendicularly magnetized $Co_{20}Fe_{60}B_{20}$ layer sandwiched between Au with low Gilbert damping," *Journal of Physics: Condensed Matter*, vol. 29, no. 43, p. 435 803, 2017.

[145] A. Barman and J. Sinha, *Spin dynamics and damping in ferromagnetic thin films and nanostructures*. Springer, 2018, vol. 1.

[146] I. Tudosa, J. Katine, S. Mangin, and E. Fullerton, "Perpendicular spin-torque switching with a synthetic antiferromagnetic reference layer," *Applied Physics Letters*, vol. 96, no. 21, p. 212 504, 2010.

[147] J. Slonczewski, "Current-driven excitation of magnetic multilayers," *Journal of Magnetism and Magnetic Materials*, vol. 159, no. 1, p. L1, 1996.

[148] M. Schoen, D. Thonig, M. Schneider, T. Silva, H. Nembach, O. Eriksson, O. Karis, and J. Shaw, "Ultra-low magnetic damping of a metallic ferromagnet," *Nature Physics*, vol. 12, no. 9, pp. 839–842, 2016.

[149] S. Wolf, D. Awschalom, R. Buhrman, J. Daughton, V. von Molnár, M. Roukes, A. Chtchelkanova, and D. Treger, "Spintronics: A spin-based electronics vision for the future," *science*, vol. 294, no. 5546, pp. 1488–1495, 2001.

[150] C. Chappert, A. Fert, and F. Van Dau, "The emergence of spin electronics in data storage," *Nanoscience And Technology: A Collection of Reviews from Nature Journals*, pp. 147–157, 2010.

[151] P. Villard, U. Ebels, D. Houssameddine, J. Katine, D. Mauri, B. Delaet, P. Vincent, M. Cyrille, B. Viala, J. Michel, and P. J., "A GHz spintronic-based RF oscillator," *IEEE Journal of Solid-State Circuits*, vol. 45, no. 1, pp. 214–223, 2009.

[152] S. Lee, U. Pi, K. Kim, K. Kim, J. Shin, and U. Chung, "Current driven magnetic damping in dipolar-coupled spin system," *Scientific Reports*, vol. 2, no. 1, pp. 1–7, 2012.

[153] R. Arias and D. Mills, "Extrinsic contributions to the ferromagnetic resonance response of ultrathin films," *Physical Review B*, vol. 60, no. 10, p. 7395, 1999.

[154] K. Ounadjela and B. Hillebrands, *Spin dynamics in confined magnetic structures II*, 2003.

[155] M. Sparks, R. Loudon, and C. Kittel, "Ferromagnetic relaxation. I. Theory of the relaxation of the uniform precession and the degenerate spectrum in insulators at low temperatures," *Physical Review*, vol. 122, no. 3, p. 791, 1961.

[156] D. Mills and S. Rezende, "Spin damping in ultrathin magnetic films," in *Spin Dynamics in Confined Magnetic Structures II*, Springer, 2003, pp. 27–59.

[157] W. Ament and G. Rado, "Electromagnetic effects of spin wave resonance in ferromagnetic metals," *Physical Review*, vol. 97, no. 6, p. 1558, 1955.

[158] B. Heinrich, J. Cochran, and R. Hasegawa, "Fmr line broadening in metals due to two-magnon scattering," *Journal of Applied Physics*, vol. 57, no. 8, pp. 3690–3692, 1985.

[159] B. Heinrich, "Spin relaxation in magnetic metallic layers and multilayers," in *Ultrathin Magnetic Structures III*, Springer, 2005, pp. 143–210.

[160] N. Bloembergen and S. Wang, "Relaxation effects in para-and ferromagnetic resonance," *Physical Review*, vol. 93, no. 1, p. 72, 1954.

[161] L. Berger, "Emission of spin waves by a magnetic multilayer traversed by a current," *Physical Review B*, vol. 54, no. 13, p. 9353, 1996.

[162] A. Brataas, Y. Tserkovnyak, G. Bauer, and B. Halperin, "Spin battery operated by ferromagnetic resonance," *Physical Review B*, vol. 66, no. 6, p. 060 404, 2002.

[163] A. Brataas, Y. Nazarov, and G. Bauer, "Finite-element theory of transport in ferromagnet-normal metal systems," *Physical Review Letters*, vol. 84, no. 11, p. 2481, 2000.

[164] M. Tokaç, S. Bunyaev, G. Kakazei, D. Schmool, D. Atkinson, and A. Hindmarch, "Interfacial structure dependent spin mixing conductance in cobalt thin films," *Physical Review Letters*, vol. 115, no. 5, p. 056 601, 2015.

[165] Y. Liu, Z. Yuan, R. Wesselink, A. Starikov, and P. Kelly, "Interface enhancement of Gilbert damping from first principles," *Physical Review Letters*, vol. 113, no. 20, p. 207 202, 2014.

[166] J. Rojas-Sánchez, N. Reyren, P. Laczkowski, W. Savero, J. Attané, C. Deranlot, M. Jamet, J. George, L. Vila, and H. Jaffrès, "Spin pumping and inverse spin hall effect in platinum: The essential role of spin-memory loss at metallic interfaces," *Physical Review Letters*, vol. 112, no. 10, p. 106 602, 2014.

[167] K. Chen and S. Zhang, "Spin pumping in the presence of spin-orbit coupling," *Physical Review Letters*, vol. 114, no. 12, p. 126 602, 2015.

[168] W. Zhang, W. Han, X. Jiang, S. Yang, and S. Parkin, "Role of transparency of platinum–ferromagnet interfaces in determining the intrinsic magnitude of the spin Hall effect," *Nature Physics*, vol. 11, no. 6, pp. 496–502, 2015.

[169] T. Gerrits, M. Schneider, and T. Silva, "Enhanced ferromagnetic damping in Permalloy/ Cu bilayers," *Journal of Applied Physics*, vol. 99, no. 2, p. 023 901, 2006.

[170] S. Sorokin, R. Gallardo, C. Fowley, K. Lenz, A. Titova, G. Atcheson, G. Dennehy, K. Rode, J. Fassbender, J. Lindner, and A. Deac, "Magnetization dynamics in synthetic antiferromagnets: Role of dynamical energy and mutual spin pumping," *Physical Review B*, vol. 101, no. 14, p. 144 410, 2020.

[171] P. Wigen, Z. Zhang, L. Zhou, M. Ye, and J. Cowen, "The dispersion relation in antiparallel coupled ferromagnetic films," *Journal of Applied Physics*, vol. 73, no. 10, pp. 6338–6340, 1993.

[172] S. Rezende, C. Chesman, M. Lucena, A. Azevedo, F. De Aguiar, and S. Parkin, "Studies of coupled metallic magnetic thin-film trilayers," *Journal of Applied Physics*, vol. 84, no. 2, pp. 958–972, 1998.

[173] B. Heinrich, Y. Tserkovnyak, G. Woltersdorf, A. Brataas, R. Urban, and G. Bauer, "Dynamic exchange coupling in magnetic bilayers," *Physical Review Letters*, vol. 90, no. 18, p. 187 601, 2003.

[174] K. Tanaka, T. Moriyama, M. Nagata, T. Seki, K. Takanashi, S. Takahashi, and T. Ono, "Linewidth broadening of optical precession mode in synthetic antiferromagnet," *Applied Physics Express*, vol. 7, no. 6, p. 063 010, 2014.

[175] G. Bräuer, B. Szyszka, M. Vergöhl, and R. Bandorf, "Magnetron sputtering–Milestones of 30 years," *Vacuum*, vol. 84, no. 12, pp. 1354–1359, 2010.

[176] R. Parsons, "Sputter deposition processes," *Thin Film Processes II*, vol. 2, p. 177, 1991.

[177] M. Waite, S. Shah, and D. Glocker, "Sputtering sources," *SVC Bulletin, No. Spring*, vol. 2010, pp. 42–50, 2010.

[178] J. Thornton, "High rate thick film growth," *Annual Review of Materials Science*, vol. 7, no. 1, pp. 239–260, 1977.

[179] J. Oliver, "Analysis of a planetary-rotation system for evaporated optical coatings," *Applied optics*, vol. 55, no. 30, pp. 8550–8555, 2016.

[180] R. Waits, "Planar magnetron sputtering," *Journal of Vacuum Science and Technology*, vol. 15, no. 2, pp. 179–187, 1978.

[181] S. Shah, *Handbook of thin film process technology*. Institute of Physics Publishing, 1995.

[182] S. Rossnagel, J. Vossen, and W. Kern, "Thin film processes II," *Thin Film Processes II*, vol. 2, p. 7, 1991.

[183] E. G. and W. W., *Handbook of Thin Film Process Technology: 98/1 Reactive Sputtering*. IOP Publishing, 1998.

[184] *AJA International: ATC Flagship Series Sputtering Systems.* `http://www.ajaint.com/atc-series-sputtering-systems.html` Last accessed on 2020-08-04.

[185] J. Mallison, "Gettering of gas by titanium," *Journal of Physics*, vol. 26, no. 1488, pp. 550–557, 1955.

[186] C. Saw, W. Grant, J. Stanford, and L. Dinh, "An investigation on X-ray reflectivity technique at LLNL," Lawrence Livermore National Lab(LLNL), Livermore, CA (United States), Tech. Rep., 2016.

[187] E. Chason and T. Mayer, "Thin film and surface characterization by specular X-ray reflectivity," *Critical Reviews in Solid State and Material Sciences*, vol. 22, no. 1, pp. 1–67, 1997.

[188] I. Hamley and J. Pedersen, "Analysis of neutron and X-ray reflectivity data. I. Theory," *Journal of Applied Crystallography*, vol. 27, no. 1, pp. 29–35, 1994.

[189] M. Björck and G. Andersson, "Genx: An extensible x-ray reflectivity refinement program utilizing differential evolution," *Journal of Applied Crystallography*, vol. 40, no. 6, pp. 1174–1178, 2007.

[190] D. Sivia, *Elementary scattering theory: for X-ray and neutron users*. Oxford University Press, 2011.

[191] A. Gibaud, G. Vignaud, and S. Sinha, "The correction of geometrical factors in the analysis of X-ray reflectivity," *Acta Crystallographica Section A: Foundations of Crystallography*, vol. 49, no. 4, pp. 642–648, 1993.

[192] M. Yasaka, "X-ray thin-film measurement techniques," *The Rigaku Journal*, vol. 26, no. 2, pp. 1–9, 2010.

[193] *Rigaku: Smartlab - intelligent X-ray diffraction (xrd) system.* `https://www.rigaku.com/en/products/xrd/smartlab` Last accessed on 2020-08-04.

[194] L. Parratt, "Surface studies of solids by total reflection of X-rays," *Physical Review*, vol. 95, no. 2, p. 359, 1954.

[195] M. Tolan, *X-ray scattering from soft-matter thin films: materials science and basic research*. Springer, 1999, vol. 148.

[196] R. Storn and K. Price, "Differential evolution-aa simple and efficient heuristic for global optimization over continuous spaces," *Journal of Global Optimization*, vol. 11, no. 4, pp. 341–359, 1997.

[197] K. Ounadjela and B. Hillebrands, *Https://genx.sourceforge.io/howtouse.html*, 2003.

[198] M. Björck, "A structural viewpoint of magnetism in Fe and Co based superlattices," Ph.D. dissertation, Acta Universitatis Upsaliensis, 2007.

[199] G. Binnig, C. Quate, and C. Gerber, "Atomic force microscope," *Physical Review Letters*, vol. 56, no. 9, p. 930, 1986.

[200] "Introduction to bruker's scanasyst and peakforce tapping afm technology," *Bruker application note. Bruker Nano Inc., Santa Barbara, CA*, 2011.

[201] P. Eaton and P. West, *Atomic force microscopy*. Oxford university press, 2010.

[202] *Bruker: FastScan-A*, `https://www.brukerafmprobes.com/p-3759-fastscan-a.aspx` Last accessed on 2021-02-20.

[203] S. Foner, "Versatile and sensitive vibrating-sample magnetometer," *Review of Scientific Instruments*, vol. 30, no. 7, pp. 548–557, 1959.

[204] T. Thomson, "Magnetic properties of metallic thin films," in *Metallic Films for Electronic, Optical and Magnetic Applications*, Elsevier, 2014, pp. 454–546.

[205] *Microsense: Vector magnetometer model 10 vsm.* `http://www.microsense.net/products-vsm-model-10.html` Last accessed on 2020-08-04.

[206] G. Lehner, *Electromagnetic field theory for engineers and physicists*. Springer Science & Business Media, 2010.

[207] *Model 10 Mk II vibrating sample magnetometer*, `http://www.microsense.net/9b6a11d9-8acb-4b96-bc03-4a1a4c3961cf/resource-center-downloads-delivery.htm` Last accessed on 2020-10-07.

[208] *South Bay Technology: Model 360 Abrasive Slurry Disc Cutter*, `http://www.southbaytech.com/shop/360.shtml` Last accessed on 2020-08-04.

[209] G. Paterson, X. Zhao, M. Jackson, and D. Heslop, "Measuring, processing, and analyzing hysteresis data," *Geochemistry, Geophysics, Geosystems*, vol. 19, no. 7, pp. 1925–1945, 2018.

[210] A. Aspelmeier, M. Tischer, M. Farle, M. Russo, K. Baberschke, and D. Arvanitis, "AC susceptibility measurements of magnetic monolayers: MCXD, MOKE, and mutual inductance," *Journal of magnetism and magnetic materials*, vol. 146, no. 3, pp. 256–266, 1995.

[211] S. Demokritov and V. Demidov, "Micro-brillouin light scattering spectroscopy of magnetic nanostructures," *IEEE Transactions on Magnetics*, vol. 44, no. 1, pp. 6–12, 2007.

[212] S. Bushnell, W. Nowak, S. Oliver, and C. Vittoria, "The measurement of magnetostriction constants of thin films using planar microwave devices and ferromagnetic resonance," *Review of scientific instruments*, vol. 63, no. 3, pp. 2021–2025, 1992.

[213] P. Fannin, T. Relihan, and S. Charles, "Investigation of ferromagnetic resonance in magnetic fluids by means of the short-circuited coaxial line technique," *Journal of Physics D: Applied Physics*, vol. 28, no. 10, p. 2003, 1995.

[214] M. Unwin, P. Haycock, S. Hoon, and P. Grannell, "A novel broadband ferromagnetic resonance spectrometer," *Journal of Magnetism and Magnetic Materials*, vol. 205, no. 2-3, pp. 199–208, 1999.

[215] C. Wen, "Coplanar waveguide: A surface strip transmission line suitable for nonreciprocal gyromagnetic device applications," *IEEE Transactions on Microwave Theory and Techniques*, vol. 17, no. 12, pp. 1087–1090, 1969.

[216] W. Barry, "A broad-band, automated, stripline technique for the simultaneous measurement of complex permittivity and permeability," *IEEE Transactions on Microwave Theory and Techniques*, vol. 34, no. 1, pp. 80–84, 1986.

[217] W. Weir, "Automatic measurement of complex dielectric constant and permeability at microwave frequencies," *Proceedings of the IEEE*, vol. 62, no. 1, pp. 33–36, 1974.

[218] W. Alayo, F. Pelegrini, and E. Baggio-Saitovitch, "Ferromagnetic resonance study of sputtered NiFe/V/NiFe heterostructures," *Journal of Magnetism and Magnetic Materials*, vol. 377, pp. 104–110, 2015.

[219] N. Johansson, "Interlayer exchange coupling in Co/Pd-NiFe Films studied by vector network analyser ferromagnetic resonance.," Ph.D. dissertation, The University of Manchester, 2018.

[220] *Model 425 gaussmeter user's manual. lake shore cryotronics.* https://www.lakeshore.com/docs/default-source/product-downloads/425manual.pdf?sfvrsn=71200aed_1 Last accessed on 2020-08-04.

[221] *N5224A pna microwave network analyzer, 43.5 Ghz.* https://www.keysight.com/en/pdx-x201876-pn-N5224A/pna-microwave-network-analyzer-435-ghz?cc=GB&lc=eng Last accessed on 2020-08-04.

[222] *Calibration substrate*, https://ggb.com/home/calibration-substrate/ Last accessed on 2020-08-04.

[223] T. Klemmer, K. Ellis, L. Chen, B. Van Dover, and S. Jin, "Ultrahigh frequency permeability of sputtered FeCoB thin films," *Journal of Applied Physics*, vol. 87, no. 2, pp. 830–833, 2000.

[224] C. Bilzer, T. Devolder, P. Crozat, C. Chappert, S. Cardoso, and P. Freitas, "Vector network analyzer ferromagnetic resonance of thin films on coplanar waveguides: Comparison of different evaluation methods," *Journal of Applied Physics*, vol. 101, no. 7, p. 074 505, 2007.

[225] E. Montoya, T. McKinnon, A. Zamani, E. Girt, and B. Heinrich, "Broadband ferromagnetic resonance system and methods for ultrathin magnetic films," *Journal of Magnetism and Magnetic Materials*, vol. 356, pp. 12–20, 2014.

[226] V. Flovik, F. Macià, A. Kent, and E. Wahlström, "Eddy current interactions in a ferromagnet-normal metal bilayer structure, and its impact on ferromagnetic resonance lineshapes," *Journal of Applied Physics*, vol. 117, no. 14, p. 143 902, 2015.

[227] H. Maier-Flaig, S. Goennenwein, R. Ohshima, M. Shiraishi, R. Gross, H. Huebl, and M. Weiler, "Note: Derivative divide, a method for the analysis of broadband ferromagnetic resonance in the frequency domain," *Review of Scientific Instruments*, vol. 89, no. 7, p. 076 101, 2018.

[228] M. Harder, Z. Cao, Y. Gui, X. Fan, and C.-M. Hu, "Analysis of the line-shape of electrically detected ferromagnetic resonance," *Physical Review B*, vol. 84, no. 5, p. 054 423, 2011.

[229] R. Topkaya, S. Kazan, R. Yilgin, N. Akdoğan, and B. Özdemir M.and Aktaş, "Ferromagnetic resonance studies of exchange biased CoO/Fe bilayer grown on MgO substrate," *Journal of Superconductivity and Novel Magnetism*, vol. 27, no. 6, pp. 1503–1512, 2014.

[230] *NanOsc: Wave guides*, `http://www.nanosc.se/wave-guides.html` Last accessed on 2021-02-20.

[231] "Introduction to network analyzer measurements:Fundamentals and background," National Instruments RF Academy, Tech. Rep., 2012.

[232] K. Kurokawa, "Power waves and the scattering matrix," *IEEE Transactions on Microwave Theory and Techniques*, vol. 13, no. 2, pp. 194–202, 1965.

[233] J. Dunsmore, *Handbook of microwave component measurements: with advanced VNA techniques*. John Wiley Sons, 2020.

[234] D. Kim, H. Kim, C. You, and H. Kim, "Optimization of ferromagnetic resonance spectra measuring procedure for accurate Gilbert damping parameter in magnetic thin films using a vector network analyzer," *Journal of Magnetics*, vol. 16, no. 3, pp. 206–210, 2011.

[235] F. Caspers, "Rf engineering basic concepts: S-parameters," *arXiv preprint arXiv:1201.2346*, 2012.

[236] O. Heaviside, "XIX. On the extra current," *The London, Edinburgh, and Dublin Philosophical Magazine and Journal of Science*, vol. 2, no. 9, pp. 135–145, 1876.

[237] R. Simons, *Coplanar waveguide circuits, components, and systems*. Wiley Online Library, 2001, vol. 15.

[238] J. Leliaert and J. Mulkers, "Tomorrow's micromagnetic simulations," *Journal of Applied Physics*, vol. 125, no. 18, p. 180 901, 2019.

[239] A. Vansteenkiste, J. Leliaert, M. Dvornik, M. Helsen, F. Garcia-Sanchez, and B. Van Waeyenberge, "The design and verification of Mumax^3," *AIP Advances*, vol. 4, no. 10, p. 107 133, 2014.

[240] S. Mazumder, *Numerical methods for partial differential equations: finite difference and finite volume methods*. Academic Press, 2016.

[241] T. Schrefl, D. Suess, W. Scholz, H. Forster, V. Tsiantos, and J. Fidler, "Finite element micromagnetics," in *Computational Electromagnetics*, Springer, 2003, pp. 165–181.

[242] R. Liu, J. Wang, Q. Liu, H. Wang, and C. Jiang, "Micromagnetic simulation of the magnetic spectrum of ferromagnetic nanowire," *Journal of Applied Physics*, vol. 103, no. 1, p. 013 910, 2008.

[243] A. Baker, M. Beg, G. Ashton, M. Albert, D. Chernyshenko, W. Wang, S. Zhang, M. Bisotti, M. Franchin, C. Hu, and S. R., "Proposal of a micromagnetic standard problem for ferromagnetic resonance simulations," *Journal of Magnetism and Magnetic Materials*, vol. 421, pp. 428–439, 2017.

[244] R. McMichael and M. Stiles, "Magnetic normal modes of nanoelements," *Journal of Applied Physics*, vol. 97, no. 10, 10J901, 2005.

[245] E. Brigham and R. Morrow, "The fast Fourier transform," *IEEE Spectrum*, vol. 4, no. 12, pp. 63–70, 1967.

[246] P. Mikheev, "Application of the fast Fourier transform to calculating pruned convolution," in *Doklady Mathematics*, Springer, vol. 92, 2015, pp. 630–633.

[247] W. Press, S. Teukolsky, W. Vetterling, and B. Flannery, *Numerical recipes 3rd edition: The art of scientific computing*. Cambridge university press, 2007.

[248] G. Gbur, *Mathematical methods for optical physics and engineering*. Cambridge University Press, 2011.

[249] T. Burkert, L. Nordström, O. Eriksson, and O. Heinonen, "Giant magnetic anisotropy in tetragonal FeCo alloys," *Physical Review Letters*, vol. 93, no. 2, p. 027 203, 2004.

[250] X. Liu, W. Zhang, M. Carter, and G. Xiao, "Ferromagnetic resonance and damping properties of CoFeB thin films as free layers in MgO-based magnetic tunnel junctions," *Journal of Applied Physics*, vol. 110, no. 3, p. 033 910, 2011.

[251] A. Conca, E. Papaioannou, S. Klingler, J. Greser, T. Sebastian, B. Leven, J. Lösch, and B. Hillebrands, "Annealing influence on the Gilbert damping parameter and the exchange constant of CoFeB thin films," *Applied Physics Letters*, vol. 104, no. 18, p. 182 407, 2014.

[252] M. Desai, A. Misra, and W. Doyle, "Effect of interface roughness on exchange coupling in synthetic antiferromagnetic multilayers," *IEEE transactions on magnetics*, vol. 41, no. 10, pp. 3151–3153, 2005.

[253] *Inorganic crystal structure database.* `https://icsd.psds.ac.uk/` Last accessed on 2020-08-04.

[254] L. Zhang, W. Zhang, X. Liu, Y. Wang, J. Bai, D. Wei, and F. Wei, "High frequency characteristics of synthetic antiferromagnetic coupling FeCoN sandwich films," *IEEE Transactions on Magnetics*, vol. 47, no. 10, pp. 3932–3934, 2011.

[255] N. Chowdhury and S. Bedanta, "Controlling the anisotropy and domain structure with oblique deposition and substrate rotation," *AIP advances*, vol. 4, no. 2, p. 027 104, 2014.

[256] S. Mallik, N. Chowdhury, and S. Bedanta, "Interplay of uniaxial and cubic anisotropy in epitaxial fe thin films on MgO (001) substrate," *AIP Advances*, vol. 4, no. 9, p. 097 118, 2014.

[257] A. Hindmarch, A. Rushforth, R. Campion, C. Marrows, and B. Gallagher, "Origin of in-plane uniaxial magnetic anisotropy in CoFeB amorphous ferromagnetic thin films," *Physical Review B*, vol. 83, no. 21, p. 212 404, 2011.

[258] S. Li, C. Wang, X. Chu, G. Miao, Q. Xue, W. Zou, M. Liu, J. Xu, Q. Li, Y. Dai, S. Yan, S. Kang, and Y. Long Y. Lü, "Engineering optical mode ferromagnetic resonance in FeCoB films with ultrathin Ru insertion," *Scientific reports*, vol. 6, no. 1, pp. 1–10, 2016.

[259] N. Wiese, T. Dimopoulos, M. Rührig, J. Wecker, H. Brückl, and G. Reiss, "Antiferromagnetically coupled CoFeB/Ru/CoFeB trilayers," *Applied Physics Letters*, vol. 85, no. 11, pp. 2020–2022, 2004.

[260] B. Heinrich, J. Cochran, M. Kowalewski, J. Kirschner, Z. Celinski, A. Arrott, and K. Myrtle, "Magnetic anisotropies and exchange coupling in ultrathin fcc Co (001) structures," *Physical Review B*, vol. 44, no. 17, p. 9348, 1991.

[261] C. Wang, S. Zhang, S. Qiao, H. Du, X. Liu, R. Sun, X. Chu, G. Miao, Y. Dai, S. Kang, and S. Yan, "Dual-mode ferromagnetic resonance in an FeCoB/Ru/FeCoB synthetic antiferromagnet with uniaxial anisotropy," *Applied Physics Letters*, vol. 112, no. 19, p. 192 401, 2018.

[262] K. Lee, M. Stiles, H. Lee, J. Moon, K. Kim, and S. Lee, "Self-consistent calculation of spin transport and magnetization dynamics," *Physics Reports*, vol. 531, no. 2, pp. 89–113, 2013.

[263] H. Yang, Y. Li, and W. Bailey, "Large spin pumping effect in antisymmetric precession of $Ni_{79}Fe_{21}$/Ru/$Ni_{79}Fe_{21}$," *Applied Physics Letters*, vol. 108, no. 24, p. 242 404, 2016.

[264] J. Nibarger, R. Lopusnik, Z. Celinski, and T. Silva, "Variation of magnetization and the Landé g factor with thickness in Ni-Fe films," *Applied Physics Letters*, vol. 83, no. 1, pp. 93–95, 2003.

[265] T. Devolder, E. Liu, J. Swerts, S. Couet, T. Lin, S. Mertens, A. Furnemont, G. Kar, and J. De Boeck, "Ferromagnetic resonance study of composite co/nifecob free layers with perpendicular anisotropy," *Applied Physics Letters*, vol. 109, no. 14, p. 142 408, 2016.

[266] T. McKinnon and E. Girt, "Exchange coupling in FeCoB/Ru, Mo/FeCoB trilayer structures," *Applied Physics Letters*, vol. 113, no. 19, p. 192 407, 2018.

[267] S. Yakata, H. Kubota, T. Seki, K. Yakushiji, A. Fukushima, S. Yuasa, and K. Ando, "Enhancement of thermal stability using ferromagnetically coupled synthetic free layers in MgO-based magnetic tunnel junctions," *IEEE Transactions on Magnetics*, vol. 46, no. 6, pp. 2232–2235, 2010.

[268] Y. Wang, W. Chen, S. Yang, K. Shen, C. Park, M. Kao, and M. Tsai, "Interfacial and annealing effects on magnetic properties of CoFeB thin films," *Journal of Applied Physics*, vol. 99, no. 8, p. 08M307, 2006.

[269] S. Jang, S. Lim, and S. Lee, "Magnetic dead layer in amorphous CoFeB layers with various top and bottom structures," *Journal of Applied Physics*, vol. 107, no. 9, p. 09C707, 2010.

[270] G. Stenning, L. Shelford, S. Cavill, F. Hoffmann, M. Haertinger, T. Hesjedal, G. Woltersdorf, G. Bowden, S. Gregory, C. Back, and P. De Groot, "Magnetization dynamics in an exchange-coupled NiFe/CoFe bilayer studied by X-ray detected ferromagnetic resonance," *New Journal of Physics*, vol. 17, no. 1, p. 013 019, 2015.

[271] D. Burn, S. Zhang, G. Yu, Y. Guang, H. Chen, X. Qiu, G. van der Laan, and T. Hesjedal, "Depth-resolved magnetization dynamics revealed by X-ray reflectometry ferromagnetic resonance," *Physical Review Letters*, vol. 125, no. 13, p. 137 201, 2020.

[272] C. Vaz, J. Bland, and G. Lauhoff, "Magnetism in ultrathin film structures," *Reports on Progress in Physics*, vol. 71, no. 5, p. 056 501, 2008.

[273] A. Navabi, C. Chen, A. Barra, M. Yazdani, G. Yu, M. Montazeri, M. Aldosary, J. Li, K. Wong, Q. Hu, and J. Shi, "Efficient excitation of high-frequency exchange-dominated spin waves in periodic ferromagnetic structures," *Physical Review Applied*, vol. 7, no. 3, p. 034 027, 2017.

[274] N. Smith, "Modeling of thermal magnetization fluctuations in thin-film magnetic devices," *Journal of Applied Physics*, vol. 90, no. 11, pp. 5768–5773, 2001.

[275] D. Gopman, J. Lau, K. Mohanchandra, K. Wetzlar, and G. Carman, "Determination of the exchange constant of $Tb_{0.3}Dy_{0.7}Fe_2$ by broadband ferromagnetic resonance spectroscopy," *Physical Review B*, vol. 93, no. 6, p. 064 425, 2016.

[276] S. Vernon, S. Lindsay, and M. Stearns, "Brillouin scattering from thermal magnons in a thin co film," *Physical Review B*, vol. 29, no. 8, p. 4439, 1984.

[277] X. Liu, R. Sooryakumar, C. Gutierrez, and G. Prinz, "Exchange stiffness and magnetic anisotropies in bcc $Fe_{1-x}Co_x$ alloys," *Journal of Applied Physics*, vol. 75, no. 10, pp. 7021–7023, 1994.

[278] X. Liu, M. Steiner, R. Sooryakumar, G. Prinz, R. Farrow, and G. Harp, "Exchange stiffness, magnetization, and spin waves in cubic and hexagonal phases of cobalt," *Physical Review B*, vol. 53, no. 18, p. 12 166, 1996.

[279] C. Kooi, P. Wigen, M. Shanabarger, and J. Kerrigan, "Spin-wave resonance in magnetic films on the basis of the surface-spin-pinning model and the volume inhomogeneity model," *Journal of Applied Physics*, vol. 35, no. 3, pp. 791–797, 1964.

[280] M. Belmeguenai, F. Zighem, Y. Roussigné, S. Chérif, P. Moch, K. Westerholt, G. Woltersdorf, and G. Bayreuther, "Microstrip line ferromagnetic resonance and Brillouin light scattering investigations of magnetic properties of Co_2MnGe heusler thin films," *Physical Review B*, vol. 79, no. 2, p. 024 419, 2009.

[281] B. Samantaray, A. Singh, C. Banerjee, A. Barman, A. Perumal, and P. Mandal, "Perpendicular standing spin wave and magnetic anisotropic study on amorphous FeTaC films," *IEEE Transactions on Magnetics*, vol. 52, no. 7, pp. 1–4, 2016.

[282] J. BenYoussef, H. Le Gall, N. Vukadinovic, V. Gehanno, A. Marty, Y. Samson, and B. Gilles, "Ferromagnetic resonance in epitaxial FePd thin films with perpendicular anisotropy," *Journal of Magnetism and Magnetic Materials*, vol. 202, no. 2-3, pp. 277–284, 1999.

[283] T. Rossing, "Spin-wave resonance in thin films at oblique angles," *Journal of Applied Physics*, vol. 34, no. 4, pp. 1133–1135, 1963.

[284] M. Nisenoff and R. Terhune, "Standing spin wave mode spectra in thin permalloy films prepared in vacuum of $10-7$ Torr," *Journal of Applied Physics*, vol. 36, no. 3, pp. 732–738, 1965.

[285] W. Kwiatkowski and S. Tumanski, "The permalloy magnetoresistive sensors-properties and applications," *Journal of Physics E: Scientific Instruments*, vol. 19, no. 7, p. 502, 1986.

[286] A. English and G. Chin, "Metallurgy and magnetic properties control in permalloy," *Journal of Applied Physics*, vol. 38, no. 3, pp. 1183–1187, 1967.

[287] M. Fitzsimmons, T. Silva, and T. Crawford, "Surface oxidation of permalloy thin films," *Physical Review B*, vol. 73, no. 1, p. 014 420, 2006.

[288] G. Nahrwold, J. M. Scholtyssek, O. Motl-Ziegler S.and Albrecht, U. Merkt, and G. Meier, "Structural, magnetic, and transport properties of permalloy for spintronic experiments," *Journal of Applied Physics*, vol. 108, no. 1, p. 013 907, 2010.

[289] J. Shaw, H. Nembach, T. Silva, and C. Boone, "Precise determination of the spectroscopic g-factor by use of broadband ferromagnetic resonance spectroscopy," *Journal of Applied Physics*, vol. 114, no. 24, p. 243 906, 2013.

[290] W. Meiklejohn and C. Bean, "New magnetic anisotropy," *Physical Review*, vol. 102, no. 5, p. 1413, 1956.

[291] P. Wigen, C. Kooi, M. Shanabarger, U. Cummings, and M. Baldwin, "Angular dependence of spin pinning in thin ferromagnetic films," *Journal of Applied Physics*, vol. 34, no. 4, pp. 1137–1139, 1963.

[292] J. De Clercq, J. Leliaert, and B. Van Waeyenberge, "Modelling compensated antiferromagnetic interfaces with Mumax^3," *Journal of Physics D: Applied Physics*, vol. 50, no. 42, p. 425 002, 2017.

[293] J. Thiele, L. Folks, M. Toney, and D. Weller, "Perpendicular magnetic anisotropy and magnetic domain structure in sputtered epitaxial FePt (001) L10 films," *Journal of Applied Physics*, vol. 84, no. 10, pp. 5686–5692, 1998.

[294] M. Oogane, H. Watanabe K.and Saruyama, M. Hosoda, P. Shahnaz, Y. Kurimoto, M. Kubota, and Y. Ando, "L10-ordered MnAl thin films with high perpendicular magnetic anisotropy," *Japanese Journal of Applied Physics*, vol. 56, no. 8, 0802A2, 2017.

[295] C. Cowache, B. Dieny, A. Chamberod, D. Benizri, F. Berthet, S. Auffret, L. Giacomoni, and S. Nossov, "Magnetic and transport properties of NiFe/Ag and Co/NiFe/Co/Ag multilayers," *Physical Review B*, vol. 53, no. 22, p. 15 027, 1996.

[296] D. Polishchuk, M. Persson, M. M. Kulyk, E. Holmgren, G. Pasquale, and V. Korenivski, "Tuning thermo-magnetic properties of dilute-ferromagnet multilayers using RKKY interaction," *Applied Physics Letters*, vol. 117, no. 2, p. 022 402, 2020.

[297] S. Parkin, "Dramatic enhancement of interlayer exchange coupling and giant magnetoresistance in $Ni_{81}Fe_{19}$/Cu multilayers by addition of thin Co interface layers," *Applied Physics Letters*, vol. 61, no. 11, pp. 1358–1360, 1992.